A THEORETICAL INVESTIGATION OF
ROLL COATING PHENOMENA

by

Harvey Morpeth Thompson

Submitted in accordance with the regulations for the degree of

Ph.D. in Applied Mathematics.

University of Leeds,

Department of Applied Mathematical Studies,

May 1992.

The candidate confirms that the work submitted is his own and that appropriate credit has been given where reference has been made to the work of others.

ABSTRACT

This thesis is primarily concerned with the theoretical modelling of steady, forward roll coating systems under different degrees of starvation by the use of analytical and numerical techniques.

The concept of 'starvation' in a two roll coater is introduced and three possibilities identified: the fully-flooded, moderately-starved and ultra-starved situations. An extensive literature survey of work related to the fully-flooded case is given, together with a discussion of the difficulties associated with, and application of finite element methods to, free surface coating flows.

Four models of ultra-starved roll coating are developed, the first of which neglects the flux between the rollers. The analytical solution of this first 'Zero Flux' model predicts streamlines and pressures that are in qualitative agreement with experiment. This model is refined further: first of all to allow a *small*, non-zero flux, then to enable prediction of the film thicknesses produced on the rollers during the forward case. The theoretical film thickness predictions agree well with Malone's [1992] experimental data. The final model also allows a small flux between the rollers, but retains all other assumptions of the 'Zero Flux' model. Streamline predictions from this last model agree well with experiment.

A FORTRAN finite element code is developed to solve free surface coating flows and is used to obtain film thickness ratio predictions in fully-flooded roll coating over a wider velocity ratio range than previously reported. These predictions agree reasonably well with Savage's [1992] model.

A numerical model of starvation in roll coating systems is developed and the predicted velocity and pressure fields are in qualitative agreement with both experimental observations and the analytical predictions for ultra-starved flow. Finally, numerical film thickness ratio predictions are obtained over the gamut of starvation: they are almost independent of the degree of starvation and are in good agreement with Malone's [1992] experimental data.

This thesis is dedicated to my parents,

George and Jenny

ACKNOWLEDGEMENTS

Contents

NOMENCLATURE

In some cases the use of a symbol is local to a short section of the text and is not listed here, in which case it is defined when first introduced. In certain other cases the · same notation has been given interpretations which vary from one chapter to another. Although the meaning should be clear from the text of the chapter concerned, the number of the chapter to which the particular interpretation applies is given in brackets after the explanation of the notation.

Unless otherwise stated, quantities written in upper case are physical, i.e. dimensional, whereas those in lower case are dimensionless.

A^*	Dimensionless aspect ratio of a rectangular cavity (for flow in lid-driven and open, driven cavities)
A_0	Local triangle
C	Position of the downstream fluid-air interface
Ca	Capillary number
Ca^*	Critical value of Ca for ribbing
$\underline{e}_i$	Spinal direction vectors
H_0	Semi-nip width in a two-roll coater or minimum gap in a flat plate/ roller geometry (Chapter 5)
H^*	Dimensionless cavity depth in the zero and small flux models
$H(X)$	Roller separation
$h(x)$	Dimensionless form of $H(X)$
$\underline{h}$	Spine heights
$\underline{\underline{J}}$	Global Jacobian matrix
$\underline{\underline{J}}^e$	Element-level Jacobian
L_i	Area co-ordinates
N_k	Quadratic shape functions
P	Fluid pressure
p	Dimensionless fluid pressure
$\bar{p}$	Average dimensionless pressure at the nip

p^*	Modified dimensionless pressure
P_a	Ambient air pressure
p_a	Dimensionless ambient air pressure
p_n	Upper right hand quadrant roots of $\sin 2p_n = 2p_n$
Q	Flow rate
Q_1, Q_2	Fluxes on the upper and lower rollers respectively
q	Dimensionless flow rate in a slot coater
R_1, R_2	Radii of upper and lower rollers respectively
$\overline{R}$	Average roller radius ($2/\overline{R} = 1/R_1 + 1/R_2$)
$\underline{R}$	Vector of finite element residuals
R_{curv}	Radius of curvature of a fluid-air interface
r	radial co-ordinate
r_{curv}	Dimensionless form of R_{curv}
Re	Reynolds number
S	Velocity ratio $S = V_1/V_2$ or X co-ordinate of separation point (Chapter 1)
St	Stokes number
s_n	Upper right hand quadrant roots of $\sin 2s_n = -2s_n$
T_1, T_2	Average thickness of uniform layers on upper and lower rollers respectively
T_0	Average inlet thickness in forward roll coating
T	Surface Tension
t_1, t_2, t_0	Dimensionless forms of T_1, T_2, T_0 respectively
U, V, W	Velocities of flow in X, Y, Z directions respectively
u, v, w	Dimensionless forms of U, V, W
V_1, V_2	Peripheral speeds of upper and lower rollers respectively
$\tilde{V}$	Peripheral speed of each roller in symmetric forward roll coating
$\overline{V}$	Average roller speed ($=(V_1 + V_2)/2$)
XM	Base line in mesh generation algorithm for roll coating
X_m	Dimensionless horizontal co-ordinate of XM
X, Y, Z	Global cartesian co-ordinates

x, y, z	Dimensionless global co-ordinates
Y_L^*	Location of top of lower vortex in forward meniscus roll coating
Y_U^*	Location of bottom of upper vortex in forward meniscus roll coating
α	Contact angle in the slot coater
$\underline{\alpha}$	Vector of finite element coefficients
β	Modified capillary number
$\underline{\beta}$	Vector of finite element coefficients for the flow field
$\partial\Omega$	Fluid boundary
η	Newtonian viscosity or local co-ordinate (Chapter 4 and Appendix B) or dimensionless vertical nip co-ordinate (Chapters 4 and 5)
θ	Modified x co-ordinate or azimuthal angle used in corner expansions (Appendix B)
θ_c	Apparent contact angle
$\mathcal{J}$	Local Jacobian matrix of an isoparametric mapping
λ	Dimensionless flow rate in roll coating
λ_1, λ_2	Dimensionless fluxes on upper and lower rollers respectively
λ_n	Eigenvalues in analytical solution of the zero flux model $(= (n - 1/2)\pi)$
ξ	Local co-ordinate
Π	Functional used to generate streamfunction-vorticity finite element equations
ρ	Fluid density
Σ_{ij}	Newtonian stress tensor
σ_{ij}	Dimensionless form of Σ_{ij}
$\phi_1^n, \tilde{\phi}_1^n$	Even and odd Papkovich-Fadle eigenfunctions respectively
Ψ	Streamfunction
ψ	Dimensionless streamfunction
ψ_i	Linear shape functions for pressure
Ω	Fluid domain
ω	Dimensionless vorticity

Chapter 1: General Introduction

Chapter 1

General Introduction

1.1 Applications of Coating Processes

Coating processes arise in many areas of the chemical engineering industry. These include the coating of paper, fabrics and metal sheets as well as the production of adhesive tapes, surgical dressings and photographic film. Coating flows are small-scale, viscous, free surface flows in which a film of liquid is continuously deposited on a deformable or rigid moving substrate (the web). The preferred flows are steady and deposit a uniformly thin layer devoid of imperfections of any kind.

The problem of applying a thin liquid layer is by no means trivial since the specifications of coating thickness are often very strict and, for productivity reasons, a high speed of application may be required. Moreover, several discrete layers may have to be applied simultaneously.

The geometry of the coating process varies with the application; industrial coating operations come in great variety: dip-, bead-, knife-, forward and reverse roll-, slide- and curtain-coating are illustrated in Figure 1.1. Each one shares common features such as free surfaces and/or wetting lines (see §1.3). Although this thesis is primarily concerned with an investigation of roll coating it is clear that the techniques developed, in particular the free surface code described in Chapter 4, will also be applicable to many different coating processes.

1.2   The Two Roll Coater

1.2.1   Introduction

The two roll coating process, by which a thin liquid film is laid down on a moving web, is illustrated in Figures 1.2 (a) and (b). The lower roller (often referred to as an applicator roller) is immersed in a bath of liquid while the second, upper roller, is aligned vertically above it such that there is a narrow, uniform gap between the roller surfaces. When the lower roller rotates liquid is transferred onto its surface by viscous lifting and flows into the 'nip' region (the 'nip' is the point of minimum roller separation) between the web and lower roller. A fraction of this liquid is transferred onto the web of material in contact with the upper roller and the remainder is returned to the bath via the lower roller. In a typical industrial process the liquid film on the coated web is subsequently dried or cured.

Industrial roll coating systems can be categorized into several distinct groups. For example, they can be operated in either forward (as shown in Figures 1.1 (e), 1.2 (a)) or reverse (Figure 1.1 (f)) mode and may have either (i) rigid (non-deformable), (ii) deformable (rubber-coated), or (iii) gravure (knurled/engraved) rollers. The theoretical predictions and experimental measurements reported in this thesis pertain to the forward mode of operation with rigid rollers. In this case it is observed that flow in the nip-region and sufficiently far from the ends of the rollers is essentially two-dimensional since the component of liquid velocity *parallel* to the roller axes, W, is small compared to those, i.e. (U, V), *perpendicular* to these axes (see e.g. Coyle [1984], Carter [1985], Malone [1992]). Moreover since it is the flow in the nip region which determines how the liquid splits into the two films shown in Figures 1.2 (a) and (b), the analyses of roll coating presented in this thesis are two-dimensional models of the flow in the nip region.

The usual mode of operation of a forward roll coater is that in which the clearance space at inlet is bathed in an ample supply of liquid; in this case the coater is said to be 'fully-flooded'. Figure 1.3 shows an experimentally-obtained view of the nip region of a fully-flooded forward roll coater, along the axis of the rollers, due to Malone

[1992]: the rollers are moving from left to right and the relatively bright regions are indicative of the meniscus positions. This picture clearly demonstrates the existence of a downstream, film-splitting meniscus and a bank of liquid extending far upstream of the nip. Malone [1992] used a dye injection technique to elucidate the nature of the flow in the upstream bank – see Figure 1.4. The presence of blue dye introduced into an optically clear oil revealed the existence of large eddies in the upstream bank.

A consequence of using fully-flooded roll coating is that, by a conservation of mass argument, the thickness of the films T_1, T_2 produced on the web and lower roller respectively are necessarily of the same order of magnitude as the minimum roller separation. However, practical engineering constraints limit this minimum separation to the order of 100 micrometres ($10^{-4}m$) (see Malone [1992]). Since all previous roll coating analysts have assumed that the inlet is always fully-flooded, this would seem to label roll coating as unsuitable for the production of uniform films whose thicknesses are significantly less than 100 micrometres. Fortunately, a different roll coating regime can be used which, although used in industry for a number of years, appears to have escaped the attention of the coating community at large. When very thin films are desired, for example, as in the manufacture of optical data storage equipment, it is possible to operate the roll coater under conditions in which the supply of liquid at inlet is less than that required to flood the inlet. In this case the coater is said to be 'starved' (c.f. Dowson and Taylor's [1979] work on the lubrication of bearings).

In fact it is possible to generate liquid films whose thicknesses are an order of magnitude less than the gap width by using the same coating geometry but with a much reduced inlet flux. This situation is illustrated in Figure 1.5, which shows that reducing the supply of liquid leads to the disappearance of the upstream bank giving rise instead to a second, inlet meniscus upstream of the nip and a 'bead' of liquid suspended in the nip region. In this case the coater is said to be 'ultra-starved'.

It is convenient to classify forward roll coating according to the inlet conditions. Three cases can be identified: 'fully-flooded', 'moderately-starved' (in which the supply of liquid is only slightly less than that required to flood the inlet) and 'ultra-starved' (when the supply has been significantly reduced), which are illustrated schematically

in Figures 1.6 (a)-(c), respectively. Previous work related to, and the salient features of, each case are now discussed.

1.2.2   The Fully-Flooded Case

Fully-flooded forward roll coating has been studied extensively. From his experiments, Taylor [1963] suggested that the flow field divides naturally into two parts : a two-dimensional portion in the immediate vicinity of the downstream, film-splitting meniscus, and a nearly rectilinear portion elsewhere. These observations have been reproduced by Malone [1992] – see Figure 1.7 – by injecting blue dye into the inlet film of a fully-flooded forward roll coater. In those regions which are relatively clear, little dye has been entrained; this indicates the presence of a recirculation in the flow. Hence the existence of eddies near the downstream meniscus is clearly demonstrated and the assumption of rectilinear flow is seen to be valid upstream of this recirculation region.

In fully-flooded roll coating the extent of the liquid upstream of the nip is large compared to $(\overline{R}H_0)^{\frac{1}{2}}$ – a typical length scale in the X-direction – where $\overline{R}$ is an 'average' roller radius defined by

$$\frac{1}{\overline{R}} = \frac{1}{2}\left(\frac{1}{R_1} + \frac{1}{R_2}\right) \tag{1.1}$$

and H_0 is the semi-nip width. Therefore it is usual to assume that the liquid extends to 'infinity' upstream of the nip and, as a result of this, lubrication theory is used to model the flow in a semi-infinite region extending from far upstream of the nip to the downstream recirculation region (Taylor [1963], Savage [1977 a, b]). In the symmetric case, with equal roller speeds, Savage [1984] employed Reynolds' lubrication equation for the pressure distribution $P(X, Y)$:

$$\frac{\partial}{\partial X}\left[H^3(X)\frac{\partial P}{\partial X}\right] + \frac{\partial}{\partial Y}\left[H^3(X)\frac{\partial P}{\partial Y}\right] = 12\eta\tilde{V}\frac{\partial H}{\partial X} \tag{1.2}$$

where P is the liquid pressure, $\tilde{V}$ the speed of each roller, η is the Newtonian viscosity and $H(X)$ the roller separation. In hydrodynamic lubrication, the normal procedure is to solve Reynolds' equation subject to two boundary conditions on liquid pressure. Assuming that the pressure is ambient sufficiently far upstream yields the first (upstream)

pressure condition

$$P(-\infty) = 0 \tag{1.3}$$

The second pressure condition is usually given by considering the balance of normal stresses at the downstream free surface (e.g. Greener and Middleman [1975], Savage [1982, 1984], Coyle, Macosko and Scriven [1986]). Referring to Figure 1.8 this condition, which relates the liquid pressure at $X = C$ to surface tension pressure at the liquid-air interface, yields (Batchelor [1985] pp 60-70)

$$P(X = C) = -\frac{\mathcal{T}}{R_{curv}} \tag{1.4}$$

where $\mathcal{T}$ is the surface tension of the liquid and R_{curv} is the effective radius of curvature of the downstream liquid-air interface at its leading edge.

Unfortunately, the location of the meniscus is unknown and in order to obtain a solution a further boundary condition is required. A major difficulty in applying the lubrication approximation to flow where a liquid-air interface forms, lies in supplying boundary conditions at the point of formation of the interface that are consistent with the lubrication approximation (Taylor [1963]). The first attempt to model a liquid-air cavity was made by Reynolds [1886] when he suggested the following conditions at rupture of the liquid film

$$P = 0 \ , \ \frac{\partial P}{\partial X} = 0 \tag{1.5}$$

Swift [1931] and Steiber [1933] independently derived the same condition as Reynolds and (1.5) is often referred to as the 'Swift-Steiber' condition. A new approach to modelling liquid-air interfaces was introduced by Birkhoff and Hays [1963], who suggested that the lubrication regime terminates at the 'separation' point $(S, \overline{Y})$ – see Figure 1.8 – which marks the onset of the reverse flow region and where both

$$U = 0 \ \text{and} \ \frac{\partial U}{\partial Y} = 0 \tag{1.6}$$

i.e., velocity and shear stress are zero. These 'separation' conditions are often used in conjunction with the additional assumption that the liquid pressure is constant throughout the reverse flow region $S \leq X \leq C$ (see e.g. Savage [1982], Carter [1985]).

Pitts and Greiller [1961] also used lubrication theory for the rectilinear flow portion and attempted an approximate solution near the meniscus by using experimental evidence which suggested that the meniscus had a parabolic profile. They were able to predict regions of recirculation upstream of the coating meniscus and the position of the separation point was in satisfactory agreement with their experimental data. Williamson [1972] adopted a similar approach when studying the problem of the tearing of an adhesive layer between two flexible tapes wound around adjacent rollers. By approximating the shape of the meniscus as a sixth order polynomial he was able to predict the existence of eddies behind the meniscus similar to those observed by Pitts and Greiller.

Greener and Middleman [1975] analysed the symmetric problem, shown in Figure 1.9, in which roller speeds ($\tilde{V}$) and radii (R) are equal. Their model is based on the assumption that the liquid extends over a semi-infinite domain terminating at a liquid-air interface where there is a stagnation point and where symmetry conditions imply that the gradient of velocity is zero, i.e. $\partial U/\partial Y = 0$. Since the uniform layers attached to each roller have the same thickness, $T_1 = T_2 = \tilde{T}$, they showed how the dimensionless film thickness $\tilde{T}/H_0$ (H_0 is the semi-nip width) varied with β a modified capillary number defined by

$$\beta = \left(\frac{T}{\eta \tilde{V}}\right)\left(\frac{H_0}{R}\right)^{\frac{1}{2}} \tag{1.7}$$

Benkreira, Edwards and Wilkinson [1981] performed 1500 fully-flooded forward roll coating experiments using sets of rollers with size ratios in the range $0.5 \leq R_1/R_2 \leq 2.0$, to measure the ratio of the film thicknesses on upper and lower rollers, i.e. T_1/T_2. From their data they found T_1/T_2 to be independent of the size ratio R_1/R_2, but strongly dependent on the velocity ratio $S = V_1/V_2$. They summarized their results by the functional relationship

$$\frac{T_1}{T_2} = 0.87 \, S^{0.65} \text{ for } 0.03 \leq S \leq 14.9 \tag{1.8}$$

Note that (1.8) gives an asymmetric split even in the symmetric case of $S = 1$; they suggested that this was due to the effect of gravity.

Savage [1982] extended the work of Greener and Middleman to the general coating situation which involves rollers of arbitrary size and speed. He determined the coating thickness T_1 on the upper roller by formulating two mathematical models for the pressure distribution over a semi-infinite domain : the Reynolds and Separation models. In the Reynolds model, the pressure curve terminates at a point at which the Reynolds conditions (1.5) apply; in the Separation model these conditions are replaced by the separation conditions (1.6). Taylor [1963] and Dowson and Taylor [1979] pointed out that the Reynolds conditions are appropriate when high liquid pressures are generated and the film is split by cavitation within the liquid; this situation is characterized by the rollers being highly loaded against each other. Since, in this thesis, attention is restricted to the case of rigidly fixed rollers in which the film splits by flow separation rather than cavitation, it is only the Separation model which is relevant. A typical pressure profile arising from the solution of the Separation model is shown in Figure 1.10. The overall shape of this curve, which features a sub-atmospheric pressure loop immediately upstream of the interface, has been experimentally verified by Floberg [1965], Smith [1975], and, more recently, Malone [1992] – see Chapter 5.

Coyle et al [1986] solved the full asymmetric forward roll coating problem using the finite element (F.E.) technique (see §1.5). They found that their numerical film thickness ratio predictions could, in the absence of gravity, be fitted by $T_1/T_2 = S^{0.65}$ in agreement with Benkreira et al [1981]. The discrepancy between film thickness ratio predictions from Savage's [1982] Separation model (which predicted $T_1/T_2 = S^{0.5}$), and those of Benkreira et al [1981] and Coyle et al [1986], prompted Savage [1992] to question the validity of the zero tangential shear stress assumption, i.e. $\partial U/\partial Y = 0$, when $S \neq 0$ or 1. This has resulted in a more rigorous mathematical model in which the lubrication regime terminates at the first stagnation point downstream of the nip where $U = V = 0$; the predictions of his 'stagnation-point' model may be summarized as:

$$\frac{T_1}{T_2} = \frac{S(S+3)}{(1+3S)} \qquad (1.9)$$

The inability of lubrication theory to model the two-dimensional flow near the

downstream meniscus has led to the development of powerful computational techniques based on the F.E. method. These techniques are discussed in §1.5. In Chapter 5, numerical predictions of T_1/T_2 for fully-flooded forward roll coating are obtained over a wider range than reported by Coyle et al [1986], and are compared with Malone's [1992] experimental data, equation (1.9) and Benkreira et al's [1981] functional correlation (equation (1.8)).

In contrast to the forward case, fully-flooded reverse roll coating, shown in Figure 1.1 (f), has received little attention to date. This is surprising because it is a common coating method due to its versatility, speed and precision. Ho and Holland [1978] and Greener and Middleman [1981] have presented simple lubrication-type models for this which are useful over a limited, yet important, range of parameters. More recently, Coyle, Macosko and Scriven [1990 a] have obtained F.E. solutions of the Navier-Stokes equations for the flow in the entire gap exhibiting good agreement with experiment.

1.2.3   The Moderately-Starved Case

In the analyses of roll coating described in §§1.2.2, it is assumed that the clearance space at inlet is fully-flooded in the sense that there is a rolling 'bank' of liquid upstream of the nip – see Figure 1.4. In this case the resulting liquid flow/pressure distribution is similar to that found in hydrodynamic bearings. If the supply of liquid is reduced, however, the inlet becomes 'starved' and the 'bank' of liquid gradually disappears – the situation depicted in Figure 1.6 (b).

Although there appears to be no previously published work in the literature relating to either moderately- or ultra-starved roll coating, the effects of moderate-starvation on the load carrying capacity of bearings has been widely studied (see Dowson and Taylor [1979]). On the basis of his experimental findings for a flat plate loaded against a rotating flywheel, Lauder [1966] proposed that in a moderately-starved inlet the lubricant pressure builds up at a location where $U = \partial U/\partial Y = 0$, which he named the 'zero-reverse-flow' boundary condition. Wolveridge, Baglin and Archard [1971] studied the effect of moderate-starvation on the load carrying capacity of two cylinders in both the rigid and elastohydrodynamic (E.H.L.) cases. They modelled the degree of

starvation by simply altering the distance from the point of minimum roller separation at which the boundary condition $P = 0$ is applied. This was considered to be the point at which the lubricant pressure builds up; the outlet boundary conditions were the Reynolds conditions (1.5). A typical pressure profile which they obtained for the rigid case is shown in Figure 1.11.

In his study of starved E.H.L. bearings, Saman [1974] realised that it is important to define precisely what is meant by a starved inlet and proposed that a system is starved if all the lubricant supplied at inlet passes uni-directionally through the conjunction (i.e. there is no reverse flow at inlet or in the nip; that is to say the rolling bank of liquid is no longer present). Unfortunately, Saman's starvation criterion has only limited application in roll coating since it cannot differentiate between cases of 'moderate'-starvation, in which the supply of liquid is only slightly less than that required to flood the inlet, and 'ultra'-starvation in which it has been significantly reduced – see Figures 1.6 (a)-(c).

1.2.4 The Ultra-Starved Case: Meniscus Roll Coating

In §§1.2.1 we saw that it is possible to operate a roll coater under conditions in which the supply of liquid at inlet has been substantially reduced from that needed to flood the inlet – see Figure 1.5 for the forward case. This ultra-starvation, shown schematically in Figure 1.6 (c), results in the additional complications of a second, upstream meniscus which meets the web/upper roller at a dynamic wetting line. Owing to the existence of two meniscii in this case, one on either side of the nip, ultra-starved roll coating is henceforth referred to as 'Meniscus Roll Coating'.

The complications introduced by the existence of the inlet meniscus and dynamic wetting line are common to many coating operations – in the following section they are discussed in the wider context of general coating flows.

1.3 Complications Associated with Free Surface Coating Flows

1.3.1 Free Surfaces

By their very nature, coating flows are free surface flows. Free surfaces are meniscii, i.e. fluid-fluid interfaces. A meniscus is a layer of finite thickness in which the density varies rapidly from that of the bulk liquid to that of the bulk gas. However, since the meniscus thickness is usually no more than a few tens of Angstroms and is therefore negligible in comparison with fluid mechanical length scales, it is convenient to approximate meniscii as mathematical surfaces (see Chapter 4). The steep density gradient at a meniscus, which is effectively a discontinuity, gives rise to a property known as surface tension which produces an isotropic *capillary* stress within the meniscus not unlike that in a stretched rubber membrane.

The presence of one or more free surfaces greatly complicates flow field analyses because their location, and thus the flow domain, must be determined as part of any solution. Moreover the boundary conditions which are applicable at free surfaces – see Chapter 4 – are highly non-linear which means that any solution technique must necessarily be iterative. As a result, viscous free surface problems cannot be solved by standard analytical techniques and recourse must be made to numerical methods (see §1.5).

1.3.2 Contact Lines

Coating flows invariably contain three-phase contact lines, formed at the intersection of two immiscible fluids with a solid boundary. Contact lines can be either:

- **Static**, if the *apparent* point of contact is stationary (relative to the solid surface).

- **Dynamic**, if the *apparent* point of contact translates (relative to the solid surface).

Dynamic contact lines are also referred to as wetting lines. Every coating flow has a wetting line since liquid must come into contact with, and displace air from, a dry web,

i.e. the sheet being coated. The wetting line in the forward meniscus roll coater is illustrated in Figure 1.12.

Despite their practical importance, very little is known about the physical mechanisms by which one fluid displaces another at a dynamic wetting line either from a molecular or a continuum point of view (Dussan V [1979]). During coating, liquid displaces air from the surface of the substrate at the three-phase contact line where air, liquid, and solid meet (see Figure 1.12). When this region is magnified and viewed through an optical microscope, the liquid-air interface appears to intersect the substrate at a well-defined angle θ_c. This angle is termed the *apparent dynamic contact angle*. Burley and Kennedy [1976] carried out an experimental investigation of the behaviour of a dynamic wetting line, with particular reference to the mechanism of air entrainment. At very low speeds (of the order of millimetres/ sec) the apparent dynamic contact angle equals the static contact angle. As speed is increased, the apparent dynamic contact angle monotonically increases, ultimately reaching a nominal value of 180°. At sufficiently high speeds thereafter, air bubbles are entrained. Burley and Kennedy present an experimental correlation for the critical velocity V_c, above which air is entrained, in terms of fundamental liquid properties. In coating flows therefore, it is generally necessary to avoid this critical condition, and consequently the factors which determine the dynamic contact angle are of great interest.

Modelling of the flow near the three-phase contact line is complicated by the 'apparent breakdown' of the classical hydrodynamical equations and/or boundary conditions in this region. Huh and Scriven [1971], for example, modelled a dynamic wetting line by assuming that the fluid-fluid interface was planar, see Figure 1.13. Their analysis was essentially a generalisation of that of Moffatt [1964] from a vacuum-fluid system to a fluid-fluid one. Unfortunately their model, in which the wetting line movement was approximated by the equations of creeping flow, predicted a physically unrealistic non-integrable stress singularity at the dynamic wetting line. They suggested that the most likely cause of this anomaly was the inapplicability of the conventional no-slip condition very close to the wetting line but they did not discount other explanations such as non-Newtonian fluid effects, breakdown of the continuum model or elasticity

of the solid. However recent work by Savage [1992] suggests that their singularity is caused by imposing the contact angle, θ_c, to a value other than $180°$, i.e. the singularity disappears when $\theta_c = 180°$.

In the absence of any clear understanding, many authors have made ad hoc modelling assumptions to overcome the problem of the non-integrable stress singularity. Most analyses have achieved this by postulating slip between liquid and solid in the immediate vicinity of the wetting line (Dussan V [1976], Hocking [1976, 1977], Cox [1986]) but they suffer from the disadvantage that they do so at the expense of introducing an unknown slip length scale, measuring the distance from the contact line over which slip occurs.

A proper treatment of the flow near a dynamic wetting line requires a knowledge of physical chemistry and in the light of the small length scales involved it is perhaps not surprising that there have been so few papers proposing mechanisms for slip near a dynamic wetting line. However, notable exceptions are those due to Ruckenstein and Dunn [1977] and Ruckenstein and Rajora [1983] which have proposed mechanisms in terms of a chemical potential in the liquid along a solid-liquid interface.

Nevertheless, in practice, the most commonly used expedient to remove the singularity which arises if the no-slip condition is used right up to the wetting line, is to simply impose a slip velocity distribution which satisfies the requirement that there should be perfect slip between solid and liquid very close to the wetting line. A boundary condition for the free surface is also required. At present there appears to be two alternatives (see for example, Kistler and Scriven [1983], Chen and Higgins [1988]): (i) the position of the wetting line is prescribed and the apparent dynamic contact angle θ_c has to be determined, or (ii) θ_c is specified (from experimental observation) and the wetting line position is a variable to be evaluated. It is evident, from the above discussion, that much work still remains to be done on the modelling of flows near dynamic wetting lines.

1.3.3 The Behaviour of a Thin Liquid Film on a Rotating Roller

In meniscus roll coating the liquid which passes into the bead is transported from the bath by the viscous lifting action of the lower (applicator) roller – see Figure 1.2 (a). It is important to examine the 'inlet' film which enters the bead since (i) the degree of starvation of the system, and (ii) the film thickness T_1 produced on the web, are critically dependent on the flux entrained by the applicator roller. Most previous roll coating analysts seem to have assumed that a thin liquid film on a rotating roller undergoes a rigid body rotation – unfortunately in most cases this assumption is simply not justifiable. Therefore the aim of the present section is to describe the key theoretical results relating to the behaviour of a thin liquid film on a rotating roller and to discuss the practical problems encountered when measuring the film thicknesses produced during roll coating.

Yih [1960] appears to have been the first to study thin film flow in a roll coating context: he studied the behaviour of a liquid film on a single roller in order to understand the liquid flow on the rollers of a paper-making machine. Moffatt [1977] reviewed previous work in this area and analysed the flow of a viscous film on the outer surface of a horizontal roller using lubrication theory. He concluded that the liquid layer experiences substantial shear and the motion can certainly not be approximated by a rigid body rotation.

In view of its practical importance, it is surprising that the subject of viscous lifting of liquid onto a rotating roller has received so little attention to date. However the closely related 'drag-out' problem in which a thin liquid film is entrained by the steady withdrawal of a sheet from a bath of liquid (see Figure 1.14) has been extensively studied. The work of Landau and Levich [1942] initiated a series of detailed theoretical and experimental studies of this problem. Their theory was extended by White and Tallmadge [1965] to a wider capillary number ($Ca = \eta V_s/T$) range, while the effects of liquid inertia have been considered by Soroka and Tallmadge [1972] and Esmail and Hummel [1975]. Wilson [1982] consolidated the work of the previous authors and demonstrated that the Landau and Levich result is an asymptotic solution valid as

the capillary number tends to zero. Tharmalingham and Wilkinson [1978] adapted the aforementioned theories to predict the liquid flux picked up by a rotating roller partially submerged in a Newtonian liquid and the variation of film thickness around the periphery of the roller – the 'free-coating' problem, see Figure 1.15 (a). Their analysis involved the numerical integration of the momentum equation in the dynamic meniscus region (region 2 of Figure 1.15 (a)) and the matching of the surface curvature with that derived for the static meniscus region (region 1) near the liquid surface. Their predictions compare well with experiment for low capillary number (up to about 0.1), but thickness predictions for higher values are much too large because of the neglect of liquid inertia in their analysis.

Tekic and Jovanovic [1982] used a two-dimensional non-linear theory to obtain a correlation for predicting the liquid flux picked up by a partially submerged roller during free coating. In their 'Inclined-Plane' model they assumed that at the point at which the roller leaves the liquid, the situation can be approximated by a flat surface being withdrawn at the same angle of contact, as shown in Figure 1.15 (b). Wu, Weng and Chen [1985] also adopted an 'inclined-plane' model and, using the flow regions proposed by Landau and Levich, they included inertia force terms and more realistic two-dimensional boundary conditions at the free surface to produce reasonably accurate film thickness ratio predictions over a wide range of capillary number.

Even if the difficulties in analysing the entrainment of liquid onto the surface of a partially submerged roller are ignored, it is important to account for the behaviour of a thin liquid film on a roller in any attempt to measure film thickness at a specific point (Malone [1992]). Consider the partially submerged roller shown in Figure 1.15 (a); at no time does the liquid film achieve an asymptotic thickness. In fact the thickness decreases as θ_i increases. In simple terms, the explanation involves the fact that the component of gravity in the direction of motion changes as the orientation of the layer is changed: the liquid farthest away from the roller surface is affected most, and this determines the velocity profile across the depth of the liquid layer.

Tharmalingham and Wilkinson [1978] present results of predicted film thickness for variations of system parameters. In particular their Figure 5 shows how the film thick-

ness varies around the roller for a range of capillary numbers. Their results predict that the variation in thickness around the periphery of the roller increases as Ca increases and, furthermore, for θ_i in the range -90° to 60° with $\theta_L = 120^\circ$ (refer to Figure 1.15 (a)),

- At $Ca = 0.01$, film thickness varies by 10%

- At $Ca = 0.1$, film thickness varies by 20%

- At $Ca = 0.5$, film thickness varies by 40%

Now under typical fully-flooded roll coating conditions, $Ca \approx 1.0$. Therefore, single point film thickness measurements will not give a typical average film thickness reading, unless the operator can equate the position of measurement with the velocity profile there (Malone [1992]).

However, viscosities of liquids for industrial meniscus roll coating applications are low (of the order of $1 \times 10^{-3}\ Nm^{-2}s$) compared with those used in fully-flooded roll coating where viscosities can range from $0.05 - 500\ Nm^{-2}s$. This fact, coupled with the slower roller speeds necessary to maintain the bead, means that a typical capillary number in industrial meniscus roll coating is given by $Ca < 0.01$. This alleviates the problems caused by film thickness variation around the roller since for this range of capillary number the variation is predicted to be less than 10%. In the experimental measurements quoted in this thesis (which are due to Malone [1992]), a Newtonian oil, Shell Tellus R5, was used whose viscosity at the laboratory temperature of $20^\circ C$ was $8.4 \times 10^{-3} Nm^{-2}s$ – higher than that of typical industrial coating liquids. Fortunately, Malone [1992] circumvented any possible film thickness variation problems by employing a scraper collection method on both rollers, which involves removing the liquid film from a roller surface using a scraper blade. This gives the fluxes of the films on each roller, which are easily converted to *average* film thicknesses since average thickness equals the ratio of flux to roller speed.

1.4   The Phenomenon of Ribbing

The main purpose of this thesis is to investigate *steady* roll coating processes which produce uniform films (uniform in the sense that there is no variation along the axes of the rollers) under different degrees of starvation. It is important, however, to realise that all industrial coating processes are susceptible to instabilities which limit the possible operating conditions since there are usually stringent tolerances on the uniformity of films required. In the case of the fully-flooded forward roll coater the speed of operation, for a given liquid and geometry, is limited by the appearance of the 'ribbing' instability at high roller speeds. This is demonstrated by Carter's [1985] experiments at Warren Spring Laboratory, an example of which is shown in Figure 1.16. The ribbing instability is characterised by a periodic, i.e. waved, variation in film thickness along the axes of the rollers. There exists an extensive literature on the ribbing phenomenon, the salient features of which are summarized below.

The first documented observation of ribbing seems to have been made by Hoare [1937] in which he reported the formation of ribs when forward rolling is used to tin metal sheets. Pearson [1960] was the first person to undertake a theoretical investigation of this class of problem. He examined the effect of a small perturbation of the form $\epsilon\, e^{st} \cos(nZ)$ on the position of the liquid-air interface and solved for the velocity field describing the motion of a viscous liquid under a wedge-shaped spreader – see Figure 1.17. Unfortunately his analysis lacked a complete set of boundary conditions. Consequently the distance, C, from the centre of the spreader to the free surface had to be determined from experiments and as such the theory in itself did not yield an explicit criterion for the onset of the instability.

A second, important theoretical contribution to this problem was made by Pitts and Greiller [1961]. They investigated coating in the system shown in Figure 1.9 and analysed the liquid motion by means of a linear stability analysis. This contribution was at two levels of sophistication. The first, also considered by Savage [1977 a], involved a relatively crude stability analysis in which the equilibrium of the liquid-air interface

was considered and shown to remain stable to small disturbances provided

$$\frac{d}{dX}\left[P + \frac{T}{R_{curv}}\right] \leq 0 \tag{1.10}$$

where P is the liquid pressure immediately upstream of the interface, T the surface tension of the liquid, and R_{curv} the radius of curvature of the interface. However, though necessary, (1.10) is not sufficient to predict the onset of ribbing. Using (1.10) Pitts and Greiller obtained conditions for the onset of ribbing involving the Capillary number, $Ca = \eta \bar{V}/T$, and the geometry parameter, H_0/R which enabled prediction of the critical Capillary number, Ca^*, above which ribbing can be expected. This took the form

$$Ca^* \approx 5.0 \left(\frac{H_0}{R}\right) \tag{1.11}$$

Subsequently using a second, more sophisticated stability analysis they obtained the result

$$Ca^* \approx 14.0 \left(\frac{H_0}{R}\right) \tag{1.12}$$

Both of these predictions were in poor agreement with their experimental data to which they fitted the line

$$Ca^* = 31.0 \left(\frac{H_0}{R}\right) \tag{1.13}$$

A more refined experimental study was carried out by Mill and South [1967] in which they used rollers of equal speed but with different radii. They found the critical Capillary number to be given by

$$Ca^* = 17.3 \left(\frac{H_0}{R}\right)^{3/4} \tag{1.14}$$

Greener, Sullivan, Turner and Middleman [1980], using rollers of equal size and speed, found the following criterion for ribbing

$$Ca^* = 1875.0 \left(\frac{H_0}{R}\right)^{2} \tag{1.15}$$

Cheng [1981] and Savage [1984], noting these widely differing theoretical predictions, also observed that the experimental data reported fell into separate regions of the $(Ca, H_0/R)$ plane. Following a suggestion of Cheng, Savage [1984] performed a linear

stability analysis for both the flat plate/ roller (see Chapter 5) and equal speed two roll coater geometries using the separation boundary conditions. This analysis yields a criterion for ribbing involving the two dimensionless parameters $(T/\eta U)(H_0/R)$ and $(T/\eta U) (H_0/R)^{\frac{1}{2}}$. For the case of the equal speed two roll coater, theoretical predictions exhibit remarkably close agreement with the experimental data of Pitts and Greiller [1961], Mill and South [1967] and Greener et al [1980] for $0 < Ca < 1$ which is almost the whole region of interest for coating problems. Carter and Savage [1987] and Carter [1985] have conducted an analytical and experimental study into the effect of varying the peripheral speeds of the two rollers, in a roll coater, on the onset of ribbing. They were able to determine the approximate value of the capillary number at the onset of ribbing for a given speed ratio and roll coater geometry. Their predictions agreed well with data from Carter's [1985] experiments at the Warren Spring Laboratory.

1.5   Numerical Methods For Free Surface Flows : Finite Elements

The last twenty-five years has seen many theoreticians working in the area of coating and free surface flows turn to computers as a means of obtaining numerical solutions to their problems. In any numerical solution, the differential equations governing the flow are written in an approximate, discrete form resulting in a system of algebraic equations whose solution yields the physical quantities of interest – for example, the streamfunction and vorticity or the fluid velocity and pressure – at a number of points (the nodes) within the flow domain. The primary difference between numerical techniques lies in the way in which the governing equations are recast into algebraic equations (Chen [1991]). Once these equations have been derived, they are solved by an efficient solution algorithm.

In the finite-difference (F.D.) method, which is widely used in Computational Fluid Dynamics, the differentials arising in the governing equations are approximated by finite differences – see for example Hirsch [1988]. Unfortunately this method is prone to difficulties when solving flows in domains of irregular shape, as is the case in general

for free surface flows, because of the problem of constructing finite difference approximations to these differentials on irregular grids. For this reason the F.D. method is not a natural choice for the solution of free surface problems; nevertheless Ryskin and Leal [1984] have tackled this interpolation problem by using a numerically generated orthogonal co-ordinate system which is 'Boundary-Fitted' in the sense that all boundaries coincide with a co-ordinate line of the co-ordinate system.

A second method that has been employed for free surface flow problems is the Boundary Element (B.E.) technique, used by Kelmanson [1983] for the 'die-swell' problem in extrusion, shown in Figure 1.18. The B.E. technique has two advantages over the F.D. method: it has the topological flexibility required for the solution of free surface problems and is cheaper since only boundary information is evaluated. It has, however, serious limitations. It is restricted to the limiting cases of zero Reynolds number, where the governing equations are the linear Stokes' equations, or inviscid, irrotational flow where the equations reduce to Laplace's equations for a velocity potential. In this method, fundamental solutions of the linear governing equations are used to reduce the general n-dimensional problem to the solution of a set of (n-1)-dimensional integral equations.

The finite element (F.E.) technique is the most commonly used numerical method for solving free surface problems. It is more expensive than F.D. or B.E. methods, but this is more than compensated for by its inherent advantages of being able to combine the desirable features of the F.D. method, namely an ability to include the effects of non-linear fluid inertia, three-dimensionality and time dependency, with the topological flexibility of the B.E. method. In the light of these benefits, all free surface problems in this thesis are solved by the F.E. method; the basic philosophy behind F.E. is described in Chapter 4 and in Appendix B.

Many computational methods in fluid mechanics use either the streamfunction or the streamfunction and vorticity as computational variables in incompressible flow problems – see for example Olson and Tuann [1978] and Burggraf [1966]. In these methods the streamfunction is calculated first and the pressure must be recovered via a separate computation. This is a serious drawback when solving free surface flows

because the conditions at the free surface are given in terms of the stress components which involve the pressure explicitly. It is therefore preferable to choose a F.E. scheme with fluid velocity and pressure, known as the 'primitive' variables, for the solution of free surface flows.

The F.E. method, with its traditional predominance in the area of stress analysis, only really began to attract the attention of computational fluid mechanicists after Zienkiewicz [1977, first published 1967] and Heubner [1975] showed that it could solve flow problems which up until then had been beyond the scope of F.D. methods. For example, Thompson, Lawrence and Fong-Sheng [1969] solved the problem of a liquid being squeezed between two flat plates, giving a fairly detailed account of the F.E. techniques used. These early techniques were gradually extended to accomodate the effects of a free surface – the first published F.E. solutions of free surface flows (both involving liquid jets) were those of Nickell, Tanner and Caswell [1974] and Tanner, Nickell and Bilger [1975]. Tanner et al [1975] also solved problems involving Poiseiulle flow and contraction effects in a tube from which they were able to test the reliability of their program before applying it to more complex free surface flows.

However, there still remained a considerable restriction on further progress due to the large amounts of storage required by the F.E. method. Hence, in addition to the increased power and efficiency of modern computing machines, the advent of frontal solution programs, first developed by Irons [1970] and later refined by Hood [1976] and Beer and Haas [1982], was a second important factor influencing the growth of research in the area of free surface flows. These Frontal Methods greatly improved the efficiency of computer storage for F.E. programs and the principle behind them is explained in Appendix C.

Iterative methods of various kinds are required when solving free surface flows since the free surface position is unknown *a priori*. In the first few papers on this subject, successive approximation techniques which proceeded in a three part cycle were used: (i) a free surface shape is assigned, (ii) a flow field within that shape is found from the Navier-Stokes system with one of the free surface boundary conditions omitted, (iii) the free surface is updated to satisfy as closely as possible the previously omitted

boundary condition. This method, although fairly simple to implement, experienced severe convergence difficulties: convergence, if at all, was slow and depended on the choice of omitted boundary condition (Silliman and Scriven [1980]).

Ruschak's [1980] boundary location method, which he called the 'Boundary Supports' technique, led to a significant improvement in the parametrisation of free surface boundaries by the F.E. method. He succesfully applied this free surface representation, shown in Figure 1.19, to the flow of a liquid from a slit which agreed well with Richardson's [1970] analytical solution. Following the work of Silliman and Scriven [1978, 1980], Saito and Scriven [1981] used a simpler version of Ruschak's boundary location method to analyse the slot coating problem shown in Figure 1.20. They introduced a new solution technique based on Newton iteration which dramatically improved the convergence characteristics – in particular the convergence rate – for free surface flows. In this Newton iteration procedure, the shape and location of the free surface, and the velocity and pressure fields are all calculated simultaneously.

Figure 1.21 (a) illustrates the F.E. grid Silliman [1979] used to analyse a slot coating problem. Using the method described by Ruschak [1980], the vertical co-ordinates of the nodes were given as fixed ratios of the height, H, of the vertical line on which the node lay, thus giving an even distribution of elements at each iteration. Unfortunately as the Reynolds number and Capillary number increased for a fixed flow rate or the flow rate was decreased for fixed Reynolds or Capillary numbers, the curvature of the free surface increased until an invading meniscus occurred. This led to singularities in Silliman's formulation which Saito and Scriven [1981] and Carter [1985] were able to avoid by parametrising the free surface into two separate regions – see Figure 1.21 (b).

In the region where the curvature of the meniscus is large, the radial distance between a polar origin O (outside the liquid) and the free surface is parametrised by r. The co-ordinates of the nodes within this region are given as fixed ratios of the distance between the free surface and a fixed point in the liquid. This representation is successfully applied to the slot coater in Chapter 4.

Ruschak [1982] seems to have been the first to seek a numerical solution of the full two-dimensional flow between a pair of partially submerged counter-rotating rollers (the

situation first studied by Pitts and Greiller). He realised that the difficulty in applying the lubrication approximation lies in the specification of boundary conditions at the point of formation of the liquid-air interface. He obtained a solution by the method of matched asymptotic expansions in which the first term of the outer expansion is generated from the lubrication approximation; the first term in the inner expansion describes the two-dimensional flow in the vicinity of the interface. These inner equations are analytically intractable, so he obtained approximate solutions by the F.E. method. Matching between inner and outer expansions provides conditions on the pressure and pressure gradient which allow the completion of the outer, lubrication flow. Ruschak's asymptotic analysis is restricted to flow between a pair of rollers in the limit $H_0/\overline{R} \to 0$, i.e. the limit of parallel roll surfaces at the film splitting region. This asymptotic analysis has been extended by Coyle et al [1986] to the asymmetric case.

Coyle, Macosko and Scriven [1982] developed a generally applicable F.E. analysis of fully-flooded flow between rollers with flux splitting for the relatively simple case of symmetric flux splitting. They obtained good agreement with the experimental results of Pitts and Greiller for the position of the interface over the range $0.05 < Ca < 0.4$ and zero Reynolds number. Though primarily interested in Newtonian liquids, they were able to predict that a shear-thinning rheology has the effect of increasing the size of the eddies as well as causing the position of the meniscus to move away from the nip. This method has been extended to: (i) asymmetric forward roll coating of Newtonian (Coyle et al [1986]) and non-Newtonian (shear-thinning) (Coyle, Macosko and Scriven [1987]) liquids, (ii) reverse roll coating (Coyle et al [1990a]), (iii) forward roll coating with deformable rollers (Coyle [1988, 1990]), and (iv) to analyse the stability of symmetric forward roll coating (Coyle, Macosko and Scriven [1990b]). Note that in all of these analyses the flow is assumed to be fully-flooded at inlet. Examples of computational grids used in the solution of these problems are shown in Figure 1.22.

All of these studies of roll coating have been based on the 'Spine Method' developed by Kistler [1983] from Ruschak's boundary location technique. The 'Spine Method' is described in the excellent review of Kistler and Scriven [1983]. This work discusses at length (i) how the free surface is represented; (ii) techniques for handling contact

lines (static and moving); (iii) outflow and inflow conditions. These ideas are further extended from the case of a liquid-gas interface to the treatment of the interface between two viscous liquids, as is required for example in multilayer printing processes.

The theory and practical application of the 'Spine Method' to the solution of free surface flows is discussed at length in Chapter 4.

1.6   Outline of The Present Work

This thesis considers the steady roll coating, principally in the forward mode of operation, of a Newtonian, incompressible liquid under different degrees of starvation. The main aim of Chapter 2 is to develop a simple, analytical model of meniscus roll coating. In order to achieve this two related flow problems, namely the flow in (i) a lid-driven cavity and (ii) an open, driven cavity are modelled as creeping flows in rectangular cavities and are solved analytically in the form of a truncated biharmonic series. The main features of these two problems are incorporated into a simple model of meniscus roll coating (the Zero Flux Model) in which the curvature of the meniscii and flux through the bead are neglected. The analytical solution of this model, which also takes the form of a truncated biharmonic series, predicts streamline patterns and pressure profiles radically different from those observed in the fully-flooded case. The analytically-obtained streamline patterns are compared with numerical ones obtained from a streamfunction-vorticity F.E. method (see Gaskell, Savage and Thompson [1991]).

In Chapter 3, the results of Chapter 2 are used to further simplify the flow in the central 'core' of the meniscus roll coating bead, i.e. the region sufficiently far from the meniscii. The core flow is modelled as a combination of Poiseiulle and Couette flow with a small flux through the bead and a film thickness model is developed to predict the average film thicknesses produced on upper and lower rollers in forward meniscus roll coating as a function of the operating parameters. These film thickness predictions are compared with experimentally obtained results due to Malone [1992] and then utilised to develop a simple model for the flow in the *entire* liquid bead when a small flux passes through the nip. This extended model is solved numerically by

the streamfunction-vorticity F.E. method. Streamlines obtained from this numerical solution are compared to those seen experimentally.

The full two-dimensional flow near free surfaces, including the effects of surface tension, can only be analysed by computational means. In Chapter 4, a FORTRAN F.E. code based on Kistler's [1983] 'Spine Method' is developed and applied to flow problems of gradually increasing complexity. The code is validated against previously obtained results for the slot- , symmetric forward roll- , and asymmetric forward roll-coating free surface problems.

In Chapter 5 the code is used to obtain numerical predictions of the film thickness ratio T_1/T_2 for a fully-flooded forward roll coater over a wider range of velocity ratio than previously reported. The code is then extended to investigate the effects of starvation in two closely related roll coating geometries. The first of these, known as the flat plate/roller geometry, is chosen since experimental pressure profiles may be obtained. The second is the familiar two roll system. Numerically obtained velocity vectors and pressure profiles are plotted as a function of the degree of starvation in both cases and compared with Malone's [1992] experimental results for similar flow situations. Finally, numerical predictions of the dependence of the average film thickness ratio T_1/T_2 on the velocity ratio S for both the moderately- and ultra-starved cases are compared with Malone's [1992] experimental film thickness results, Benkreira et al's [1981] experimental correlation and Savage's [1992] analytical prediction.

Chapter 6 summarizes the main results of the work presented in this thesis and looks at ways in which it might be extended, including some suggestions for future work.

Appendix A describes the theory developed by Smith [1952] and Joseph and Sturges [1978] which is used in Chapter 2 to obtain analytical solutions for the flows in lid-driven and open, driven cavities by the method of biorthogonal series expansions. Appendix B describes the streamfunction-vorticity F.E. technique used in Chapters 2 and 3 with particular reference to the application of boundary conditions and the treatment of corner nodes by expanding the solution about the corners. Appendix C contains a basic

introduction to the Banded-Matrix and Frontal Solution methods for solving the F.E.

equations.
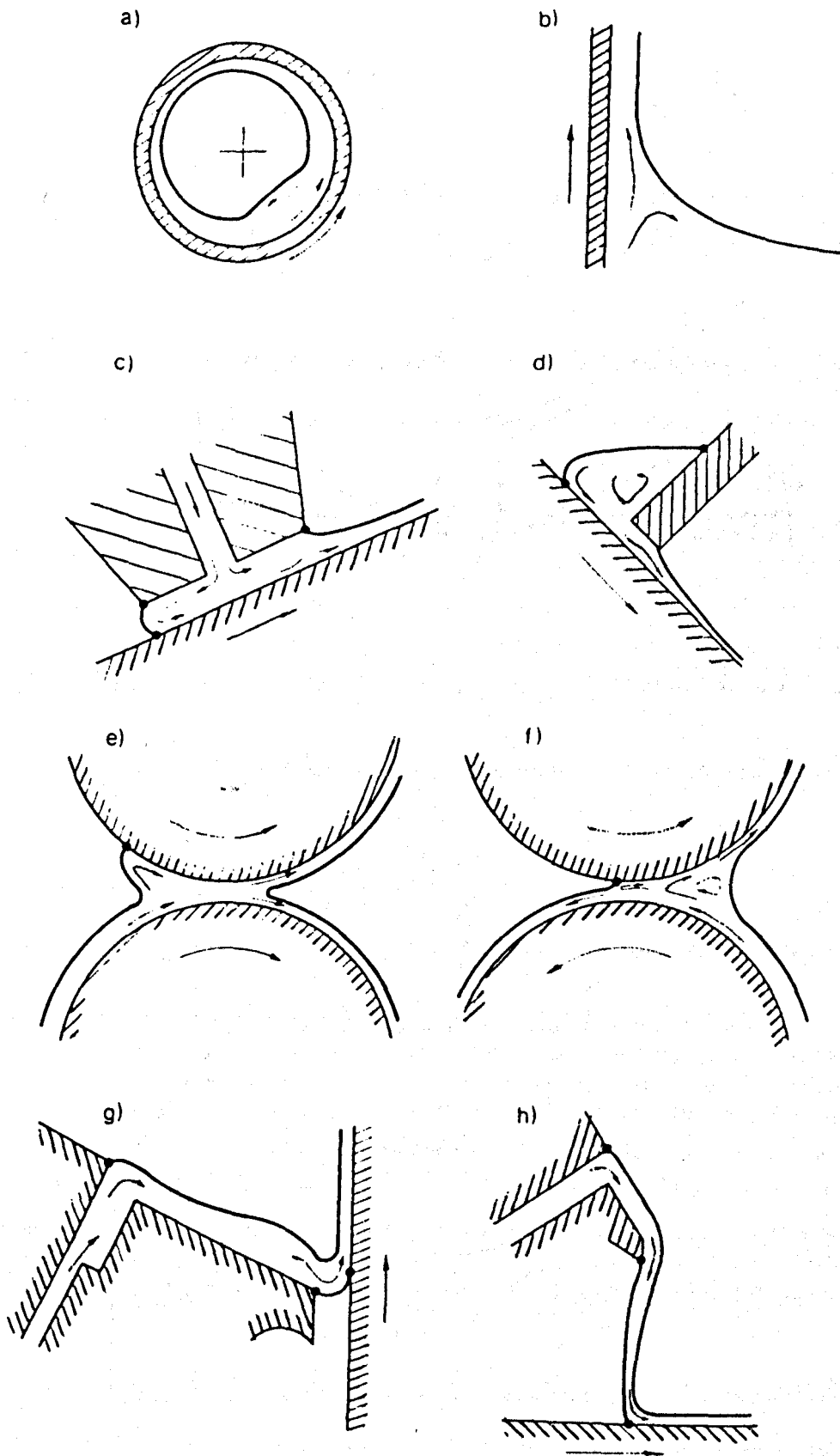
Figure 1.1: Selected Coating Operations (Kistler and Scriven [1983]): (a) Rimming flow; (b) dip coating; (c) bead coating; (d) knife coating; (e) forward roll coating; (f) reverse roll coating; (g) slide coating; (h) curtain coating
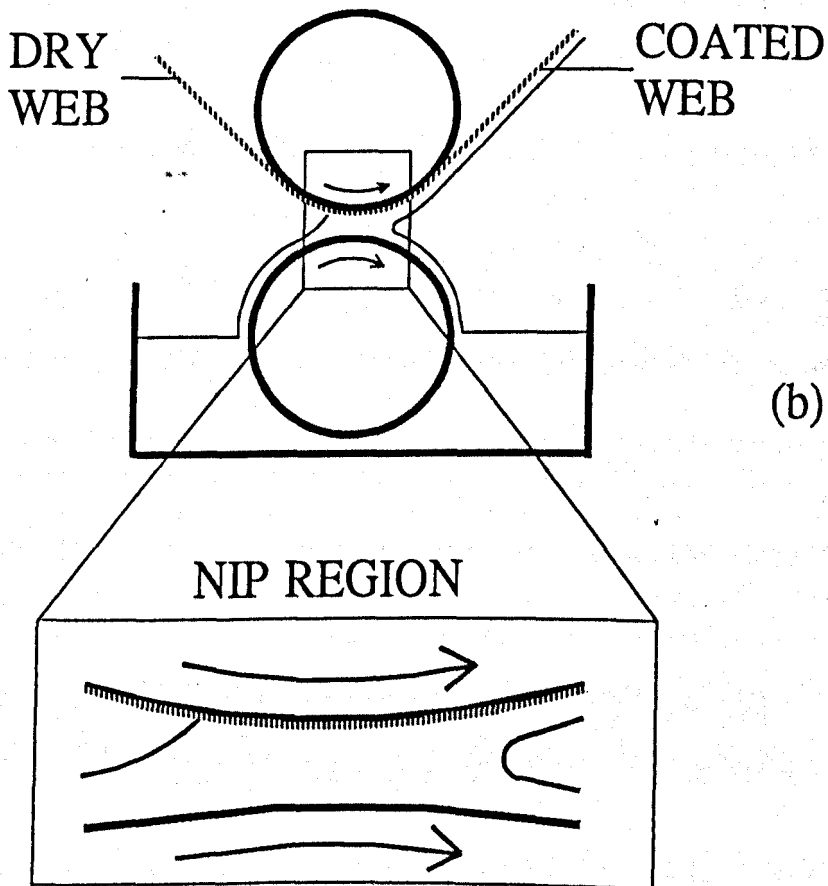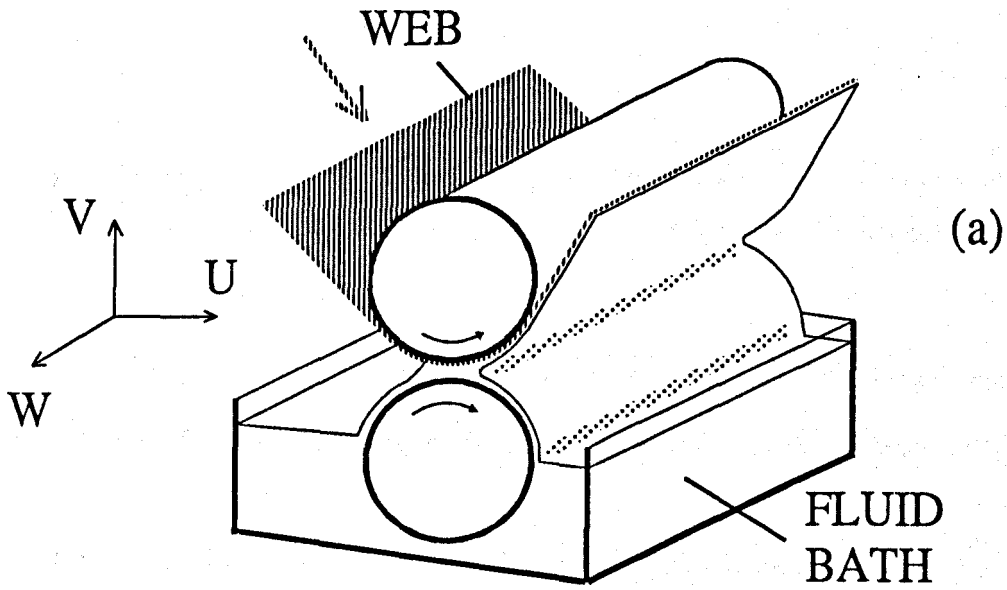
Figure 1.2: The Two Roll Coating Configuration; (a) three-dimensional oblique view, (b) cross-section showing the nip region

Figure 1.3: An Experimentally-Obtained View of the Nip Region of a Fully-Flooded Forward Roll Coater (Malone [1992])
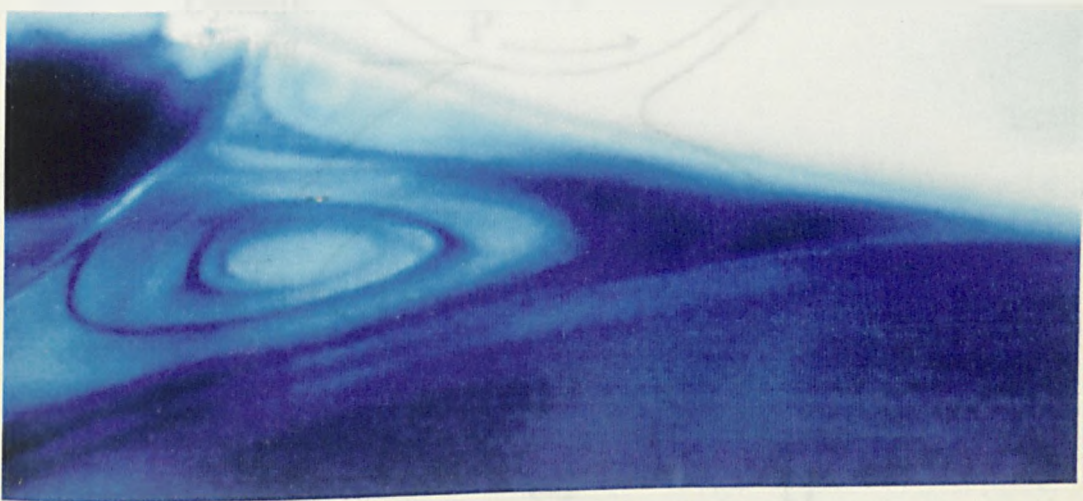
Figure 1.4: The Upstream Bank of Liquid Characteristic of a Fully-Flooded Forward Roll Coater (Malone [1992])
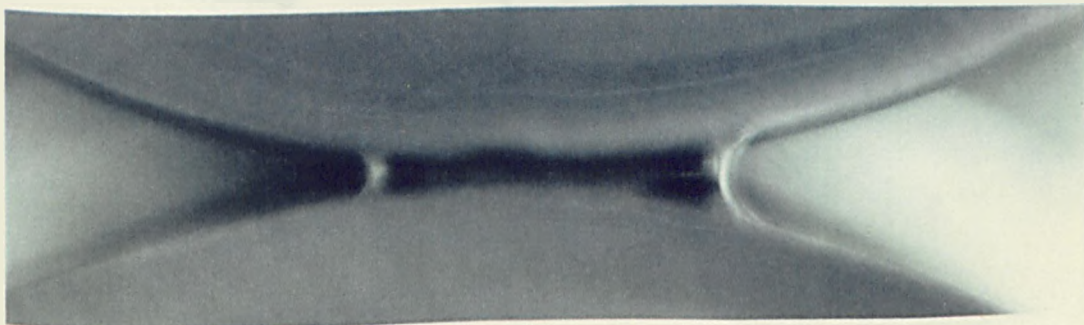
Figure 1.5: An Experimentally-Obtained View of the Nip Region of an 'Ultra-Starved' Forward Roll Coater (Malone [1992])
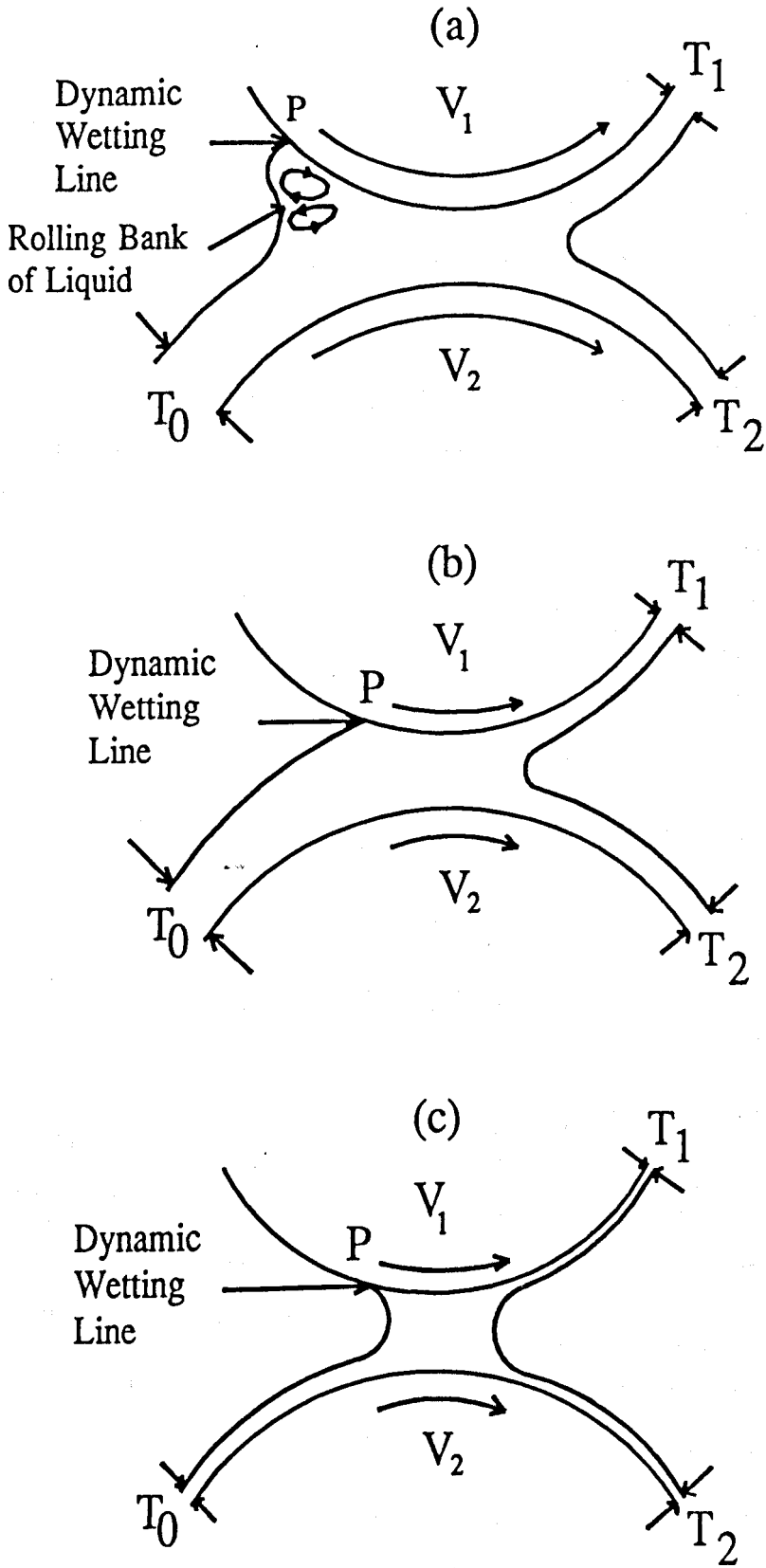
Figure 1.6: Inlet Conditions for a Forward Roll Coater: (a) fully-flooded, (b) moderately-starved, (c) ultra-starved
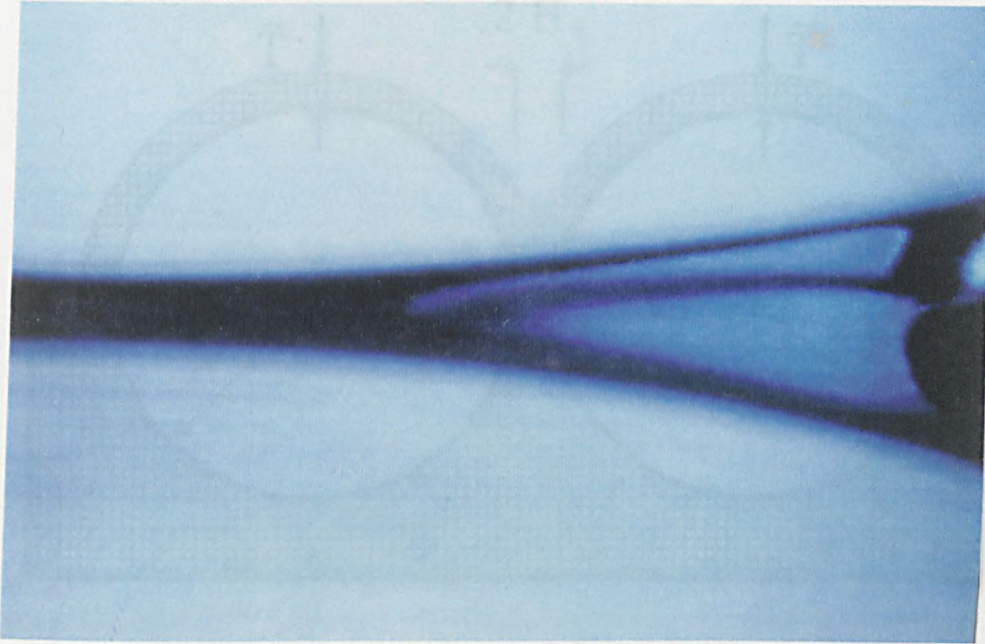
Figure 1.7: Flow Visualisation of a Fully-Flooded Forward Roll Coater (Malone [1992])
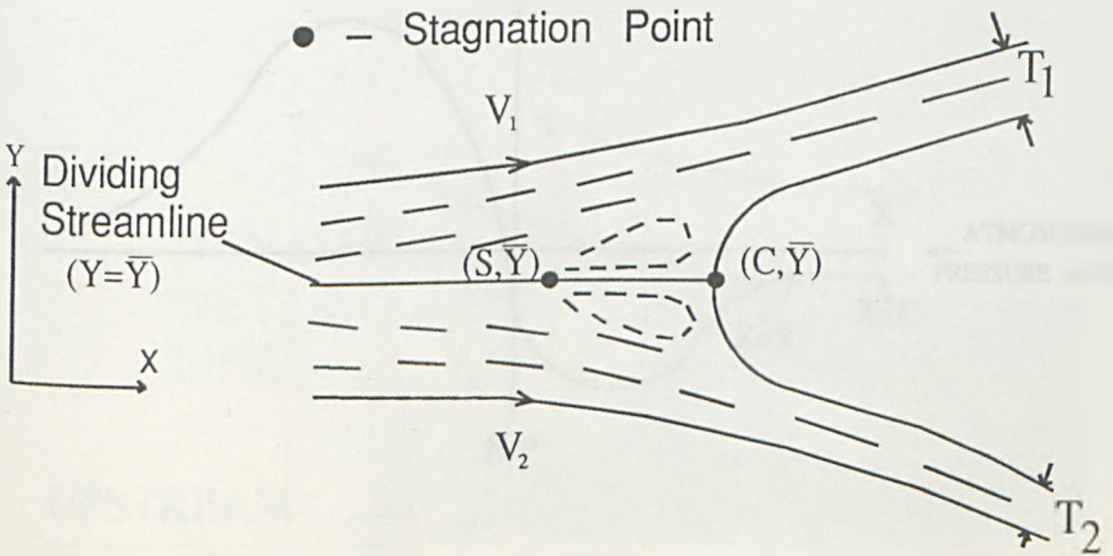
Figure 1.8: Flow Near the Film-Splitting Point in Forward Roll Coating
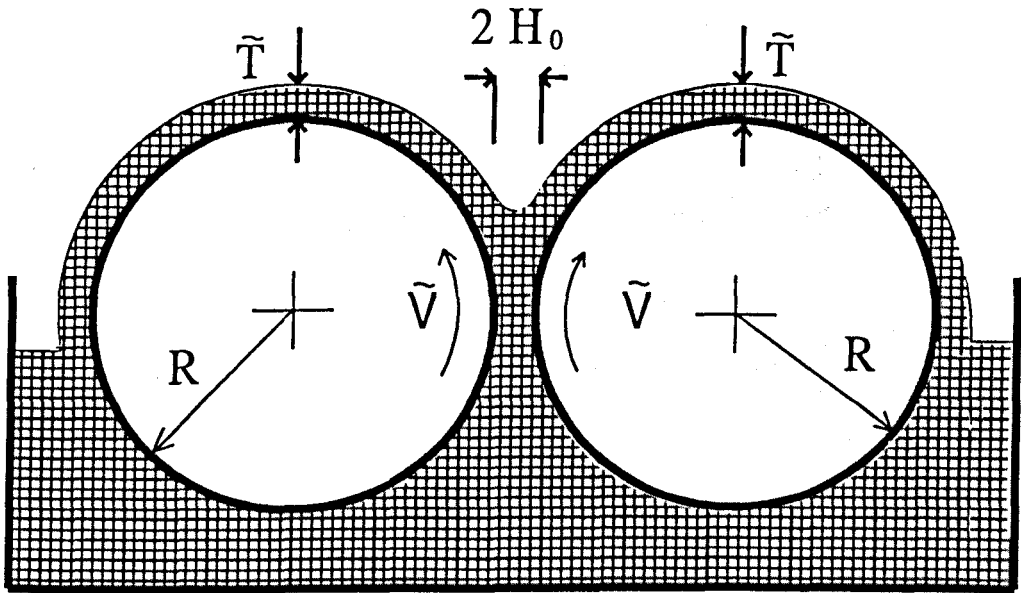
Figure 1.9: Symmetric Film Splitting in Forward Roll Coating
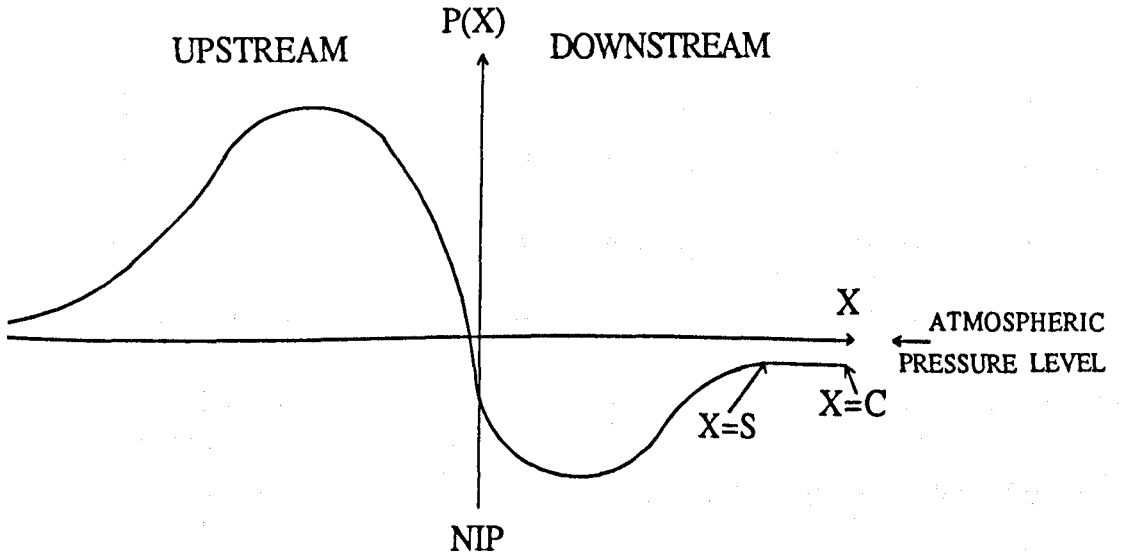
Figure 1.10: A Typical Pressure Profile from the Separation Model
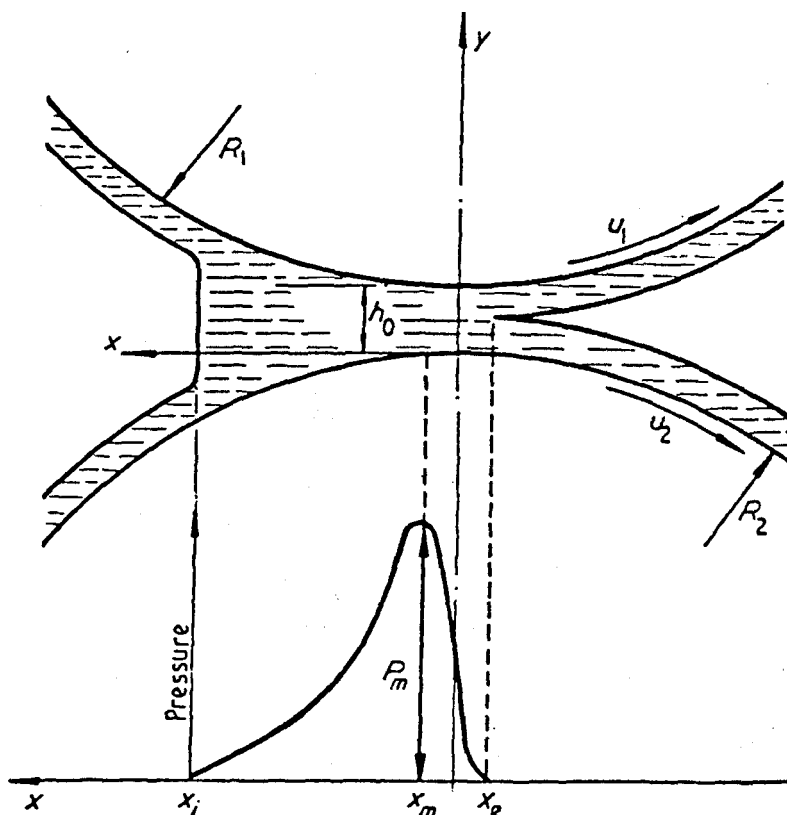
Figure 1.11: A Typical Pressure Profile with Reynolds Conditions at Outlet (Wolveridge et al [1971])
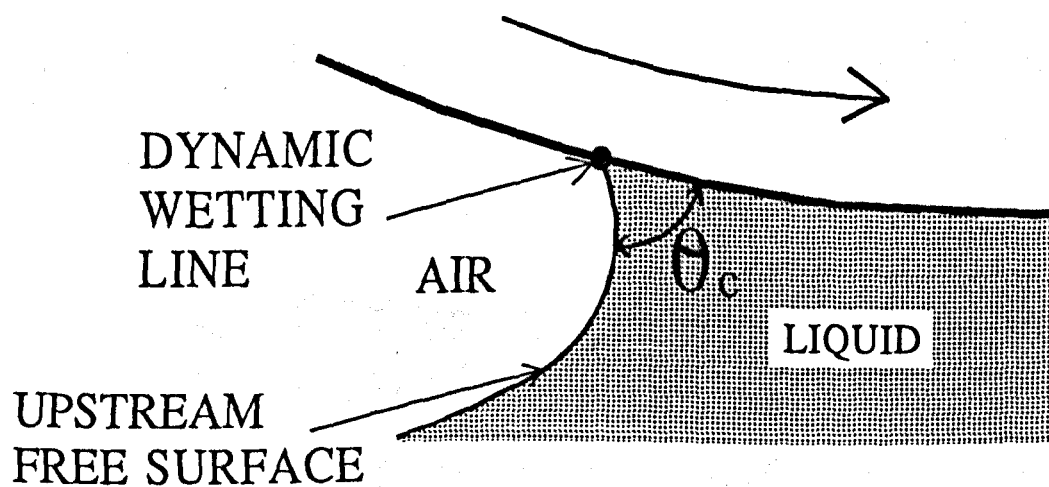
Figure 1.12: The Dynamic Wetting Line in Forward Meniscus Roll Coating

Dynamic Wetting Line

Fluid B

Planar Fluid-Fluid Interface

θ_c

Fluid A

U
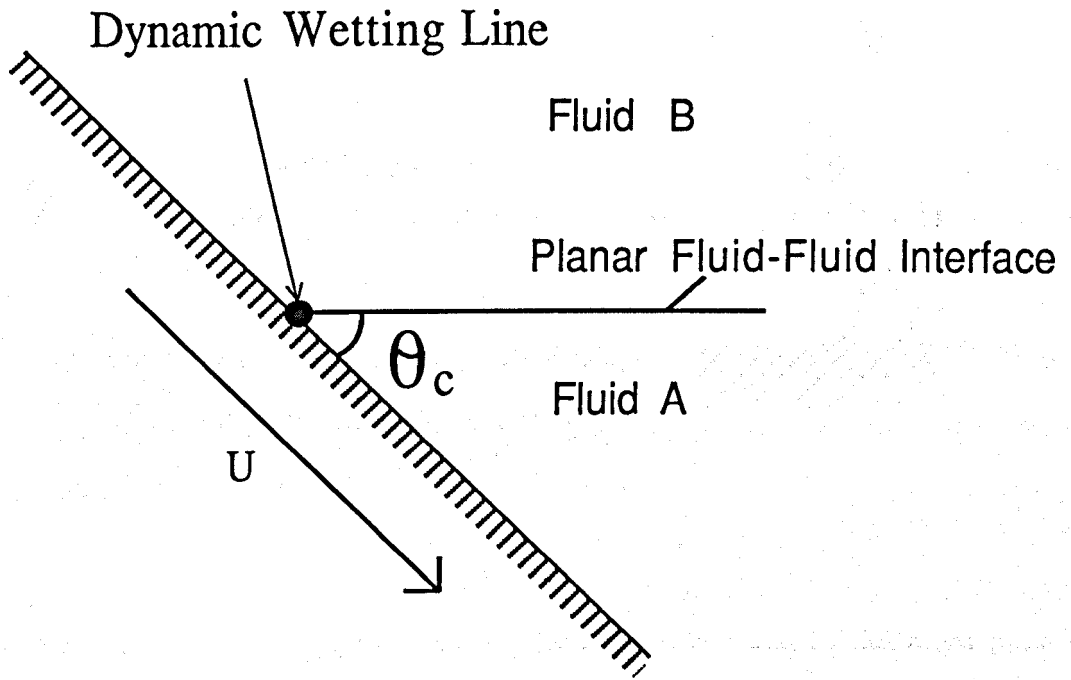
Figure 1.13: Huh and Scriven's [1971] Model of a Dynamic Wetting Line

UNIFORM
FILM

g

V_s

FLUID BATH
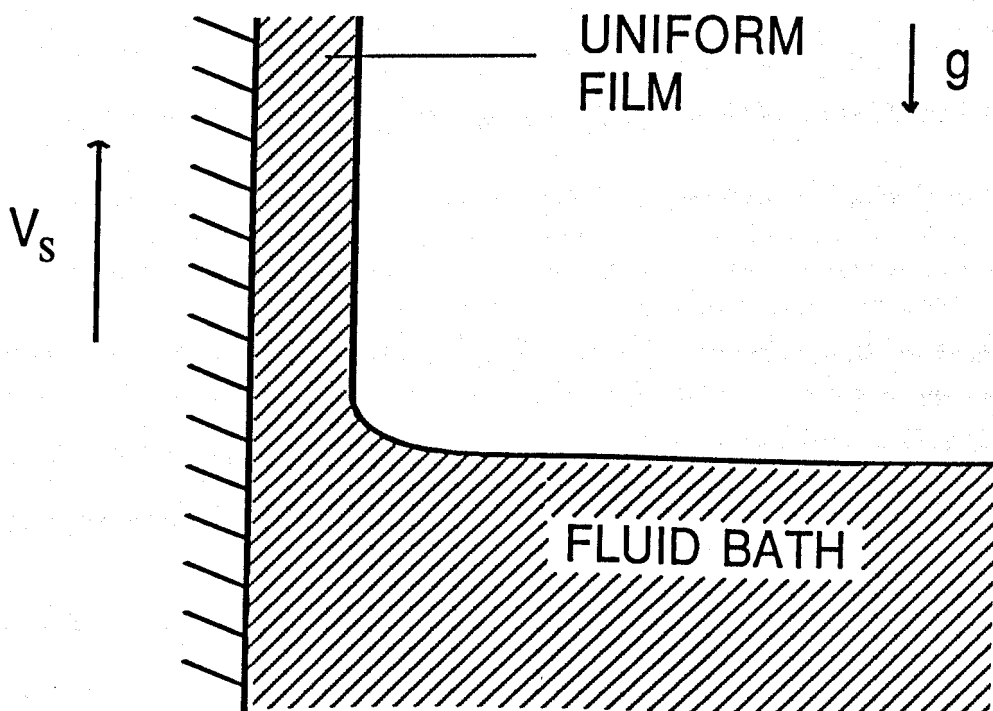
Figure 1.14: The Drag-Out Problem
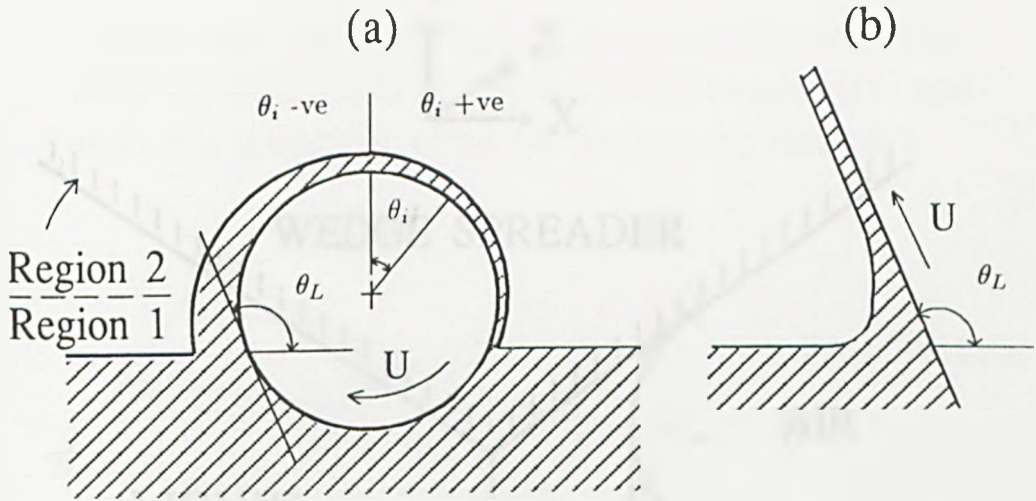
Figure 1.15: The Free Coating Problem; (a) for a rotating roller, (b) for a flat plate analogy
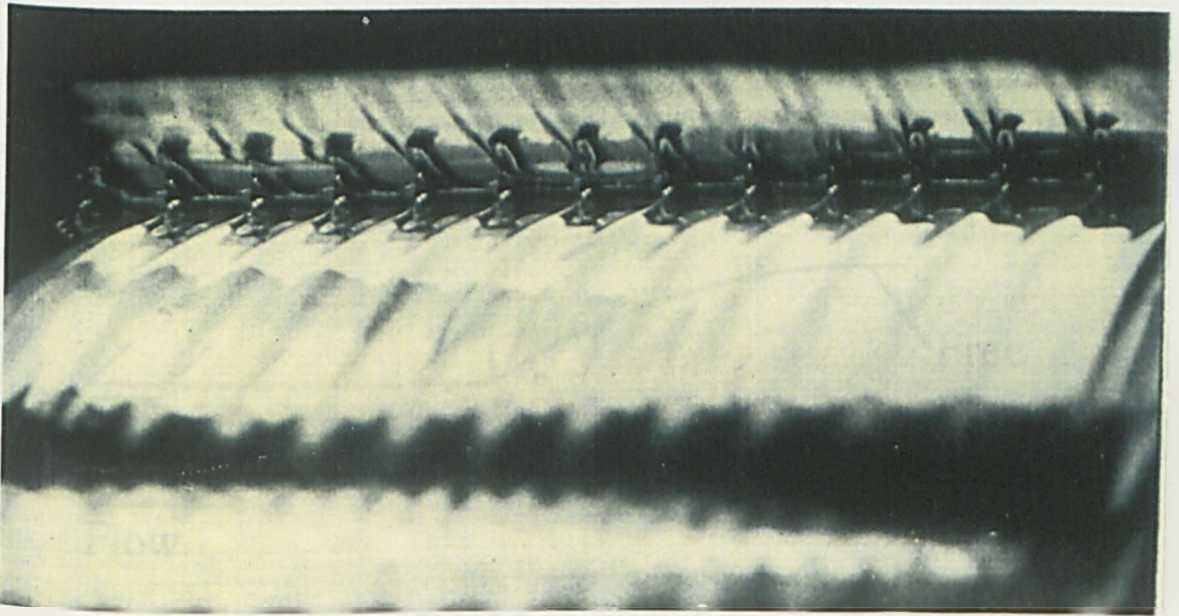
Figure 1.16: The Ribbing Phenomenon (Carter [1985])
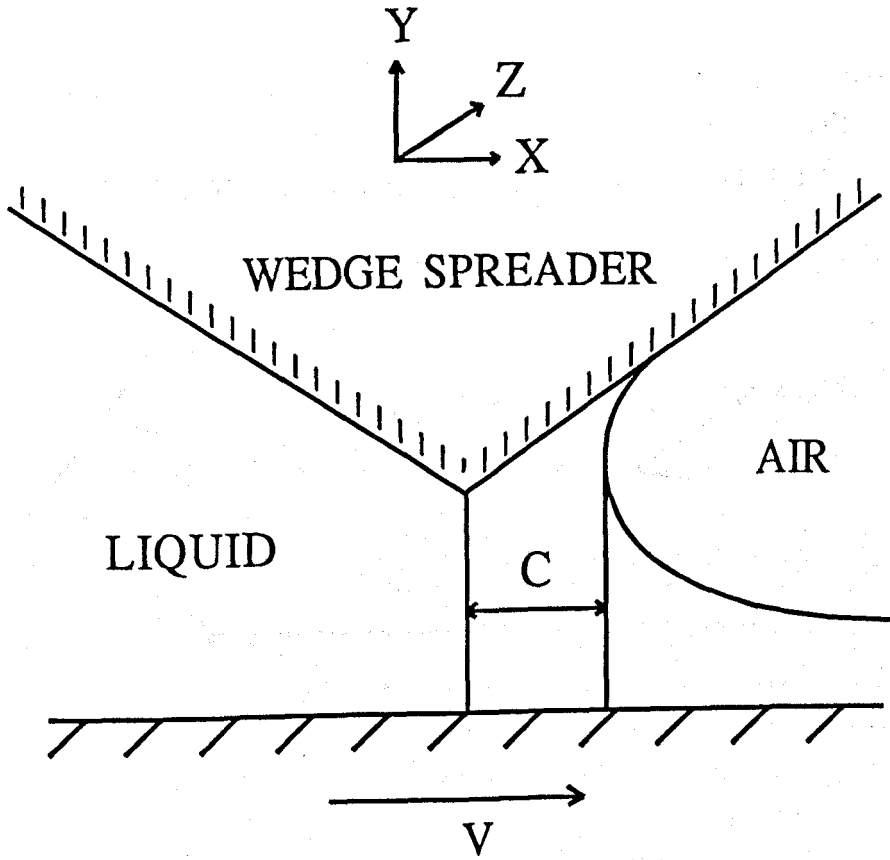
Figure 1.17: The Wedge-Shaped Spreader (Pearson [1960])
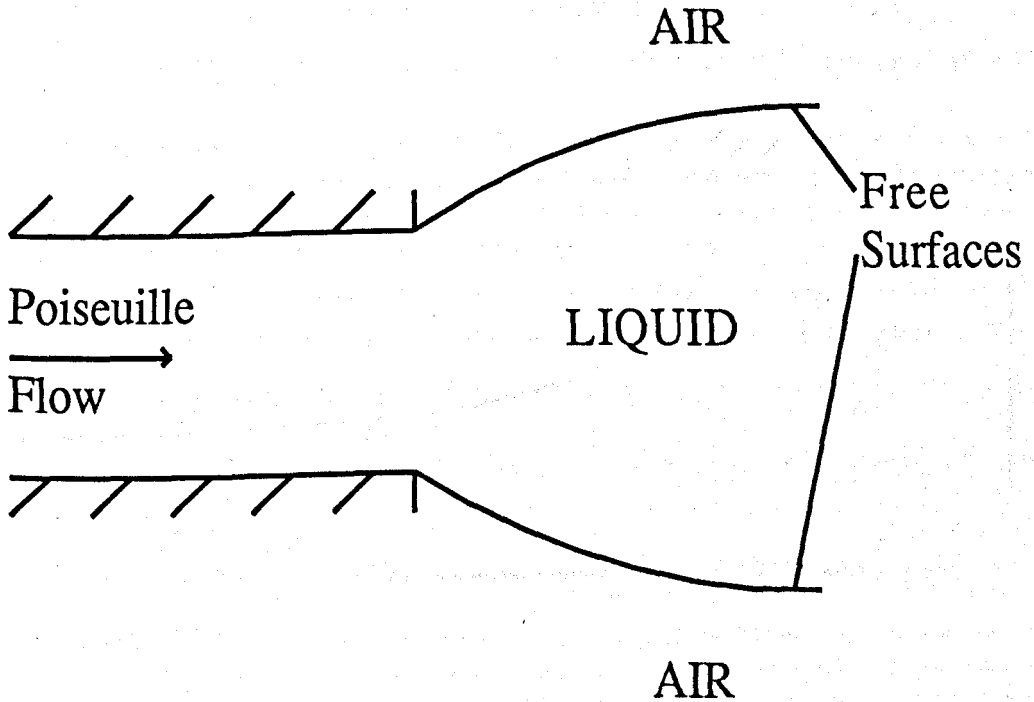
Figure 1.18: The Die-Swell Phenomenon

Section of a grid showing three boundary supports.
Each support starts at a node fixed in space (□) and
ends at a moveable node on the free surface (●)
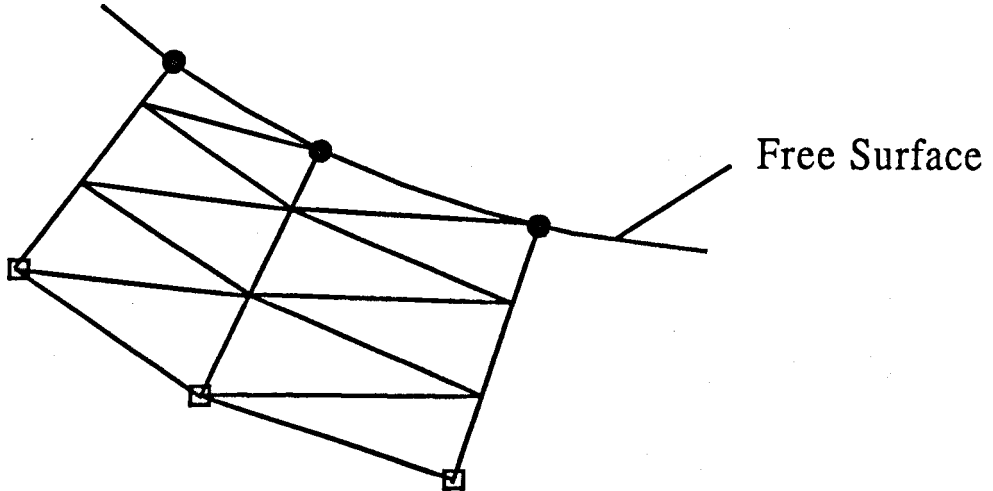
Free Surface

Figure 1.19: Ruschak's [1980] 'Boundary Supports' Free Surface Representation

RIGID
BOUNDARY

SEPARATION LINE P →

α

AIR

LIQUID

H

$H\infty$

Y

X

VEB SPEED U_{web}
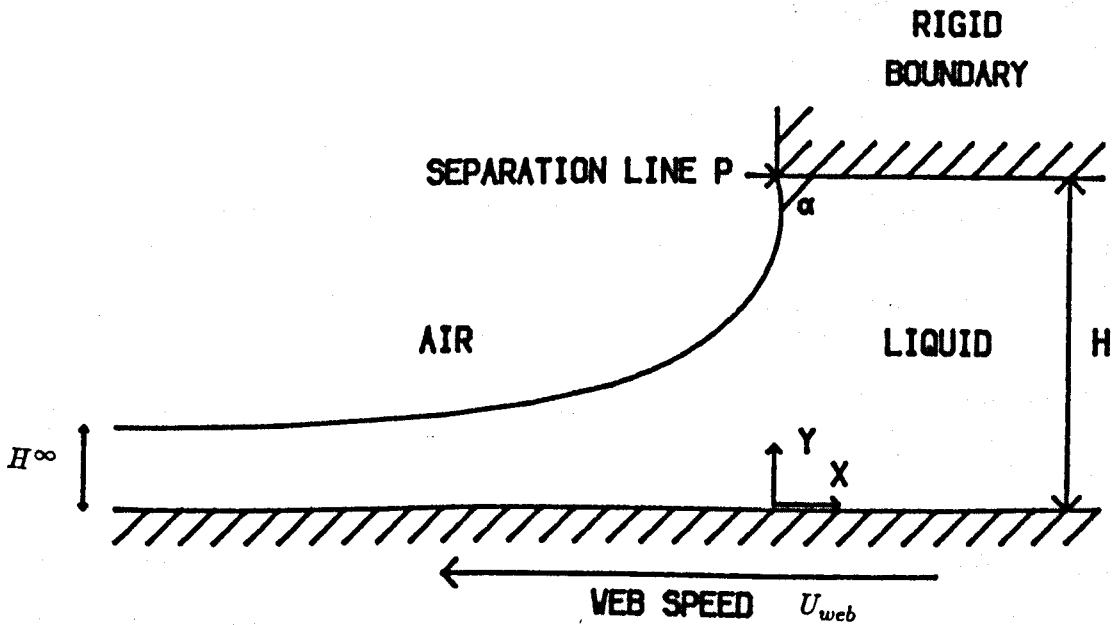
Figure 1.20: The Slot Coater

(a)

(b)
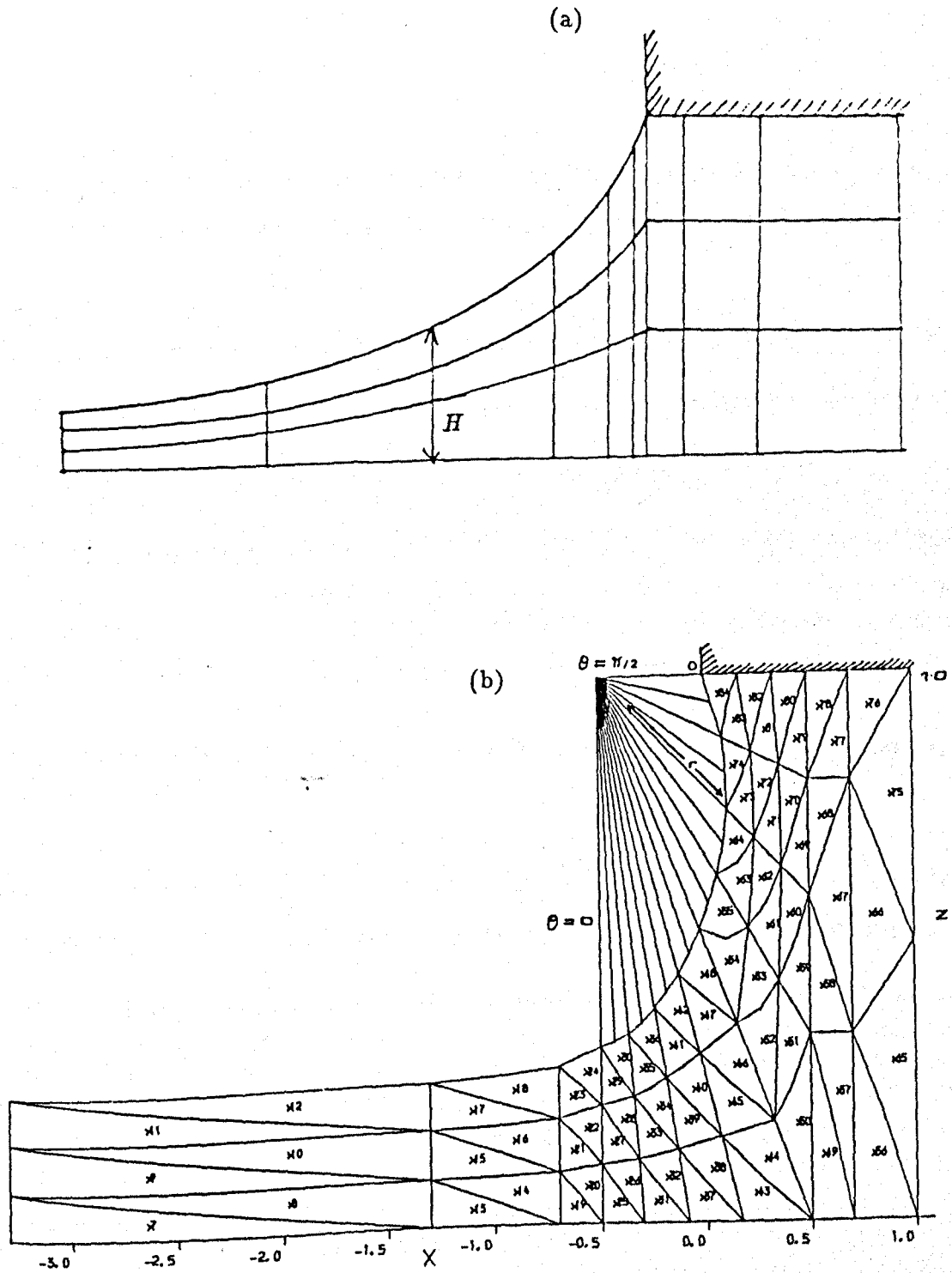
Figure 1.21: F.E. Grids for the Slot Coater: (a) Silliman [1980]; (b) Carter [1985], including construction lines for region 2

(a)

(b)
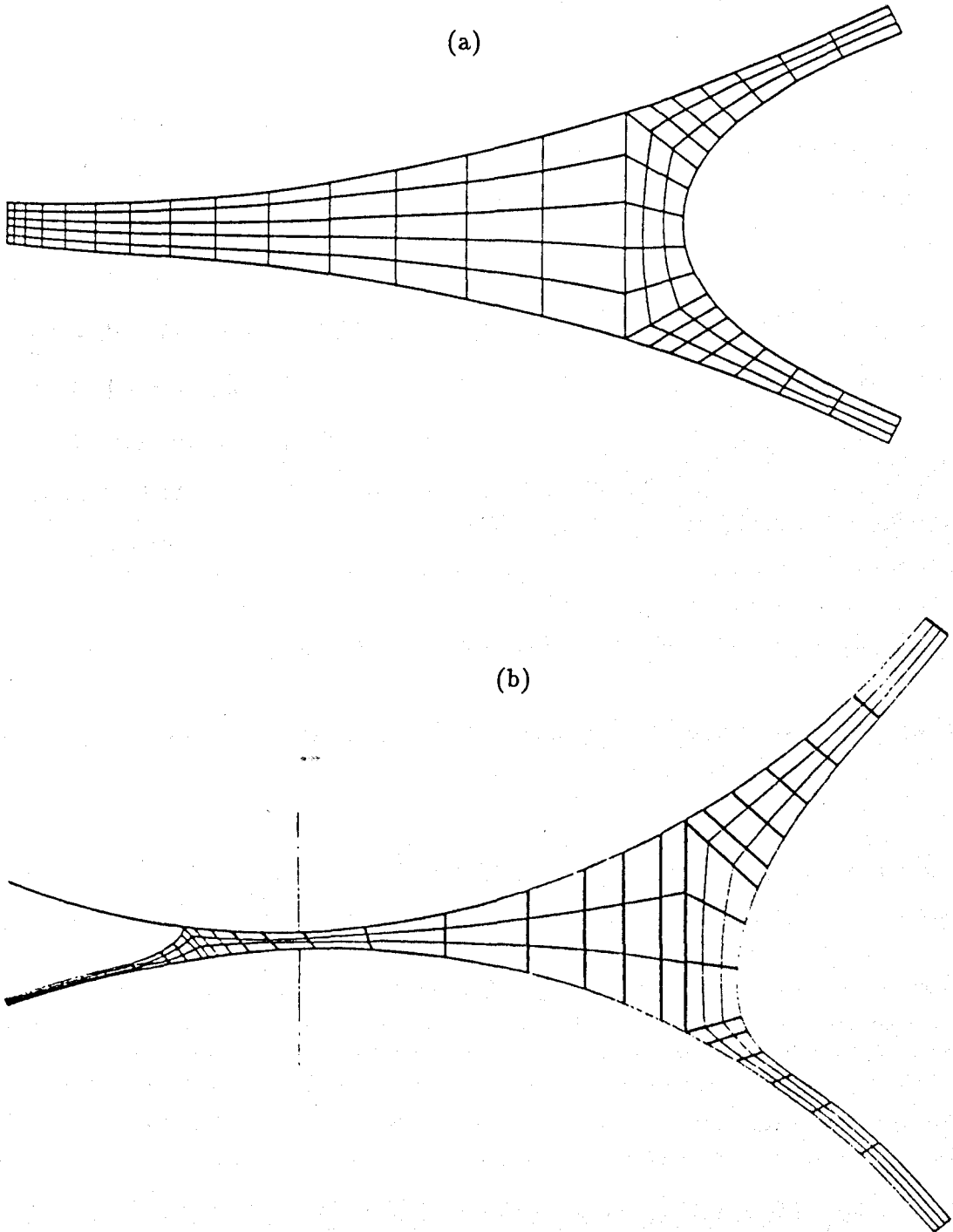
Figure 1.22: F.E. Grids Used in Numerical Solutions of (a) asymmetric forward roll coating (Coyle et al [1986]), (b) reverse roll coating (Coyle et al [1990a])

Chapter 2: The Zero Flux Model of Meniscus Roll Coating

Chapter 2

The Zero Flux Model of

Meniscus Roll Coating

2.1 Introduction

In Chapter 1 it was noted that roll coating may be operated under different degrees of starvation. In the fully-flooded case, the inlet is bathed in an ample supply of liquid, whereas in the moderately- and ultra-starved (meniscus roll coating) cases, insufficient liquid is picked up to flood the inlet – see Figures 1.6 (a)-(c). It is possible to define 'starvation' in terms of a *dimensionless flux* $\lambda = Q/2\overline{V}H_0$, where Q is the total flux between the rollers, $\overline{V} = (V_1 + V_2)/2$ is the average speed of the rollers, and H_0 the semi-nip width. In Chapter 4 it will be seen that in the fully flooded, symmetric (equal speed and radii rollers) case λ lies between 1.3 and 1.4, so any value of λ below that for the fully-flooded situation corresponds to a starved case.

The purpose of this and the following chapter is to mathematically model the two-dimensional flow in the bead of the meniscus roll coater, shown experimentally in Figure 1.5. However, before one can develop a mathematical model of a physical process it is important to examine all the factors which influence it. In a liquid flow problem, such a survey should consider (i) the rheological and physical properties of the working liquid, (ii) the competing forces in order to determine which are dominant, and (iii) the shape of the liquid domain. The task of the mathematical modeller is to use the results of

this survey to develop a model which includes only those features which are dominant. Having developed a model, its predictive power must be tested against experiment in order to validate and establish its range of applicability. A good correspondence suggests that the key features of the flow have been captured, otherwise either the existing model must be refined or a new one developed incorporating additional physics. Clearly the development of a mathematical model may be viewed as an iterative process.

Turning now to meniscus roll coating; in §§1.2.4, §1.3 we saw that ultra-starvation has important implications for the flow since it leads to the appearance of a second, *highly curved* meniscus on the upstream side of the liquid bead. Moreover because the domain of interest (i.e. the liquid bead) has an irregular shape, the full flow problem cannot be solved using classical analysis. In practical terms, this means that simple modelling is limited to the flow in the central 'core' of the bead, sufficiently far from the meniscii – see Figure 2.1. Although the principal aim of this chapter is to develop a simple model for meniscus roll coating, it is instructive to first focus attention on two related problems. These are the flows in (i) a lid-driven cavity, (ii) in an open, driven cavity; both are 'cavity-driven' flows which form part of a sub-class of problems known as 'creeping' (or Stokes) flows.

2.2   The Equations of Creeping Flow

The steady flow of a Newtonian, incompressible liquid of constant density ρ and viscosity η is governed by the Navier-Stokes equations, viz

$$\rho\, \underline{U}.\nabla \underline{U} \;\; = \;\; -\nabla P \;+\; \eta\, \nabla^2 \underline{U} \tag{2.1}$$

$$0 \;\; = \;\; \nabla.\underline{U} \tag{2.2}$$

where $\underline{U}$ and P are the liquid velocity and pressure respectively. Suppose that flow is 'slow' in the sense that the liquid inertia term, given by the left hand side of (2.1), is negligible compared to the viscous and pressure terms, then the Navier-Stokes equations reduce to the Stokes equations for creeping flow

$$0 \;\; = \;\; -\nabla P \;+\; \eta\nabla^2 \underline{U} \tag{2.3}$$

$$0 \;=\; \nabla.\underline{U} \qquad\qquad (2.4)$$

Taking the curl of (2.3) eliminates the pressure gradient term ∇P leaving

$$0 \;=\; \text{curl}(\nabla^2 \underline{U}) \qquad\qquad (2.5)$$

For a two-dimensional, incompressible flow it is possible to define the vector $\underline{\Psi} \;=\; (0, 0, \Psi(X,Y))$ such that $\underline{U} \;=\; \text{curl}\,(\underline{\Psi})$. Replacing $\underline{U}$ by $\text{curl}\,\underline{\Psi}$ in (2.5) yields the biharmonic equation for the streamfunction $\Psi(X,Y)$:

$$\nabla^4\,\Psi \;=\; 0 \qquad\qquad (2.6)$$

2.3   Flow in a Lid-Driven Cavity

The first creeping flow problem to be considered is that inside a 'lid-driven' cavity, illustrated in Figure 2.2 (a). It is the steady, two-dimensional flow induced in a solid-walled, rectangular cavity by shearing the liquid on top by a uniformly moving plate. This problem, a simple illustration of a flow with closed streamlines, has received much attention in the literature. Indeed it has become a benchmark problem for the testing of numerical schemes in fluid mechanics – see Gaskell, Lau and Wright [1988].

Since in this thesis we are assuming that the liquid is Newtonian and incompressible then, referring to Figure 2.2 (a), the dynamic behaviour of this flow may be described in terms of a cavity Reynolds number $Re = \rho\,UD/\eta$, where ρ and η are the liquid density and viscosity respectively, while the effect of the cavity geometry is described by the aspect ratio $A^* = D/L$. In his paper Burggraf [1966] obtained finite-difference (F.D.) numerical solutions for the flow in a square cavity ($A^* = 1$) for $0 \leq Re \leq 400$. Pan and Acrivos [1967] presented a detailed F.D. numerical solution for the creeping flow case ($Re = 0$) for cavities with aspect ratio $0.25 \leq A^* \leq 5$. Their fundamental paper also includes experimental data taken in cavities with $A^* = 1$ and $A^* = 10$ over the range $20 \leq Re \leq 4000$; their flow visualisations were in good agreement with streamline predictions from Burggraf's numerical solution. Other experimental and theoretical studies of flows in lid-driven cavities include those of Ghia, Ghia and Shin [1982] and Prasad, Perng and Koseff [1988].

The flow in a lid-driven cavity is commonly reformulated in terms of a boundary value problem for the streamfunction (see e.g. Burggraf [1966]). In order to achieve this, the boundary conditions shown in Figure 2.2 (a) must be rewritten in terms of the streamfunction.

Boundary Conditions

(a) No-Slip Conditions

The no-slip hypothesis of conventional fluid mechanics states that the liquid velocity at a solid surface is equal to the velocity of the solid surface. It may be shown that if Ψ is the streamfunction of a flow and $\underline{U} = (U, V)$ are the cartesian components of liquid velocity then

$$U = \frac{\partial \Psi}{\partial Y} \quad , \quad V = -\frac{\partial \Psi}{\partial X} \tag{2.7}$$

Hence relations (2.7) enable the no-slip conditions in Figure 2.2 (a) to be written in terms of derivatives of the streamfunction.

(b) A Closed Liquid Domain

In the lid-driven cavity flow, the liquid domain is closed, i.e. no liquid crosses the boundaries. However, the difference in value of the streamfunction at two different points represents the net liquid flux between these points. Therefore if there is no net liquid flux between two points, then the streamfunction has the same value at these points. This means that the streamfunction is constant on the boundaries of a closed liquid domain; this constant is usually taken to be zero.

Now focus attention on the case in which the lid velocity U is so small that the governing equations are those of creeping flow (equation (2.6)). Introducing the dimensionless quantities (refer to Figure 2.2 (a)) $\underline{u} = \underline{U}/U$, $x = X/(L/2)$, $y = Y/(L/2)$, $\psi = \Psi/(UL/2)$, and $A^* = D/L$ (the cavity 'aspect ratio'), enables the slow flow in a lid-driven cavity to be reformulated as the dimensionless boundary value problem shown in Figure 2.2 (b). Since the flow field is closed, it is convenient to take $\psi = 0$ on all four boundaries. From equation (2.7) the boundary conditions on the side walls are

$$\psi(\pm 1, y) = \frac{\partial \psi}{\partial x}(\pm 1, y) = 0 \tag{2.8}$$

while those on the upper and lower walls yield

$$\frac{\partial \psi}{\partial y}(x, 2A^*) = 1 \ , \ \psi(x, 2A^*) = 0 \tag{2.9}$$

$$\frac{\partial \psi}{\partial y}(x, 0) = 0 \ , \ \psi(x, 0) = 0 \tag{2.10}$$

Joseph and Sturges [1978] postulated a solution to this boundary value problem in the form of a biharmonic series

$$\psi = \sum_{n=-\infty}^{\infty} \left\{ A_n \, e^{s_n(y-2A^*)} + B_n \, e^{-s_n y} \right\} \frac{\phi_1^n(x, s_n)}{s_n^2} \tag{2.11}$$

where (A_n, B_n) are (complex) constant coefficients, s_n are complex eigenvalues and the functions ϕ_1^n are *even* Papkovich-Fadle eigenfunctions – see Appendix A. The eigenvalues s_n are chosen so that the side wall conditions (2.8) are automatically satisfied.

The complex coefficients (A_n, B_n) are evaluated using a truncation technique employing Smith's [1952] biorthogonality relation. This is described in Appendix A. When the coefficients have been determined the streamfunction at any interior point of the liquid may be obtained by simply summing the series (2.11). Table 2.1 shows values of the streamfunction (ψ) and horizontal component of liquid velocity ($\partial \psi / \partial y$) on the upper and lower lids of a cavity with $A^* = 5$, calculated by truncating (2.11) after 20 terms. The convergence to the boundary conditions (2.9), (2.10) is satisfactory. Note that at the upper right hand corner, which is formed at the junction of the moving lid with the right hand side wall, the liquid velocity is zero. This is a consequence of selecting the eigenvalues s_n in order to satisfy the conditions (2.8). In fact the exact nature of the flow near this junction cannot be determined; this point is expanded upon in Appendix B, which deals with numerical techniques for modelling junctions of this kind.

It is possible to compare the streamfunction values obtained from the semi-analytical solution (2.11) with those from a corresponding numerical solution obtained using the 'streamfunction-vorticity' F.E. method for creeping flows, described in Appendix B. Numerical solutions are obtained using triangular elements, for the reasons described in §B.2, while the storage requirement needed to solve the F.E. equations (equations (B.20), (B.21) of Appendix B) is reduced by using a 'banded-matrix' solver from the

NAg F.E. library of subroutines – see Appendix C for the philosophy behind this solution technique. It is important, however, to check any F.E. solution since its accuracy depends on (i) the degree of refinement of the computational mesh; (ii) the numerical integration (in this case Gaussian Quadrature) schemes chosen. For the former, it is sometimes possible to use theoretical error analysis, e.g. the 'Patch Test' (see Carter [1985] pp 145-148), but in the present application it is more convenient to simply obtain solutions on two or more grid levels, and then test whether the solutions are in reasonable agreement. A similar process must also be carried out to test the effect of the quadrature scheme on the solution's accuracy.

Numerical solutions were obtained using the 3 grids shown in Figure 2.3: grids (a) and (b) are symmetric about the vertical cavity centreline, $x = 0$, and consist of 144 elements (329 nodes) and 216 elements (481 nodes) respectively. Grid (c) also has 144 elements and 329 nodes, but is asymmetric about the cavity centreline; this enables us to examine the effect of grid asymmetry on the numerical results. All grids are refined at the upper corners due to the indeterminate nature of the flow near these points. Numerical results were obtained using each grid and every possible combination of quadrature schemes for area integrals (i.e. (A), (B), (C), (D) of Figure B.6) and boundary integrals ((a), (b), (c) of Figure B.7) described in Appendix B. Close examination of these results showed that solutions obtained using any of the above combinations were in agreement to the third decimal place with an analytical solution obtained by truncating (2.11) after 30 terms (see Gaskell, Savage and Thompson [1991]), regardless of which grid was used. However as expected, grid (c) introduced a slight asymmetry (about the line $x = 0$) into the numerical solutions.

When scheme (D) (with one negative weight) was used, the numerical solutions were in extremely poor agreement with the analytical solution (2.11). This is a problem identified by previous authors (e.g. Smith [1982], Carter [1985]) and is thought to be a product of using a quadrature scheme with a negative weight, which can lead to severe rounding errors during the computation. Changing the quadrature scheme had only a minor effect on execution times for the numerical solutions: those obtained using grids (a) and (c) took approximately 70 c.p.u. seconds (all computations were performed on

an AMDAHL 5860 computer), compared with 110 c.p.u. seconds when grid (b) was used. On the basis of these numerical results it was decided that all streamfunction-vorticity F.E. solutions presented in this thesis would be calculated using the 4-point scheme (A) for area integrals and the 2-point scheme (a) for boundary integrals.

Figure 2.4 shows streamlines computed (a) analytically (with 20 terms in the series (2.11)) and (b) numerically, using grid (a) of Figure 2.3, and (c) due to Pan and Acrivos [1967] for a square cavity ($A^* = 1$). The agreement between the analytical, numerical and published solutions is excellent; note that truncating the series after 20 terms is sufficient to resolve the corner eddies. Figure 2.5 shows streamlines for a cavity with $A^* = 5$. The analytical results agree well with those from Pan and Acrivos' [1967] numerical study; again the corner eddies are resolved by taking 20 terms in the series (2.11). Note the interesting prediction that the vortex structure depends on the cavity aspect ratio A^*. This suggests a possible extension to the work presented here, namely a study in order to determine the exact nature of the transition in the vortex structure as A^* is increased.

..

2.4 Flow in an Open, Driven Cavity

The next problem to be studied is the slow flow of a Newtonian, incompressible liquid in an open cavity generated by the steady rotation of a cylinder, shown in Figure 2.6 (a). This problem has received recent attention from Canedo and Denson [1989]. In their mathematical model of this flow, they augmented the assumptions, used in §2.3, of a creeping, steady, two-dimensional flow, with the following additional ones:

(i) Neglect the curvature of the roller.

(ii) Neglect the influence of the thin lubrication film attached to the roller which flows from the cavity at the bottom and re-enters at the dynamic wetting line.

(iii) Assume a planar liquid-gas interface.

(iv) The gas above the liquid remains at uniform pressure P_a and its viscosity is negligible compared with the liquid viscosity.

Assumption (i) results in the cross-section of the flow, shown in Figure 2.6 (b), having a rectangular shape, whereas (ii) is equivalent to assuming a closed liquid domain. In Chapter 1 it was noted that meniscii, including the effects of surface tension, cannot be modelled by purely analytical means. However with assumption (iii), Canedo and Denson made the problem tractable by imposing a simple meniscus shape. Unfortunately by doing so, it is no longer possible to satisfy all (three) – see Chapter 4 – free surface boundary conditions. For a steady flow, two of these conditions stipulate that both the normal and tangential stresses must balance. In their model, Canedo and Denson chose to balance the shear, i.e. tangential, stresses at the planar interface and accept the fact that the normal stresses are unbalanced. Of course in practice the interface is curved and these normal stresses are balanced by surface tension stresses due to this curvature (see §§1.2.2). This condition may also be expressed in terms of the streamfunction Ψ.

(c) Balance of Shear Stress at a Planar Liquid-Gas Interface

If $\underline{n}$, $\underline{t}$ are unit vectors normal and tangential to the liquid-gas interface respectively (see Figure 2.7), then in the general situation the equation expressing the equilibrium of this interface (Batchelor [1985] p 69) is

$$\underline{\underline{\Sigma}} \cdot \underline{n} = \underline{\underline{\Sigma_g}} \cdot \underline{n} + \frac{T}{R_{curv}} \underline{n} \tag{2.12}$$

where $\underline{\underline{\Sigma}}$, $\underline{\underline{\Sigma_g}}$ are the stress tensors of the liquid and gas respectively, T is the surface tension of the liquid, and R_{curv} the radius of curvature of the liquid-gas interface. For a Newtonian liquid the stress tensor is given by

$$\Sigma_{ij} = -P\delta_{ij} + \eta \left(\frac{\partial U_i}{\partial X_j} + \frac{\partial U_j}{\partial X_i} \right) \tag{2.13}$$

where δ_{ij} is the Kronecker delta symbol

$$\delta_{ij} = \begin{cases} 1 & \text{if i=j} \\ 0 & \text{otherwise} \end{cases} \tag{2.14}$$

In Canedo and Denson's model, the liquid-gas interface is planar with $\underline{n} = (0,1)$ and $\underline{t} = (1,0)$. It can be shown that balancing shear stresses there yields

$$\eta \left(\frac{\partial U}{\partial Y} + \frac{\partial V}{\partial X} \right) = \eta_g \left(\frac{\partial U_g}{\partial Y} + \frac{\partial V_g}{\partial X} \right) \tag{2.15}$$

where the subscript g refers to the gas. However by assumption (iv) $\eta_g/\eta \ll 1$, so equation (2.15) reduces to a 'zero-shear stress' condition, namely

$$\frac{\partial U}{\partial Y} + \frac{\partial V}{\partial X} = 0 \quad \text{at } Y = 0 \tag{2.16}$$

Using relations (2.7), this may be written in terms of the streamfunction, giving

$$\frac{\partial^2 \Psi}{\partial Y^2} - \frac{\partial^2 \Psi}{\partial X^2} = 0 \quad \text{at } Y = 0 \tag{2.17}$$

Since the liquid domain is closed (assumption (ii)), Ψ is constant on the liquid boundaries so $\partial\Psi/\partial X = \partial^2\Psi/\partial X^2 = 0$ at $Y = 0$. Therefore this zero shear stress condition may be rewritten as

$$\frac{\partial^2 \Psi}{\partial Y^2} = 0 \quad \text{at } Y = 0 \tag{2.18}$$

All the remaining boundary conditions are of the form (a), (b) or (c) described above. For the purposes of the analysis it is convenient to scale lengths by D, liquid velocities by U and the streamfunction by UD. In this case the aspect ratio $A^* = L/D$ is also the dimensionless cavity width. This non-dimensionalisation, coupled with the creeping flow and geometry assumptions described above, enables the slow flow in an open, driven cavity to be reformulated as the dimensionless boundary value problem shown in Figure 2.8. Once again, for convenience the streamfunction is set equal to zero on the boundaries.

Canedo and Denson [1989] solved this problem numerically using a F.D. scheme and have presented an analytical solution only valid for infinitely deep cavities of finite width. It is, however, possible to obtain a semi-analytical solution valid for all values of aspect ratio by using a truncated biharmonic series similar to that described in §2.3 for the lid-driven cavity flow. Postulate a solution of the form

$$\psi = \sum_{n=-\infty}^{\infty} \left(C_n e^{p_n(x-A^*)} + D_n e^{-p_n x} \right) \frac{\tilde{\phi}_1^n(y, p_n)}{p_n^2} \tag{2.19}$$

where (C_n, D_n) are complex coefficients, $\tilde{\phi}_1^n$ are *odd* Papkovich-Fadle eigenfunctions, and p_n are complex eigenvalues chosen to satisfy the conditions at the bottom lid and the planar liquid-gas interface. The coefficients are obtained by using a modified form of Joseph and Sturges' truncation technique, the main points of which are summarized

in Appendix A. As in §2.3, it is found that truncating the biharmonic series (2.19) after 20 terms gives satisfactory convergence to the boundary conditions on the side walls – see Table 2.2 for analytical results for a square cavity with $A^* = 1$. As in the lid-driven cavity flow case, the no-slip conditions on the moving wall are inapplicable very close to the cavity corners because this would lead to mathematical singularities there – see Appendix B.

Streamlines obtained from a semi-analytical solution of this problem, truncated after 20 terms, are shown in Figure 2.9 (a); they agree well with those obtained numerically by the streamfunction-vorticity F.E. technique (Figure 2.9 (b)), and Canedo and Denson [1989] (Figure 2.9 (c)). As in §2.3, the corner eddies may be resolved by taking only 20 terms in the series (2.19). The two F.E. grids used in the streamfunction-vorticity solutions of this problem are shown in Figure 2.10: grid (a) consists of 144 elements and 329 nodes, whereas grid (b) has 216 elements and 481 nodes. Both grids are refined at the right hand side corners in order to alleviate inaccuracies due to corner singularities there. Once again it is found that grid (a) is sufficiently refined for this application. The F.E. equations (B.20), (B.21) are solved by the same banded matrix solver as was used in §2.3. Solutions obtained using grids (a) and (b) had execution times of approximately 70 and 110 c.p.u. seconds respectively.

The semi-analytical solution (2.19) has many advantages over numerical solutions to this problem: in addition to the obvious ones such as convenience, cost-effectiveness and an ability to resolve corner eddies, it is possible to calculate the (unbalanced) normal stresses at $y = 0$. This is useful because one can then, in principle, postulate a *small* perturbation to the liquid-gas interface from the assumed, planar shape (which corresponds to the hypothetical case in which capillary number $Ca = \eta U/T$ is zero) to one with small disturbances from a planar shape (corresponding to a small, finite Ca). This could be achieved by balancing the normal stresses in the liquid by surface tension stresses due to interface curvature. However this point is not pursued here.

2.5 The Zero Flux Model of Meniscus Roll Coating

2.5.1 Introduction

In this section a mathematical model for the flow of a Newtonian, incompressible liquid in a meniscus roll coating bead is developed. In order to make the problem tractable to analysis, a number of simplifying assumptions are made. The value of considering the 'cavity-driven' flows described above will soon become apparent since the model of meniscus roll coating developed here, and termed the 'Zero Flux Model', is strongly influenced by them.

In an initial survey of meniscus roll coating there are many interesting observations to be made. The first is that, under normal operating conditions, the flow in the bead does achieve a two-dimensional, steady state (Malone [1992]). Now in fully-flooded roll coating the liquid inertia terms in the governing equations (equations (2.1), (2.2)) are rarely important compared to the viscous and pressure terms (see e.g. Savage [1982], Coyle et al [1986]). In §§1.3.3 we noted that meniscus roll coating is operated at lower speeds and with liquids of lower viscosity than in the fully-flooded case. Although these lower liquid viscosities tend to increase the relative importance of the liquid inertia terms in meniscus roll coating, the lower roller speeds mean that the Reynolds numbers $Re = \rho U L / \eta$ (where U, L are characteristic velocity and length scales respectively), measuring the significance of the inertia terms in the flow, are of similar magnitudes to those encountered in the fully-flooded case (Malone [1992]). Consequently it should also be valid to assume that liquid inertia effects are negligible in meniscus roll coating. For this reason the creeping flow approximation used in §2.3, 2.4 is also employed in the Zero Flux Model.

Another important feature of meniscus roll coating is that the dimensionless flux λ, defined in §2.1, is small compared to a typical fully-flooded value where $1.3 \leq \lambda \leq 1.4$. A key assumption of the Zero Flux model therefore, which explains the origin of its name, is to neglect the flux through the bead; this is equivalent to assuming a closed liquid domain as in the two previous problems. In §1.3 we saw that other important factors complicating analyses of meniscus roll coating are: (i) the existence of two

meniscii, one on either side of the bead, and the shape of the rollers. These features are modelled as in §2.4, i.e. the meniscii are represented as planar interfaces on which a condition of zero shear stress is imposed, and the rollers as flat lids.

These assumptions enable the flow to be modelled as shown in Figure 2.11: the liquid bead is rectangular and the flow is generated by the motion of the lids. The analysis is simplified by introducing the following dimensionless quantities

$$\underline{u} = \underline{U}/V_2 \,, \ x = X/(L/2) \,, \ y = Y/(L/2) \tag{2.20}$$

$$\psi = \Psi/(V_2 L/2) \,, \ S = V_1/V_2 \,, \ H^* = 2H_0/(L/2) \tag{2.21}$$

where L is the bead width, V_2 the bottom lid velocity, S the velocity ratio of the lids and H^* the dimensionless cavity depth ($2H_0$ is the separation of the lids). This non-dimensionalisation, coupled with the creeping flow assumption, enables the Zero Flux Model and associated boundary conditions to be reformulated as the boundary value problem shown in Figure 2.12. Note that since the liquid-gas interfaces are now vertical planes with $\underline{n} = (\pm 1, 0)$, $\underline{t} = (0, \mp 1)$, the zero shear stress conditions are modified, giving

$$\frac{\partial^2 \psi}{\partial x^2} = 0 \ \text{ at } x = \pm 1 \tag{2.22}$$

in contrast to expression (2.18).

It is found that this boundary value problem is much simpler than those in §2.3, §2.4 since it can be solved using the 'natural' eigenfunctions of the biharmonic equation, namely

$$\psi = \sum_{n=1}^{\infty} \left\{ (y - H^*)(A_n e^{\lambda_n(y-H^*)} + B_n e^{-\lambda_n y}) + D_n(e^{-\lambda_n y} - e^{\lambda_n(y-2H^*)}) \right\} \cos(\lambda_n x) \tag{2.23}$$

where λ_n are eigenvalues and (A_n, B_n, D_n) are constant coefficients to be determined from the boundary conditions. In fact the form of this solution is the same as that used by Harper and Wake [1983] to model the flow in the earth's mantle. The conditions on the side walls may be satisfied if $\cos \lambda_n = 0 \ \forall \ \lambda_n$, giving

$$\lambda_n = \left(n - \frac{1}{2} \right) \pi \quad \text{for } n = 1, 2, \dots \tag{2.24}$$

Note that these eigenvalues, and consequently the coefficients also, are *real* in contrast to those given in Appendix A. The unknown coefficients are determined by satisfying the boundary conditions on the lids and it may be shown that these conditions reduce the search to a standard Fourier expansion problem. Of course, it is only possible to include a finite number of terms in the series (2.23) in practice, so it is important to determine the number of terms which need to be taken to ensure that the series has converged satisfactorily. Since expression (2.23) is an even function of x, the convergence characteristics may be investigated by considering streamfunction values in the right half of the bead only. Table 2.3 shows the values of the streamfunction calculated from (2.23) for the flow in a liquid bead with $H^* = 0.25$ and $S = 1$ and 2 by truncating the series after (i) 20 and (ii) 50 terms. These values agree to the third decimal place and the streamfunctions satisfy the conditions $\psi = 0$ on the upper and lower lids to six decimal places. Of further interest is the convergence of the analytical expression for the horizontal liquid velocity (obtained from the streamfunction (2.23) by the relation $u = \partial\psi/\partial y$) to velocity conditions on the moving lids. Table 2.4 shows horizontal velocities on the lids for flows with (a) $H^* = 0.25$, $S = 1$, (b) $H^* = 0.25$, $S = 2$ obtained by truncating the series for u after (i) 20, (ii) 50 terms. These results show that by taking only 20 terms of the biharmonic series, the convergence to the velocity boundary conditions is satisfactory. The agreement improves as more terms are taken; this is to be expected because as noted earlier, the convergence to the boundary conditions will have the same properties as the convergence of a Fourier series on an interval. In fact, in all cases studied it was found to be sufficient to take only 20 terms of the biharmonic series (2.23) in order to attain satisfactory convergence to the lid velocity conditions

In §§1.2.4 we saw that in meniscus roll coating there is one dynamic wetting line where the inlet meniscus meets the web/upper roller (see Figure 1.12). However in the zero flux model, there are dynamic wetting lines at all four corners of the liquid bead. At each of these corners, the form of the solution (2.23) ensures that $\partial\psi/\partial y = 0$ there, i.e. zero liquid velocity; this means that a condition of perfect slip between solid and liquid at these corners is implicit in the model. This feature of the model, which is important in any numerical solution of the boundary value problem, is discussed in

Appendix B.

2.5.2   Predictions of the Zero Flux Model

<u>(i) Streamline Patterns</u>

In a liquid flow, curves on which the streamfunction is constant are known as 'stream-lines'. Since they trace out the actual paths of liquid particles in a steady flow, stream-line plots provide a useful means of representing a flow field. Indeed one of the major objectives of the zero flux model is to predict the streamline patterns that arise during mensicus roll coating.

In Figure 2.13 streamlines obtained from (i) an analytical solution (expression (2.23) truncated after 20 terms), and (ii) a numerical (streamfunction-vorticity F.E.) solution of the boundary value problem shown in Figure 2.12, are presented for the 3 cases in which $H^* = 0.5$ and S=1, 2 and -1. Numerical solutions were obtained using grids (a) (160 elements, 369 nodes) and (b) (232 elements, 521 nodes) shown in Figure 2.14. Both grids are refined at the four cavity corners in order to alleviate problems caused by the dynamic wetting lines which exist there in the zero flux model. The numerical results obtained using either grid were in excellent agreement with the analytical solution – those illustrated in Figure 2.13 employed grid (a) as the computational mesh. As before the F.E. equations (B.20), (B.21) are solved by a banded-matrix solver from the NAg F.E. library, solutions obtained using grids (a) and (b) taking approximately 80 and 120 c.p.u. seconds respectively.

In the unit velocity ratio case ($S = 1$), the predicted flow consists of a double vortex structure in which the eddies are of equal size and separated by a dividing streamline. Note that the existence of this streamline separating flow in the upper and lower regions of the bead is an inevitable consequence of imposing a condition of zero net flux across the bead. When S is increased to 2, the double vortex vortex structure changes: the upper vortex is now twice the size of the lower one, although they are still separated by a dividing streamline. For the reverse case with $S = -1$, i.e. lids moving with equal speeds but in opposite directions, the double vortex structure is replaced by a single vortex *without* a dividing streamline.

These interesting streamline predictions can be compared to Malone's flow visualisations of meniscus roll coating in similar situations – see Figure 2.15. In Figure 2.15 (a) Malone injected blue dye into the inlet film of a forward meniscus roll coater with $S = 1$. As noted in §§1.2.2, the regions which are relatively clear indicate the presence of recirculations in the flow. Hence the prediction of two large recirculations in the forward case is borne out in practice. Since the dye is injected into the inlet film before it reaches the bead, the darker liquid region indicates the path taken by the liquid which originated in the inlet film. Note that there cannot be a dividing streamline in reality, as predicted by the zero flux model, since there must be a net flux across the bead in the forward case. Malone's experiments reveal that the liquid in the inlet film splits into two parts. The lower part flows straight out of the bead in a layer attached to the lower roller. The path of liquid in the upper part is, however, far more complicated. This liquid moves in an 'S'-shaped motion between the two large eddies and eventually flows out attached to the upper roller. Although it is difficult to get a complete appreciation of this complex motion with Figure 2.15 (a), the presence of dark liquid between the eddies indicates the 'snaking' of liquid between them.

In Figure 2.15 (b) the velocity ratio of the rollers has been increased to 2. Again the existence of two large eddies is clearly demonstrated, with the liquid coating the upper roller moving in an 'S'-shape between them. The larger eddy is that associated with the upper (faster moving) roller. This is also in qualitative agreement with the predictions of Figure 2.13 (b) with $S = 2.0$. Finally, Figure 2.15 (c) presents Malone's experimental flow visualisation for a reverse meniscus roll coater with $S = -1.0$. As in the corresponding theoretical prediction, the flow is seen to be essentially that of a single eddy. In his thesis Malone [1992] presents far more detailed flow visualisations of meniscus roll coating than those reported here.

The effect of liquid bead aspect ratio H^* on the streamline patterns predicted by the zero flux model with $S=1, 2, -1$ is investigated in Figure 2.16. Since the agreement between all analytical and numerical solutions is excellent, only analytical solutions with (2.23) truncated after 20 terms are presented. The predicted streamline patterns are qualitatively unchanged for aspect ratios in the range $1.0 \leq H^* \leq 4.0$.

(ii) Liquid Velocities in the Bead

We have already noted that liquid velocities in the bead can be predicted from the streamfunction (2.23) by using the fact that $u = \partial\psi/\partial y$, $v = -\partial\psi/\partial x$; Table 2.5 presents theoretical u and v values for a bead with $H^* = 0.5$ and $S = 1$. Within each box, the upper and lower results have been obtained by truncating the relevant series after 50 and 20 terms respectively. They are in very good agreement, which suggests that it is sufficient to take only 20 terms in the u and v series in order to obtain predictions for the liquid velocities in the bead. Moreover they show that the flow in the central 'core' is essentially one-dimensional, i.e. horizontal, and uniform. In Table 2.6, horizontal components of liquid velocity are obtained for flows with $H^* = 0.5$ and $S=2$, -1; again the flow in the core is uniform in both cases. Finally, Table 2.7 presents horizontal components of liquid velocity for flows with $S = 1$ and $H^* = 0.1$, 1.0. These results predict that the flow in the core is also uniform for cavities of dimensionless depth in the range $0.1 \leq H^* \leq 1.0$. The prediction that the flow in the bead core is uniform is extremely important and will be exploited in Chapter 3 during the development of a simple model for the core flow in the case of a small flux passing through the bead.

(iii) Pressure Gradient/ Pressure Profiles in the Bead

In the results of the Zero Flux Model presented so far, attention has been restricted to consideration of streamline patterns and liquid velocities. However, in roll coating the horizontal pressure gradient is also of fundamental importance as it is this gradient which provides the mechanism driving the flow. In §1.2 we saw that a typical pressure profile in fully-flooded roll coating has both a pressure maximum and a minimum – see Figure 1.10. It is now possible to obtain pressure gradient/pressure profile predictions in meniscus roll coating by using the analytical solution (2.23) of the zero flux model. If we define the *dimensionless* pressure $p = PL/2\eta V_2$ where P is the physical pressure and L, V_2 have been defined earlier then, under the creeping flow assumption, the dimensional horizontal pressure gradient $\partial p/\partial x$ is given by the Stokes' equation:

$$\frac{\partial p}{\partial x} = \nabla^2 u = \frac{\partial^3\psi}{\partial y^3} + \frac{\partial^3\psi}{\partial x^2\partial y} \qquad (2.25)$$

where u is the horizontal component of liquid velocity and ψ is the streamfunction. Substituting (2.23) into (2.25) yields

$$\frac{\partial p}{\partial x} = 2 \sum_{n=1}^{\infty} \lambda_n^2 \left(A_n e^{\lambda_n(y-H^*)} + B_n e^{-\lambda_n y} \right) \cos(\lambda_n x) \qquad (2.26)$$

for flow governed by the assumptions of the zero flux model. Fortunately the coefficients (A_n, B_n) and the eigenvalues λ_n have been defined above so the expression (2.26) may be conveniently calculated. Table 2.8 shows the values of $\partial p/\partial x$ calculated from the zero flux model for a liquid bead with $H^* = 0.5$ and $S = 1$ by taking either 20 or 50 terms in the pressure gradient expression (2.26). The agreement between the predictions obtained using 20 and 50 terms in the series is reasonably good, suggesting that sufficiently accurate values of $\partial p/\partial x$ may be obtained by truncating (2.26) after 20 terms. These predictions are very interesting since they suggest that $\partial p/\partial x$ is uniform in the bead core.

Table 2.9 presents values of $\partial p/\partial x$ obtained by truncating (2.26) after 20 terms for the cases of $H^* = 0.5$ and $S = 0.5$, 1.5, 2.0 and -1.0. In all cases $\partial p/\partial x$ is uniform in the bead core; in fact there is a discernible pattern to the values of the uniform pressure gradient since for $S = 0.5$, 1.0, 1.5, 2.0 and -1.0, $\partial p/\partial x$ is equal to 36.0, 48.0, 60.0, 72.0 and 0.0 respectively – these values are proportional to the value of $(1 + S)$ where S is the velocity ratio of the lids. There is, however, another parameter on which $\partial p/\partial x$ depends. Tables 2.10 gives predicted values of $\partial p/\partial x$ (with (2.26) truncated after 20 terms) for flows with $S = 1$ in which H^* assumes values equal to 0.1, 0.2, 0.8 and 1.0. Once again $\partial p/\partial x$ is uniform in the bead core in all cases, taking values equal to 1200, 300, 18.75 and 12 for $H^* = 0.1$, 0.2, 0.8 and 1.0 respectively. In this case the pattern is that these values are proportional to $1/H^{*2}$. Combining these two observations about the predicted values of $\partial p/\partial x$, suggests that the magnitude of the horizontal pressure gradient in the bead core predicted by the zero flux model is such that

$$\frac{\partial p}{\partial x} \propto \frac{(1 + S)}{H^{*2}} \qquad (2.27)$$

This finding is also of crucial importance for the development of the small flux model in the next chapter.

Expression (2.26) for the horizontal pressure gradient may be readily integrated with respect to x to give

$$p = 2\sum_{n=1}^{\infty} \lambda_n \left(A_n e^{\lambda_n(y-H^*)} + B_n e^{-\lambda_n y}\right) \sin(\lambda_n x) + \text{constant} \qquad (2.28)$$

Unfortunately, the value of this constant of integration cannot be determined by this simple analysis because it neglects the curvature of the meniscii – see Chapter 5 for a full explanation of this point. However it is still possible to show the predicted *shape* of the pressure profiles in meniscus roll coating since this is unaffected by the value of this constant. In Figure 2.17 dimensionless pressures on the bead centreline, i.e. equidistant from the upper and lower lids, are obtained by truncating (2.28) after 20 terms. They are plotted against horizontal position in the bead or flows with (a) $H^*=0.5$ for $S=1$, 2, 3; (b) $S=1$ with $H^*=0.25$, 1.0 and 2.0. The indeterminate constant of integration is set to zero for convenience. As is to be expected from the above observations that $\partial p/\partial x$ is uniform in the bead core, these pressure profiles are linear in all cases. They do, however, lose their linearity as the liquid boundaries are approached – this is not surprising since the assumptions of the zero flux model are certainly not valid close to the liquid boundaries.

The prediction of a linear pressure profile in the central core of a meniscus roll coating bead stands in marked contrast to those observed in the fully-flooded case – see Figure 1.10. Subsequent experimental and numerical investigations (in Chapter 5) confirm the validity of this prediction for ultra-starved flow. The information given in this chapter will now be used to refine the Zero Flux Model to include a small flux λ.
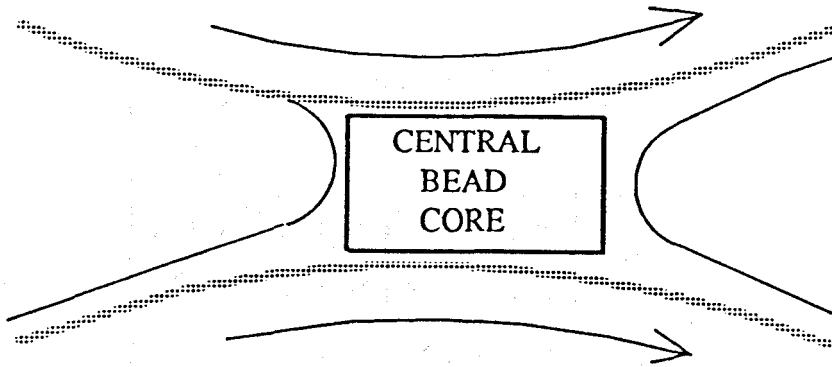
Figure 2.1: The Central 'Core' of a Forward Meniscus Roll Coater

(a)

(b)

Figure 2.2: Flow in a Lid-Driven Cavity: (a) a two-dimensional cross-section, (b) dimensionless boundary value problem for the creeping flow case
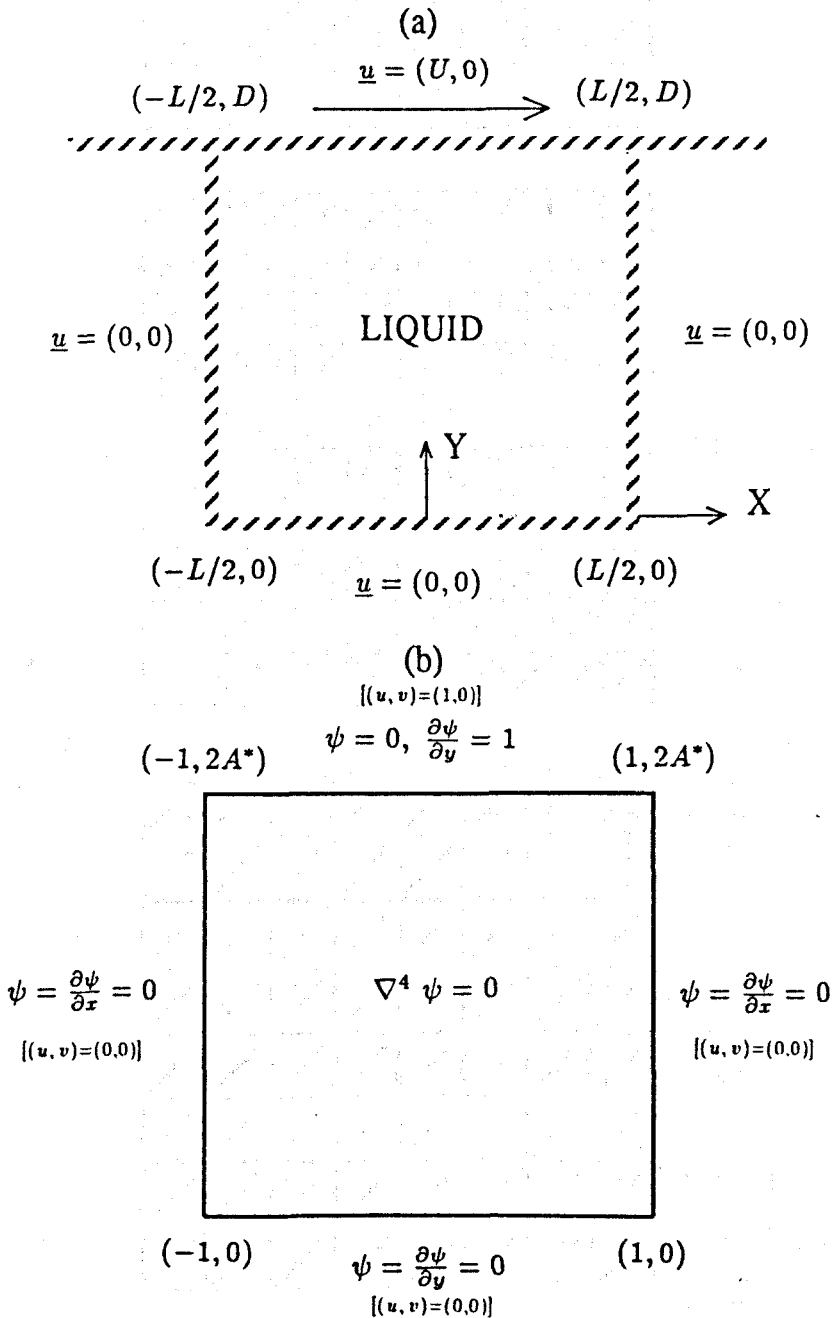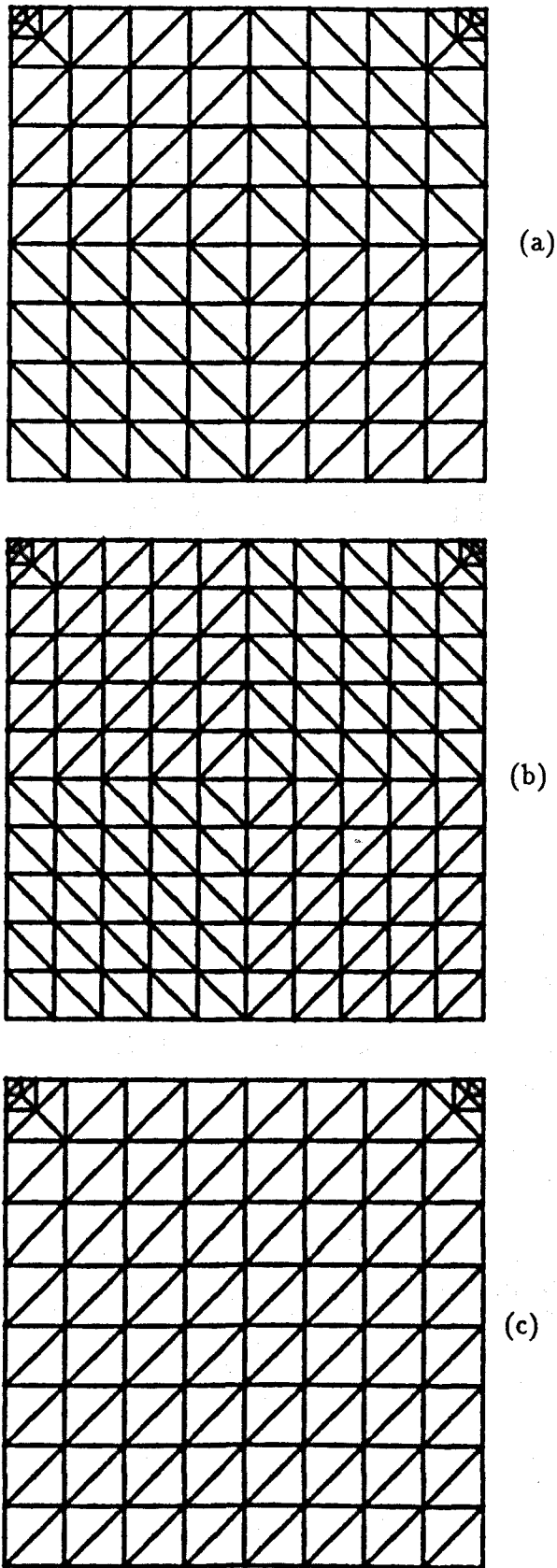
Figure 2.3: F.E. Grids used in Numerical Solution of Flow in a Lid-Driven Cavity: (a) 144 elements, 329 nodes; (b) 216 elements, 481 nodes; (c) 144 elements, 329 nodes
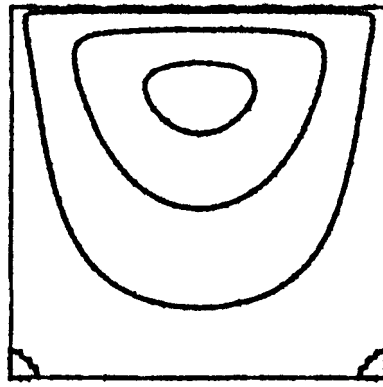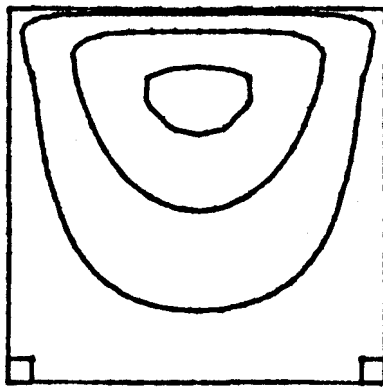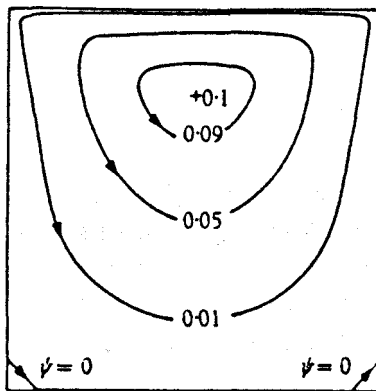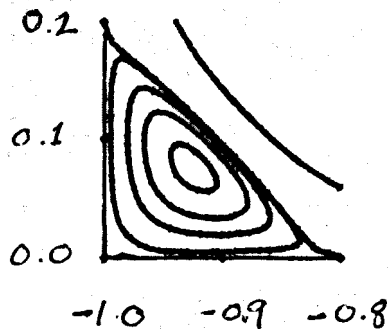
Figure 2.4: Streamlines of Creeping Flow in a Lid-Driven Cavity with $A^* = 1.0$: (a) Semi-Analytical (20 terms in series), (b) numerical (F.E.), (c) Pan and Acrivos [1967]

(a)   (b)
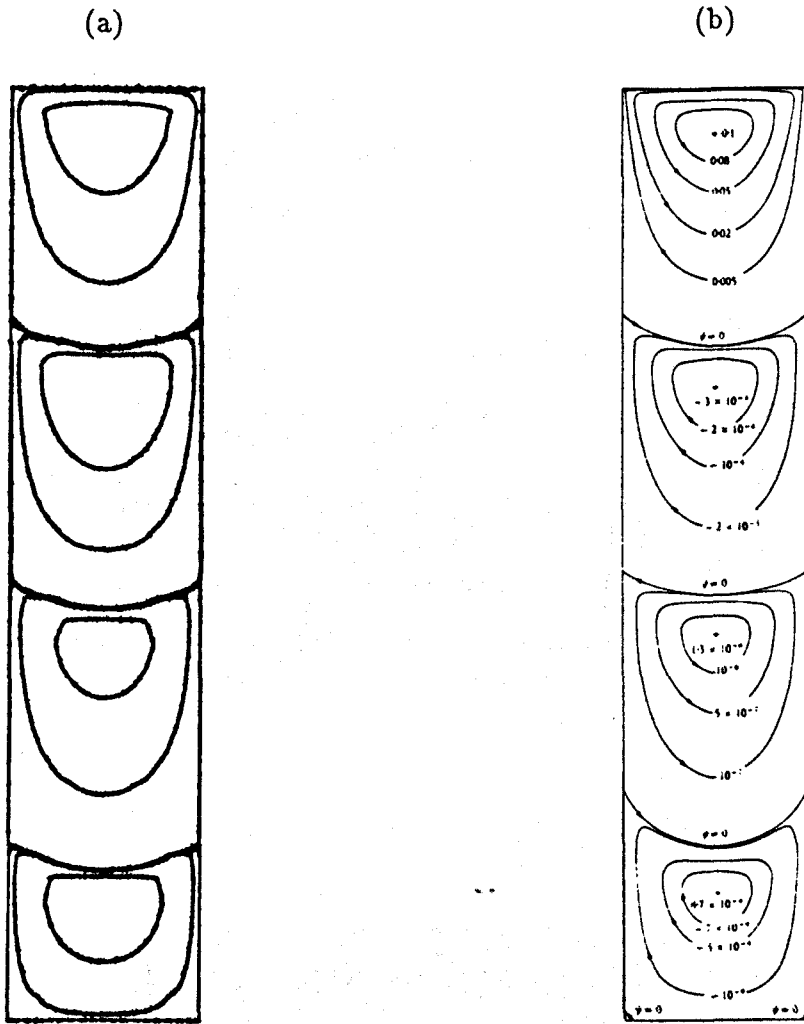
CORNER RECIRCULATING FLOW – SEMI-ANALYTICAL SOLUTION
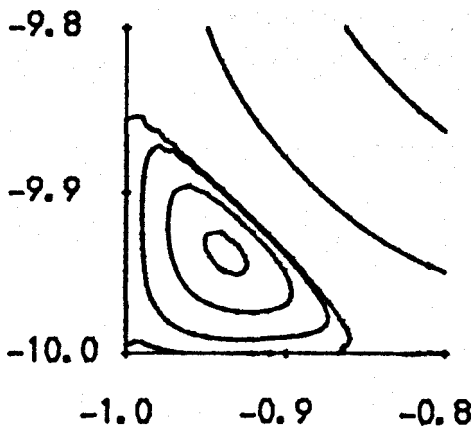
Figure 2.5: Streamlines of Creeping Flow in a Lid-Driven Cavity with $A^* = 5.0$: (a) Semi-Analytical (20 terms in series), (b) Pan and Acrivos [1967]
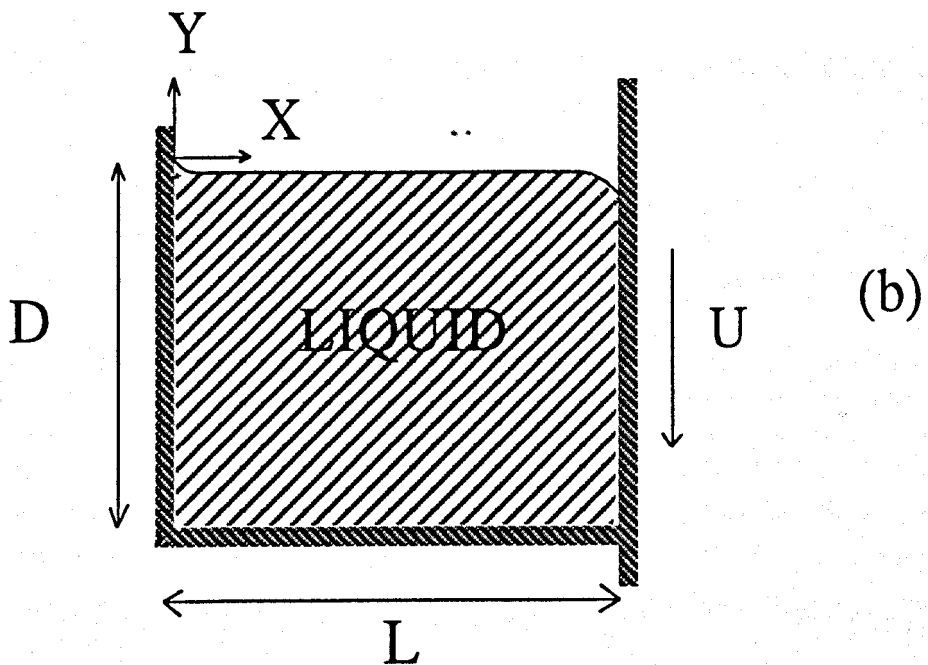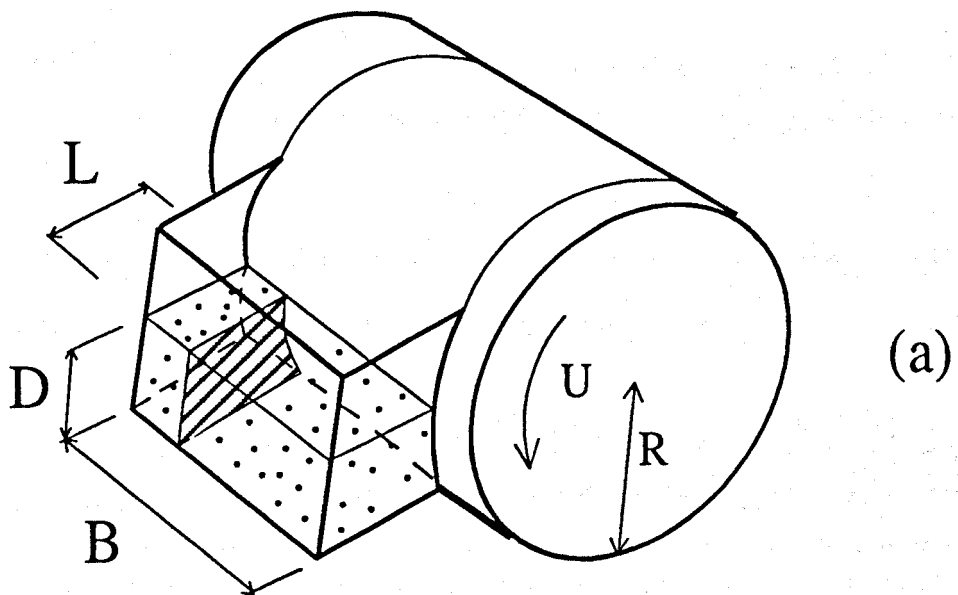
Figure 2.6: Flow in an Open, Driven Cavity (Canedo and Denson [1989]): (a) the cavity-cylinder system showing the principal geometric parameters, (b) the simplified two-dimensional flow domain
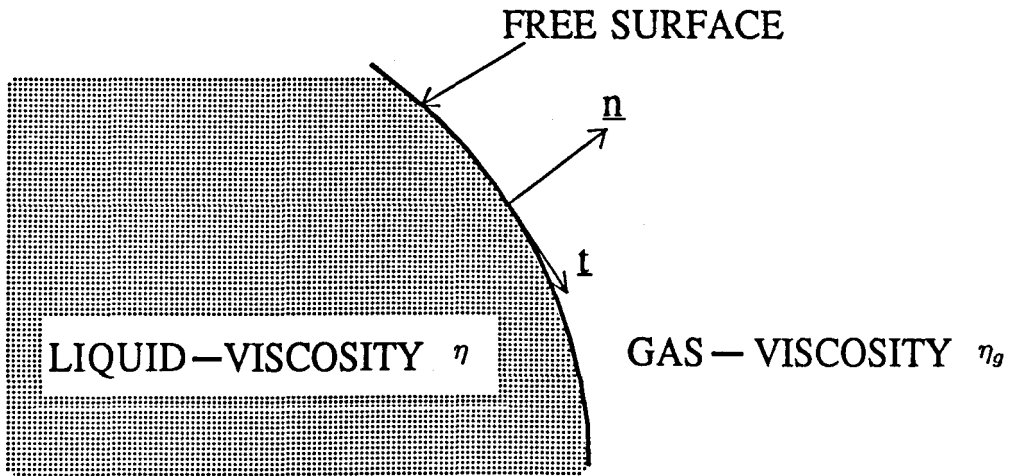
Figure 2.7: Normal and Tangential Vectors at a Liquid-Gas Interface
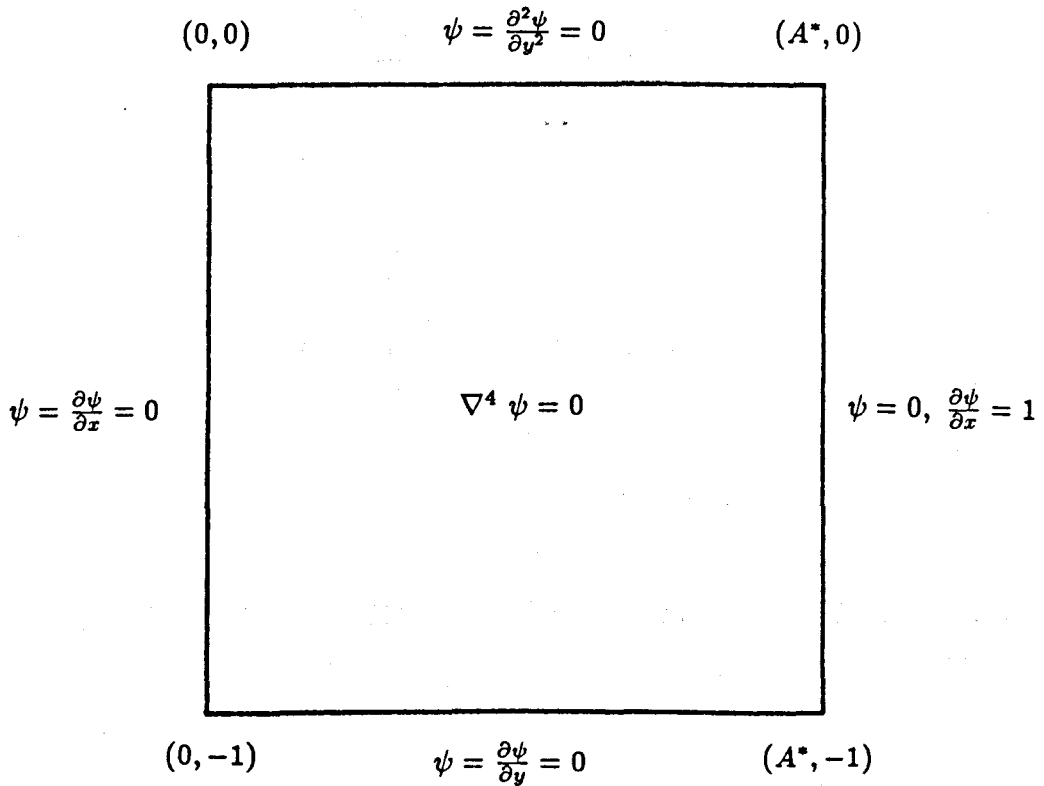
Figure 2.8: Canedo and Denson's [1989] Dimensionless Boundary Value Problem for Creeping Flow in an Open, Driven Cavity
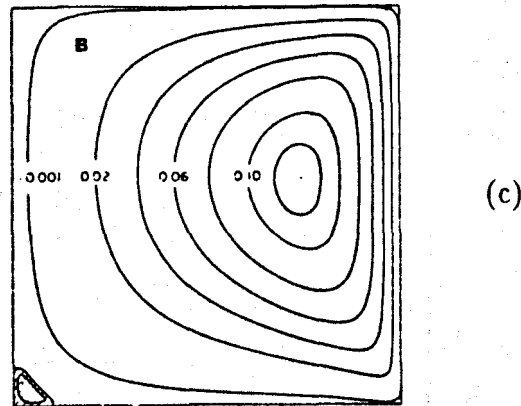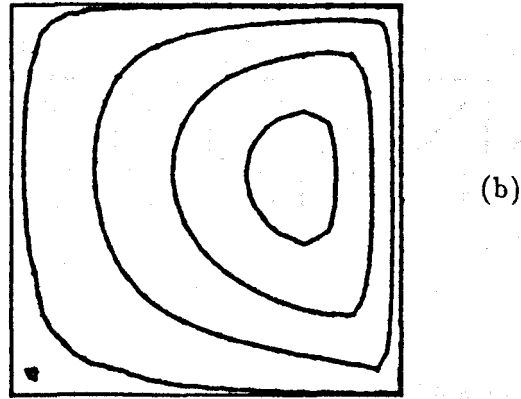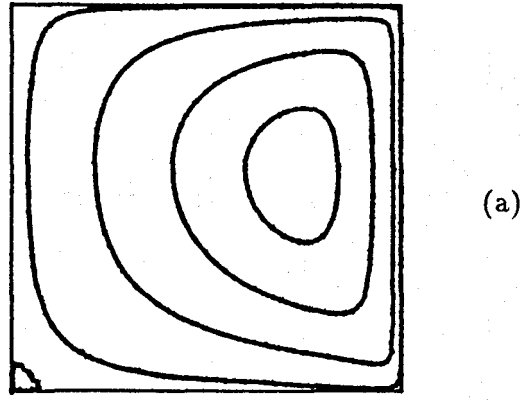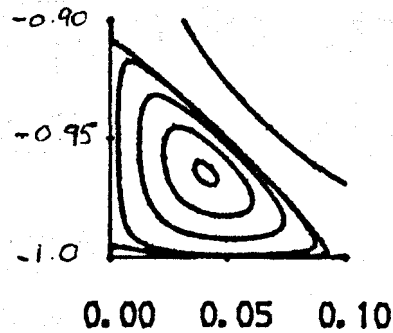
Figure 2.9: Streamlines of Creeping Flow in an Open,Driven Cavity with $A^* = 1.0$:
(a) Semi-Analytical (20 terms in series), (b) Numerical (F.E.), (c) Canedo and Denson
[1989]
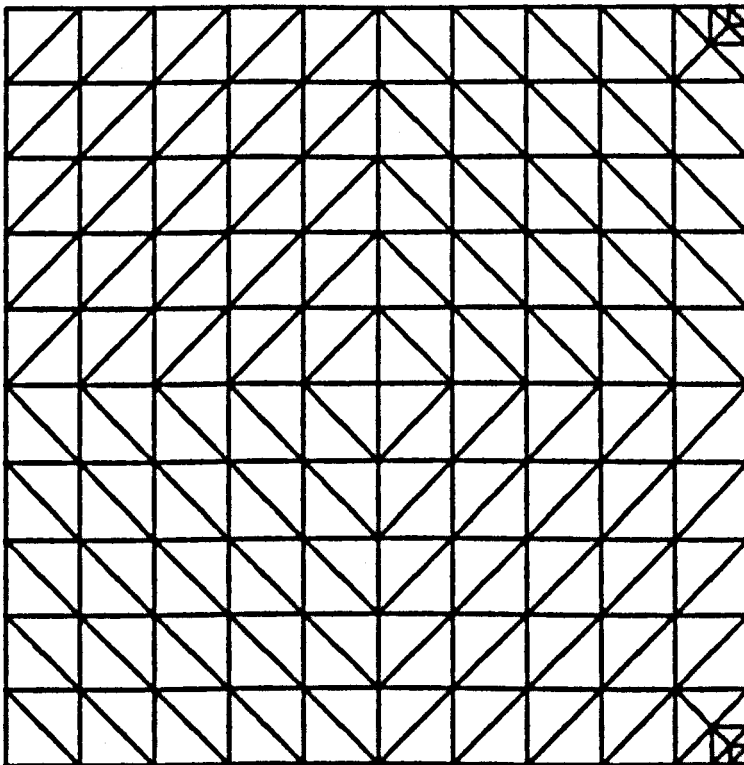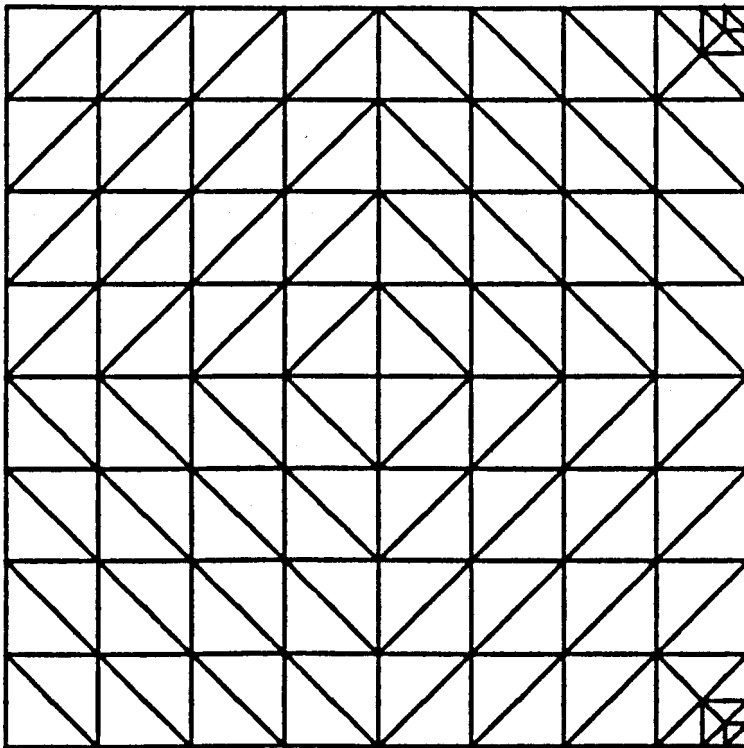
Figure 2.10: F.E. Grids Used in Numerical Solution of Creeping Flow in an Open, Driven Cavity: (a) 144 elements, 329 nodes, (b) 216 elements, 481 nodes
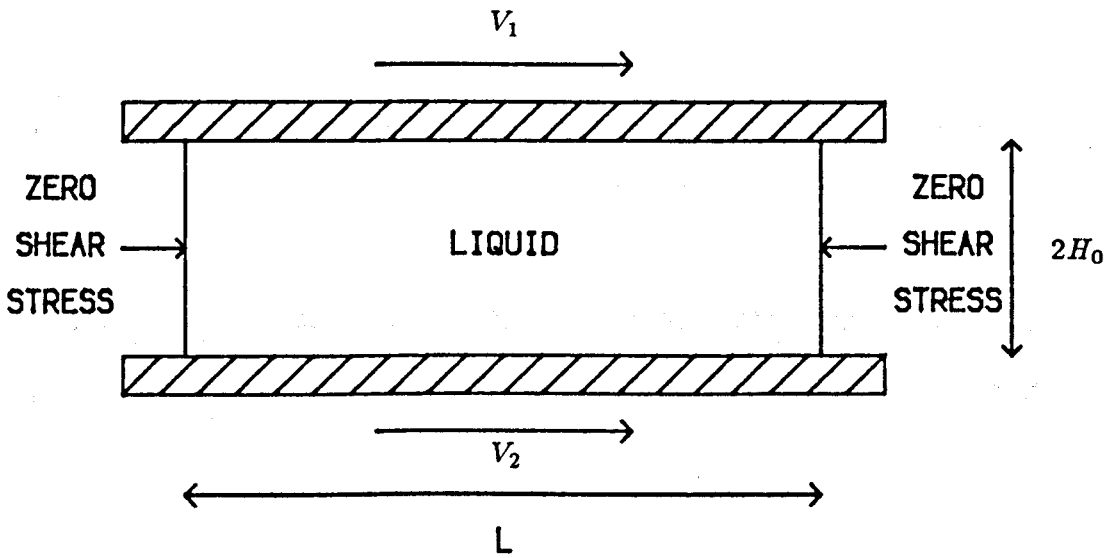
Figure 2.11: The Zero Flux Model of Meniscus Roll Coating
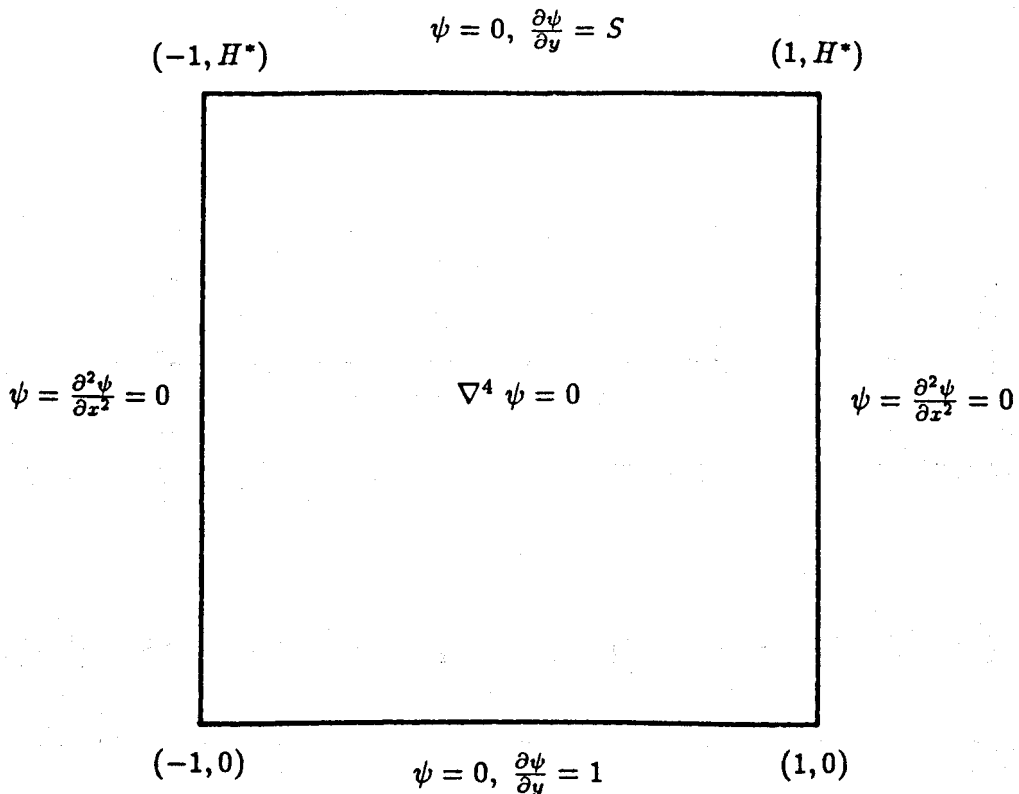
Figure 2.12: Dimensionless Boundary Value Problem from the Zero Flux Model of Meniscus Roll Coating

ANALYTICAL (20 TERMS)   NUMERICAL (F.E.)

(a)

(b)

(c)
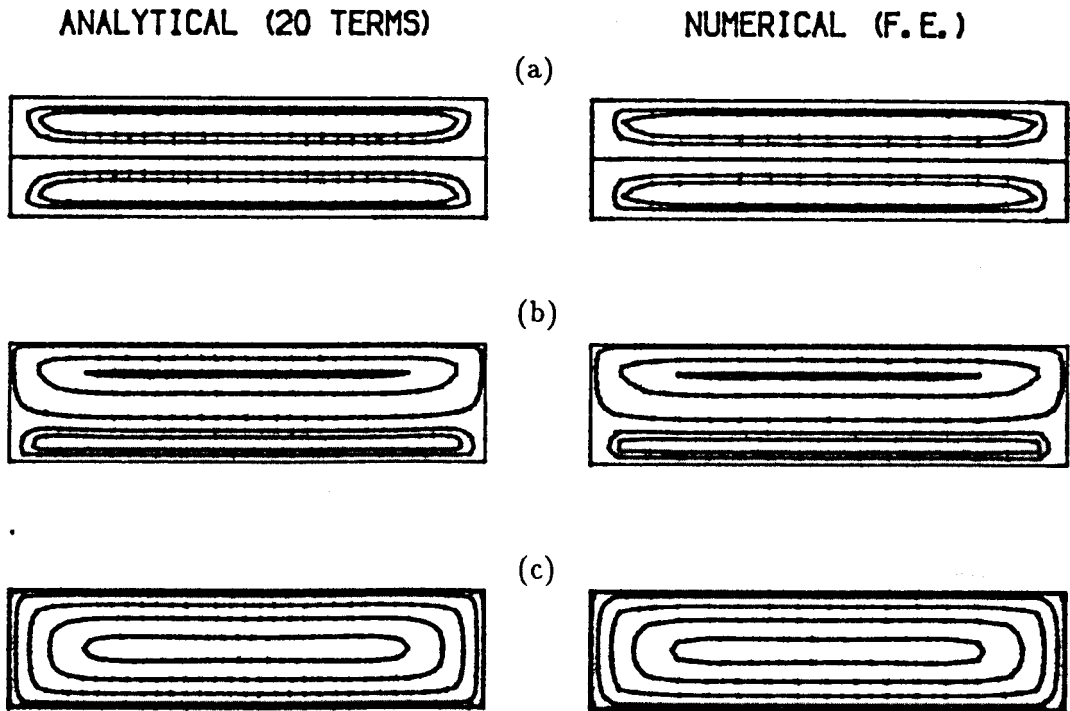
Figure 2.13: Streamlines From the Zero Flux Model with $H^* = 0.5$ and (a) $S = 1$, (b) $S = 2$, (c) $S = -1$

(a)

(b)
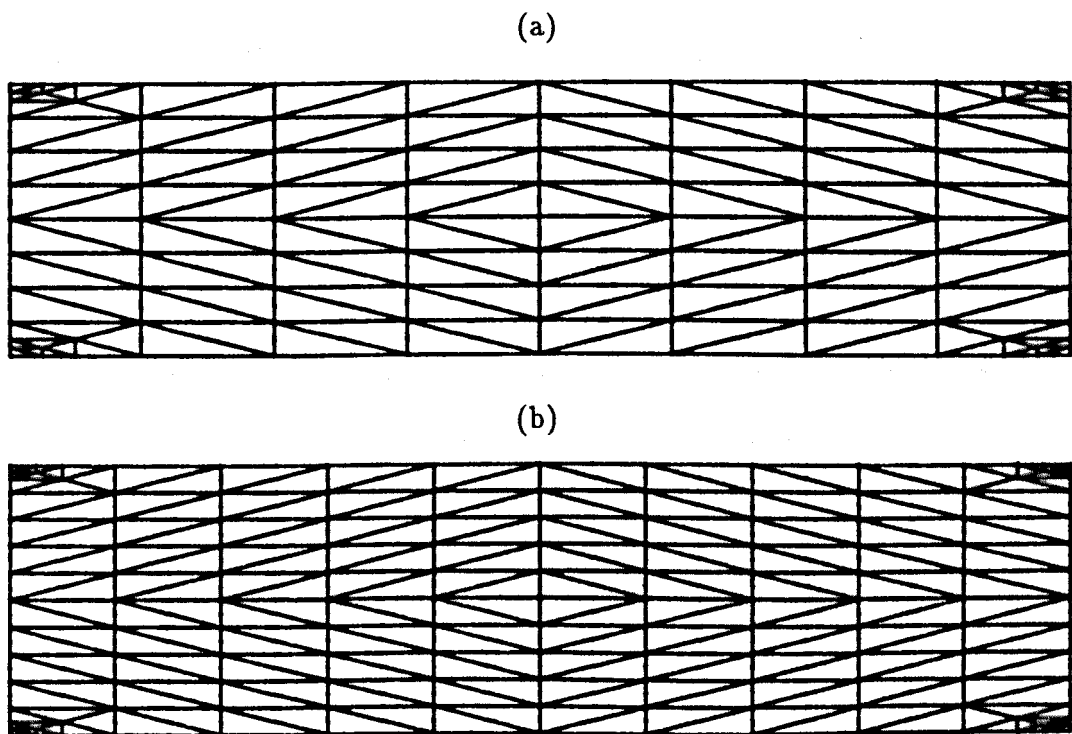
Figure 2.14: F.E. Grids used in Numerical Solutions of the Zero Flux Model: (a) 160 elements, 369 nodes, (b) 232 elements, 521 nodes

(a)
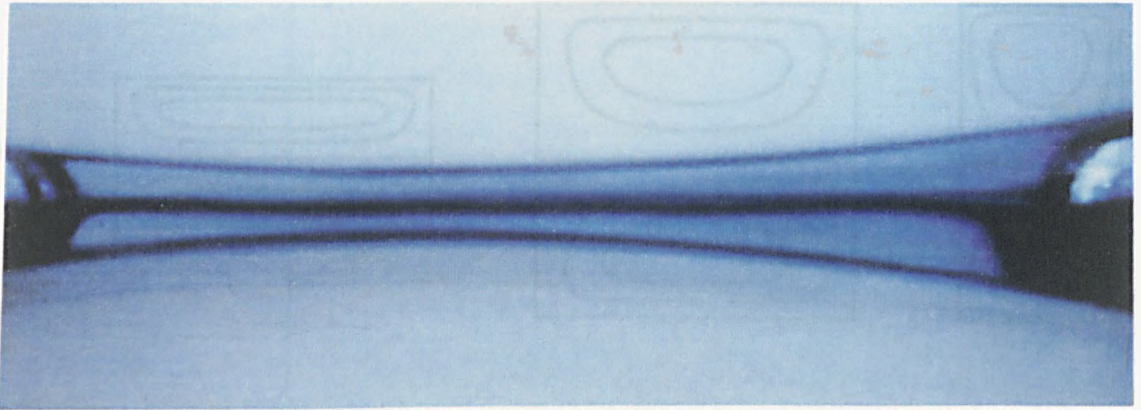
(b)
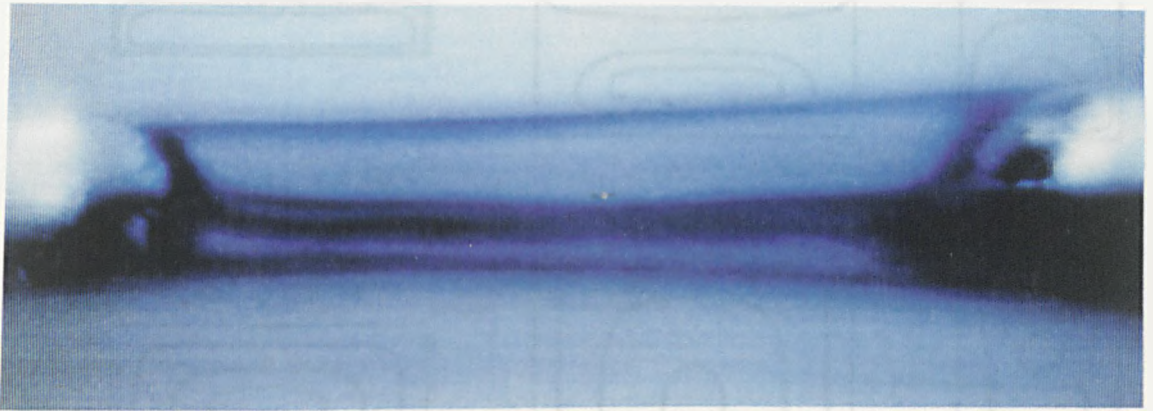
(c)

Figure 2.15: Flow Visualisations of Meniscus Roll Coating (Malone [1992]): (a) $S = 1$, (b) $S = 2$, (c) $S = -1$

(a)   (b)   (c)

(1) S=1

(2) S=2

(3) S=-1
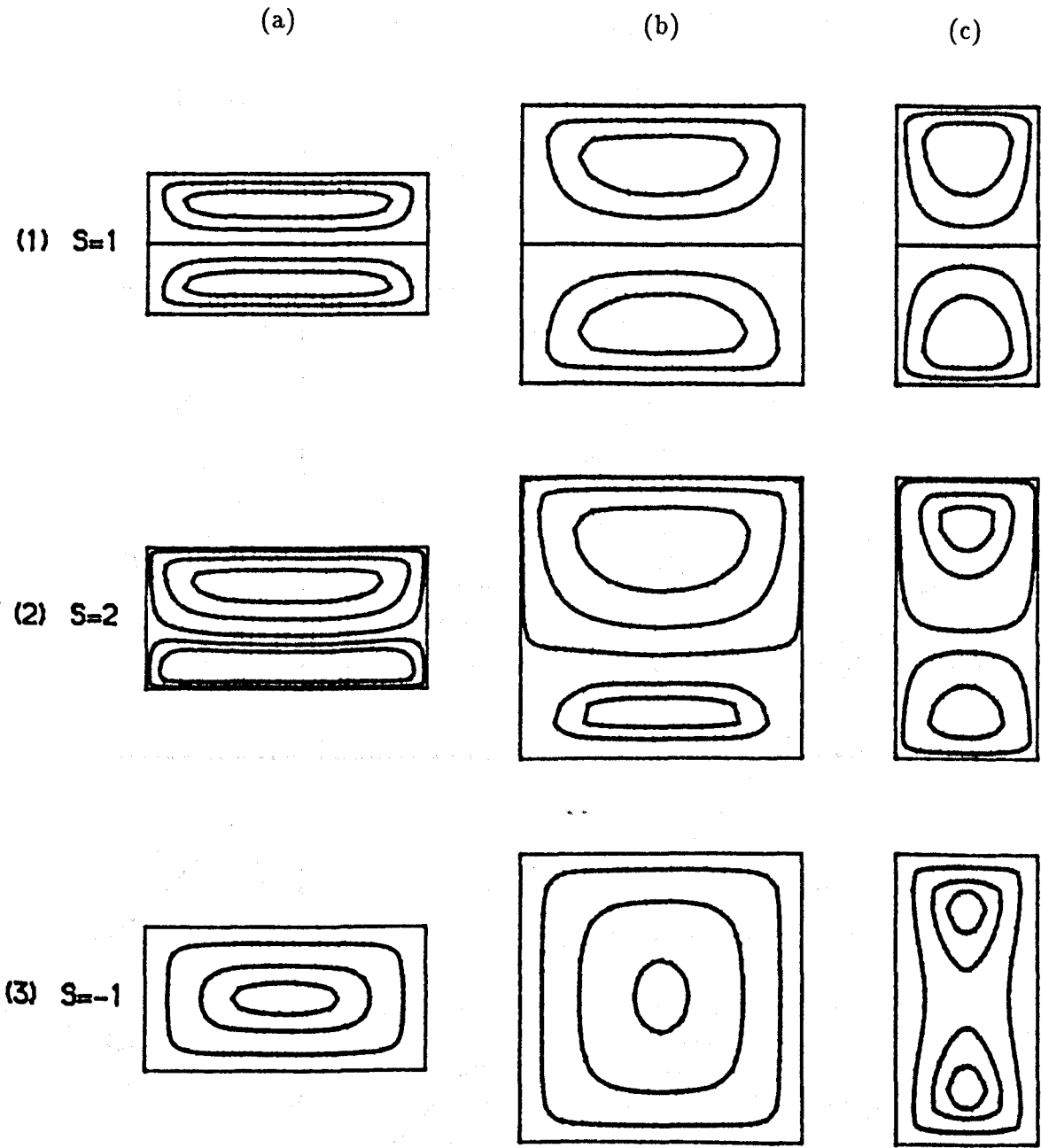
Figure 2.16: Streamlines From Analytical Solution of the Zero Flux Model – Dependence on Aspect Ratio for flows with $S = 1$, 2 and -1: (a) $H^* = 1.0$, (b) $H^* = 2.0$, (c) $H^* = 4.0$
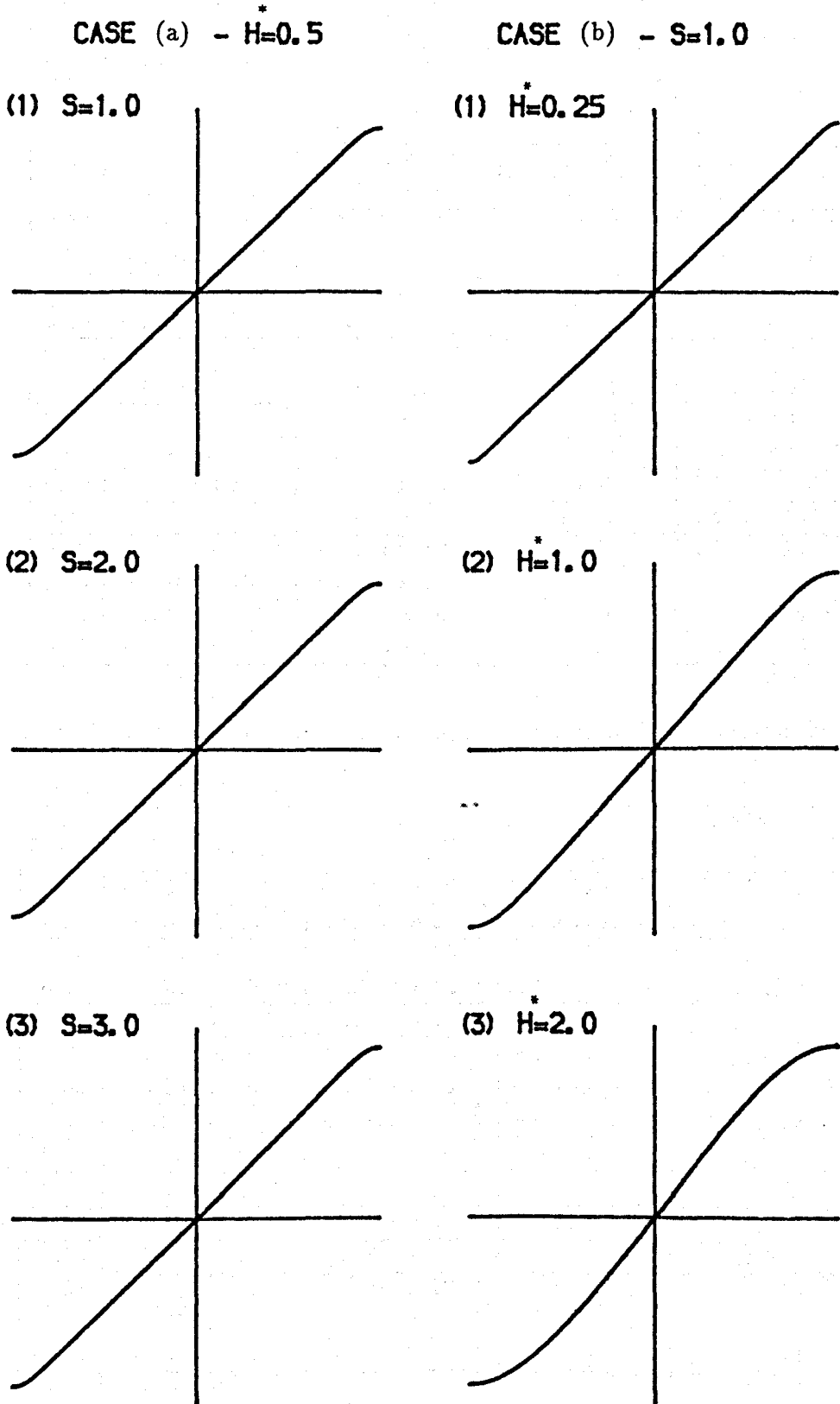
Figure 2.17: Dimensionless Pressure Profiles on the Horizontal Bead Centreline – Dependence on Velocity/Aspect ratio (Constant of Integration set to Zero)

x	$\psi(x,10)$	$\psi(x,0)$	$\partial\psi/\partial y(x,10)$	$\partial\psi/\partial y(x,0)$
0.00	$+1.704 \times 10^{-4}$	-1.100×10^{-16}	1.081	3.807×10^{-9}
0.05	-1.656×10^{-4}	$+1.058 \times 10^{-16}$	0.920	3.787×10^{-9}
0.10	$+1.512 \times 10^{-4}$	-9.289×10^{-17}	1.076	3.725×10^{-9}
0.15	-1.278×10^{-4}	$+7.221 \times 10^{-17}$	0.932	3.625×10^{-9}
0.20	$+9.607 \times 10^{-5}$	-4.435×10^{-17}	1.058	3.486×10^{-9}
0.25	-5.736×10^{-5}	$+1.101 \times 10^{-17}$	0.956	3.312×10^{-9}
0.30	$+1.335 \times 10^{-5}$	$+2.622 \times 10^{-17}$	1.028	3.106×10^{-9}
0.35	$+3.366 \times 10^{-5}$	-6.438×10^{-17}	0.991	2.872×10^{-9}
0.40	-8.068×10^{-5}	$+1.004 \times 10^{-16}$	0.988	2.614×10^{-9}
0.45	$+1.239 \times 10^{-4}$	$+1.297 \times 10^{-16}$	1.035	2.339×10^{-9}
0.50	-1.587×10^{-4}	$+1.473 \times 10^{-16}$	0.941	2.051×10^{-9}
0.55	$+1.795 \times 10^{-4}$	-1.466×10^{-16}	1.081	1.756×10^{-9}
0.60	-1.812×10^{-4}	$+1.212 \times 10^{-16}$	0.899	1.462×10^{-9}
0.65	$+1.545 \times 10^{-4}$	-6.481×10^{-17}	1.111	1.176×10^{-9}
0.70	-9.799×10^{-5}	-2.504×10^{-17}	0.893	9.046×10^{-9}
0.75	$+1.073 \times 10^{-5}$	$+1.422 \times 10^{-16}$	1.079	6.555×10^{-10}
0.80	$+9.631 \times 10^{-5}$	$+3.083 \times 10^{-16}$	0.896	2.544×10^{-10}
0.85	-1.910×10^{-4}	$+3.083 \times 10^{-16}$	0.897	2.544×10^{-10}
0.90	$+2.082 \times 10^{-4}$	-1.580×10^{-16}	1.264	1.170×10^{-10}
0.95	-8.245×10^{-5}	-2.615×10^{-16}	0.673	3.059×10^{-11}
1.00	0.000	0.000	0.000	0.000

Table 2.1: Convergence of the Semi-Analytical Solution For Creeping Flow in a Lid-Driven Cavity to the Boundary Conditions – $A^* = 5.0$ and 20 terms in series

y	$\psi(0,y)$	$\psi(1,y)$	$\partial\psi/\partial x(0,y)$	$\partial\psi/\partial x(1,y)$
0.00	0.000	0.000	0.000	0.000
-0.05	-5.327×10^{-9}	-4.645×10^{-5}	$+4.725 \times 10^{-8}$	1.183
-0.10	$+8.632 \times 10^{-9}$	$+8.764 \times 10^{-5}$	-8.734×10^{-8}	0.894
-0.15	-1.372×10^{-8}	-1.187×10^{-4}	-1.092×10^{-7}	1.080
-0.20	$+1.266 \times 10^{-8}$	$+1.353 \times 10^{-4}$	$+2.393 \times 10^{-7}$	0.930
-0.25	-1.587×10^{-8}	-1.346×10^{-4}	-9.680×10^{-7}	1.068
-0.30	$+9.321 \times 10^{-9}$	$+1.148 \times 10^{-4}$	$+1.395 \times 10^{-6}$	0.930
-0.35	-9.649×10^{-9}	-7.685×10^{-5}	-2.799×10^{-6}	1.076
-0.40	-8.120×10^{-10}	$+2.266 \times 10^{-5}$	$+3.727 \times 10^{-6}$	0.917
-0.45	$+2.954 \times 10^{-9}$	$+4.138 \times 10^{-5}$	-5.720×10^{-6}	1.091
-0.50	-1.294×10^{-8}	-1.076×10^{-4}	$+7.278 \times 10^{-6}$	0.902
-0.55	$+1.398 \times 10^{-8}$	$+1.639 \times 10^{-4}$	-9.724×10^{-6}	1.102
-0.60	-1.714×10^{-8}	-1.975×10^{-4}	$+1.167 \times 10^{-5}$	0.900
-0.65	$+1.065 \times 10^{-8}$	$+1.931 \times 10^{-4}$	-1.428×10^{-5}	1.089
-0.70	-1.013×10^{-9}	-1.398×10^{-4}	$+1.593 \times 10^{-5}$	0.938
-0.75	-1.594×10^{-8}	$+3.424 \times 10^{-5}$	-1.734×10^{-5}	1.013
-0.80	$+3.247 \times 10^{-8}$	$+1.061 \times 10^{-4}$	$+1.558 \times 10^{-5}$	1.064
-0.85	-3.777×10^{-8}	-2.290×10^{-4}	-7.902×10^{-6}	0.829
-0.90	$+1.299 \times 10^{-8}$	$+2.350 \times 10^{-4}$	-1.914×10^{-5}	1.281
-0.95	$+4.630 \times 10^{-8}$	-4.719×10^{-5}	$+1.012 \times 10^{-4}$	0.783
-1.00	0.000	0.000	0.000	0.000

Table 2.2: Convergence of the Semi-Analytical Solution For Creeping Flow in an Open, Driven Cavity to the Boundary Conditions – $A^* = 1.0$ and 20 terms in the series

(a) $H^* = 0.25$, $S = 1$

(i) series truncated after 20 terms

$x =$	0.0	0.25	0.5	0.75	1.0
$y = 0.25$	0.000000	0.000000	0.000000	0.000000	0.000000
$y = 0.1875$	−0.023148	−0.024358	−0.023410	−0.023495	0.000000
$y = 0.125$	0.000000	0.000000	0.000000	0.000000	0.000000
$y = 0.0625$	0.023148	0.024358	0.023410	0.023495	0.000000
$y = 0.0$	0.000000	0.000000	0.000000	0.000000	0.000000

(ii) series truncated after 50 terms

$x =$	0.0	0.25	0.5	0.75	1.0
$y = 0.25$	0.000000	0.000000	0.000000	0.000000	0.000000
$y = 0.1875$	−0.023437	−0.023438	−0.023438	−0.023449	0.000000
$y = 0.125$	0.000000	0.000000	0.000000	0.000000	0.000000
$y = 0.0625$	0.023437	0.023438	0.023438	0.023449	0.000000
$y = 0.0$	0.000000	0.000000	0.000000	0.000000	0.000000

(b) $H^* = 0.25$, $S = 2$

(i) series truncated after 20 terms

$x =$	0.0	0.25	0.5	0.75	1.0
$y = 0.25$	0.000000	0.000000	0.000000	0.000000	0.000000
$y = 0.1875$	−0.058594	−0.058594	−0.058596	−0.058740	0.000000
$y = 0.125$	−0.031250	−0.031250	−0.031254	−0.031452	0.000000
$y = 0.0625$	0.011719	0.011719	0.011717	0.011616	0.000000
$y = 0.0$	0.000000	0.000000	0.000000	0.000000	0.000000

(ii) series truncated after 50 terms

$x =$	0.0	0.25	0.5	0.75	1.0
$y = 0.25$	0.000000	0.000000	0.000000	0.000000	0.000000
$y = 0.1875$	−0.058555	−0.058636	−0.058542	−0.058834	0.000000
$y = 0.125$	−0.031249	−0.031251	−0.031253	−0.031453	0.000000
$y = 0.0625$	0.011699	0.011740	0.011690	0.011653	0.000000
$y = 0.0$	0.000000	0.000000	0.000000	0.000000	0.000000

Table 2.3: The Convergence of the Analytical Solution for the Zero Flux Model

(a) $H^* = 0.25$, $S = 1$

(i) series truncated after 20 terms

$x =$	0.0	0.2	0.4	0.6	0.8	1.0
$u(x, H^*)$	0.984	0.983	0.980	0.973	0.949	0.000
$u(x, 0)$	0.984	0.983	0.980	0.973	0.949	0.000

(ii) series truncated after 50 terms

$x =$	0.0	0.2	0.4	0.6	0.8	1.0
$u(x, H^*)$	0.993	0.993	0.992	0.989	0.979	0.000
$u(x, 0)$	0.993	0.993	0.992	0.989	0.979	0.000

(b) $H^* = 0.25$, $S = 2$

(i) series truncated after 20 terms

$x =$	0.0	0.2	0.4	0.6	0.8	1.0
$u(x, H^*)$	1.968	1.966	1.961	1.946	1.898	0.000
$u(x, 0)$	0.984	0.983	0.980	0.973	0.949	0.000

(ii) series truncated after 50 terms

$x =$	0.0	0.2	0.4	0.6	0.8	1.0
$u(x, H^*)$	1.987	1.987	1.984	1.980	1.960	0.000
$u(x, 0)$	0.993	0.993	0.992	0.989	0.979	0.000

Table 2.4: Horizontal Components of Liquid Velocity Predicted by the Zero Flux Model
– Convergence to the Lid Velocity Conditions

(a) Horizontal Components (50 terms upper, 20 terms lower)

$x =$	0.0	0.2	0.4	0.6	0.8
$y = 0.5$	0.99363	0.99331	0.99213	0.98917	0.97944
	0.98409	0.98328	0.98035	0.97300	0.94910
$y = 0.4$	0.04000	0.04000	0.04006	0.04008	0.01634
	0.04016	0.04017	0.04025	0.04033	0.01675
$y = 0.3$	-0.44000	-0.44000	-0.44008	-0.44028	-0.41248
	-0.44000	-0.44000	-0.44008	-0.44028	-0.41248
$y = 0.2$	-0.44000	-0.44000	-0.44008	-0.44028	-0.41248
	-0.44000	-0.44000	-0.44008	-0.44028	-0.41248
$y = 0.1$	0.04000	0.04000	0.04006	0.04008	0.01634
	0.04016	0.04017	0.04025	0.04033	0.01675
$y = 0.0$	0.99363	0.99331	0.99213	0.98917	0.97944
	0.98409	0.98328	0.98035	0.97300	0.94910

Table 2.5: Liquid Velocity Predictions in the Central Core of Meniscus Roll Coating
Bead with $H^* = 0.5$, $S = 1$

(b) Vertical Components (50 terms upper, 20 terms lower)

$x =$	0.0	0.2	0.4	0.6	0.8
$y = 0.5$	0.00000	0.00000	0.00000	0.00000	0.00000
	0.00000	0.00000	0.00000	0.00000	0.00000
$y = 0.4$	0.00000	0.00000	-0.00008	0.00014	0.03698
	0.00000	-0.00001	-0.00011	0.00008	0.03675
$y = 0.3$	0.00000	0.00000	-0.00007	0.00042	0.03179
	0.00000	0.00000	-0.00007	0.00042	0.03179
$y = 0.2$	0.00000	0.00000	0.00007	-0.00042	-0.03179
	0.00000	0.00000	0.00007	-0.00042	-0.03179
$y = 0.1$	0.00000	0.00000	0.00008	-0.00014	-0.03698
	0.00000	0.00001	0.00011	-0.00008	-0.03675
$y = 0.0$	0.00000	0.00000	0.00000	0.00000	0.00000
	0.00000	0.00000	0.00000	0.00000	0.00000

Table 2.5 (continued)

(a) $S = 2.0$

$x =$	0.0	0.2	0.4	0.6	0.8
$y = 0.5$	1.96819	1.96656	1.96070	1.94601	1.89817
$y = 0.4$	0.36041	0.36088	0.36271	0.35932	0.25043
$y = 0.3$	-0.55993	-0.55969	-0.55904	-0.56243	-0.55965
$y = 0.2$	-0.76007	-0.76032	-0.76120	-0.75840	-0.67779
$y = 0.1$	-0.23995	-0.24039	-0.24195	-0.23832	-0.20019
$y = 0.0$	0.98409	0.98328	0.98035	0.97300	0.94910

(b) $S = -1.0$

$x =$	0.0	0.2	0.4	0.6	0.8
$y = 0.5$	-0.98409	-0.98328	-0.98035	-0.97300	-0.94910
$y = 0.4$	-0.60036	-0.60127	-0.60467	-0.59764	-0.45062
$y = 0.3$	-0.20015	-0.20063	-0.20216	-0.19596	-0.11814
$y = 0.2$	0.20015	0.20063	0.20216	0.19596	0.11814
$y = 0.1$	0.60036	0.60127	0.60467	0.59764	0.45062
$y = 0.0$	0.98409	0.98328	0.98035	0.97300	0.94910

Table 2.6: Horizontal Liquid Velocity Predictions in the Central Core of a Meniscus Roll Coating Bead – Dependence on Velocity Ratio for $H^* = 0.5$

(a) $H^* = 0.1$

$x =$	0.0	0.2	0.4	0.6	0.8
$y = 0.10$	0.98409	0.98328	0.98035	0.97300	0.94910
$y = 0.08$	0.04168	0.04176	0.04207	0.04286	0.04552
$y = 0.06$	-0.43695	-0.43680	-0.43624	-0.43486	-0.43050
$y = 0.04$	-0.43695	-0.43680	-0.43624	-0.43486	-0.43050
$y = 0.02$	0.04168	0.04176	0.04207	0.04286	0.04552
$y = 0.00$	0.98409	0.98328	0.98035	0.97300	0.94910

(b) $H^* = 1.0$

$x =$	0.0	0.2	0.4	0.6	0.8
$y = 1.0$	0.98409	0.98328	0.98035	0.97300	0.94910
$y = 0.8$	0.04036	0.04014	0.03704	0.01634	-0.05909
$y = 0.6$	-0.44050	-0.44036	-0.43710	-0.41249	-0.29742
$y = 0.4$	-0.44050	-0.44036	-0.43710	-0.41249	-0.29742
$y = 0.2$	0.04036	0.04014	0.03704	0.01634	-0.05909
$y = 0.0$	0.98409	0.98328	0.98035	0.97300	0.94910

Table 2.7: Horizontal Liquid Velocity Predictions in the Central Core of a Meniscus Roll Coating Bead – Dependence on Dimensionless Depth for $S = 1$

(a) series truncated after 20 terms

$x =$	0.0	0.2	0.4	0.6	0.8	1.0
$y = 0.5$	-77.66	-84.13	-107.34	166.45	-368.72	0.00
$y = 0.4$	47.78	47.76	47.70	47.45	52.43	0.00
$y = 0.3$	48.00	48.00	48.00	48.25	49.42	0.00
$y = 0.25$	48.00	48.00	48.01	48.30	48.33	0.00
$y = 0.2$	48.00	48.00	48.00	48.25	49.42	0.00
$y = 0.1$	47.78	47.76	47.70	47.45	52.43	0.00
$y = 0.0$	-77.66	-84.13	-107.34	-166.45	-368.72	0.00

(b) series truncated after 50 terms

$x =$	0.0	0.2	0.4	0.6	0.8	1.0
$y = 0.5$	-266.16	-282.33	-340.33	-487.44	-978.31	0.00
$y = 0.4$	48.00	48.00	47.98	47.83	53.08	0.00
$y = 0.3$	48.00	48.00	48.00	48.25	49.42	0.00
$y = 0.25$	48.00	48.00	48.01	48.30	48.33	0.00
$y = 0.2$	48.00	48.00	48.00	48.25	49.42	0.00
$y = 0.1$	48.00	48.00	47.98	47.83	53.08	0.00
$y = 0.0$	-216.16	-282.33	-340.33	-487.44	-978.31	0.00

Table 2.8: The Convergence of Dimensionless Pressure Gradient Predictions in the Central Core of A Meniscus Roll Coating Bead for $H^* = 0.5$ and $S = 1$

(a) $S = 0.5$

$x =$	0.0	0.2	0.4	0.6	0.8	1.0
$y = 0.5$	-26.84	-30.06	-41.43	-70.06	-171.71	0.00
$y = 0.4$	35.88	35.90	36.04	36.19	36.60	0.00
$y = 0.3$	36.00	36.01	36.07	36.27	35.61	0.00
$y = 0.25$	36.00	36.00	36.00	36.26	36.25	0.00
$y = 0.2$	36.00	35.99	35.94	36.10	38.51	0.00
$y = 0.1$	35.77	35.73	35.51	34.98	42.04	0.00
$y = 0.0$	-89.65	-96.14	-119.58	-179.61	-380.78	0.00

(b) $S = 1.5$

$x =$	0.0	0.2	0.4	0.6	0.8	1.0
$y = 0.5$	-128.48	-138.20	-173.25	-262.84	-564.94	0.00
$y = 0.4$	59.65	59.61	59.35	58.70	68.25	0.00
$y = 0.3$	59.99	59.99	59.94	60.23	63.22	0.00
$y = 0.25$	60.00	60.00	60.01	60.37	60.42	0.00
$y = 0.2$	60.00	60.01	60.03	60.40	60.32	0.00
$y = 0.1$	59.77	59.78	59.89	59.91	62.83	0.00
$y = 0.0$	-65.67	-72.17	-95.09	-153.29	-355.87	0.00

(c) $S = 2.0$

$x =$	0.0	0.2	0.4	0.6	0.8	1.0
$y = 0.5$	-49.30	-192.98	-239.16	-359.22	-761.55	0.00
$y = 0.4$	71.54	71.46	71.01	69.96	84.08	0.00
$y = 0.3$	72.00	71.97	71.87	72.21	77.02	0.00
$y = 0.25$	72.00	72.00	72.01	72.45	72.50	0.00
$y = 0.2$	72.00	72.02	72.15	72.55	71.23	0.00
$y = 0.1$	71.77	71.81	72.68	72.38	73.22	0.00
$y = 0.0$	-58.69	-60.81	-82.86	-140.13	-343.42	0.00

(d) $S = -1.0$

$x =$	0.0	0.2	0.4	0.6	0.8	1.0
$y = 0.5$	125.62	132.17	156.30	219.09	418.13	0.00
$y = 0.4$	0.23	0.35	1.07	0.24	-10.86	0.00
$y = 0.3$	0.00	0.05	0.28	0.34	-5.79	0.00
$y = 0.25$	0.00	0.00	0.00	0.00	0.00	0.00
$y = 0.2$	0.00	-0.05	-0.28	-0.34	5.79	0.00
$y = 0.1$	-0.23	-0.35	-1.07	-0.24	10.86	0.00
$y = 0.0$	-125.62	-132.17	-156.30	-219.09	-418.13	0.00

Table 2.9: Dimensionless Pressure Gradient Predictions in the Central Core of A Meniscus Roll Coating Bead with $H^* = 0.5$ – Dependence on Velocity Ratio

(a) $H^* = 0.1$

$x =$	0.0	0.2	0.4	0.6	0.8	1.0
$y = 0.10$	885.8	869.7	811.7	665.5	183.4	0.0
$y = 0.08$	1186.4	1185.7	1183.2	1176.9	1156.2	0.0
$y = 0.06$	1199.4	1199.4	1199.2	1199.0	1198.1	0.0
$y = 0.05$	1199.8	1199.7	1199.7	1199.6	1199.2	0.00
$y = 0.04$	1199.4	1199.4	1199.2	1199.0	1198.1	0.00
$y = 0.02$	1186.4	1185.7	1183.2	1176.9	1156.2	0.00
$y = 0.00$	885.8	896.7	811.7	665.5	183.4	0.00

(b) $H^* = 0.2$

$x =$	0.0	0.2	0.4	0.6	0.8	1.0
$y = 0.20$	-14.2	-30.3	-88.3	-234.5	-717.3	0.0
$y = 0.16$	299.4	299.9	299.3	299.0	297.7	0.0
$y = 0.12$	300.0	300.0	300.0	300.0	300.3	0.0
$y = 0.10$	300.0	300.0	300.0	300.0	300.4	0.0
$y = 0.08$	300.0	300.0	300.0	300.0	300.3	0.0
$y = 0.04$	299.4	299.9	299.3	299.0	297.7	0.0
$y = 0.00$	-14.2	-30.3	-88.3	-234.5	-717.3	0.00

(c) $H^* = 0.8$

$x =$	0.0	0.2	0.4	0.6	0.8	1.0
$y = 0.80$	-295.4	-311.6	-369.9	-517.8	-1000.6	0.0
$y = 0.64$	18.74	18.72	18.68	19.28	27.91	0.0
$y = 0.48$	18.75	18.77	18.89	19.27	17.74	0.0
$y = 0.40$	18.75	18.78	18.91	19.14	16.43	0.0
$y = 0.32$	18.75	18.77	18.89	19.27	17.74	0.0
$y = 0.16$	18.74	18.72	18.68	19.28	27.91	0.0
$y = 0.00$	-295.4	-311.6	-369.9	-517.9	-1000.6	0.00

(d) $H^* = 1.0$

$x =$	0.0	0.2	0.4	0.6	0.8	1.0
$y = 1.0$	-302.2	-318.5	-377.0	-524.9	-1010.8	0.00
$y = 0.8$	11.96	11.95	12.03	13.27	20.61	0.00
$y = 0.6$	12.02	12.06	12.22	12.35	10.32	0.00
$y = 0.5$	12.03	12.07	12.21	12.08	9.30	0.00
$y = 0.4$	12.02	12.06	12.22	12.35	10.32	0.00
$y = 0.2$	11.96	11.95	12.03	13.27	20.61	0.00
$y = 0.0$	-302.2	-318.5	-377.0	-524.9	-1010.8	0.00

Table 2.10: Dimensionless Pressure Gradient Predictions in the Central Core of A Meniscus Roll Coating Bead with $S = 1$ – Dependence on Aspect Ratio

Chapter 3: The Small Flux Model of Meniscus Roll Coating

3.1 - Introduction

3.2 - Formulation of the Small Flux Model

3.3 - The Prediction of Film Thicknesses in Forward Meniscus Roll Coating

   3.3.1 - Determination of Y_L^*

   3.3.2 - Determination of Y_U^*

   3.3.3 - Predictions of the Film Thickness Model

3.4 - Streamline Patterns: Non-Zero Flux

3.5 - Conclusions

Figures 3.1 - 3.8

Tables 3.1 - 3.2

Chapter 3

The Small Flux Model of Meniscus Roll Coating

3.1 Introduction

Mensicus roll coating is characterized by having a much reduced dimensionless flux (as defined in §2.1) compared to the fully-flooded situation. In Chapter 2, this observation motivated an analysis of the problem based on the simplest of models – the Zero Flux model. As we have seen this model reveals the key features of the flow field (vortex structure) within the bead as speed ratio and aspect ratio are varied, yet in its present form it is unable to predict the film thicknesses produced during the actual coating operation. The ultimate goal of the present chapter is to refine the Zero Flux model in order to enable film thickness predictions to be made.

The first step towards this goal is to refine the Zero Flux model to include a small, non-zero flux passing through the bead. This is achieved using Richardson's [1988] suggestion, which is supported by the theoretical results given in §§2.5.2, that the flow in the central core of the bead can be modelled as a combination of Poiseuille and Couette terms under the assumption of a constant pressure gradient. This proposal leads to the development of a simple model for the flow in the central 'core' of a meniscus roll coating bead, i.e. the region sufficiently far away from the curved meniscii, as indicated in Figure 2.1. The next stage is to extend the 'Poiseuille plus Couette' small

flux model to predict the average film thicknesses produced on upper and lower rollers during forward meniscus roll coating.

In §1.2 we saw that there are many film thickness theories for fully-flooded roll coating (e.g. those of Savage [1982], Coyle et al [1986]), all of which attempt to locate the 'dividing streamline' – see Figure 1.8 – which separates the liquid coating the upper and lower rollers. More recently, Savage [1992] proposed that the liquid coating the upper and lower rollers is divided by a stagnation point; in §3.3 the predictions of this 'stagnation-point' theory are compared with Malone's [1992] fully-flooded roll coating data. However, until now no film thickness theory has been developed for the meniscus roll coating situation. Such a film thickness model for forward meniscus roll coating (see Figure 1.6 (c)) is now developed which takes account of parameters such as the roller speeds, minimum roller separation, and the magnitude of the flux passing through the bead. The predictions of this model are validated against experiment.

3.2   Formulation of the Small Flux Model

The results of §§2.5.2 for the Zero Flux Model predict the flow in the central core of the bead to be one-dimensional with a constant pressure gradient. These observations are now developed further to produce of a simple model of the core flow for the case of a small, non-zero flux.

The flow visualisations in Figure 2.15 (a), (b) demonstrate that the curvature of the rollers is small in the region of interest (i.e. the central core of the bead). Hence, for convenience, in this chapter we shall describe the theory for the special case in which we assume that, in the bead core, the roller separation is equal to the minimum roller separation. This is equivalent to modelling the rollers as *flat lids*, but note that the following models can easily be extended to accomodate the effects of a variable roller separation, $H(X)$, (as is the case in practice) by simply replacing the nip width, $2H_0$, by $H(X)$ (see later, §§ 4.5.2). The other assumptions of the Zero Flux model (see §2.5) are retained with one modification: the assumption of planar liquid-gas interfaces is no longer relevant because the model only deals with the flow in the 'core', sufficiently far

away from the meniscii and lids. It will be seen that the idealised situation of zero flux arises as a special case.

In a private communication Richardson [1988] suggested that, even in the case of small, non-zero flux, the pressure gradient would be constant. Using the non-dimensionlisation of §2.5 (i.e. equations (2.20), (2.21)), the Stokes equations governing this creeping flow reduce to their one-dimensional form:

$$\frac{\partial p}{\partial x} = \frac{\partial^2 u}{\partial y^2} \ , \ \frac{\partial p}{\partial y} = 0 \qquad (3.1)$$

Assuming that $\partial p/\partial x$ is constant and applying the no-slip boundary conditions on the lids, see Figure 3.1, $u = S$ at $y = H^*$, $u = 1$ at $y = 0$ yields

$$u = \overbrace{\frac{1}{2}\frac{\partial p}{\partial x}y(y - H^*)}^{Poiseuille} + \overbrace{(S - 1)\frac{y}{H^*} + 1}^{Couette} \qquad (3.2)$$

Expression (3.2) is a combination of Poiseuille and Couette terms. The Poiseuille term, which depends on $\partial p/\partial x$, models the flow due to an external pressure gradient. In meniscus roll coating this external pressure gradient arises due to the difference in curvature of the upstream and downstream meniscii, as shown in Figure 1.6 (c); this feature is discussed further in Chapter 5. The Couette term is much easier to interpret: it is the flow generated by the motion of the lids.

In §2.1 the flux through the bead Q was non-dimensionalised by $2\overline{V}H_0$ where $\overline{V}$ is the *average* roller speed. For the purposes of this chapter, however, it is convenient to define the dimensionless flux λ past any station x (which by continuity of flux is constant) by $\lambda = Q/2V_2H_0$, where V_2 is the *lower* roller speed. This yields

$$\lambda = \frac{Q}{2V_2H_0} = \frac{\int_0^{H^*} u(y)dy}{H^*} = -\frac{H^{*2}}{12}\frac{\partial p}{\partial x} + \frac{(S + 1)}{2} \qquad (3.3)$$

Equation (3.3) may be rearranged to give

$$\frac{\partial p}{\partial x} = \frac{6}{H^{*2}}((S + 1) - 2\lambda) \qquad (3.4)$$

which, when substituted in the velocity profile (3.2), yields

$$u(y) = \frac{3}{H^{*2}}(S + 1 - 2\lambda)(y^2 - H^*y) + (S - 1)\frac{y}{H^*} + 1 \qquad (3.5)$$

The Poiseuille plus Couette model treats the idealised situation of zero flux as a special case. Indeed by setting $\lambda = 0$ in (3.4) and (3.5) we obtain estimates for the pressure gradient $(\partial p/\partial x)_0$ and velocity profile u_0 in the case of zero flux:

$$\left(\frac{\partial p}{\partial x}\right)_0 = \frac{6(S+1)}{H^{*2}} \tag{3.6}$$

$$u_0 = \frac{3}{H^{*2}}(S+1)(y^2 - H^*y) + (S-1)\frac{y}{H^*} + 1 \tag{3.7}$$

Note that expression (3.6) agrees with the prediction of the Zero Flux model that the horizontal pressure gradient in the core of a meniscus roll coating bead is proportional to the value of $(1 + S)/H^{*2}$ (see equation (2.27)). In fact Table 3.1 shows that the values of the pressure gradient, $\partial p/\partial x$, given in §§2.5.2 are in exact agreement with those predicted by equation (3.6) in the zero flux case. Further evidence for equivalence of the zero and small flux models in the idealised case of zero flux is provided by the horizontal velocity profiles shown in Table 3.2. There is exact agreement between those obtained (i) by truncating the series for u obtainable from equation (2.23) after 20 terms, (ii) from the Poiseuille plus Couette profile (3.7).

3.3 The Prediction of Film Thicknesses in Forward Meniscus Roll Coating

In this section the small flux model is extended to tackle a question of fundamental practical significance: how is the inlet liquid film, which is entrained by the viscous lifting action of the applicator roller during forward meniscus roll coating, eventually distributed between the upper and lower rollers? In particular we develop a model for predicting the dimensionless fluxes λ_1, λ_2 of the films produced on the upper and lower rollers respectively when a *known*, small flux λ flows through the bead. Once the fluxes λ_1, λ_2 have been determined, they are easily converted to *average* film thicknesses on the rollers for comparison with Malone's [1992] experimental data. It is not, however, the aim of our analysis to predict λ, i.e. the flux through the bead under a given set of circumstances, as this can be achieved by applying the theory of Tharmalingham and Wilkinson [1978] (see §§1.3.3).

The complex nature of the flow in the bead of a forward meniscus roll coater has already been described (see §§2.5.2 and Figure 2.15): the liquid in the inlet film eventually splits into two parts; the upper one 'snakes' between the eddies before coating the upper roller, while the lower one simply coats the lower roller. Although this 'flux-splitting' actually occurs near the downstream meniscus where the flow is fully two-dimensional, it is still possible to predict λ_1 and λ_2 without analysing the flow near the film split point. Figure 3.2 illustrates the model for flow in a meniscus roll coating bead developed here. As in the Zero Flux model, it pertains to the creeping flow of a Newtonian, incompressible liquid in which the rollers are modelled as flat lids, but it also has the additional assumption that the flow across any vertical cross-section (in the bead core) is given by the Poiseuille plus Couette profile (3.5). It is important to realise that the analysis which follows is only valid in the case in which the the dimensionless flux λ passing through the bead is so small that terms $O(\lambda^2)$ are negligible. As in the actual situation, liquid flows into the bead in a thin film ($\lambda \ll 1$) which eventually splits into upper (shaded) and lower (unshaded) films of dimensionless fluxes (thicknesses) λ_1, λ_2 (t_1, t_2) respectively. Note that due to its snaking motion, liquid in the upper film lies in three regions of every vertical cross-section of the flow: between (i) the lower (unshaded) film and lower eddy, (ii) the top of the lower eddy ($y = Y_L^*$) and the bottom of the upper eddy ($y = Y_U^*$), and (iii) the top of the upper eddy and the upper lid. Since these regions all form part of the same film, then by continuity of flux the magnitudes of the fluxes across each of them must equal λ_1. An important consequence of this is that it is possible to predict λ_1 by examining the 'reverse jet' between the eddies (region (ii)) since the flux in this jet, F_{jet}, equals λ_1. Indeed the problem of predicting λ_1 and λ_2 reduces to that of determining the positions Y_L^*, Y_U^* since F_{jet} could then be obtained by integrating the assumed velocity profile (3.5) between these limits, i.e.

$$\lambda_1 = F_{jet} = -\frac{\int_{Y_L^*}^{Y_U^*} u \, dy}{H^*} \tag{3.8}$$

Note also that the flux on the lower roller λ_2 follows immediately, once λ_1 has been determined, since the total flux λ is known and by continuity of flux

$$\lambda = \lambda_1 + \lambda_2 \tag{3.9}$$

3.3.1 Determination of Y_L^*

The top of the bottom eddy, $y = Y_L^*$, is located by considering the flux beneath it. Figure 3.2 shows that below Y_L^* there is an inlet film of flux λ and a *closed* eddy, which by definition has zero net flux across it. This means that the total flux beneath Y_L^* equals λ, or

$$\frac{\int_0^{Y_L^*} u \, dy}{H^*} = \lambda \tag{3.10}$$

where u is the Poiseuille plus Couette velocity profile (3.5). This condition yields a cubic equation for Y_L^*, the relevant solution of which is

$$Y_L^*(S, \lambda) = H^* \left(\frac{1}{(1+S)} - \frac{S(S+3)}{(1+S)^2} \lambda \right) + O(\lambda^2) \tag{3.11}$$

The other solutions for Y_L^* are (i) $Y_L^* = \lambda$ corresponding to the top of the inlet film and (ii) $Y_L^* = H^*$ corresponding to the upper lid.

3.3.2 Determination of Y_U^*

This is far more difficult than the determination of Y_L^*. In §2.5 we saw that in the case of zero net flux, the flow consists of upper and lower eddies separated by a dividing streamline (see Figures 2.13 (a), (b)). In this idealised situation the locations Y_L^* and Y_U^* coincide and the reverse jet, which flows between the eddies when $\lambda \neq 0$, degenerates into a dividing streamline, $y = Y_s^*$ say, where

$$Y_s^* = \frac{H^*}{(1+S)} \tag{3.12}$$

This enables (3.11) to be reinterpreted: when a small flux λ flows through the bead, the top of the lower vortex, $y = Y_L^*(S, \lambda)$, is displaced downwards by the $O(\lambda)$ amount $H^* S(S+3)\lambda/(1+S)^2$. This shows that the problem of determining Y_U^* is equivalent to finding the amount $\delta(S, \lambda)$ by which Y_U^* is displaced from Y_s^* when a non-zero flux λ passes through the bead, i.e.

$$Y_U^*(S, \lambda) = \frac{H^*}{(1+S)} + \delta(S, \lambda) \tag{3.13}$$

Since this theory is neglecting the effects of gravity, the model must satisfy the symmetric film splitting condition

(i) $\lambda_1(1, \lambda) = \lambda_2(1, \lambda) = \lambda/2$

and in the asymptotic limits

(ii) $\lambda_1 \to \lambda$ as $S \to \infty$

(iii) $\lambda_2 \to \lambda$ as $S \to 0$

Since both Y_U^* and Y_L^* are displaced from Y_*^* by an $O(\lambda)$ amount, the thickness of the reverse jet, $Y_U^* - Y_L^*$, is also $O(\lambda)$. Hence by a simple order of magnitude argument the $O(\lambda)$ flux in the reverse jet (which equals λ_1 by hypothesis) is determined by considering only the $O(1)$ liquid velocity in the jet at the location Y_*^*, u_{jet} say. Now substituting (3.12) into the profile (3.5) yields $u_{jet} = -S/(S + 1)$, so equation (3.8) gives

$$F_{jet} = -\frac{S}{(S+1)} \frac{(Y_U^* - Y_L^*)}{H^*} \tag{3.14}$$

From (3.11) it can be shown that for a small flux λ, condition (i) gives $\delta(1, \lambda) = 0$ while conditions (ii) and (iii) yield $\delta(S, \lambda) \to 0$ as $S \to \infty$, 0 respectively. These results motivate the key assumption of the film thickness model developed here: postulate that $\delta(S, \lambda) = 0$ for all S and λ. Under this hypothesis

$$Y_U^*(S, \lambda) = \frac{H^*}{(1 + S)} \text{ for all } S \text{ and } \lambda \tag{3.15}$$

i.e. when any *small* flux λ flows through the bead Y_U^* remains at the same position (as at $\lambda = 0$) and Y_L^* drops by an amount $H^* S(S+3)\lambda/(1+S)^2$ to accomodate the reverse jet.

3.3.3 Predictions of the Film Thickness Model

Combining equations (3.9), (3.11), (3.14) and (3.15) yields

$$\lambda_1 = \frac{S^2(S+3)}{(1+S)^3}\lambda \quad , \quad \lambda_2 = \frac{(1+3S)}{(1+S)^3}\lambda \tag{3.16}$$

If Q_1, Q_2 are the *actual* fluxes on the upper and lower rollers respectively, (3.16) is easily rewritten in terms of, Q, the *actual* flux through the bead:

$$Q_1 = \frac{S^2(S+3)}{(1+S)^3}Q \quad , \quad Q_2 = \frac{(1+3S)}{(1+S)^3}Q \tag{3.17}$$

In §§1.3.3 we noted that it is more precise to talk about *average*, rather than asymptotic, film thicknesses during meniscus roll coating owing to possible variations in film

thicknesses around the periphery of the rollers. It is a simple task to convert (3.17) into average film thicknesses T_1, T_2 since by definition

$$Q_1 = V_1 T_1 \quad , \quad Q_2 = V_2 T_2 \tag{3.18}$$

It is easily demonstrated that equations (3.17), (3.18) combine to predict

$$\frac{T_1}{T_2} = \frac{S(S+3)}{(1+3S)} \tag{3.19}$$

This result is very interesting because it is identical to the prediction of Savage's [1992] 'stagnation point' model for the fully-flooded case. It also begs another question which will be addressed here: is the ratio T_1/T_2 the same in both fully-flooded and ultra-starved forward roll coating?

In Figure 3.3 the prediction (3.19) is compared with Malone's average film thickness data for both meniscus- and fully-flooded forward roll coating. Malone estimates that the degree of starvation in his meniscus roll coating results is such that $\tilde{\lambda}$ ($=Q/2\overline{V}H_0$ where $\overline{V}$ is the *average* roller speed) ≈ 0.1 compared to his fully-flooded results where $1.3 \leq \tilde{\lambda} \leq 1.4$. Although the ultra-starved data only extends over the range $0.2 \leq S \leq 2.0$ (owing to an inability to maintain a liquid bead outside this range), it is possible to conclude that the agreement between theory, i.e. equation (3.19), and experiment is quite poor at low S, improves as S increases, and is, in fact, reasonably good for flows with $S > 1$. Malone noted the discrepancy between theory and experiment at low S and has attributed this to the effects of gravity, which are neglected in the theory, but he has also highlighted the experimental difficulties in measuring the low fluxes (with $T_1, T_2 \approx$ 10 micrometres typically) in this range. Indeed he has even suggested that there may be appreciable losses due to liquid evaporation off the upper roller in this range, although he admits that this effect is difficult to quantify. The close agreement between Malone's data for the ultra-starved and fully-flooded cases confirms the hypothesis that T_1/T_2 is very similar in both instances. This result is completely unexpected, given the major differences in their flow structures. There is no apparent reason why this should be so. In Chapter 5, (3.19) will be compared with film thickness ratio predictions from a numerical simulation of forward meniscus roll coating.

Although the film thickness ratios T_1/T_2 are similar, there are, of course, many differences between the fully-flooded and ultra-starved cases. For example, when the speed of the lower roller is increased during meniscus roll coating, the flux passing into the bead, the thickness of the inlet film and, more significantly, the dimensionless flux λ (defined by equation (3.3)) also increases (see e.g. Tharmalingham and Wilkinson [1978], Figure 4). This increase in the dimensionless flux, which also results in increased average film thicknesses T_1 and T_2, means that they depend not only on the *ratio* of the roller speeds but also on the magnitude of the lower roller speed V_2. This contrasts with the fully-flooded situation where the extra liquid picked up when V_2 increases cannot pass through the nip; consequently in this case T_1 and T_2 depend only on the ratio of the roller speeds, not their magnitudes. A second difference, which arises for similar reasons, lies in the dependence of the individual film thicknesses on the minimum roller separation $2H_0$. In meniscus roll coating the inlet thickness $T_0 \ll 2H_0$ (see Figure 1.6 (c)) so T_1, T_2 are almost *independent* of H_0, whereas in the fully-flooded case the amount of liquid passing through the nip (and hence the film thicknesses T_1, T_2) is limited by the roller separation. In his meniscus roll coating experiments Malone has, in fact, confirmed the independence of T_1, T_2 from H_0.

Since it is impossible to keep all operating parameters in an industrial coating process exactly constant, it is important to be in a 'stable' operating environment in the sense that small changes in the operating parameters do not radically alter the film thicknesses obtained. We have already seen that the velocity ratio S is extremely important since it can be used to alter the industrially important film thickness T_1, i.e. the one which coats the final product. In practice it is convenient to adjust S by simply increasing the upper roller speed whilst fixing the speed of the lower one. This means that T_0, an average inlet film thickness where $Q = V_2 T_0$, is (almost) fixed so variations in T_1 as S changes can be measured by variations in the average thickness ratio T_1/T_0. The latter ratio can also be predicted by the model developed here by simply rearranging the film-splitting results (3.17) in terms of T_0 to yield

$$\frac{T_1}{T_0} = \frac{S(S+3)}{(1+S)^3} \ , \quad \frac{T_2}{T_0} = \frac{(1+3S)}{(1+S)^3} \qquad (3.20)$$

The predicted T_1/T_0 ratio is tested against Malone's [1992] experimental meniscus roll coating data in Figure 3.4 (a); again the agreement between theory and experiment is poor at low S but improves as S increases until for $S > 1$ the agreement is reasonable. Of greater interest, however, is the predicted graph of T_1/T_0 in the range $1 \leq S \leq 10$ shown in Figure 3.4 (b). It predicts T_1 (for a fixed T_0) to be extremely sensitive to small variations in S in the range $0 \leq S \leq 2$, but relatively insensitive when $S \geq 3$. Commercial considerations dictate that the flow should be operated with S as high as possible in order to maximise the amount of coated product and in fact it is possible, using industrial coating liquids different from the Shell Tellus R5 oil used by Malone [1992], to operate with S as high as 10. Unfortunately because the bead becomes unstable if S is too high (see Malone [1992], Chapter 7), it is necessary to reach a compromise between commercial aspirations and practical constraints. In practice $S \approx 3$ is found to offer a suitable compromise.

Finally, in Figure 3.5 the predicted graph of T_2/T_0, i.e. ratio of outlet to inlet average film thicknesses on the lower roller, is compared with Malone's [1992] meniscus roll coating data. The theoretical prediction and experimental data agree well over the entire velocity ratio range.

3.4   Streamline Patterns: Non-Zero Flux

In Chapter 2, we saw that streamline patterns obtained from the Zero Flux model of meniscus roll coating showed many of the experimentally observed characteristics, but were limited to the idealised case of zero net flux across the bead (see Figure 2.13). In this section we show how the assumption relating to the neglect of flux through the bead may be relaxed whilst retaining all the other assumptions of the Zero Flux model (see §2.5). This enables streamlines to be obtained in the more interesting case in which a small, non-zero flux passes through the bead, by means of a numerical solution.

The basic idea of this small flux model is illustrated in Figure 3.6. The bead is again rectangular in shape, but it is no longer closed; instead an inlet film of *dimensionless* thickness t_0 meets a planar liquid-gas interface, on which the usual assumptions apply,

at the point P with the result that a small, non-zero flux λ flows into the bottom left hand corner of the bead. Meanwhile liquid is allowed to flow out of the bead in upper and lower outlet films of dimensionless thicknesses t_1, t_2 and fluxes λ_1, λ_2 respectively. These outlet films meet an outlet planar liquid-gas interface at Q and R respectively.

In principle one could impose any relationship between λ_1, λ_2 and λ provided they satisfied the continuity of flux condition (3.9), but in this model λ is assumed to split according to the forward meniscus roll coating prediction (3.16). The boundary value problem shown in Figure 3.6 cannot be solved by analytical means and must be solved numerically instead. Before describing this numerical solution it is necessary to focus on the form of the inlet and outlet films.

Without loss of generality consider the inlet film of thickness t_0 and flux λ which meets the planar interface at P. Assuming that the flow in the inlet film is horizontal and one-dimensional, the equations governing the flow in the film are the one-dimensional Stokes equations (3.1); expressed in terms of the local co-ordinates $(\hat{x}, \hat{y})$ shown in Figure 3.7, they reduce to

$$\frac{\partial^2 u_{inlet}}{\partial \hat{y}^2} = \frac{\partial p}{\partial \hat{x}} \; , \; \frac{\partial p}{\partial \hat{y}} = 0 \qquad (3.21)$$

where u_{inlet} is the inlet velocity profile and p is the dimensionless pressure defined in §2.5.

At first one might propose a fully-developed 'plug' flow inlet velocity profile in this film. However this would not be compatible with the conditions at the inlet planar interface at P, which are that both the horizontal component of liquid velocity and shear stress should vanish (see §2.5). Therefore for the inlet velocity profile, u_{inlet}, to be compatible with these conditions, it must satisfy

$$u_{inlet} = \frac{\partial u_{inlet}}{\partial \hat{y}} = 0 \; \text{ at } \hat{y} = t_0 \qquad (3.22)$$

Moreover the no-slip condition at the bottom lid, $u_{inlet} = 1$ at $\hat{y} = 0$, enables $\partial p / \partial \hat{x}$ to be evaluated and yields

$$u_{inlet}(\hat{y}) = \left(\frac{\hat{y}}{t_0} - 1 \right)^2 \qquad (3.23)$$

the so-called 'semi-parabolic' velocity profile. By imposing the velocity profile (3.23) at inlet, the total influx into the bead is

$$\lambda = \frac{\int_0^{t_0} u_{inlet}\, d\hat{y}}{H^*} = \frac{t_0}{3H^*} \tag{3.24}$$

Note that if a 'plug' flow profile was imposed at inlet we would have $\lambda = t_0/H^*$ instead.

It is now possible to calculate the values of the streamfunction and vorticity at each point of the inlet film from equation (3.23). In §2.3 it was noted that the difference in value of the streamfunction at two different points in a liquid represents the flux between them. In the boundary value problem shown in Figure 3.6 it is convenient to take the streamfunction $\psi = 0$ on the bottom lid so the value of the streamfunction at a point $\hat{y} = \hat{y}'$ of the inlet fluid film is ψ' where

$$\psi' = \frac{\int_0^{\hat{y}'} u_{inlet}\, d\hat{y}}{H^*} = \lambda \left\{ 1 - \left(1 - \frac{\hat{y}'}{t_0}\right)^3 \right\} \tag{3.25}$$

Moreover since, by assumption, there is no flux across the planar interface, the streamfunction is equal to λ along it. The vorticity ω, defined by $\omega = -\nabla^2\psi$, at any point of the inlet film is given by $\omega = -\partial u_{inlet}/\partial\hat{y}$. Hence at a point $\hat{y} = \hat{y}'$ of this film, the vorticity ω' is given by

$$\omega' = -\frac{2}{t_0}\left(\frac{\hat{y}'}{t_0} - 1\right) \tag{3.26}$$

The velocity profiles in the outlet films are also semi-parabolic. The values of the streamfunction and vorticity at points of the outlet films may be obtained by using expressions similar to (3.25) and (3.26).

The boundary value problem shown in Figure 3.6 is solved using the streamfunction-vorticity F.E. method described in Appendix B. In this solution, the values of the streamfunction and vorticity at nodes touching either the inlet or outlet flow boundaries are imposed to values given by expressions of the form (3.25) and (3.26). At the upper left hand corner, where the inlet planar interface meets the upper lid, there exists a dynamic wetting line of exactly the same form as existed for the Zero Flux model. The techniques for treating this wetting line have been used earlier in §2.5 and are described in Appendix B. Numerical solutions of this boundary value problem were obtained using the two F.E. grids shown in Figure 2.14, having execution times of 80

and 110 c.p.u. seconds when grids (a) and (b) were used respectively. As in §§2.5.2, the coarser grid (grid (a)) was found to be sufficiently refined for the present application, and streamlines presented here are derived from numerical solutions employing grid (a).

Figure 3.8 (a) shows streamlines obtained from a numerical solution of this boundary value problem (see Figure 3.6) with $S = 1$, $H^* = 0.5$ and $t_0 = 0.05$, for which (3.20) gives $t_1 = t_2 = 0.025$. They capture the essential features of those obtained experimentally in Figure 2.15 (a): the effect of allowing a small flux through the bead is to separate eddies of roughly equal size by a thin jet of liquid which moves in an 'S'-shape between them. In Figure 3.8 (b), streamlines are presented for the different case in which $S = 2$, $H^* = 0.5$ and $t_0 = 0.05$. In this case (3.20) gives

$$t_1 = 10/27 \times 0.05 \quad , \quad t_2 = 7/27 \times 0.05 \tag{3.27}$$

The eddies are once again separated by a thin jet of liquid which flows between them before coating the upper lid. In this case, however, as in the corresponding zero flux prediction (Figure 2.13 (b)), the upper eddy is roughly twice the size of the lower one, in qualitative agreement with Malone's [1992] experimental observation, as shown in Figure 2.15 (b).

3.5 Conclusions

In this chapter we have developed the first predictive model for the film thicknesses produced on upper and lower rollers during forward meniscus roll coating. It is based entirely on the flow in the central 'core' of the bead, sufficiently far from the curved meniscii. The model predicts that $T_1/T_2 = S(S + 3)/(1 + 3S)$ – a function of velocity ratio S only – which is identical to Savage's [1992] prediction for fully-flooded forward roll coating. Malone's [1992] forward meniscus roll coating data is in reasonable agreement with the theory developed here and also shows a close correlation with his data for the fully-flooded case.

As the model is unable to account for the effects of the curved meniscii which exist cn either side of the meniscus roll coating bead, it is possible that the accuracy of

prediction may be improved by a numerical simulation of the problem which includes these effects. This hypothesis is tested in Chapter 5 where numerical predictions of T_1/T_2 are compared with the analytical result (3.19) and Malone's experimental data.

No doubt a conspicuous feature of this chapter is the lack of a predictive film thickness theory for reverse meniscus roll coating. This may seem surprising in view of the relative simplicity of its flow structure compared with the forward case (compare Figure 2.15 (c) with Figure 2.15 (a)). Regrettably, the analysis of the forward case developed here cannot be extended to the reverse case because there is no reverse flow between eddies during the latter. Therefore at present it appears that further information on reverse meniscus roll coating may only be furnished by numerical solutions of the problem.
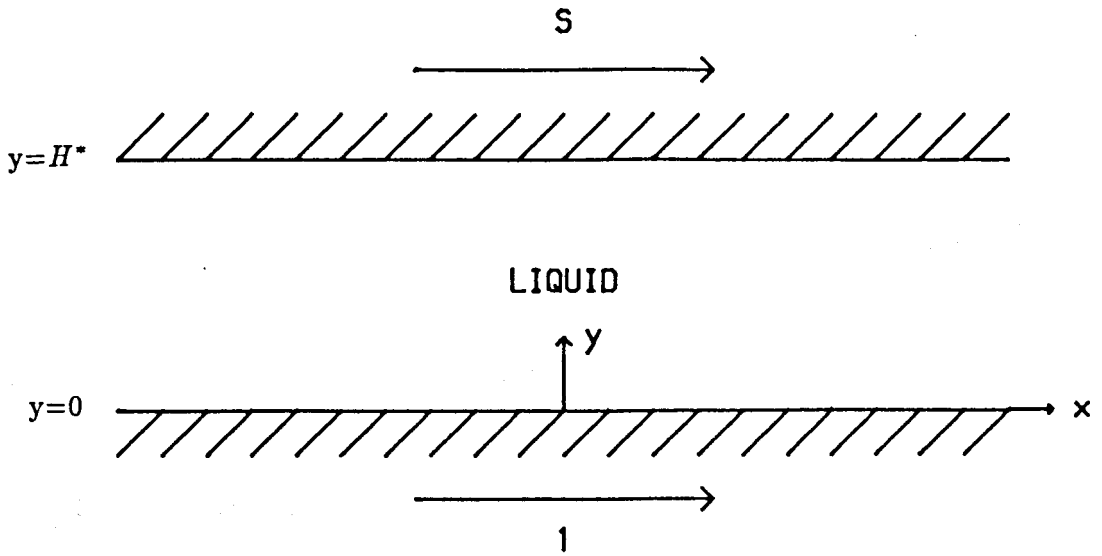
Figure 3.1: The Co-ordinate System For the Core Flow Model of Forward Meniscus Roll Coating
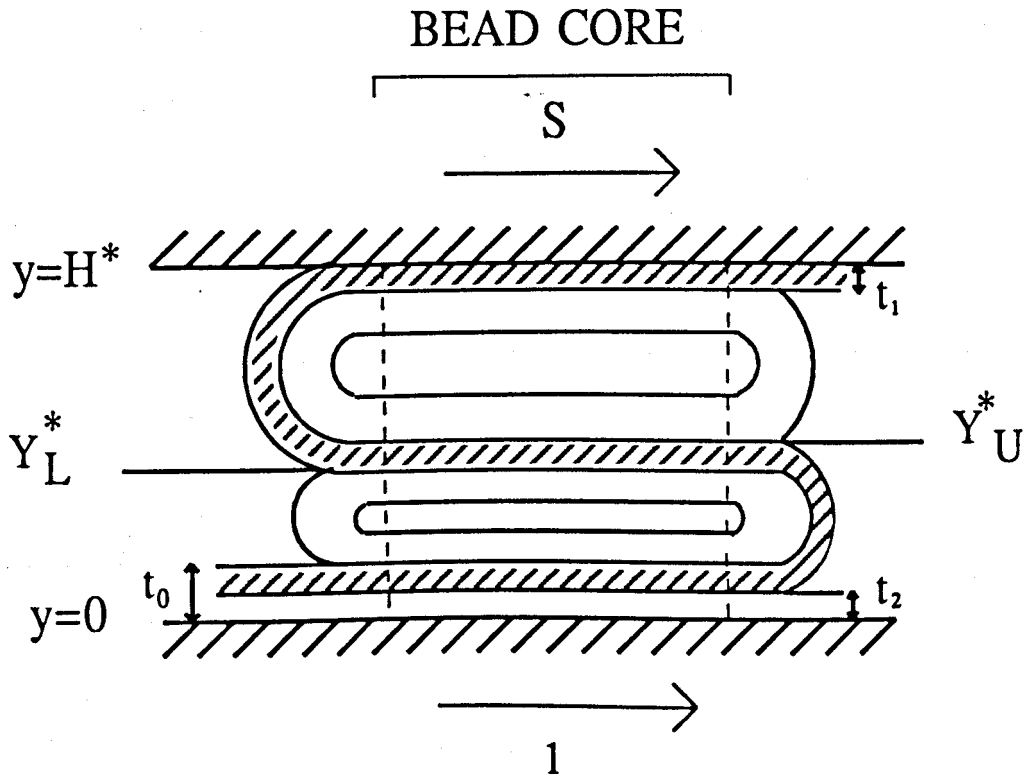
Figure 3.2: Schematic Diagram of the Core Flow Model For Forward Meniscus Roll Coating

△ ULTRA-STARVED EXPERIMENTAL DATA (MALONE [1992])

T_1/T_2 ○ FULLY-FLOODED EXPERIMENTAL DATA (MALONE [1992])

― S (S+3) / (3S+1)
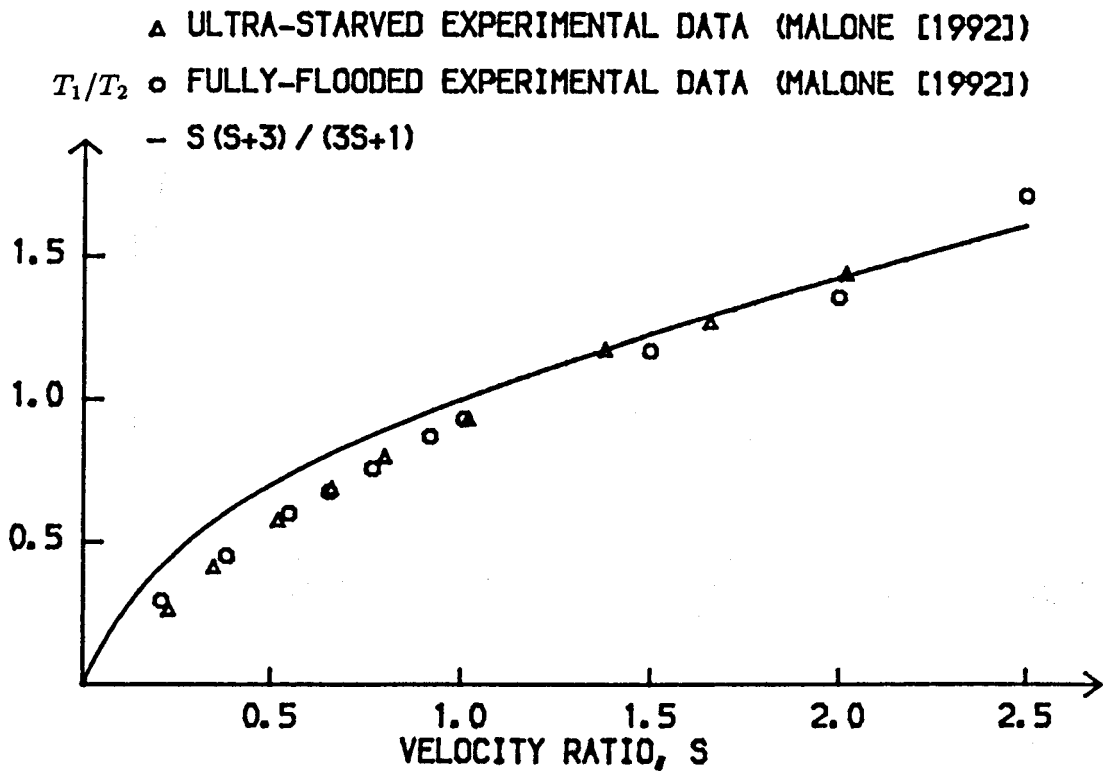
Figure 3.3: A Comparison Between Theoretical Prediction and Experimental Measurements of T_1/T_2 in Forward Meniscus Roll Coating

(a)

□ EXPERIMENTAL DATA (MALONE [1992])

T_1/T_0 ― $S(S+3)/(1+S)^3$
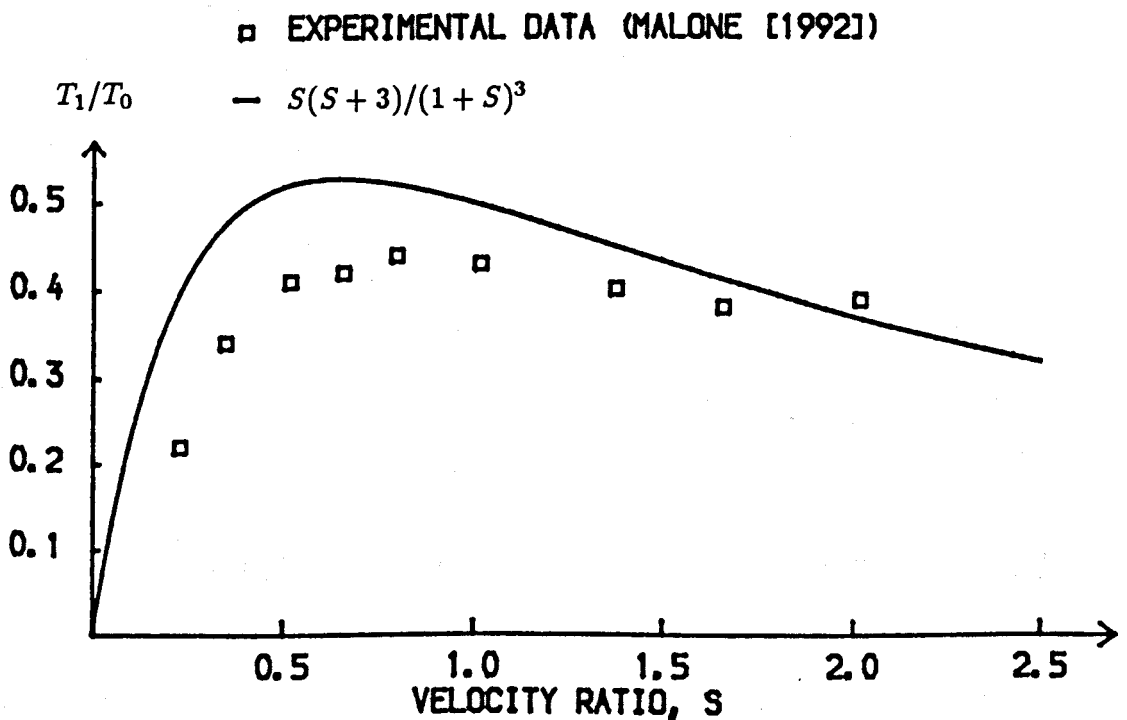
Figure 3.4: The Theoretical Prediction of T_1/T_0 in Forward Meniscus Roll Coating:

(a) Comparison with Experiment; (b) Prediction in the Range $0 \leq S \leq 10$

(b)

$S(S+3)/(1+S)^3$
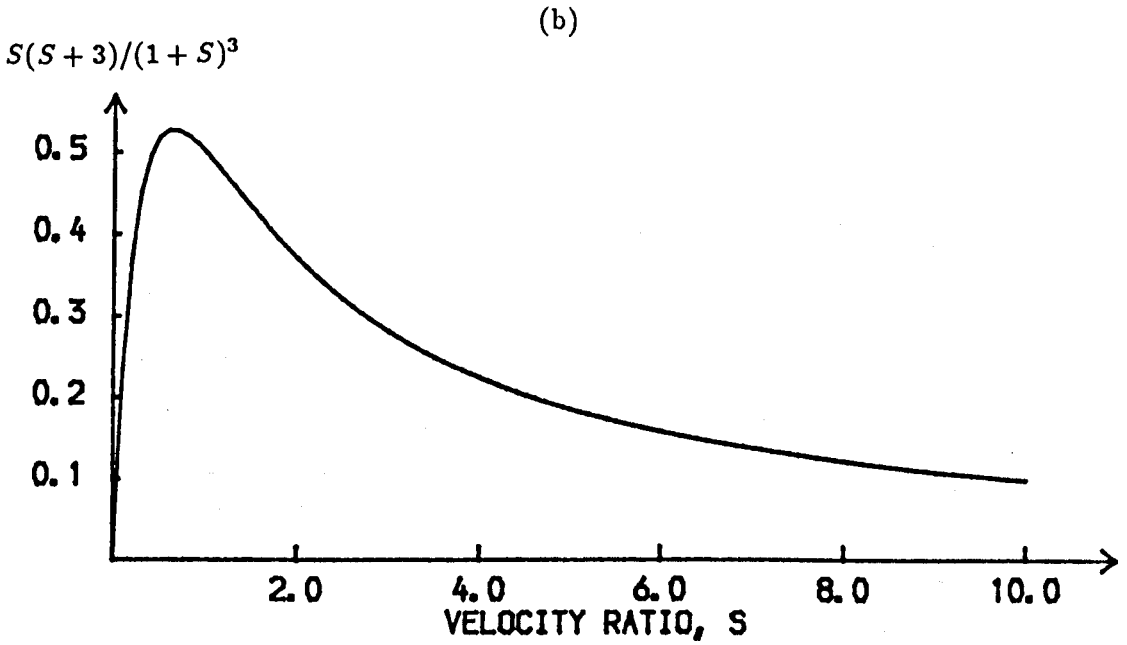
Figure 3.4 (continued)
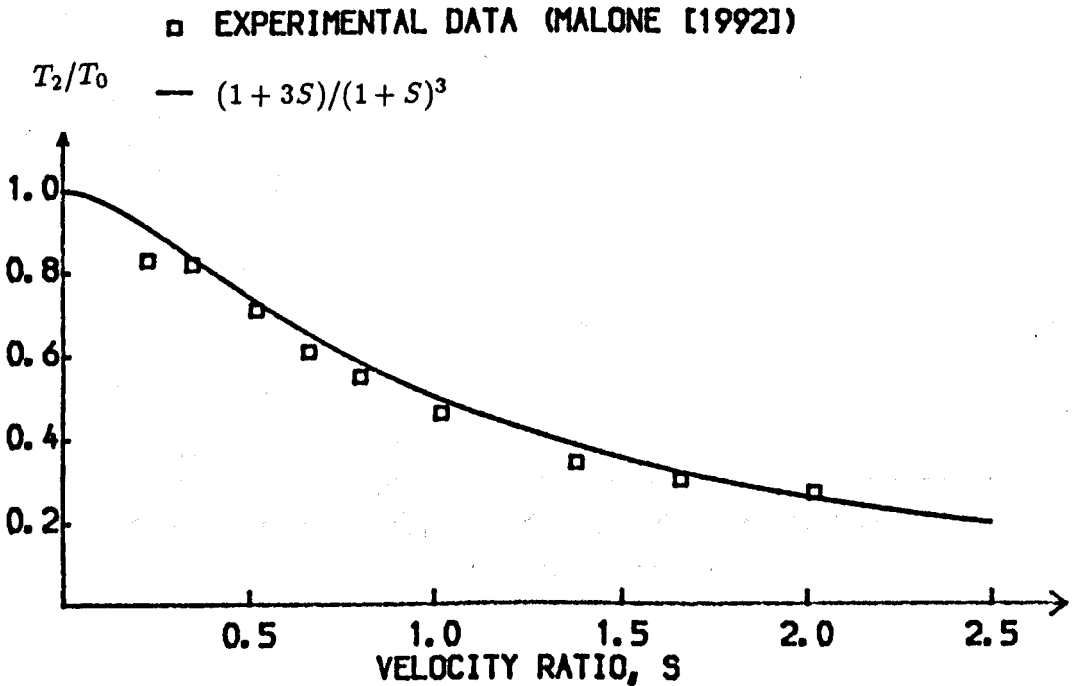
Figure 3.5: A Comparison between Theoretical Prediction and Experimental Measurement of T_2/T_0 in Forward Meniscus Roll Coating
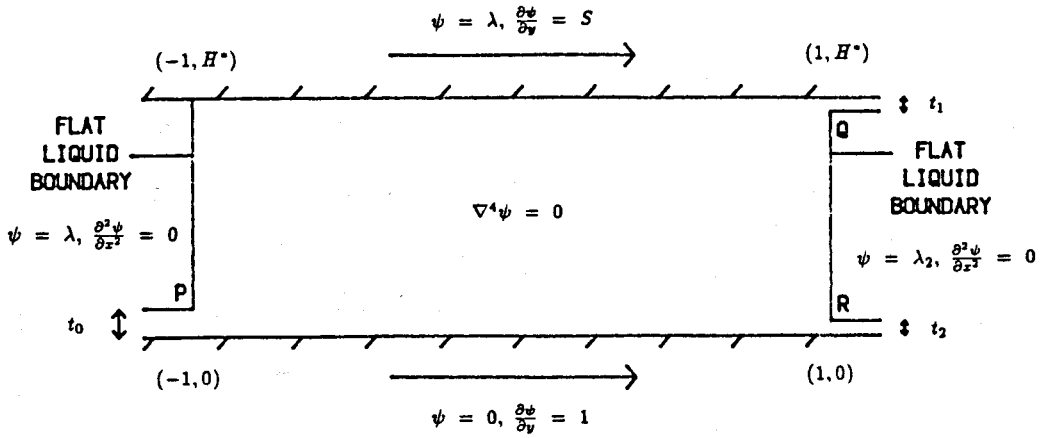
Figure 3.6: The Boundary Value Problem Arising from the Small Flux Model of a Forward Meniscus Roll Coating Bead
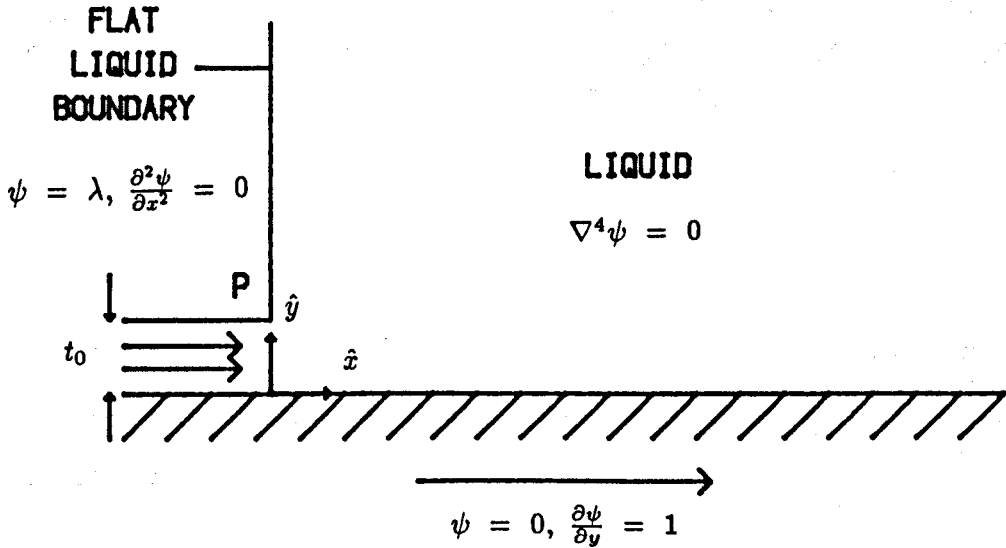
Figure 3.7: The Inlet Liquid Film

(a)

(b)
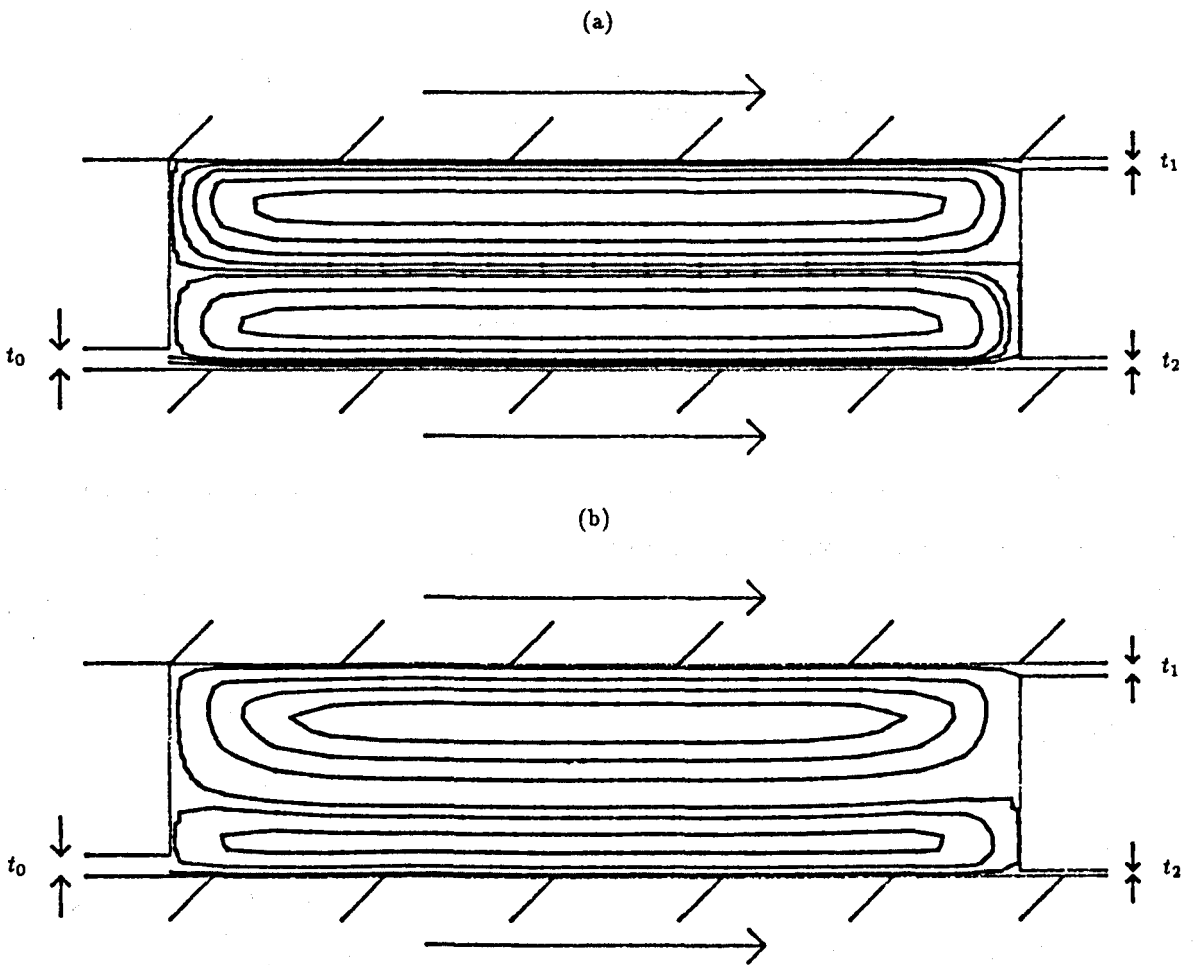
Figure 3.8: Streamlines Obtained from Numerical (F.E.) Solutions of the Small Flux Model for a Forward Meniscus Roll Coating Bead: (a) $S = 1$, $H^* = 0.5$; (b) $S = 2$, $H^* = 0.5$

(a) Dependence on Velocity Ratio S with $H^* = 0.5$

$S =$	0.5	1.0	1.5	2.0	-1.0
Zero Flux	36.0	48.0	60.0	72.0	0.0
Poiseuille + Couette	36.0	48.0	60.0	72.0	0.0

(b) Dependence on Dimensionless Depth H^* with $S = 1$

$H^* =$	0.1	0.2	0.5	0.8	1.0
Zero Flux	1200	300	48.0	18.75	12.0
Poiseuille + Couette	1200	300	48.0	18.75	12.0

Table 3.1: Dimensionless Horizontal Pressure Gradients in the Central Core of the Bead – A Comparison between Predictions from the Zero Flux and 'Poiseuille plus Couette' Models

(a) $S = 1$, $H^* = 0.25$

y	Zero Flux	Poiseiulle + Couette
0.25	1.0	1.0
0.20	0.4	0.4
0.15	-0.44	-0.44
0.10	-0.44	-0.44
0.05	0.4	0.4
0.00	1.0	1.0

(b) $S = 2$, $H^* = 0.25$

y	Zero Flux	Poiseuille + Couette
0.25	2.0	2.0
0.20	0.36	0.36
0.15	-0.56	-0.56
0.10	-0.76	-0.76
0.05	-0.24	-0.24
0.00	1.0	1.0

Table 3.2: Horizontal Velocity Profiles Across the Bead in the Zero Flux Case

Chapter 4: The Development of the Free Surface Code

4.1 - Introduction

4.2 - The Galerkin Finite Element Method

    4.2.1 - The Divergence Form of the Equations of Motion

    4.2.2 - The Galerkin Finite Element Equations

    4.2.3 - Solution of the Galerkin F.E. Equations: Newton Iteration

4.3 - The Solution of Cavity-Driven Flows

    4.3.1 - Flow in a Lid-Driven Cavity

    4.3.2 - Flow in an Open, Driven Cavity

    4.3.3 - The Zero Flux Model of Meniscus Roll Coating

4.4 - The Slot Coater

    4.4.1 - Introduction

    4.4.2 - Incorporation of Free Surface Stress Conditions into the Galerkin Equations

    4.4.3 - Free Surface Representation: The Spine Method

    4.4.4 - Evaluation of Free Surface Integrals

    4.4.5 - Finding an Initial Approximation

    4.4.6 - Results and Discussion

4.5 - The Symmetric, Fully-Flooded, Forward Roll Coater

    4.5.1 - Introduction

    4.5.2 - Coyle et al's [1986] Model

    4.5.3 - The Computational Mesh For the Symmetric Forward Roll Coater

    4.5.4 - The Structure of Element-Level Jacobians in Forward Roll Coating

    4.5.5 - Results and Discussion

4.6 - The Asymmetric Fully-Flooded Forward Roll Coater

    4.6.1 - Boundary Conditions and Computational Mesh

    4.6.2 - Results and Discussion

4.7 - Conclusions

Figures 4.1 - 4.29

Tables 4.1 - 4.4

Chapter 4

The Development of the Free

Surface Code

4.1 Introduction

In the two previous chapters, meniscus roll coating has been analysed using simple,
lubrication models for the flow in the central 'core' region (see Figure 2.1). Although
these analytical models have successfully predicted the main features of the flow field,
its dependence on velocity ratio, and the average film thicknesses produced on up-
per and lower rollers during forward meniscus roll coating, they are still, in some
senses, incomplete. This is because they are unable to elucidate the nature of the two-
dimensional, surface tension-dependent flow near the meniscii. Since Malone's [1992]
forward meniscus roll coating experiments clearly demonstrate that the flux-splitting
process actually occurs near the downstream meniscus, it is possible that a fuller anal-
ysis of the problem, including the flow near the meniscii, may lead to more accurate
film thickness predictions. However the task of modelling these meniscii and the at-
tendant dynamic wetting line (see Figure 1.6 (c)) is extremely difficult since they lead
to the liquid domain having a non-standard shape. Nevertheless, these difficulties,
which are intractable to traditional mathematical analysis, may be surmounted using
modern computational techniques (see §1.5) in which the meniscii are represented as
mathematical boundaries known as 'Free Surfaces'. In the present chapter we describe

a popular finite element (F.E.) approach for solving steady, two-dimensional flows with free surfaces, and illustrate some of the practical difficulties encountered, e.g. in mesh generation for flows with highly curved meniscii. It is not, however, the intention to discuss the programming methodology behind the F.E. technique itself in any detail for two reasons: (i) this would form a thesis in its own right, (ii) there are already many excellent texts dealing with this topic – see for example Cook [1981], Carter [1985] or Chen [1991].

In §1.5, we concluded that the most suitable numerical technique for solving steady, free surface flows is that employing the F.E. method in conjunction with a 'primitive variables' $(u - v - p)$ formulation. It will soon become apparent that even the development of a computer code to solve steady free surface flows is a formidable undertaking because the following non-linear boundary conditions

(i) Zero normal velocity – the kinematic condition

(ii) Zero tangential (shear) stress

(iii) Normal stress is balanced by surface tension stresses and atmospheric pressure

must be applied at the unknown, and often highly curved, free surface locations.

In the FORTRAN code described here, the free surface formulation is based on Kistler's [1983] 'Spine Method'. During its development a programme of work was devised in which flow problems of increasing complexity are solved, beginning with flows in which there are no free surfaces present. At each stage the F.E. predictions are validated against either analytical results, previously published numerical solutions or experimental data.

4.2   The Galerkin Finite Element Method

4.2.1   The Divergence Form of the Equations of Motion

The motion of a Newtonian, incompressible liquid of constant density ρ and viscosity η, over the solution domain Ω, is governed by the Navier-Stokes equations (see §2.2). Following Kistler and Scriven [1983], these equations can be non-dimensionalised by

scaling lengths with D, a length scale appropriate to Ω; velocities by U, a characteristic velocity; and pressure and viscous stresses by $\eta U/D$. It is also convenient to introduce the dimensionless groups $Re = \rho U D/\eta$, the Reynolds number, which gives a measure of the relative magnitude of inertial to viscous forces and $St = \rho g D^2/\eta U$, the Stokes number, which indicates the relative importance of gravity to viscous forces (g is the gravitational acceleration). Under this non-dimensionalisation, the Navier-Stokes equations, expressing local conservation of linear momentum and mass, may be written as

$$Re \, \underline{u}.\nabla \underline{u} \;\; = \;\; \nabla.\underline{\underline{\sigma}} \; + \; St \underline{f} \tag{4.1}$$

$$\nabla.\underline{u} \;\; = \;\; 0 \tag{4.2}$$

where $\underline{u} = (u,v)$ is the dimensionless liquid velocity, $\underline{f}$ is the unit vector in the direction in which gravity acts, and $\underline{\underline{\sigma}}$ is the dimensionless stress tensor. From equation (2.13) we see that for a Newtonian liquid

$$\underline{\underline{\sigma}} \; = \; -p\underline{\underline{I}} \; + \; [\nabla \underline{u} \; + \; (\nabla \underline{u})^T] \tag{4.3}$$

where $\underline{\underline{I}}$ is the unit tensor and p is the dimensionless liquid pressure. Note, that as the effects of gravity are neglected in this thesis, the Stokes number St is set equal to zero in equation (4.1). For the purposes of the analysis, it is convenient to introduce the tensor $\underline{u}\underline{u}$ which is the *diadic product* of $\underline{u}$ with itself such that

$$(\underline{u}\underline{u})_{ij} \; = \; u_i u_j \tag{4.4}$$

This enables the governing equations (4.1), (4.2) to be cast in 'divergence form' (Kistler and Scriven [1983])

$$Re \, \nabla.(\underline{u}\underline{u}) \; = \; \nabla.\underline{\underline{\sigma}} \; ; \; \nabla.\underline{u} \; = \; 0 \tag{4.5}$$

from which the F.E. equations for the approximate solution of such a system can be derived.

4.2.2   The Galerkin Finite Element Equations

In Appendix B the philosophy behind the F.E. method is described in relation to the solution of the creeping flow equations by a streamfunction-vorticity method. Unfortu-

nately, this method is unsuitable for the solution of general free surface flow problems because (a) the normal stress condition (iii) cannot be conveniently formulated in terms of the ψ, ω variables, (b) no variational principle exists for flow at non-zero Reynolds number (see Carter [1985] p 117). These problems can, however, be solved by the 'Galerkin Method of Weighted Residuals' in which the Navier-Stokes equations are formulated in terms of the primitive variables. In this formulation the dependent variables are the nodal values of (u, v, p).

In Chapters 2 and 3, numerical solutions of the creeping flow equations employing 6-node triangular elements with quadratic shape functions for both the streamfunction and vorticity have been seen to give acceptable results. However when primitive variables are used the question of the order of the shape functions used to interpolate the velocity and pressure fields is an important one because the lack of an explicit equation for the pressure coupling can lead to severe numerical difficulties. For example, an improper combination of velocity and pressure interpolations may lead to an ill-conditioned global matrix which yields a spurious pressure solution, or, in extreme cases, no solution at all because of the singular nature of this matrix (see Chen [1991] pp 39-40). The explanation for such occurences is given by Olson et al [1978] in terms of the existence of zero eigenvalues, a phenomenon that is often referred to as *pressure modes*, see Sani, Gresho, Lee and Griffiths [1981].

An approach which overcomes these difficulties is the 'mixed-interpolation' formulation introduced by Hood and Taylor [1974]. They used elements with different order shape functions for fluid velocities and pressure in order to curb the oscillatory pressure solutions that resulted from employing equal order interpolations. In the literature, elements which have different order interpolations for fluid velocity and pressure are known as 'mixed elements'. In certain cases, even mixed elements may give a spurious mode; for example an improper arrangement of mixed elements for certain boundary conditions may also result in a 'locking' problem as explained by Hughes [1987].

It is now generally recognized that in the primitive variable F.E. formulation of the Navier-Stokes equations, the pressure should be interpolated at least one order lower than the velocities; see for example Fortin and Thomasset [1979], Huyakorn, Taylor,

Lee and Gresho [1978], Lee, Gresho and Sani [1979]. Theoretically speaking, if a mixed element satisfies the so-called *Ladyzenskaya-Babuska-Brezzi*, or LBB stability condition (see Babuska and Aziz [1972]) with the pressure interpolation one order lower than that for the velocities, the rate of convergence is said to be 'optimal' and no locking will occur. Unfortunately it is a rather complex procedure to verify whether an element satisfies the LBB condition – a detailed description of the mathematical aspects is given by Oden and Carey [1984]. The most widely used elements that appear in the literature which satisfy the LBB condition are shown in Figure 4.1 (a)-(d), they are

(a) Triangular: Six node velocity - three node pressure (V6/P3)

(b) Quadrilateral: Nine node velocity - one node pressure (V9/P1)

(c) Quadrilateral: Nine node velocity - three node pressure (V9/P3)

(d) Quadrilateral: Nine node velocity - four node pressure (V9/P4)

In their study, Kistler and Scriven [1983] used quadrilateral V9/P4 elements. Here, however, triangular V6/P3 ones are preferred for the same reasons given in Appendix B, namely

(i) it is much easier to locally refine a particular grid

(ii) (important in the early development of the code) the F.E. equations produce a global stiffness matrix with a smaller bandwidth, thereby reducing the storage requirement (see Appendix C)

If N_k represents a 6-node biquadratic shape function for the velocity field $\underline{u}$ and ψ_l a three node bilinear one for the pressure field p, then (see §B.5)

$$N_k = \begin{cases} 1 & \text{at node } k \\ 0 & \text{at all other nodes} \end{cases} \qquad \psi_l = \begin{cases} 1 & \text{at the } l\text{th pressure node} \\ 0 & \text{at all other corner nodes} \end{cases} \qquad (4.6)$$

If $\underline{u}_k = \underline{i}u_k + \underline{j}v_k \ (k = 1, \ldots, K)$ are the values of the velocities at the velocity nodes and $p_l \ (l = 1, \ldots, L)$ are the nodal values of the pressure, then the F.E. approximation to the velocity and pressure fields are written in terms of these nodal values

$$\underline{u} = \sum_{k=1}^{K} \underline{u}_k N_k \quad , p = \sum_{l=1}^{L} p_l \psi_l \qquad (4.7)$$

Note that equation (4.7) is of the same form as the F.E. approximation to ψ and ω given in Appendix B.

The local node numbering scheme used in the primitive variable formulation is shown in Figure 4.2. It differs from that used in Appendix B since the first 3 local nodes are the corner nodes. This convention simplifies the problem of incorporating pressure freedoms into the code (see Carter [1985] pp 199-200). As in Appendix B the shape functions N_k and ψ_l associated with a particular element may be conveniently expressed in terms of local 'area' co-ordinates. If N_k is the velocity shape function associated with the kth local node (under the local node numbering scheme shown in Figure 4.2) and L_1, L_2, L_3 are defined by equation (B.33) then

$$
\begin{aligned}
N_1 &= L_1(2L_1 - 1) \quad, \quad N_4 = 4L_1L_2 \\
N_2 &= L_2(2L_2 - 1) \quad, \quad N_5 = 4L_2L_3 \\
N_3 &= L_3(2L_3 - 1) \quad, \quad N_6 = 4L_1L_3
\end{aligned}
\tag{4.8}
$$

while the ψ_l shape functions associated with the lth corner node are simply,

$$
\psi_1 = L_1 \quad, \quad \psi_2 = L_2 \quad, \quad \psi_3 = L_3
\tag{4.9}
$$

Note that at any point in the element, these shape functions satisfy the relationship

$$
\sum_{k=1}^{6} N_k(\xi, \eta) = \sum_{l=1}^{3} \psi_l(\xi, \eta) = 1
\tag{4.10}
$$

Now for the theory. We illustrate Galerkin's method of weighted residuals by describing how it can be used to solve a relatively simple fluid flow problem in which the fluid velocity on the boundary $\partial\Omega$ is known – additional theory needed to solve more complicated free surface flow problems will be described in subsequent sections. The idea is very simple: the $2K + L$ equations needed to determine the $2K + L$ unknowns, i.e. the nodal values of u, v, and p, are provided by weighting residuals of the momentum and continuity equations with the shape functions N_k and ψ_l respectively, and setting them equal to zero – see Kistler and Scriven [1983] p 261. Note that if we weighted the momentum and continuity residuals by ψ_l and N_k respectively this would provide only $2L + K$ equations, not the requisite $2K + L$. Weighting the momentum

equation of (4.5) with each N_k and setting it equal to zero gives

$$\underline{R}_M^k = \int_\Omega N_k(Re \, \nabla.(\underline{uu}) - \nabla.\underline{\sigma}) \, d\Omega = 0 \qquad (4.11)$$

Using the fact that

$$N_k \, \nabla.(\underline{uu}) = \nabla.(N_k\underline{uu}) - \nabla N_k.(\underline{uu}) \qquad (4.12)$$

and

$$N_k \, \nabla.\underline{\sigma} = \nabla.(N_k\underline{\sigma}) - \nabla N_k.(\underline{\sigma}) \qquad (4.13)$$

enables (4.11) to be rewritten as

$$\underline{R}_M^k = \int_\Omega [Re\nabla.(N_k\underline{uu}) - Re\nabla N_k.(\underline{uu}) + \nabla N_k.\underline{\sigma} - \nabla.(N_k\underline{\sigma})] \, d\Omega = 0 \quad (4.14)$$

Finally, applying the divergence theorem to the purely divergent terms yields

$$\underline{R}_M^k = \int_\Omega [\nabla N_k.(-Re\underline{uu} + \underline{\sigma})] \, d\Omega - \int_{\partial\Omega} N_k\underline{n}.(-Re\underline{uu} + \underline{\sigma}) \, ds = 0 \qquad (4.15)$$

Equation (4.15) provides the 2 scalar algebraic equations needed to determine the velocity freedoms (u_k, v_k) which are associated with node k.

There are two contributions to each momentum residual, namely those due to (i) the domain Ω, $(\underline{R}_M^k)_\Omega$, and (ii) the boundary $\partial\Omega$, $(\underline{R}_M^k)_{\partial\Omega}$. The latter contribution is only important in free surface flows and does not need to be evaluated in the present simple problem for the following reasons. Since we are assuming that $\underline{u}$ is prescribed on $\partial\Omega$, the velocity freedoms (u_k, v_k) associated with each of the (K_b say) boundary nodes are already known. This means that the only weighted residuals which need to be evaluated are those associated with the K' ($=K - K_b$) nodes which do not lie on the boundary. From the properties of shape functions given in (4.6) it follows that each N_k associated with the K' interior nodes is identically equal to zero on $\partial\Omega$. Therefore their associated momentum residuals $\underline{R}_M^k$ simply reduce to $\underline{R}_M^k = (\underline{R}_M^k)_\Omega$ where

$$(\underline{R}_M^k)_\Omega = \int_\Omega \nabla N_k.(-Re\underline{uu} + \underline{\sigma}) \, d\Omega \qquad (4.16)$$

As these domain residuals have to be evaluated in all subsequent solutions, we describe their form in detail.

Since $\nabla.\underline{u} = 0$, it is easily shown that $\nabla N_k.(\underline{uu}) = (\nabla N_k.\underline{u})\underline{u}$ which may be written in the following vector form

$$\nabla N_k.(\underline{uu}) = \left(u\frac{\partial N_k}{\partial x} + v\frac{\partial N_k}{\partial y}\right)(u,v) \qquad (4.17)$$

For a Newtonian fluid, $\underline{\sigma}$ is given by (4.3) and after algebraic manipulation, the contribution $\nabla N_k.\underline{\sigma}$ may be split into x and y components since

$$(\nabla N_k.\underline{\sigma})_x = -p\frac{\partial N_k}{\partial x} + \frac{\partial u}{\partial y}\frac{\partial N_k}{\partial y} + \frac{\partial v}{\partial x}\frac{\partial N_k}{\partial y} + 2\frac{\partial u}{\partial x}\frac{\partial N_k}{\partial x} \qquad (4.18)$$

$$(\nabla N_k.\underline{\sigma})_y = -p\frac{\partial N_k}{\partial y} + \frac{\partial v}{\partial x}\frac{\partial N_k}{\partial x} + \frac{\partial u}{\partial y}\frac{\partial N_k}{\partial x} + 2\frac{\partial v}{\partial y}\frac{\partial N_k}{\partial y} \qquad (4.19)$$

In the F.E. code, it was found convenient to introduce arrays $X1(K),...,X5(K)$ and $Y1(K),...,Y5(K)$, such that the contributions to the x and y components of the momentum residuals (4.15) due to the domain Ω, $(R_M^k)_{\Omega,x}$ and $(R_M^k)_{\Omega,y}$ respectively, are

$$(R_M^k)_{\Omega,x} = \int_\Omega [-ReX1(K) + X2(K) + X3(K) + X4(K) + X5(K)]\, d\Omega \qquad (4.20)$$

and

$$(R_M^k)_{\Omega,y} = \int_\Omega [-ReY1(K) + Y2(K) + Y3(K) + Y4(K) + Y5(K)]\, d\Omega \qquad (4.21)$$

where

$$X1(K) = u^2\frac{\partial N_k}{\partial x} + uv\frac{\partial N_k}{\partial y} \quad , \quad Y1(K) = uv\frac{\partial N_k}{\partial x} + v^2\frac{\partial N_k}{\partial y} \qquad (4.22)$$

$$X2(K) = -p\frac{\partial N_k}{\partial x} \quad , \quad Y2(K) = -p\frac{\partial N_k}{\partial y} \qquad (4.23)$$

$$X3(K) = \frac{\partial u}{\partial y}\frac{\partial N_k}{\partial y} \quad , \quad Y3(K) = \frac{\partial v}{\partial x}\frac{\partial N_k}{\partial x} \qquad (4.24)$$

$$X4(K) = \frac{\partial v}{\partial x}\frac{\partial N_k}{\partial y} \quad , \quad Y4(K) = \frac{\partial u}{\partial y}\frac{\partial N_k}{\partial x} \qquad (4.25)$$

$$X5(K) = 2\frac{\partial u}{\partial x}\frac{\partial N_k}{\partial x} \quad , \quad Y5(K) = 2\frac{\partial v}{\partial y}\frac{\partial N_k}{\partial y} \qquad (4.26)$$

The F.E. equations needed to determine the L pressure coefficients in (4.7) are provided by the 'Continuity Residuals', obtained by weighting the continuity equation of (4.5) by the presssure shape functions ψ_l:

$$R_C^l = \int_\Omega \psi_l \left(\frac{\partial u}{\partial x} + \frac{\partial v}{\partial y}\right) d\Omega = 0 \qquad (4.27)$$

4.2.3 Solution of the Galerkin F.E. Equations: Newton Iteration

Now that the F.E. equations (4.15), (4.27) have beed obtained, it is necessary to solve them. In this work, a solution technique based on Newton iteration, which was first used by Ruschak [1980] and Saito and Scriven [1981], is chosen because the convergence rate is much faster than alternative methods based on successive approximation techniques (see §1.5). Although in the present simple problem there are Dirichlet conditions (i.e. where the value of the variable itself is prescribed) on the boundary node velocities (u_k, v_k), it is more convenient to describe Newton's method under the assumption that all $2K + L$ freedoms have to be found; we will then describe how the theory is altered to take account of these boundary conditions.

Newton's method requires the evaluation of the derivatives of the momentum and continuity residuals with respect to the finite element coefficients $\{u_k, v_k, p_l\}$. In the present simple flow problem, the vector of F.E. coefficients $\underline{\alpha}$ can be subdivided into $\underline{u}^T = [u_1, \ldots, u_K]$, $\underline{v}^T = [v_1, \ldots, v_K]$ and $\underline{p}^T = [p_1, \ldots, p_L]$ where

$$\underline{\alpha}^T = [\underline{u}^T, \underline{v}^T, \underline{p}^T] \tag{4.28}$$

Similarly, the weighted residuals of the momentum equations, $\underline{R}_M^k$, have x and y components $(R_M^k)_x$, $(R_M^k)_y$ so

$$\underline{R}_M^k = (R_M^k)_x \underline{i} + (R_M^k)_y \underline{j} \tag{4.29}$$

where $\underline{i}$ and $\underline{j}$ are unit vectors in the x and y directions respectively. The residuals $(R_M^k)_x$, $(R_M^k)_y$ can be combined with the continuity residuals R_C^l in a vector of weighted residuals, $\underline{R}(\underline{\alpha})$, given by

$$\underline{R}^T = [(\underline{R}_M)_x^T, (\underline{R}_M)_y^T, \underline{R}_C^T] \tag{4.30}$$

where $(\underline{R}_M)_x^T = [(R_M^1)_x, \ldots, (R_M^K)_x]$, $(\underline{R}_M)_y^T = [(R_M^1)_y, \ldots, (R_M^K)_y]$ and $\underline{R}_C^T = [R_C^1, \ldots, R_C^L]$.

The Newton iteration process finds the updated coefficients $\underline{\alpha}_{n+1}$ from the last computed set, $\underline{\alpha}_n$, by solving the linear system of equations given by

$$\underline{\underline{J}} [\underline{\alpha}_{n+1} - \underline{\alpha}_n] = \underline{\underline{J}} \, \Delta\underline{\alpha}_n = -\underline{R}(\underline{\alpha}_n) \tag{4.31}$$

where the Jacobian $\underline{\underline{J}}$ is defined as

$$\underline{\underline{J}} = \frac{\partial \underline{R}}{\partial \underline{\alpha}}(\underline{\alpha} = \underline{\alpha}_n) \qquad (4.32)$$

Now for the boundary conditions. The Dirichlet conditions on boundary velocities (u_k, v_k) (referred to as *essential* conditions in F.E. terminology) are imposed by (i) setting the velocity freedoms associated with boundary nodes to their known values; (ii) deleting the momentum residuals (4.15) formed from those shape functions N_k that are associated with boundary nodes from the equation set (4.31); (iii) deleting derivatives $\partial \underline{R}/\partial \alpha_i$ with respect to those α_i which are known (in this case the boundary velocities (u_k, v_k)). In other words the size of the Jacobian $\underline{\underline{J}}$ is actually $(2K' + L) \times (2K' + L)$ rather than $(2K + L) \times (2K + L)$.

In §B.5 we saw that the practical problem of computing the F.E. equations in flows with elements of general size and orientation (as is definitely the case in free surface flows) can be alleviated by *isoparametrically* mapping a standard element, defined in local co-ordinate space, into each of the deformed elements in the flow domain. This technique enables the residuals and their derivatives with respect to the F.E. coefficients to be evaluated in the local (ξ, η) space, shown in Figure 4.2, by invoking equations (B.41)–(B.43). As in the streamfunction-vorticity method, the full residual vector $\underline{R}$ and global matrix $\underline{\underline{J}}$ are assembled from contributions at element level. These element-level contributions take the form of either area or boundary integrals and are again evaluated using Gaussian quadrature. The matrix $\underline{\underline{J}}$ is stored in a 'banded-matrix' form in order to reduce the storage requirement – see Appendix C.

As Newton's method is an iterative technique, we have to decide on an initial approximation and a convergence criterion. The former is, of course, problem dependent and must be tailored to the specific problem of interest, whereas the suitability of the latter should always be evaluated by comparison with different criteria. However, the author's experience suggests that both the maximum change among the unknown coefficients, $|\alpha_{n+1}^i - \alpha_n^i|_{max}$ and the largest among the unknown residuals $|R^i(\alpha_n)|_{max}$ are useful indicators for viscous, free surface flows. It can be shown that Newton iteration converges quadratically as a solution is approached (see Isaacson and Keller [1966])

which means that if $n - 1$, n, $n + 1$ refer to successive iterations, then

$$\left| \alpha^i_{n+1} - \alpha^i_n \right|_{max} \leq C \left| \alpha^i_n - \alpha^i_{n-1} \right|^2_{max} \tag{4.33}$$

for some constant C when n is large. This convergence rate means that Newton iteration not only offers a drastic improvement on convergence rates of alternative successive approximation techniques, it also affords a useful test of the correctness of the Jacobian and the iteration procedure: if the convergence rate is not quadratic as the solution is approached then the Jacobian has been evaluated incorrectly (Kistler and Scriven [1983]). In the work carried out here, an iteration was terminated when $\left| \alpha^i_{n+1} - \alpha^i_n \right|_{max} < 10^{-10}$

The theory developed so far has not considered free surface flow problems; the additional theory needed to solve them will be discussed in subsequent sections. Nevertheless, the power of Galerkin's method is amply demonstrated in the next section, in which primitive variable solutions are obtained for the 3 creeping flow problems developed in Chapter 2.

4.3   The Solution of Cavity-Driven Flows

4.3.1   Flow in a Lid-Driven Cavity

The flow in a lid-driven cavity is of exactly the same form as the hypothetical problem used in §§4.2.2 to illustrate Galerkin's weighted residual method. It provides a suitable initial test problem when developing a fluid mechanics code because the boundary conditions are simple, the liquid domain is a regular shape, and there are no free surfaces to complicate the analysis. The problem is non-dimensionalised as in §2.3, leading to the dimensionless boundary value problem shown earlier in Figure 2.2 (b); note that the essential boundary conditions on liquid velocity, in terms of the primitive variables, are shown in brackets. They are imposed by the technique described in §§4.2.3. Once again the Reynolds number, $Re = \rho U D / \eta$, is assumed to be so small that inertia effects are negligible. In this section, solutions for this creeping flow problem are only presented for the special case of a square cavity.

The iterative procedure begins from a start-up approximation in which only the (known) liquid velocities at the boundaries are imposed. All other unspecified freedoms, namely the liquid velocities at internal nodes and every pressure freedom, are initialised to zero. In §2.3 we learned that it is important to check the accuracy of any F.E. solution since its accuracy depends on the degree of refinement of the computational grid and also the numerical integration schemes chosen. For this reason primitive variable solutions to this problem are obtained using every combination of the 3 grids shown in Figure 2.3 and quadrature schemes (A)-(D) for area integrals shown in Figure B.6. In the numerical results presented here, the F.E. equations (4.31) are solved by the same 'banded-matrix' solver as was used earlier in Chapter 2. Once again changing the number of quadrature points had only a minor effect on the execution time of an iteration: results obtained using grids (a) and (c) taking approximately 70 c.p.u. seconds, whereas those employing grid (b) took 110 c.p.u. seconds. In all cases, converged solutions from the start-up approximation were obtained in 3 iterations.

Table 4.1 shows (a) horizontal components of liquid velocity on the vertical centreline $x = 0.0$, (b) vertical components of liquid velocity on the horizontal centreline $y = 1.0$ obtained from (i) the semi-analytical solution (2.11) truncated after 20 and 40 terms, (ii) primitive variable F.E. results using grid (a) of Figure 2.3 and schemes (A) and (D) of Figure B.6. Results from schemes (B) and (C) are not shown as they agree with those of scheme (A) to the sixth decimal place. It may be seen that results obtained from the semi-analytical solution converge to 3 decimal places after 20 terms are taken and are in good agreement with primitive variable results obtained using all four quadrature schemes. Table 4.2 compares primitive variable F.E. results (obtained using grid (b) of Figure 2.3 and scheme (A)) with semi-analytical results derived from the series (2.11), truncated after 40 terms. The agreement is good, but not appreciably better than with those obtained using grid (a), thereby suggesting that grid (a) of Figure 2.3 is sufficiently refined for the present application.

In the results presented so far, we have chosen to compare the velocities generated in primitive variable F.E. solutions with those obtained analytically by representing them in tabular form. In most instances, however, it is far more convenient to represent

velocities as a set of velocity 'vectors' whose sizes are proportional to the magnitude of, and directions parallel to, the velocity at the arrow's tail. Figure 4.3 shows velocity vectors (i) from a primitive variable solution using grid (b) and scheme (A), (ii) derived from the semi-analytical solution (2.11), truncated after 40 terms. This velocity vectors representation of the results immediately emphasizes their close agreement since they are visually indistinguishable. The velocity vectors representation is used extensively in the remainder of this thesis.

Finally, when the asymmetric grid (c) of Figure 2.3 is used, a slight asymmetry in the numerical solutions is observed. Nevertheless, these results are still in good agreement with liquid velocities derived from the analytical solution (2.11).

4.3.2 Flow in an Open, Driven Cavity

In this section the Galerkin F.E. method is extended to solve Canedo and Denson's [1989] model of flow in an open pool of a Newtonian, incompressible liquid generated by a slowly moving side wall. The problem is non-dimensionalised as in §2.4 with the result that it reduces to the dimensionless boundary value problem shown in Figure 2.8 in which $Re = \rho\, U\, L/\eta$. The only case considered here is that of creeping flow ($Re = 0$) in a square cavity with $A^* = 1.0$.

At the bottom and side walls, the liquid velocity is known; these are essential conditions and are imposed in the usual way (described in §§4.2.3). At the planar liquid-air interface, however, there are two different conditions: $v = 0$ and the zero shear stress condition $\partial u/\partial y = 0$. The former is an essential condition on the vertical component of liquid velocity, hence the y-components of those momentum residuals (4.15) associated with upper boundary nodes can be discarded. The latter is different, it is not an essential condition. In this case it is necessary to evaluate $(R_M^k)_{x,\partial\Omega}$, the contributions to the x-components of those momentum residuals (4.15) associated with upper boundary nodes due the boundary $\partial\Omega$.

Since $\underline{u}.\underline{n} = 0$ on all boundaries, $(\underline{R}_M^k)_{\partial\Omega}$ may be simplified to

$$(\underline{R}_M^k)_{\partial\Omega} = -\int_{\partial\Omega} N_k\, \underline{n}.\underline{\underline{\sigma}}\, ds \qquad (4.34)$$

From equation (2.12) we see that $\underline{n}.\underline{\underline{\sigma}}$ represents the dimensionless stress exerted on a boundary due to the liquid motion, hence at the upper boundary nodes the zero shear stress condition may be interpreted as $(\underline{n}.\underline{\underline{\sigma}})_x = 0$. Consequently, from equation (4.34), the x-component of $(R_M^k)_{\partial\Omega}$ is equal to zero for those nodes on the upper boundary. Hence the only non-zero contribution to the x-components of momentum residuals associated with upper boundary nodes is that due to the domain, i.e. $(R_M^k)_\Omega$. When this residual is included into the equation set (4.31), the Newton iteration can begin.

In view of the close agreement between analytical and numerical solutions observed in §§4.3.1, the numerical solution presented here is obtained using quadrature scheme (A) of Figure B.6 for area integrals and grid (a) of Figure 2.10. The iteration is begun using an initial estimate in which only the essential conditions are imposed, all other velocity and pressure freedoms being initialised to zero. The F.E. equations (4.31) are again solved by the NAg F.E. 'banded-matrix' solver. A converged solution is obtained from the start-up approximation in 3 iterations, each iteration having an execution time of approximately 70 c.p.u. seconds. ..

Table 4.3 shows a comparison between (a) horizontal components of liquid velocity on the vertical centreline $x = 0.5$, (b) vertical components of liquid velocity on the horizontal centreline $y = -0.5$ obtained from (i) the semi-analytical solution (2.19) with 20 terms in the series, (ii) the primitive variable F.E. solution of this problem. The agreement between them is very good. Velocity vectors from the two solutions are plotted in Figure 4.4, once again they are indistinguishable from one another.

4.3.3　The Zero Flux Model of Meniscus Roll Coating

In this section Galerkin F.E. solutions of the Zero Flux Model of meniscus roll coating are compared with those obtained analytically from equation (2.23). The problem is non-dimensionalised as in §2.5 with the result that it reduces to the boundary value problem shown in Figure 2.12. The only cases considered here are those for a cavity in which the lid speeds V_1, V_2 are so small that the creeping flow approximation is valid.

The boundary conditions on the lids are essential conditions on the liquid velocity and are imposed in the usual way. The conditions on the vertical liquid-air interfaces

are similar to those given in §§4.3.2, namely $u = 0$ and the zero shear stress condition $\partial v/\partial x = 0$. The former is an essential condition on the horizontal component of liquid velocity, imposed by discarding the x-components of those momentum residuals (4.15) associated with nodes on the side walls. In this problem the zero shear stress condition can be interpreted as $(\underline{n}.\underline{\sigma})_y = 0$ on the side walls and is imposed by a method exactly analogous to the one described in §§4.3.2. This means that the only non-zero contribution to the y-components of those momentum residuals (4.15) associated with side wall nodes is that due to the the domain Ω, i.e. $(R_M^k)_y = (R_M^k)_{y,\Omega}$ This completes the equation set (4.31) for this problem.

The Galerkin F.E. results presented here refer to the cases of a cavity with $H^* = 0.5$ and $S = 1$, 2. They are obtained using quadrature scheme (A) for area integrals and grid (a) of Figure 2.14 as the computational mesh. The problem is initialised and solved as for the previous two flows. A converged solution was reached in 3 iterations, each taking approximately 80 c.p.u. seconds.

Liquid velocities, derived from the analytical solution (2.23) truncated after 40 terms, are compared with those obtained by the Galerkin F.E. method in Table 4.4. The solutions agree well in both the $S = 1$ and $S = 2$ cases. Velocity vectors from both solutions are plotted out in Figure 4.5. Although the flow fields are not as clear as they are in Figures 4.3, 4.4, close inspection reveals that the analytically- and numerically-generated flow fields are indistinguishable from one another.

4.4   The Slot Coater

4.4.1   Introduction

In the above sections, we have shown how Galerkin's weighted residual method can be used to solve simple flows in rectangular geometries with straightforward boundary conditions. In the remainder of this chapter, we describe the special techniques needed to enable the method to be extended to (i) incorporate the 3 free surface boundary conditions (see §4.1) and (ii) represent the variable free surface locations mathematically, as is required in the solution of more complicated viscous free surface flow problems.

In the present section these techniques are illustrated by applying them to the solution of a relatively simple free surface flow, that of the 'slot coater'.

The slot coater has been studied by many authors, see for example Coyne and Elrod [1970, 1971], Saito and Scriven [1981] and Carter [1985]. The geometry of this process, shown in Figure 1.20, consists of a flat substrate (the web) moving with constant velocity U_{web} from a slot of constant width H. The upper edge of the slot consists of a rigid wall terminating at the point $X = 0$, $Y = H$. Liquid moves under pressure in the slot and separates from the upper edge, relaxing far downstream to uniform 'plug' flow. The problem is non-dimensionalised by introducing the following dimensionless quantities

$$u = U/U_{web} \quad , \quad v = V/U_{web} \quad , \quad p = HP/\eta U_{web} \qquad (4.35)$$

$$q = Q/U_{web}H \quad , \quad x = X/H \quad , \quad y = Y/H \qquad (4.36)$$

where Q is the actual flux through the slot. The dimensionless boundary conditions used here follow those given by Carter [1985, pp 113-116] in his study of slot coating. Referring to Figure 1.20 these are

At Inflow ($x \rightarrow \infty, 0 \leq y \leq 1$)

$$u = g(y) \quad , \quad v = 0 \qquad (4.37)$$

where $g(y)$ represents fully developed Poiseuille-Couette flow subject to the no-slip conditions at the web and upper edge, namely

$$g(0) = -1 \quad , g(1) = 0 \qquad (4.38)$$

Since the dimensionless flux, q, is given by

$$q = -\int_0^1 g(y)\, dy \qquad (4.39)$$

the inflow conditions may be rewritten as

$$u = g(y) = (6q - 4)(y^2 - y) + y^2 - 1 \quad , v = 0 \qquad (4.40)$$

At Outflow ($x \rightarrow -\infty, 0 \leq y \leq h^\infty$)

$$u = -1 \quad , \quad v = 0 \qquad (4.41)$$

where $h^\infty = q$, the so-called 'plug' flow conditions far downstream.

At the Upper Wall ($y = 1$, $x \geq 0$)

$$u = 0 \;,\; v = 0 \qquad (4.42)$$

On the Web ($y = 0$)

$$u = -1 \;,\; v = 0 \qquad (4.43)$$

The above boundary conditions are all essential conditions on the liquid velocity and are imposed in (4.31) by the usual method; the free surface boundary conditions are, however, quite different.

4.4.2 Incorporation of Free Surface Stress Conditions into the Galerkin Equations

In §4.1 we saw that in a steady free surface flow there are three conditions to be satisfied at the unknown free surface location. The kinematic condition, $\underline{u}.\underline{n} = 0$, which expresses the fact that there should be no flux of liquid across a steady free surface, is discussed in greater detail in the following section. Instead we focus attention here on the two remaining conditions which stipulate that the normal and tangential stresses must balance.

In the usual situation where the free surface represents a liquid-air interface, the fact that air has a viscosity which is negligible compared to that of most liquids means that the tangential stresses at the free surface must also be negligible (see equation (2.15)). In this case the normal *and* tangential stress balance may be expressed via the single vector relation (Kistler and Scriven [1983])

$$\underline{n}.\underline{\underline{\sigma}} = \frac{1}{Ca} \frac{\underline{n}}{r_{curv}} - \underline{n}\, p_a \qquad (4.44)$$

where $Ca = \eta U / T$ (U is a suitable velocity scale for the flow) is the dimensionless Capillary number measuring the relative importance of viscous to surface tension stresses; p_a the dimensionless ambient air pressure; $\underline{n}$ the outward pointing (with respect to the liquid) unit normal; and r_{curv} the dimensionless radius of curvature of the free surface.

Ruschak [1980] demonstrated that by combining the useful result that

$$\frac{d\underline{t}}{ds} = \frac{\underline{n}}{r_{curv}} \tag{4.45}$$

where $\underline{t}$ is the unit tangent vector pointing in the direction of increasing arc length, s, along the free surface, with a measurement of pressures relative to the ambient pressure achieved by the transformation $p \to p - p_a$, it is possible to rewrite the stress balance (4.44) in the following computationally convenient form

$$\underline{n}.\underline{\underline{\sigma}} = \frac{1}{Ca} \frac{d\underline{t}}{ds} \tag{4.46}$$

This result is extremely important since it enables the contributions to the momentum residuals (4.15) due to the free surface, $(\underline{R}_M^k)_{f.s.}$, to be evaluated where

$$(\underline{R}_M^k)_{f.s.} = -\int_{f.s.} N_k \underline{n}.(-Re\ \underline{u}\underline{u} + \underline{\underline{\sigma}})\ ds \tag{4.47}$$

Now using the kinematic condition, $\underline{n}.\underline{u} = 0$, and (4.46) yields

$$(\underline{R}_M^k)_{f.s.} = -\frac{1}{Ca} \int_{f.s.} N_k \frac{d\underline{t}}{ds}\ ds \tag{4.48}$$

which may be integrated by parts (Ruschak [1980]) to give

$$(\underline{R}_M^k)_{f.s.} = \frac{1}{Ca} \int_{f.s.} \underline{t}\ \frac{dN_k}{ds}\ ds - \frac{1}{Ca}\ [N_k\ \underline{t}_1 - N_k\ \underline{t}_0] \tag{4.49}$$

where $\underline{t}_0$ and $\underline{t}_1$ are the unit tangent vectors to the beginning and end of the free surface respectively. Note that although boundary integrals are usually taken in an anticlockwise sense, in practice it is possible to choose the arc length s to increase in either an anticlockwise *or* a clockwise sense, provided that one is consistent in taking $\underline{t}$ to be in the same direction.

Any numerical simulation of a free surface flow problem requires the specification of a mathematical relationship between the free surface position and a set of 'free surface parameters', whose values determine its actual location (e.g. in order to determine $\underline{t}$ and s in equation (4.49)). The precise form of this relationship, of course, depends on the mathematical representation chosen. In this thesis free surfaces are represented by Kistler's [1983] 'Spine Method', the main features of which are described in the next section.

4.4.3 Free Surface Representation: The Spine Method

The basic idea of the Spine Method is to parametrise a free surface by its location along a series of conveniently placed, independent spines. In the spinal representation of the slot coater shown in Figure 4.6, each spine is defined by a fixed base point $\underline{x}_B^i$ and a fixed direction vector $\underline{e}_i$. In this representation the 'free surface parameters' are the spinal distances $\{h_i\}$ along each spine between its base and free surface nodes.

Since the free surface location is not known *a priori*, the spine distances (called 'heights' h_i) become additional unknown coefficients which have to be determined. As a result the vector of F.E. coefficients $\underline{\alpha}$ defined in (4.28) must be expanded to include the free surface parameters $\{h_i\}$; hence for the slot coater $\underline{\alpha}^T = [\underline{u}^T, \underline{v}^T, \underline{p}^T, \underline{h}^T]$ where $\underline{h} = \{h_i\}$. The additional equations needed to determine these spine heights are furnished by weighting the kinematic condition, $\underline{n}.\underline{u} = 0$, which must be satisfied at a free surface, by the shape functions N_k associated with the free surface nodes. These extra equations are given by (Kistler and Scriven [1983] p 262)

$$R_k^f = \int_{f.s.} \dot{N}_k \, \underline{n}.\underline{u} \, ds = 0 \qquad (4.50)$$

which means that in this case the algebraic equation set (4.31) is composed of equations (4.15), (4.27) and (4.50).

The computational grid used in this section is similar to those used by Saito and Scriven [1981] and Carter [1985]. This grid is shown in Figure 4.7 (where for reasons of clarity it is scaled vertically by a factor of 2) and consists of 90 elements and 215 nodes, 27 of which are free surface nodes. It divides naturally into three regions. In region 3 the position of all nodes is invariant throughout the iteration. In regions 1 and 2 however, i.e. the free surface regions, the triangular elements adjust with the free surface position during the iteration procedure. In region 2, where the curvature of the meniscus is large, the spines pass through a polar origin O outside the liquid; and in region 1 the spines are vertical.

All nodes in regions 1 or 2 lie on a free surface spine. The ith spine is defined by (i) the (fixed) position vector of its base node, $\underline{x}_B^i$, (ii) a unit vector $\underline{e}_i$ specifying its direction. The spine 'height' h_i is the distance along the spine between the base node

and the node which also lies on the free surface, known as a 'free surface node'. On each spine, between its base and free surface nodes, lie other nodes whose distances from the base node are prescribed proportions w_j of its associated spine height h_i. In fact if node k is the jth node on the ith spine, then its position vector $\underline{x}_k$ may be expressed mathematically by the relation

$$\underline{x}_k = \underline{x}_B^i + w_j\,h_i\,\underline{e}_i \tag{4.51}$$

In the grid shown in Figure 4.7, there are 7 nodes on each spine, i.e. including the base and free surface nodes, and the proportions w_j are equal to 0, 1/6, 1/3, 1/2, 2/3, 5/6 and 1. Expression (4.51) directly links the location of the nodes to the positions of the boundaries.

The F.E. equations (4.15), (4.27), (4.50) are solved by Newton iteration. As before, the global Jacobian matrix is assembled from the element-level Jacobians. Since elements in region 3 are unaffected by the free surface shape their element-level Jacobians only contain derivatives with respect to their associated velocity and pressure freedoms. These derivatives are straightforward; they are evaluated as in §4.3 on 'cavity-driven' flows.

However, nodes in regions 1 and 2 move according to equation (4.51) as the free surface parameters $\{h_i\}$ are updated during an iteration. Therefore the element-level Jacobians of elements in regions 1 and 2 must also contain derivatives with respect to the (three) spine heights on which they depend. This is by far the most difficult part of the solution process because residuals depend on $\underline{h}$ not only through the integrands, but also on the limits of integration since Ω is also a function of $\underline{h}$.

It is at this stage that the power of the isoparametric mapping (B.40) is again apparent. The momentum, continuity and kinematic residuals consist of combinations of integrals of the form

$$I(\underline{\beta},\underline{h}) = \int_{A(\underline{h})} F(\underline{x},\underline{\beta},\underline{h})\,dx\,dy \quad \text{and} \tag{4.52}$$

$$L(\underline{\beta},\underline{h}) = \int_{S(\underline{h})} G(\underline{x},\underline{\beta},\underline{h})\,ds \tag{4.53}$$

where $\underline{\beta}^T = (\underline{u}^T, \underline{v}^T, \underline{p}^T)$ is the vector of F.E. coefficients for the flow field, $A(\underline{h})$ is the liquid domain and $S(\underline{h})$ the boundary. Derivatives of (4.52) with respect to $\underline{h}$ are obtained by noting that (see §B.5)

$$I(\underline{\beta}, \underline{h}) = \sum_{elements} \left\{ \int_{A_0} F(\underline{x}, \underline{\beta}, \underline{h}) \, |\mathcal{J}| \, d\xi d\eta \right\} \qquad (4.54)$$

where $\mathcal{J}$ is the Jacobian of the element-level isoparametric mapping (B.40). This eradicates any dependence of the domain of integration on the spine heights $\{h_i\}$ so

$$\frac{\partial I}{\partial h_i} = \sum_{elements} \int_{A_0} \frac{\partial}{\partial h_i} \left\{ F(\underline{x}, \underline{\beta}, \underline{h}) |\mathcal{J}| \right\} \, d\xi d\eta \qquad (4.55)$$

where the derivatives of the integrand may be obtained analytically.

The practical evaluation of free surface integrals of the form (4.53) and their derivatives with respect to the F.E. coefficients is the subject of the following section.

4.4.4   Evaluation of Free Surface Integrals

In §B.5 a technique, based on the isoparametric mapping (B.40), was described which enables integrals along fluid boundaries to be evaluated in terms of local 'area' co-ordinates. This technique is now extended to evaluate those free surface integrals, i.e. equations (4.49), (4.50), required in Galerkin F.E. solutions of free surface flow problems.

In the slot coating grid shown in Figure 4.7, the free surface is composed of a series of sides of those 'free surface elements' which contain three free surface nodes. One such side and its associated free surface element is shown in Figure 4.8. Suppose that without loss of generality the *global* node numbering scheme is such that the side along the free surface contains local nodes 1, 3 and 6 with respect to the local node numbering scheme shown in Figure 4.2. Then under this assumption if N_i denotes the shape function associated with the ith local node, the area co-ordinate $L_2 = (N_2 = N_4 = N_5) = 0$ along the free surface side. Hence the other (non-zero) area co-ordinates along this side L_1, L_3 satisfy the relation

$$L_1 + L_3 = 1 \qquad (4.56)$$

which means that the non-zero shape functions N_1, N_3, N_6 collapse to quadratic functions of a single, independent area co-ordinate. Now in the slot coating results

presented here, the direction of integration was chosen to be in the downstream direction from the separation point P to the outflow boundary – see Figure 1.20. In this case it is more convenient to parametrise the shape functions in terms of the area co-ordinate L_1 because it increases along the side of the element in the direction of integration. The form of the isoparametric mapping (B.40) means that along the free surface side, the global free surface position is the following simple function of the global co-ordinates (x_1, y_1), (x_6, y_6) and (x_3, y_3) of local nodes 1, 3 and 6 respectively:

$$x = x_1 \, N_1(L_1) + x_6 \, N_6(L_1) + x_3 \, N_3(L_1) \tag{4.57}$$

$$y = y_1 \, N_1(L_1) + y_6 \, N_6(L_1) + y_3 \, N_3(L_1)$$

where (see equation (B.49))

$$N_1 = L_1 \, (2L_1 - 1) \;\;,\;\; N_6 = 4L_1 \, (1 - L_1) \;\;,\;\; N_3 = 1 - 3L_1 + 2L_1^2 \tag{4.58}$$

Equation (4.57) is of crucial importance since it allows the unit tangent vector $\underline{t}$ and unit normal $\underline{n}$ to take on simple and computationally convenient forms

$$\underline{t} = \frac{(dx/dL_1 \, \underline{i} + dy/dL_1 \, \underline{j})}{\sqrt{((dx/dL_1)^2 + (dy/dL_1)^2))}} \tag{4.59}$$

$$\underline{n} = \frac{(-dy/dL_1 \, \underline{i} + dx/dL_1 \, \underline{j})}{\sqrt{((dx/dL_1)^2 + (dy/dL_1)^2))}} \tag{4.60}$$

where dx/dL_1, dy/dL_1 are obtained by simply differentiating (4.57) with respect to L_1 (see also equations (B.52), (B.53)).

To aid the calculation of dN_k/ds in (4.49), we use the result that along the free surface (with parameter L_1) (Kistler and Scriven [1983] p 261)

$$\frac{dN_k}{ds} = \underline{t}.\nabla N_k = \frac{\partial N_k}{\partial L_1} \frac{dL_1}{ds} \tag{4.61}$$

where $ds/dL_1 = \sqrt{\{(dx/dL_1)^2 + (dy/dL_1)^2\}}$. These results enable the free surface stress integrals (4.49) to be calculated since

$$\int_{f.s.} \underline{t} \, \frac{dN_k}{ds} \, ds = \sum_{sides} \int_{L_1=0}^{1} \frac{(dx/dL_1 \, \underline{i} + dy/dL_1 \, \underline{j})}{ds/dL_1} \frac{\partial N_k}{\partial L_1} \, dL_1 \tag{4.62}$$

where the summation is over all sides forming part of the free surface. Moreover, in (4.62) there is no longer a dependence on $\underline{h}$ in the limits of integration; consequently,

derivatives of (4.62) with respect to h_i are also simplified since

$$\frac{\partial}{\partial h_i} \left(\int_{S(\underline{h})} \underline{t} \frac{dN_k}{ds} \, ds \right) = \sum_{sides} \int_{L_1=0}^{1} \frac{\partial}{\partial h_i} \left(\frac{(dx/dL_1 \, \underline{i} \, + \, dy/dL_1 \, \underline{j})}{ds/dL_1} \right) \frac{\partial N_k}{\partial L_1} dL_1$$

(4.63)

Note that the integrand on the right hand side of (4.63) may be evaluated analytically by using the isoparametric mapping (B.40) in conjunction with the spine relation (4.51).

Now for the kinematic residuals. It can be shown that if (u_1, v_1), (u_6, v_6) and (u_3, v_3) are the fluid velocities associated with local nodes 1, 6 and 3 respectively, and (u, v) the fluid velocity at any point of a side forming part of the free surface, then the kimematic residuals (4.50) may be written more conveniently as

$$R_k^f = \int_{S(\underline{h})} N_k \, \underline{n} . \underline{u} \, ds = \sum_{sides} \int_{L_1=0}^{1} N_k(L_1) \left(v \frac{dx}{dL_1} - u \frac{dy}{dL_1} \right) dL_1 \qquad (4.64)$$

where (see equation (4.7))

$$u = u_1 \, N_1(L_1) + u_6 \, N_6(L_1) + u_3 \, N_3(L_1) \qquad (4.65)$$

$$v = v_1 \, N_1(L_1) + v_6 \, N_6(L_1) + v_3 \, N_3(L_1)$$

The right hand side of equation (4.64) is useful because there is no longer a $\underline{h}$ dependence in the limits of integration. As u_i, v_i, h_i are *independent* parameters with $\partial u_j/\partial h_i = \partial v_j/\partial h_i = 0$ for all i and j, derivatives of (4.64) with respect to h_i are given by

$$\frac{\partial}{\partial h_i} \int_{S(\underline{h})} N_k \, \underline{n} . \underline{u} \, ds = \sum_{sides} \int_{L_1=0}^{1} N_k(L_1) \left\{ v \frac{\partial}{\partial h_i} \left(\frac{dx}{dL_1} \right) - u \frac{\partial}{\partial h_i} \left(\frac{dy}{dL_1} \right) \right\} dL_1$$

(4.66)

Similar expressions can also be obtained for derivatives of (4.64) with respect to u_i, v_i:

$$\frac{\partial}{\partial u_i} \int_{S(\underline{h})} N_k \, \underline{n} . \underline{u} \, ds = \sum_{sides} \left\{ - \int_{L_1=0}^{1} N_k \, N_i \frac{dy}{dL_1} \, dL_1 \right\} \qquad (4.67)$$

$$\frac{\partial}{\partial v_i} \int_{S(\underline{h})} N_k \, \underline{n} . \underline{u} \, ds = \sum_{sides} \left\{ \int_{L_1=0}^{1} N_k \, N_i \frac{dx}{dL_1} \, dL_1 \right\} \qquad (4.68)$$

The results of this section show that the free surface integrals (4.49), (4.50) and the derivatives with respect to their associated parameters can be written as a combination of integrals over the region [0,1]. These one-dimensional integrals are also evaluated numerically using Gaussian Quadrature – see §B.6.

4.4.5   Finding an Initial Approximation

The techniques described above allow the full Jacobian matrix (4.32), containing derivatives with respect to the full set of F.E. coefficients $\underline{\alpha}^T = (\underline{\beta}^T, \underline{h}^T)$, to be evaluated. This brings us to the problem of finding a start-up approximation, i.e. an initial approximation $\underline{\alpha}_0$ when no solutions of related cases have previously been calculated. This is far more difficult for a viscous free surface flow than it is for the 'cavity-driven' flows in §4.3, because neither the flow field nor the free surface location is known *a priori*.

The domain of convergence of the Newton iteration procedure, (4.31), from a solution with a given set of parameters (Re, Ca, etc), is a measure of the maximum increment that can be made to any of these parameters before the iteration diverges, i.e. no solution is found. For viscous free surface flows the domain of convergence of Newton iteration generally depends much more on position and shape of the free surfaces than on the flow field within the domain because the non-linearity produced by the free surface(s) is usually much stronger than those due to fluid inertia at modest Reynolds numbers (see Kistler and Scriven [1983] p 278). In practical terms this means that it is important for the start-up approximation $\underline{\alpha}_0$ to have a good initial estimate of the free surface shape, although the domain of convergence from $\underline{\alpha}_0$ can sometimes be enlarged by 'under-relaxing' the iteration process, i.e. by applying only fractions of the updating changes called for by equation (4.31).

In general, the free surface shape would be estimated from experimental observations; however, in slot coating it is fortunate that published free surface profiles already exist (e.g. those of Saito and Scriven [1981], Carter [1985]). In this study the first solution to slot coating was obtained by approximating the grid to the solution given in Carter [1985] for the case of $Re = 0.0$, $Ca = 0.4$, $q = 0.25$

Once the first converged solution is obtained the calculation of related solutions for nearby parameter values or boundary configurations is much easier. This is achieved by zero order continuation, i.e. using the solution for one set of parameters in order to begin Newton iteration for a not-too-dissimilar set of parameters.

4.4.6 Results and Discussion

All the slot coating results presented here have been obtained using the F.E. grid shown in Figure 4.7 in which (following Carter [1985]) the polar origin O, used to define the tessellation of region 2, is placed at (-0.5, 1.0). Changing the number of quadrature points (see below) had only a minor effect on the execution time required for an iteration, each iteration taking approximately 20 c.p.u. seconds. During each iteration the Galerkin F.E. equations (4.31) were solved by the NAg F.E. 'banded-matrix' solver; most converged solutions were obtained in 4 or 5 iterations.

Before accepting any results there are three key issues to be addressed. The first of these is the effect on the solution of the Gaussian quadrature scheme chosen to evaluate the free surface integrals. Converged solutions were obtained for parameters set to $Re = 0.0$, $Ca = 0.4$, $q = 0.25$ in which the area integrals were evaluated using the 4 point quadrature scheme (A) and the free surface integrals using each of the 2-, 3-, 4- point quadrature formulae, i.e. schemes (a), (b), (c) respectively of Appendix B, for one-dimensional integrals. Computed results show that in changing from a 2- to the 3- point scheme, the maximum change in any coefficient was less than 1% ; whereas in changing from a 3- to the 4- point scheme, the maximum change was less than 0.01%. In both cases there was no discernible change to the free surface profiles.

The second issue relates to the evaluation of the area integrals. Converged solutions for $Re = 0.0, Ca = 0.4, q = 0.25$ were obtained by using the 3 point scheme (b) for free surface integrals and each of the four quadrature schemes (A), (B), (C), (D) for area integrals described in Appendix B. The computed results showed that in changing (i) scheme (A) → (B), (ii) (A) → (C), the maximum change in any coefficient was less than 1%, 0.3% respectively, both of which had no appreciable effect on the free surface profile obtained. However when scheme (D) (with one negative weight) was used, no converged solution to this problem could be found. This is contrary to what might be expected, given the good agreement between analytical and numerical results (using scheme (D)) reported in §§4.3.1, but it suggests that rounding errors incurred when scheme (D) is used (see §2.3) are exacerbated by the presence of a free surface. Given

the above results it was decided to calculate all subsequent numerical solutions using the 4 point scheme (A) for area integrals and the 3 point scheme (b) for free surface integrals.

Returning to the boundary conditions for the slot coater, the inflow and outflow conditions are, in theory, applied at an infinite distance upstream/ downstream of the separation point P respectively. In practice, of course, they are imposed at a finite distance from P. It is, therefore, very important to check the sensitivity of computed solutions to the positions of the inflow/ outflow boundaries. An initial investigation confirmed Carter's [1985] observation that the results are not sensitive to the upstream end of the grid but that the length of the grid in the downstream direction is important. A grid extending over $-16 < x < 1$ was found to be adequate for the range of parameter values considered here.

Figure 4.9 shows velocity vectors and free surface profiles for a flow with $Re = 0.0$, $Ca = 0.4$, $q = 0.25$ obtained (a) in this work (b) in Carter [1985]. The free surface profiles are in very good agreement. Carter's results were, however, obtained using a variational method limited to the creeping flow case, unlike those of Saito and Scriven [1981] which were obtained using a version of Galerkin's method of weighted residuals similar to that described here, but with quadrilateral as opposed to triangular elements. For this reason it was deemed more appropriate to compare the results of this work with those of Saito and Scriven [1981]. Figure 4.10 shows the dependence of free surface profiles on the Capillary number for the case of $Re = 0.0$, $q = 0.25$ for (a) this work, (b) Saito and Scriven [1981]. These profiles are in excellent agreement in all cases; the effect of increasing Ca is to make the free surface recede into the gap.

An appealing feature of the Galerkin F.E. method is that it is capable of solving the full Navier-Stokes equations with fluid inertia, i.e. at non-zero Reynolds number. Figure 4.11 shows a comparison between velocity vectors obtained in this section and those predicted by Saito and Scriven [1981] for slot coaters with (a) $Re = 50$, $Ca = 0.125$, $q = 0.13$, (b) $Re = 50$, $Ca = 0.125$, $q = 0.25$; excellent agreement is obtained in both cases. Figure 4.12 investigates the effect of changing the liquid flux in slot coating, with $Re = 50$ and $Ca = 0.125$ constant. Once again, the results from this

work are in excellent agreement with those of Saito and Scriven in all cases. They show that decreasing q has the effect of increasing the free surface curvature, until the free surface profile eventually recedes past the separation point P and into the gap.

In all the computed solutions presented here, the contact angle between the free surface and upper plate at P is determined as part of the solution. Michael [1958] studied the problem of the separation of a viscous free surface at a straight edge and from his analysis he concluded that for the viscous stress to be bounded at the point of separation, the contact angle $\alpha = 180^o$. The 'apparent' contact angle, i.e. the contact angle observed macroscopically, does not satisfy this condition in any of the computed solutions. Kelmanson [1983] postulated that the contact angle changes rapidly from 180° to the observed value over a small distance δ say. However this hypothesis defies intuition when the meniscus recedes past the separation point P and into the nip (see e.g. Figure 4.11, case (a)). A recent analysis by Savage [1992] predicts 2 possible contact angles, namely $\alpha = 0^o$ and $\alpha = 180^o$, of which the former is more sensible when the meniscus recedes into the slot. Unfortunately, a more detailed understanding of the separation process is required before a satisfactory study of the region can be completed.

Despite all the complications described above, slot coating is a simple example of a coating flow because there is no flux splitting, dynamic wetting lines or awkward geometry in which the solution is to be found. Fully-flooded roll coating is more difficult to analyse and is considered next.

4.5   The Symmetric, Fully-Flooded, Forward Roll Coater

4.5.1   Introduction

In the previous section we obtained numerical solutions of the slot coating problem, which are in excellent agreement with previously published solutions, by incorporating the 'spinal' free surface representation into a generalised version of Galerkin's weighted residual F.E. method. However, as the raison d'etre of the present chapter is to establish the expertise needed to develop a numerical model for meniscus roll coating which

includes the effects of curved meniscii, it is now necessary to tackle the more challenging roll coating problem.

Owing to its relative simplicity, we consider the symmetric, fully-flooded, forward case first. As we shall see, the problem of representing the free surface is complicated, even in this relatively simple case, by the sensitivity of the downstream free surface location to the values of the operating parameters, and particularly to that of the capillary number. In such situations, Coyle et al [1986] showed that the key to resolving this difficulty lies in the adoption of a mesh generation algorithm in which *all* elements depend on the free surface location.

In the present section we obtain numerical solutions of Coyle et al's [1986] model for the symmetric situation by extending the slot coating code, developed above, to include a mesh generation algorithm similar to those described by Coyle et al [1986]. The salient features of their model and mesh generation algorithm are described in detail in the next section.

4.5.2 Coyle et al's [1986] Model

In the symmetric case, the rollers are of equal radii and move with equal speeds in the same direction through the nip. In their F.E. analysis of this situation, Coyle et al introduced dimensionless variables defined by

$$x = X/\sqrt{(RH_0)} \ , \ y = Y/\sqrt{(RH_0)} \ , \ p = P\sqrt{(RH_0)}/\eta \tilde{V} \qquad (4.69)$$

$$u = U/\tilde{V} \ , \ v = V/\tilde{V} \qquad (4.70)$$

where (X, Y), (U, V), P, $\tilde{V}$, R, H_0 are the global co-ordinates, global liquid velocities, liquid pressure, speed of each roller, roller radius, and semi-nip width respectively. Since the problem is symmetric, it is possible to reduce the cost of computations by restricting attention to the flow in the lower half of the domain, i.e. between the symmetry plane and lower roller. The boundary conditions for this 'half-problem', which are shown in Figure 4.13, are discussed below.

(i) On the Symmetry Plane

Both the vertical component of liquid velocity and the shear stress will vanish,

$$v = 0 \ , \ (\underline{n}.\underline{\sigma})_x = 0 \tag{4.71}$$

The first condition is an essential boundary condition and is imposed in the usual way; the zero shear stress condition is imposed by the method described in §§4.3.2, 4.3.3.

(ii) At the Roller Surface

The no-slip condition yields an essential condition on liquid velocity: $\underline{u} = \underline{t}$ where $\underline{t}$ is the unit vector tangential to the roller surface.

(iii) At the Free Surface

The usual kinematic and stress boundary conditions are imposed by the techniques described in §§4.4.2, 4.4.3.

(iv) At the Outflow Boundary

In slot coating, the flux was imposed as a parameter. Fully-flooded roll coating is different since the flux through the nip has to be determined as part of the solution. In such cases Kistler and Scriven [1983] found that the imposition of a uniform 'plug' flow condition at outlet could lead to conflicts with overall mass and momentum conservation, unless the outflow boundary is placed far downstream. Unfortunately, this course of action can lead to computational costs becoming excessive. Kistler and Scriven [1984] and Coyle et al [1986] found that a suitable alternative is to use the 'no-traction' condition, $\underline{n}.\underline{\sigma} = \underline{0}$, at the outflow boundary. They found that this condition, which may be interpreted physically as specifying that there should be no diffusive momentum flux in the streamwise direction (Kistler and Scriven [1984]), may be applied closer to the main body of the flow without appreciable loss of accuracy. Indeed this is borne out by the author's own experience.

The no-traction condition is imposed by deleting the term $\int_{\partial\Omega} N_k \, \underline{n}.\underline{\sigma}ds$ from the momentum residuals (4.15) associated with the nodes on the outflow boundary (see equation (4.47)). As a result the boundary term at these nodes is simply given by $\int_{\partial\Omega} N_k \, Re(\underline{u}.\underline{n})\underline{u}ds$, which is non-zero in general since $\underline{u}.\underline{n} \neq 0$ at an outflow boundary.

(v) At the Nip

In §1.2 we noted that the lubrication approximation provides an accurate description of the flow in the nip region during fully-flooded forward roll coating, see e.g. Greener and Middleman [1975], Savage [1992]. Coyle et al [1986] used this fact to derive boundary conditions at the nip which enable the computational domain to be reduced further; their analysis is summarized below.

If the dimensionless co-ordinates (x, y) are chosen so that $y = 0$ on the symmetry plane and $x = 0$ at the nip, it is both valid and convenient to approximate the dimensionless half-gap width, $h(x)$, by a 'parabolic approximation'

$$y = -h(x) = -\left(\frac{H_0}{R}\right)^{\frac{1}{2}} \left(1 + \frac{x^2}{2}\right) \tag{4.72}$$

Moreover by introducing transformed spatial co-ordinates θ, η, a modified dimensionless pressure, p^*, and the dimensionless flux λ where

$$\theta = \tan^{-1}(x/\sqrt{2}) \quad , \quad \eta = \frac{y + h(x)}{h(x)} \tag{4.73}$$

$$p^* = p\frac{H_0}{R} \quad , \quad \lambda = \frac{Q}{2\bar{V}H_0} \tag{4.74}$$

it may be shown that, in the limit of the lubrication approximation, the balance of x-momentum reduces to

$$\frac{\partial^2 u}{\partial \eta^2} = \left(1 + \frac{x^2}{2}\right)^2 \frac{\partial p^*}{\partial x} \tag{4.75}$$

Now, the no-slip condition at the roller surfaces gives $u(\eta = 2) = u(\eta = 0) = 1$, so integrating (4.75) twice with respect to η gives

$$u = \frac{1}{2}\left(1 + \frac{x^2}{2}\right)^2 \frac{\partial p^*}{\partial x}(\eta^2 - 2\eta) + 1 \tag{4.76}$$

When this velocity profile is substituted into the following rearranged expression for the dimensionless flux

$$\lambda = \left(1 + \frac{x^2}{2}\right) \int_0^1 u \, d\eta \tag{4.77}$$

we obtain

$$\frac{\partial p^*}{\partial x} = \frac{3}{(1 + x^2/2)^3}\left[1 + x^2/2 - \lambda\right] \tag{4.78}$$

At this stage of the analysis, it is convenient to re-express (4.76) and (4.78) in terms of θ, the transformed x co-ordinate, which yields

$$u = \frac{3}{2}(1 - \lambda \cos^2 \theta)(\eta^2 - 2\eta) + 1 \tag{4.79}$$

$$\frac{dp^*}{d\theta} = 3\sqrt{2}(\cos^2 \theta - \lambda \cos^4 \theta) \tag{4.80}$$

In fully-flooded forward roll coating, it is usual to assume that the pressure in the liquid decays to atmospheric far upstream of the nip, i.e. $p^*(-\frac{\pi}{2}) = 0$, so integrating (4.80) subject to this condition yields

$$p^*/3\sqrt{2} = -\frac{\lambda}{4}\sin\theta\cos^3\theta + \left(1 - \frac{3\lambda}{4}\right)\left(\frac{\theta}{2} + \frac{\sin 2\theta}{4} + \frac{\pi}{4}\right) \tag{4.81}$$

Hence, at the nip ($\theta = 0$)

$$p^* = \frac{3\sqrt{2}}{4}\pi\left(1 - \frac{3\lambda}{4}\right) \tag{4.82}$$

Therefore the boundary conditions at the nip in terms of the F.E. variables are

$$u = \frac{3}{2}(1 - \lambda)(\eta^2 - 2\eta) + 1 \tag{4.83}$$

$$v = 0 \tag{4.84}$$

$$p = \frac{3\sqrt{2}\pi}{4}\frac{R}{H_0}\left(1 - \frac{3\lambda}{4}\right) \tag{4.85}$$

Expressions (4.83), (4.84) are essential conditions on the liquid velocity and are imposed in the usual way. Condition (4.85) is different, its implementation will be discussed later.

(vi) At the Symmetry Line P

The symmetry of the problem means that at the symmetry line P, formed where the symmetry plane meets the downstream free surface, the following conditions apply: (i) the liquid velocity is zero, i.e. P is a stagnation line, (ii) the free surface slope is vertical. The former are essential conditions on the liquid velocity, $u = v = 0$, and are imposed in the usual way, whereas the latter condition is different. In practice it is imposed in the form $\underline{i}.\underline{t} = 0$, where $\underline{i}$ is the unit horizontal vector and $\underline{t}$ is the unit tangent vector to the free surface at P, calculated in terms of those F.E. variables which specify the position of the downstream free surface (see next section).

4.5.3 The Computational Mesh For the Symmetric Forward Roll Coater

The task of choosing a mesh generation algorithm for the forward roll coater is complicated by the fact that the (downstream) free surface location is much more sensitive to variations in the operating parameters (particularly the capillary number Ca) than in the slot coater. This characteristic means that if a spinal free surface representation similar to the one employed in §§4.4.3 for the slot coater, with fixed base points $\underline{x}_B^i$ and direction vectors $\underline{e}_i$, is used to represent the downstream free surface of a forward roll coater, elements within the grid may become distorted from their triangular shape when the operating parameters are varied. It is important to avoid element distortion, if possible, because it can have a seriously detrimental effect on a numerical solution's accuracy (see later, §§4.5.5). Since, in the author's opinion, there is inadequate coverage of the practical problems caused by meshing a forward roll coater in the literature, we devote this section to a detailed description of a mesh generation algorithm which can limit element distortion in forward roll coating. The mesh generation algorithm described here forms the basis of the F.E. grids used in all the solutions which remain to be presented in this thesis.

The first solution to symmetric forward roll coating which was attempted here (for a flow with parameters $Re = 0.0, Ca = 0.1, R/H_0 = 100$) employed the tessellation shown in Figure 4.14; it consists of 102 elements, 245 nodes with 21 spines and 21 free surface nodes. Spine 1 is horizontal and lies on the plane of symmetry between the base line XM and the symmetry line P. In practice it is more convenient to parametrise the film-split location P in terms of the position of the line XM (whose x co-ordinate is X_m) rather than with the value of h_1, the spine height associated with spine 1. This means that the value of h_1 is fixed and X_m is the film-split location parameter which needs to be determined instead.

The grid is split up into two regions: regions 1 and 2 consist of all nodes upstream and downstream of the base line XM respectively. Element distortion in region 1 is alleviated by defining the x co-ordinates of all nodes in this region to be fixed frac-

tions of the (current) value of X_m. This prescription results in the elements in region 1 undergoing a 'concertina'-type motion as the value of X_m changes throughout an iteration. This is illustrated in Figure 4.14, in which there is a series of 14 vertical lines upstream of XM on each of which lie 7 nodes evenly distributed between the symmetry plane and the bottom roller. For reasons of clarity, the positions of the vertical lines are represented below the roller surface.

In region 2 the positions of all nodes are parametrised by the base line XM and a series of free surface spines $\{h_i\}$. As in regions 1 and 2 of the slot coater (see Figure 4.7), each node lies on a free surface spine defined by the position of its base node $\underline{x}_B^i$ and a direction vector $\underline{e}_i$; once again h_i represents the distance along the ith spine between its base and free surface nodes. There are a total of 7 nodes, i.e. including the base and free surface nodes, on each spine whose distances along the spine from the base nodes are prescribed proportions w_j of h_i; in this thesis $w_j = 0, 1/6, 1/3, 1/2, 2/3, 5/6$ and 1.

The first 7 spines have their base points evenly distributed along XM between the symmetry plane and the roller surface. Their direction vectors are parallel to lines drawn from their base points to a polar origin O which lies on the plane of symmetry outside the liquid. The x co-ordinate of O is chosen to be a fixed increment from X_m, with the result that its position also changes throughout the iteration; the actual increment used has to be specified in the mesh generation algorithm (see later). The remaining spines, in this case spines 8 to 21, have their base points on the lower roller at positions whose x co-ordinates are fixed increments of the current value of X_m; the values of these increments also need to be specified in the algorithm. In subsequent sections, it will be seen that the choice of direction vectors for these spines is the most troublesome feature of the discretisation. At present this can only be done by empirical means, the best guide being visual observation, and must be tailored to the particular problem of interest.

There are many differences between this grid and the one used in slot coating; they are (i) the positions of the base nodes and direction vectors of free surface spines are functions of X_m and change during an iteration; (ii) all elements depend on the free

surface position; (iii) the only nodes whose positions are fixed are those at the nip, all the others are functions of X_m.

An initial estimate for the first solution attempted here (for the parameter set $Re = 0.0$, $Ca = 0.1$, $R/H_0 = 100$) was obtained by matching the free surface profile to a solution published by Coyle et al [1982] for the same set of parameters. After visual observation it was decided to use the grid shown in Figure 4.14, in which the parameters for the mesh generation algorithm described above should be as follows:

(i) the x co-ordinate of the 14 vertical lines of nodes upstream of XM are located at FRAC(I)$\times X_m$, where FRAC(I)= 0, 1/14, 1/7, 3/14, 2/7, 5/14, 3/7, 1/2, 4/7, 9/14, 5/7, 11/14, 6/7 and 13/14.

(ii) the x co-ordinates of the base nodes of spines 8 to 21 are at X_m+XINC(I), where XINC(I)=0.05, 0.1, 0.15, 0.2, 0.25, 0.3, 0.375, 0.45, 0.525, 0.6, 0.8, 1.0, 1.2 and 1.4

(iii) h_1, the distance between XM and P, should be fixed and equal to 0.4.

(iv) the distance between XM and the polar origin O is set equal to 1.0

(v) spines 8 to 17 are made to pass through the polar origin O, and spines 18 to 21 are made normal to the roller surface.

The specification of (i)-(v) completes the mesh generation algorithm for the grid shown in Figure 4.14. All the grids subsequently used to solve symmetric forward roll coating are based on this tessellation; the only differences being in (i) the number of vertical lines of nodes upstream of XM (and consequently the values of FRAC(I)); (ii) the number of free surface spines; (iii) the values of XINC(I) and the directions of their associated spines.

The equation set for the symmetric forward roll coater is slightly different from that obtained for the slot coater since the film-split location and dimensionless flux must also be determined. The kinematic residual associated with P would normally provide the equation needed to determine X_m (which has replaced h_1 as the film-split location parameter); however, in this case the kinematic condition, $\underline{u}.\underline{n} = 0$, is automatically

satisfied at P since it is a stagnation point. Hence another equation is needed to replace this kinematic residual. This extra equation is provided by the symmetry of the problem which implies that the free surface must be vertical at the symmetry line P. Hence

$$\underline{i}.\underline{t} = 0 \quad \text{at P} \tag{4.86}$$

where $\underline{i}$ is the unit horizontal vector and $\underline{t}$ is the unit vector which is tangential to the free surface at P. In the mesh generation algorithm described here, $\underline{t}$ is a function of the film-split parameter X_m and the 3 spines associated with the element shown in Figure 4.15, i.e. h_1, h_2 and h_3. This enables (4.86) to be rewritten in the form of a residual, $R_{symmetry}(X_m, h_1, h_2, h_3) = 0$, as is required in Galerkin's F.E. method.

One more equation is needed to enable the dimensionless flux λ to be evaluated. This is provided by the lubrication theory nip pressure condition (4.85). Following Coyle et al [1986] this is modified to

$$\bar{p} = \frac{3}{4}\sqrt{2}\pi \frac{R}{H_0}\left(1 - \frac{3\lambda}{4}\right) \tag{4.87}$$

where $\bar{p}$ is the average of the F.E. pressures at the nip, evaluated using the pressure shape functions ψ_l. Since the grid of Figure 4.14 has 3 elements evenly spaced across the bottom half of the nip – see Figure 4.16 – with pressure freedoms p_1, p_3, p_5, p_7 at nodes 1, 3, 5, 7 respectively, it can be shown that equation (4.87) yields

$$\frac{(p_1 + 2p_3 + 2p_5 + p_7)}{6} = \frac{3}{4}\sqrt{2}\pi \frac{R}{H_0}\left(1 - \frac{3\lambda}{4}\right) \tag{4.88}$$

Equation (4.88) is also rewritten in the form of a residual $R_\lambda(p_1, p_3, p_5, p_7, \lambda) = 0$ and inserted into the row of the Jacobian (4.32) associated with the unknown λ. When allied to the F.E. equations for the velocity and pressure freedoms and the kinematic residuals associated with spines 2 to 21, (4.86) and (4.88) close the equation set.

It is important to realise that not all of the F.E. coefficients for this problem, given by $\underline{\alpha}^T = (\underline{u}^T, \underline{v}^T, \underline{p}^T, \underline{h}^T, X_m, \lambda)$, are independent. For example, the velocities associated with nodes on the roller surface, at which $\underline{u} = \underline{t}$, are specified by the value of the film split parameter X_m. Consequently the momentum residuals (4.15) associated with these velocity freedoms are no longer required, so in practice we discard these

residuals and rewrite derivatives with respect to these velocities in terms of derivatives with respect to X_m. Similarly the horizontal velocity freedoms associated with those nodes at the nip, which assume values given by equation (4.83), are also dependent freedoms because they are functions of the dimensionless flux λ.

Once again, the F.E. equations (4.31) are evaluated by assembling all the element-level contributions. Before describing the numerical solutions obtained by solving these equations, it is instructive to examine the structure of the element-level Jacobian, $\underline{\underline{J}}^e$, for the symmetric forward roll coater since it is identical to all those which arise in all subsequent roll coating problems considered in this thesis.

4.5.4 The Structure of Element-Level Jacobians in Forward Roll Coating

We begin by describing the structure of the element-level Jacobians, $\underline{\underline{J}}^e$, which arise in numerical solutions of symmetric forward roll coating. It is important to realise that the number of residuals and F.E. coefficients associated with a particular element varies according to its position within the grid shown in Figure 4.14, although there are features common to all elements.

For example, all elements depend on the value of X_m, the film-split parameter, and have associated with them $\underline{u}^e$, $\underline{v}^e$ and $\underline{p}^e$, the velocity and pressure freedoms (e is the element number), and $\underline{R}^e_x$, $\underline{R}^e_y$, $\underline{R}^e_C$, the contributions to the x and y components of the momentum residuals (4.15) and continuity residuals (4.27) arising from integration over that element or its edges. As a result of this dependence, the Newton iteration procedure (4.32) requires the evaluation of the derivatives of $\underline{R}^e_x$, $\underline{R}^e_y$ and $\underline{R}^e_C$ with respect to $\underline{u}^e$, $\underline{v}^e$, $\underline{p}^e$ and X_m – see Figure 4.17.

If, however, the element lies downstream of the base line XM, it is also necessary to evaluate derivatives of $\underline{R}^e_x$, $\underline{R}^e_y$ and $\underline{R}^e_C$ with respect to the (three) spine heights, $\underline{h}^e$ say, on which it also depends (see equation (4.51)). Moreover in the special case in which one of its sides forms part of the the free surface (see Figure 4.8), it also contibutes to 3 kinematic residuals $\underline{R}^e_k$ which means that it is necessary to evaluate these contributions and their derivatives with respect to the associated velocity freedoms $\underline{u}^e$, $\underline{v}^e$. The

situation is different when the element touches the nip instead of the free surface. In this case the element is associated with the lubrication nip pressure condition (4.88) and consequently its Jacobian must also contain derivatives with respect to λ.

Finally, consider the free surface slope condition $\underline{i}.\underline{t} = 0$. This condition only affects the element-level Jacobian of the element shown in Figure 4.15, which means that only its Jacobian contains derivatives of $\underline{i}.\underline{t}$ with respect to X_m, h_1, h_2 and h_3. The most general form of an element-level Jacobian arising in the symmetric forward roll coater (with triangular V6/P3 elements) is shown in Figure 4.17. The above discussion shows that Figure 4.17 contains every conceivable type of contribution to an element-level Jacobian for elements in the grid shown in Figure 4.14. The reader is referred to Kistler and Scriven [1983] pp 270-272 for a description of the element-level Jacobians which arise when V9/P4 elements (see Figure 4.1) are used.

The fact that the entire mesh adjusts with the free surface position has one important effect on the structure of the equations (4.31) for forward roll coating: they are no longer 'banded' in the sense described in Appendix C, since in every row of the Jacobian (4.32), except that associated with the residual R_λ (equation (4.88)), there is a non-zero contribution due to a derivative with respect to X_m. Consequently, there is no longer a storage saving accruing from the use of a banded-matrix solver, as there has been in all problems solved up to now. This constitutes an unacceptable constraint on the size or problem that can be solved by this technique and for this reason it is necessary to implement an alternative technique to solve equation (4.31). Fortunately, the Frontal Solution Method, described in Appendix C, (see also Kistler and Scriven [1983], Carter [1985]) does not suffer from the bandedness constraint and is therefore suitable for the present application. Although requiring a significant investment in time to implement it, the Frontal Method offers many advantages over the banded-matrix technique, including (i) the ability to solve problems in which the storage requirement would otherwise be excessive; (ii) reductions of up to 80% in computational costs. Indeed such is its suitability that the Frontal Method is used to solve the F.E. equations in this and all subsequent free surface problems.

A condensed flow chart for the code used to solve this problem, in which the F.E.

equations are solved by the Frontal method, is shown in Figure 4.18. Zeroth order continuation is used, i.e. the iteration is begun with $\underline{\alpha}_n$, a converged solution corresponding to a set of parameters which are 'close' to those for which a solution is desired.

4.5.5   Results and Discussion

The first solution to symmetric, fully-flooded, forward roll coating attempted here was for the parameter set $Ca = 0.1$, $Re = 0.0$, $R/H_0 = 100$ and used grid (a) of Figure 4.19. An initial investigation confirmed that the outflow boundary was sufficiently far downstream so that the solutions were insensitive to changes in its position. To test the sensitivity of the calculated flows to the discretisation used, solutions were obtained using the 3 grids shown in Figure 4.19. Grid (a) is that shown in Figure 4.14 with 102 elements, 245 nodes and 21 spines; grid (b) has 132 elements, 315 nodes and 21 spines; and grid (c) has 208 elements, 477 nodes and 23 spines. In all cases, converged solutions were obtained from a start-up approximation after 5 iterations, each iteration taking 10, 12 and 14 c.p.u. seconds when grids (a), (b) and (c) were used respectively. The most sensitive variables, namely the film-split location and the pressures at the nip, changed by less than 0.1% in changing from grids (a)–(c) which indicates that all 3 grids give sufficiently accurate solutions. In fact all the numerical results presented in this section employ grid (b) as the computational mesh.

Figure 4.20 shows a comparison between solutions obtained for flows with $Re = 0.0$, $R/H_0 = 100$ and $Ca = 0.1$, 0.2, 0.5 for (a) this work, (b) those presented in Coyle et al [1982] using quadrilateral elements. Unfortunately the velocity vectors are difficult to interpret, but an inspection of the velocity fields reveals the gradual disappearance of eddies near the downstream free surface as Ca increases from 0.1 to 0.5. This prediction agrees well with the results presented by Coyle et al [1982]. Figure 4.21 shows the dependence of the free surface profiles on the Capillary number for $Re = 0.0$ and $R/H_0 = 100$; the units of the vertical scale are in terms of H_0, the semi-nip width. The results of this work are in excellent agreement with those previously obtained by Coyle et al [1982].

So far, no mention has been made of the F.E. pressures which are generated in

any solution. This may now be rectified by considering the pressures generated on the plane of symmetry in symmetric, fully-flooded, forward roll coating. In Figure 4.22 pressures upstream of the nip ($x < 0$) have been obtained from the lubrication theory of §§4.5.2, whereas those downstream of the nip have been generated by the F.E. method. These dimensionless pressures have been converted to physical pressures (pounds per square inch) in the case in which viscosity $\eta = 1 \times 10^{-1} N m^{-2} s$ and surface tension $T = 6 \times 10^{-2} N m^{-1}$; the horizontal scale is that of H_0, the semi-nip width. The pressure profiles predicted by F.E. theory seem to match well those of lubrication theory and exhibit the characteristic pressure maximum/minimum profile observed in roll coating – see Chapter 5. The profiles obtained in this work (with triangular elements) agree well with those of Coyle et al [1982] (quadrilateral elements).

In their experiments on symmetric fully-flooded forward roll coating, Pitts and Greiller [1961] measured the position of the downstream mensicus and tabulated the ratio, σ_0, of the vertical roller separation at the symmetry line P (see Figure 4.13) to the nip width, $2H_0$, for flows with a range of capillary numbers Ca and geometric parameters R/H_0. Their experiments showed that σ_0 is sensitive to the value of Ca, but almost independent of R/H_0. In Figure 4.23 their experimental data is compared with theoretical predictions of σ_0 by the F.E. method with $Re = 0.0$ and the geometric parameter $R/H_0 = 100$. The experimental results and theoretical predictions agree well over this range of Ca. Note that Figure 4.23 does actually provide a reliable comparison between theory and experiment since predictions of σ_0 (at $Re = 0.0$) over a range of values of R/H_0 agreed with Pitts and Greiller's observation that σ_0 is almost independent of R/H_0.

The final results presented here pertain to the prediction of the dimensionless flux λ as a function of Capillary number and geometrical parameter R/H_0 for $Re = 0.0$. In Figure 4.24 F.E. predictions of λ obtained here (with triangular elements) for $Re = 0.0$ and $R/H_0 = 100, 1000$ are compared with those of Coyle et al [1986] (quadrilateral elements); note that the circles (o) in Coyle et al's results relate to their asymptotic solution, valid in the limit $R/H_0 \rightarrow \infty$. The F.E. predictions are in good agreement and predict that $1.3 \leq \lambda \leq 1.4$, which corresponds well with the experimental data

of (i) Pitts and Greiller [1961] ($1.26 \leq \lambda \leq 1.38$), (ii) Benkreira et al [1981] who found an average value of λ (based on 1500 experiments, with a standard deviation of 0.4%)=1.31. However, a conspicuous feature of Figure 4.24 is that no results are shown for the case of $R/H_0 = 100$ and $Ca < 0.03$; this omission will now be explained as it illustrates an important difficulty in analysing flows with highly curved meniscii.

All the solutions shown in Figure 4.24 were easily obtained by zeroth order continuation from the first converged solution. Unfortunately, converged solutions for flows with $Re = 0.0$, $R/H_0 = 100$ and $Ca < 0.03$ could not be obtained by simply performing zeroth order continuation on the capillary number Ca. In a second attempt at obtaining solutions in this range, zeroth order continuation was carried out on the geometric parameter R/H_0, beginning with the converged solution for $Re = 0.0$, $Ca = 0.01$, $R/H_0 = 1000$. This also failed when R/H_0 was decreased below 400. After inspecting the computational grids of solutions in this range, the author has formed the firm opinion that these convergence difficulties are caused by element distortion in the downstream region (i.e. region 2) of the computational mesh. Typical element distortions are illustrated in Figure 4.25, which shows elements in region 2 for converged solutions with parameters: (a) $Re = 0.0$, $Ca = 0.03$, $R/H_0 = 100$; (b) $Re = 0.0$, $Ca = 0.01$, $R/H_0 = 400$; (c) $Re = 0.0$, $Ca = 0.01$, $R/H_0 = 1000$. These elements exhibit two kinds of distortion (i) a high 'aspect ratio' (i.e. ratio of the maximum and minimum lengths of an element's sides), (ii) loss of element triangularity. The author's experience suggests that the latter is the primary cause of convergence difficulties, whereas the former has a deleterious effect on the solution's accuracy. In fact the observation that the accuracy depends on the aspect ratio of elements used has been proved theoretically – see Chung [1978] p 133-138.

At this point one may think that employing quadrilateral rather than triangular elements could alleviate these convergence difficulties because Coyle et al [1986] have obtained converged solutions for $Re = 0.0$, $R/H_0 = 100$, $Ca = 0.01$ with the former. However this is debatable because Coyle et al [1986] have also reported convergence difficulties with quadrilateral elements; their success in obtaining solutions in this parameter range is probably due to greater skill in tessellating grids of this kind rather

than an intrinsic superiority of the quadrilateral element. Even though these observations do not enable the errors in a numerical solution to be quantified, they are nevertheless useful diagnostics since they suggest when the accuracy of a numerical solution should be questioned and, if possible, the computational grid refined.

Although the convergence difficulties experienced here could be remedied by packing more elements into the grid in region 2 or changing the the relative orientation of the downstream spines, convergence problems are an unavoidable feature of the remainder of this thesis. This is because the mesh generation algorithms used above, which are relatively primitive, are only suitable over a limited parameter range and should therefore be tailored to the parameter range of interest. The inescapable conclusion from this discussion is that it is unwise to accept the accuracy of a F.E. solution if any elements in its computational grid exhibit the two kinds of distortion described here.

4.6   The Asymmetric Fully-Flooded Forward Roll Coater

4.6.1   Boundary Conditions and Computational Mesh

In this section, the theory developed for the symmetric forward roll coater is extended to tackle the asymmetric problem. For convenience it is assumed that the asymmetry is introduced by having different roller speeds and that the radii of the upper and lower rollers are equal. Before describing the relevant boundary conditions, it is necessary to describe the computational meshes used for the asymmetric problem.

Since the flow is asymmetric, it is no longer possible to solve the problem in a half-domain, so the entire flow domain must be tessellated into elements. Quite simply, the nodal co-ordinates in the upper half of the mesh are generated in exactly the same way as the lower co-ordinates. As before, the entire grid is specified by a base line XM, spine heights $\underline{h}$ and the algorithmic parameters FRAC(I), XINC(I). This is best explained by inspecting the mesh shown in Figure 4.26. Although, in the asymmetric case, the plane which is equidistant from both rollers is no longer a plane of symmetry, it is still convenient to fix the spinal height associated with the spine which lies on it. This enables the film-split location to be specified in terms of X_m alone, as in the

symmetric case.

The boundary conditions for the asymmetric problem are shown in Figure 4.27. At the roller surface, free surface and outflow boundaries the usual no-slip, kinematic, stress, and zero traction conditions respectively are applied. The non-dimensionalisation used in this instance is, however, slightly different from that given by equations (4.69), (4.70). As in §§4.5.2, lengths are scaled by $\sqrt{(RH_0)}$ where $R = R_1 = R_2$ is the radius of each roller and H_0 the semi-nip width, but in the asymmetric problem it is more appropriate to scale velocities and pressures by $\overline{V} = (V_1 + V_2)/2$ (the *average* roller speed) and $\eta \overline{V}/\sqrt{(RH_0)}$, respectively and define a generalised dimensionless flux λ, where

$$\lambda = \frac{Q}{2\overline{V}H_0} \tag{4.89}$$

Once again, the origin of the dimensionless (x, y) co-ordinates is placed at the centre of the nip so that the upper and lower rollers are at $y = \pm h(x)$ respectively where $h(x)$ is given by (4.72), and the transformed spatial co-ordinates (θ, η) are given by (4.73).

It can be shown (Coyle et al [1986]) that a lubrication analysis exactly analagous to that described in §§4.5.2 yields the following boundary conditions at the nip

$$u = \frac{3}{2}(1 - \lambda)(\eta^2 - 2\eta) + \frac{(S - 1)}{(S + 1)}\eta + \frac{2}{(S + 1)} \tag{4.90}$$

$$v = 0 \tag{4.91}$$

$$p = \frac{3}{4}\sqrt{2}\pi\frac{R}{H_0}\left(1 - \frac{3\lambda}{4}\right) \tag{4.92}$$

where $S = V_2/V_1$ is the velocity ratio of the rollers and λ is given by (4.89). Note that the no-slip conditions at the roller surfaces are

$$\underline{u}(\eta = 0) = \frac{2}{(1 + S)}\underline{t} \ , \ \ \underline{u}(\eta = 2) = \frac{2S}{(1 + S)}\underline{t} \tag{4.93}$$

where $\underline{t}$ is the unit vector tangential to, and in the same direction as, the motion of the roller surface. Equations (4.90), (4.91) and (4.93) yield essential conditions on the velocity of the liquid which are imposed by the methods described for the symmetric case. The lubrication theory nip pressure condition (4.92) is also imposed in the form given by equation (4.88) in §§4.5.3, but note that in this case $\overline{p}$ refers to the average pressure across the *entire* nip.

Finally, note that the asymmetry of the problem means that the flow is no longer symmetric about the plane equidistant from the roller surfaces. Consequently, the stagnation and slope conditions (4.86) are no longer applicable at the free surface node which also lies on this plane (formerly the node at P in Figure 4.13). Instead the equation needed to determine the value of the film-split parameter, X_m, is provided by the kinematic residual (4.50) associated with this node, thereby completing the equation set for an asymmetric, fully-flooded, forward roll coater. In all solutions presented in the following section, equations (4.31) are solved by the Frontal Method.

4.6.2 Results and Discussion

The first solution attempted using the newly developed asymmetric code was actually for the symmetric case of $S = 1$, $Re = 0.0$, $Ca = 0.1$ and $R/H_0 = 100$. This was a convenient initial problem since the half-domain solution for the same set of parameters provided an excellent start-up approximation for the free surface shape and flow field. The solution was obtained using the grid shown in Figure 4.26 which consists of 204 elements, 469 nodes and 41 spines – the earlier convergence study of §§4.5.5 suggests that this grid is sufficiently refined for this problem. A converged solution was obtained from the start-up approximation after 2 iterations, each iteration having an execution time of approximately 20 c.p.u. seconds.

The numerical results obtained using the full asymmetric grid were in excellent agreement with those from the corresponding half-domain solution. In fact the maximum change in any F.E. coefficient between the two solutions was less than 0.01% of its previous value, which provided strong evidence to suggest that the modifications that had to be made to the symmetric code to enable it to solve the asymmetric problem had been implemented correctly.

Figure 4.28 shows F.E. predictions of the film thickness ratio T_1/T_2 (ratio of upper to lower film thicknesses) for $Ca = \infty$ and $R/H_0 = 200$ as a function of velocity ratio S, obtained by zeroth order continuation on S and Ca from the above initial solution. The F.E. grid used in these solutions has the same mesh generation algorithm as the one shown in Figure 4.26. Note that the results are presented on a logarithmic scale to

facilitate a convenient comparison with Coyle et al's [1986] F.E. results and Benkreira et al's [1981] experimental correlation (equation (1.8)). As in Figure 4.24, the circles (o) relate to Coyle et al's asymptotic solution for the limiting case of parallel roller surfaces, i.e. $R/H_0 \to \infty$. The results from this work (obtained using triangular elements) agree reasonably well with those of Coyle et al [1986] (quadrilateral elements) and Benkreira et al [1981], and moreover seem to support their proposal that $T_1/T_2 \propto S^{0.65}$ for $1 \leq S \leq 10$. Unfortunately it was not possible to obtain converged solutions for $S > 6.75$ using the grid shown in Figure 4.26. The computational grids for converged solutions with (a) $Re = 0.0$, $S = 1$, $Ca = \infty$, $R/H_0 = 200$, (b) $Re = 0.0$, $S = 6.75$, $Ca = \infty$, $R/H_0 = 200$ are shown in Figure 4.29. In view of the discussion of §§4.5.5, since the grid for $S = 6.75$ is severely distorted, the convergence difficulties experienced here are probably due to element distortion.

4.7 Conclusions

In this chapter we have developed a computer code for solving free surface flow problems by combining Galerkin's weighted residual method with Kistler's 'Spine Method' of representing a free surface. In most cases, the numerical results obtained from this code are encouraging since they agree very well with previously published numerical and experimental results.

The cases for which converged solutions could not be obtained were also very illuminating because they demonstrated that mesh generation problems are often extremely important in free surface flows. We have identified two kinds of element distortion which it is desirable to avoid in a F.E. grid: (i) high aspect ratio elements, (ii) loss of element triangularity. Unfortunately as the downstream free surface is often highly curved in general roll coating situations, these distortions may be unavoidable. In such cases one should always question the solution's validity.

These mesh generation problems are also prevalent in the next chapter, in which the code is used (i) to obtain F.E. predictions of T_1/T_2 in fully-flooded forward roll coating over a wider velocity ratio range than previously published and (ii) to investigate the effects of starvation in forward roll coating.

(a) V6/P3   (b) V9/P1

(c) V9/P3   (d) V9/P4

□   VELOCITY AND PRESSURE NODES

o   VELOCITY ONLY NODES

△   PRESSURE ONLY NODES
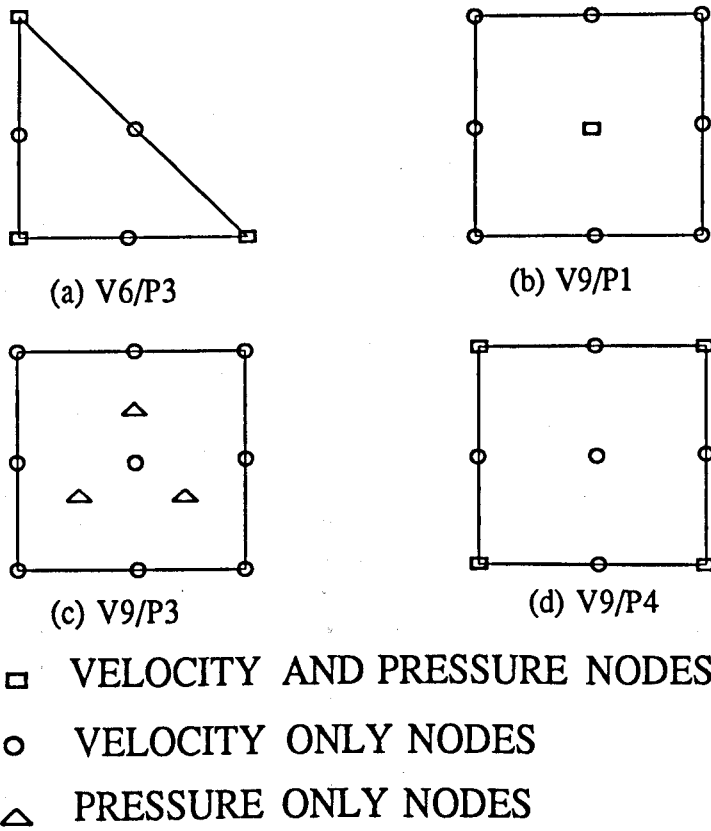
Figure 4.1: Commonly Used Elements Which Satisfy the LBB Condition

Global Space   Local Space A_0

□   VELOCITY AN PRESSURE NODES

o   VELOCITY ONLY NODES
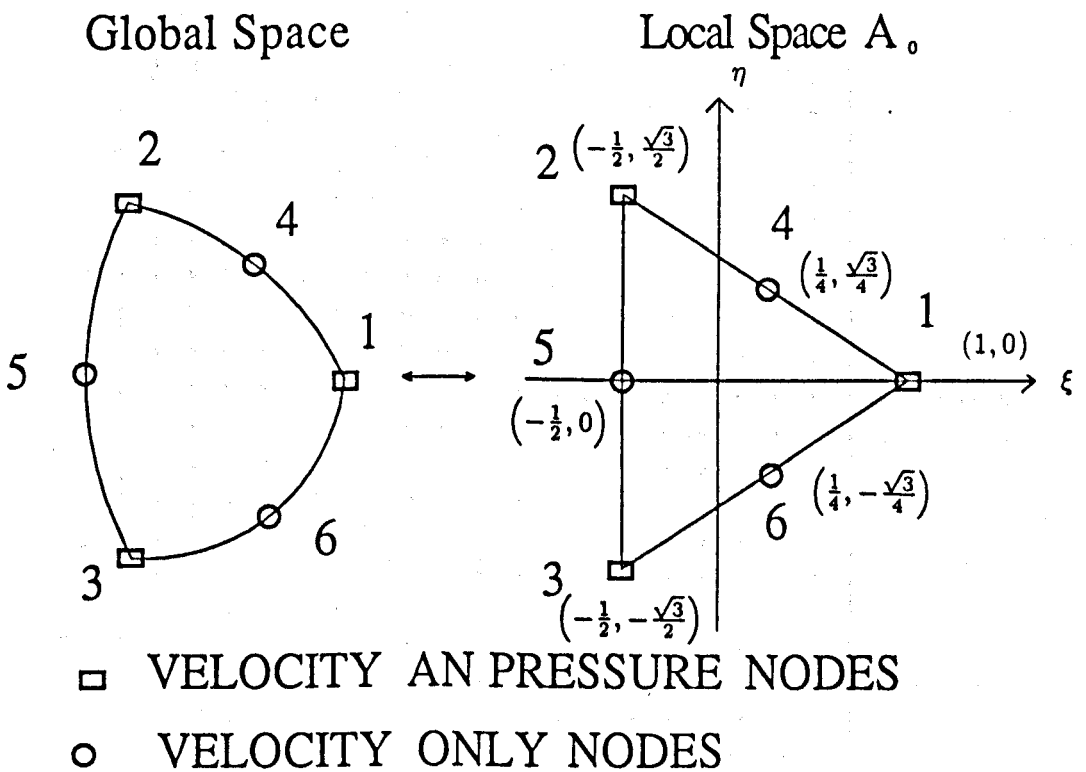
Figure 4.2: Local Node Numbering Scheme in the $u - v - p$ Formulation

(a)
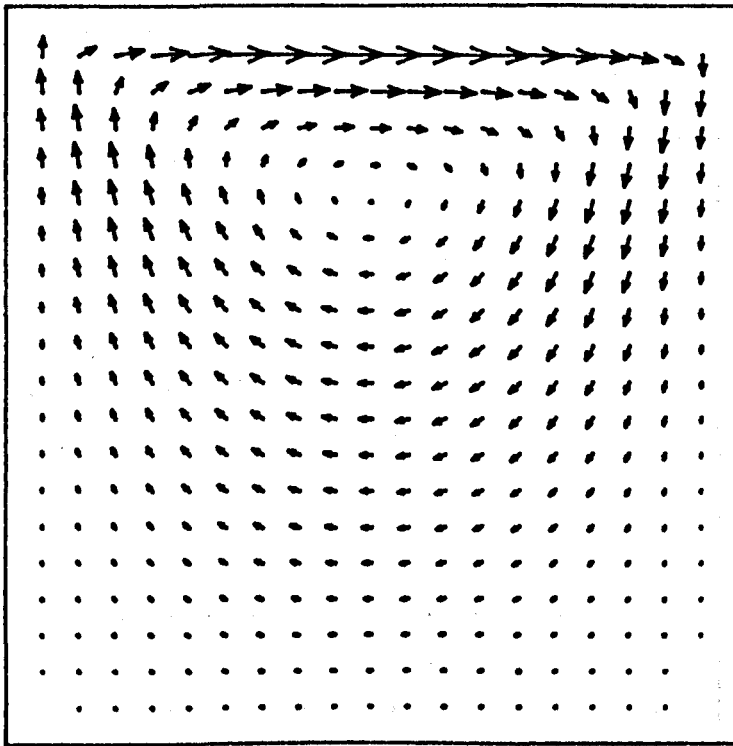
(b)
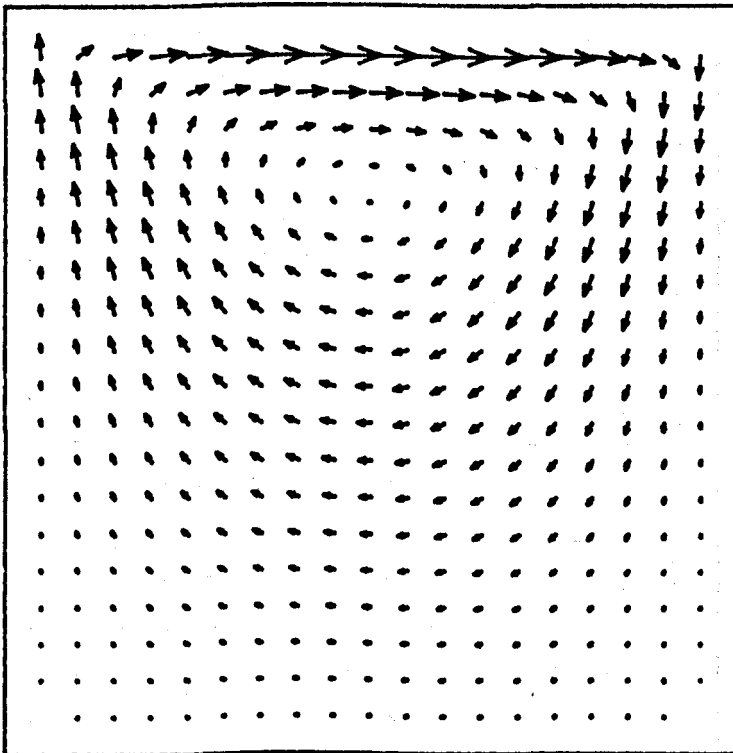
Figure 4.3: Velocity Field for Flow in a Lid-Driven (Square) Cavity with $Re = 0.0$: (a) Numerical (F.E.), (b) Semi-Analytical (40 terms in series)

(a)

(b)
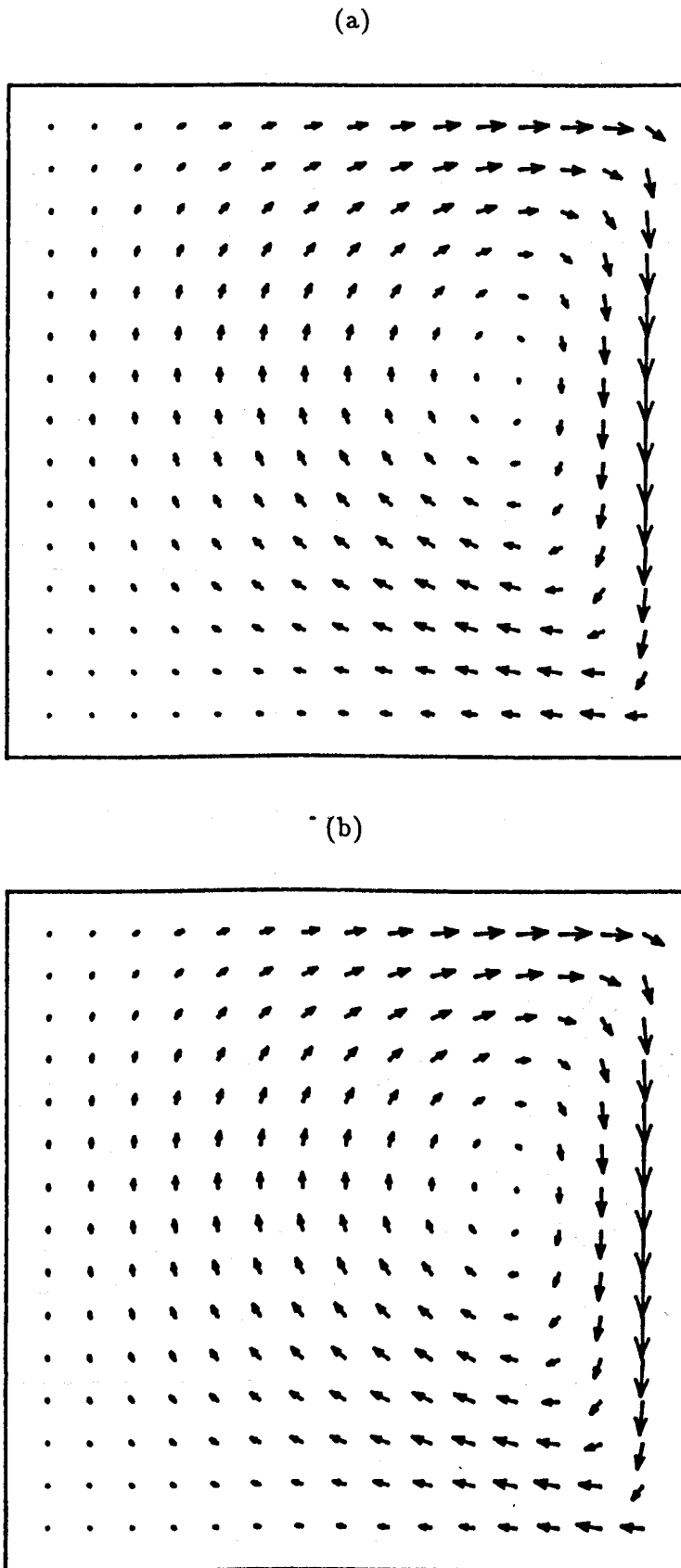
Figure 4.4: Velocity Field for Flow in an Open, Driven (Square) Cavity with $Re = 0.0$:

(a) Numerical (F.E.), (b) Semi-Analytical (40 terms in series)

(a)

(1) NUMERICAL (U-V-P)   (2) ANALYTICAL (N=40)

(b)

(1) NUMERICAL (U-V-P)   (2) ANALYTICAL (N=40)
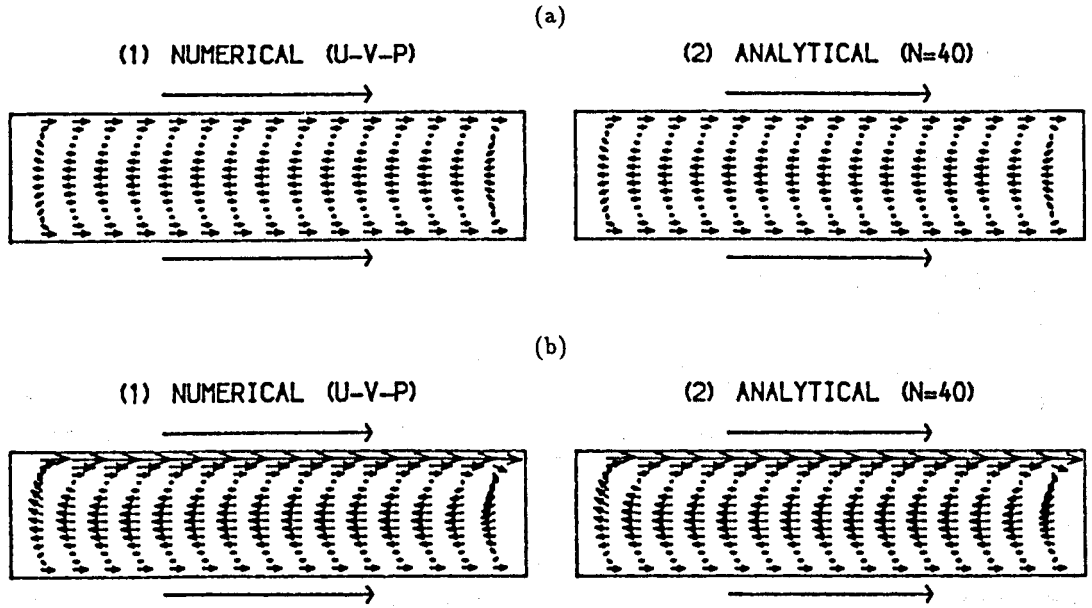
Figure 4.5: Velocity Vectors from the Zero Flux Model of Meniscus Roll Coating for Flows with (a) $S = 1$, $H^* = 0.5$, (b) $S = 2$, $H^* = 0.5$
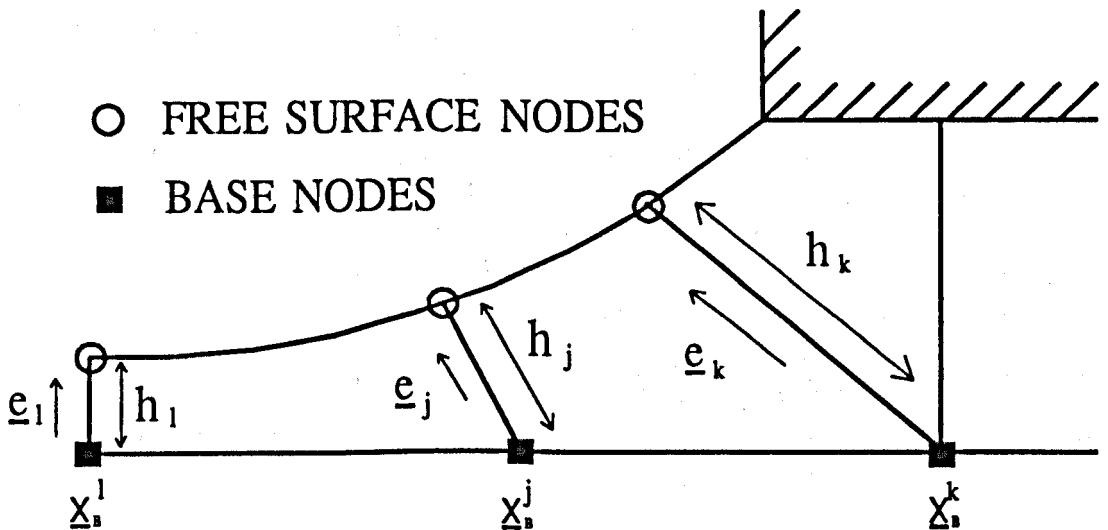
Figure 4.6: Spinal Representation of the Free Surface in Slot Coating
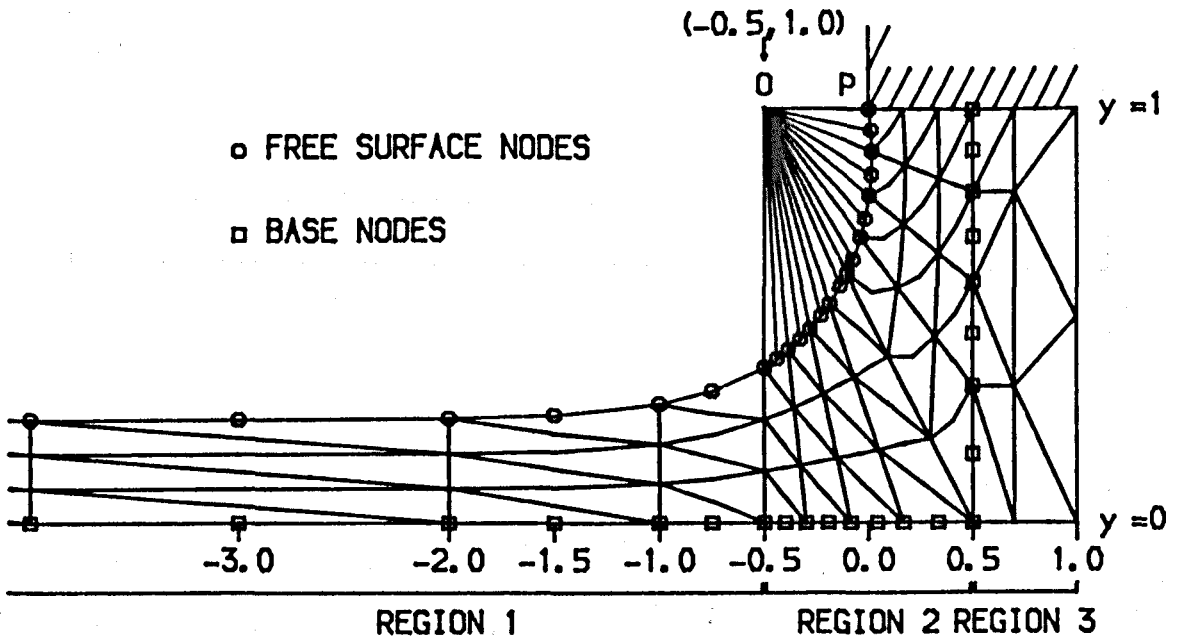
Figure 4.7: Slot Coating F.E. Grid Used in Present Work
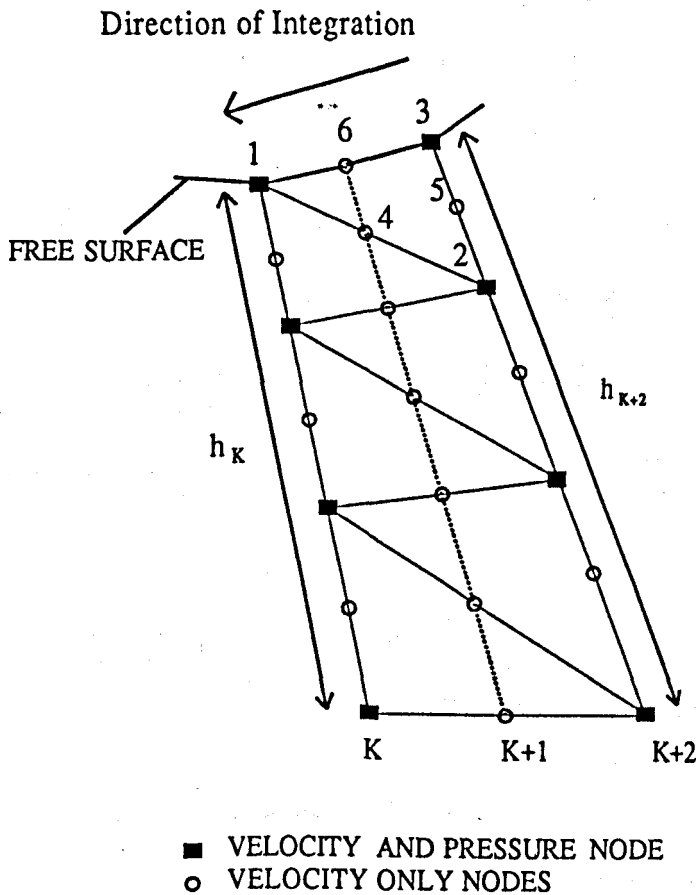
Figure 4.8: Free Surface Representation in terms of Triangular Elements

(a)

(b)
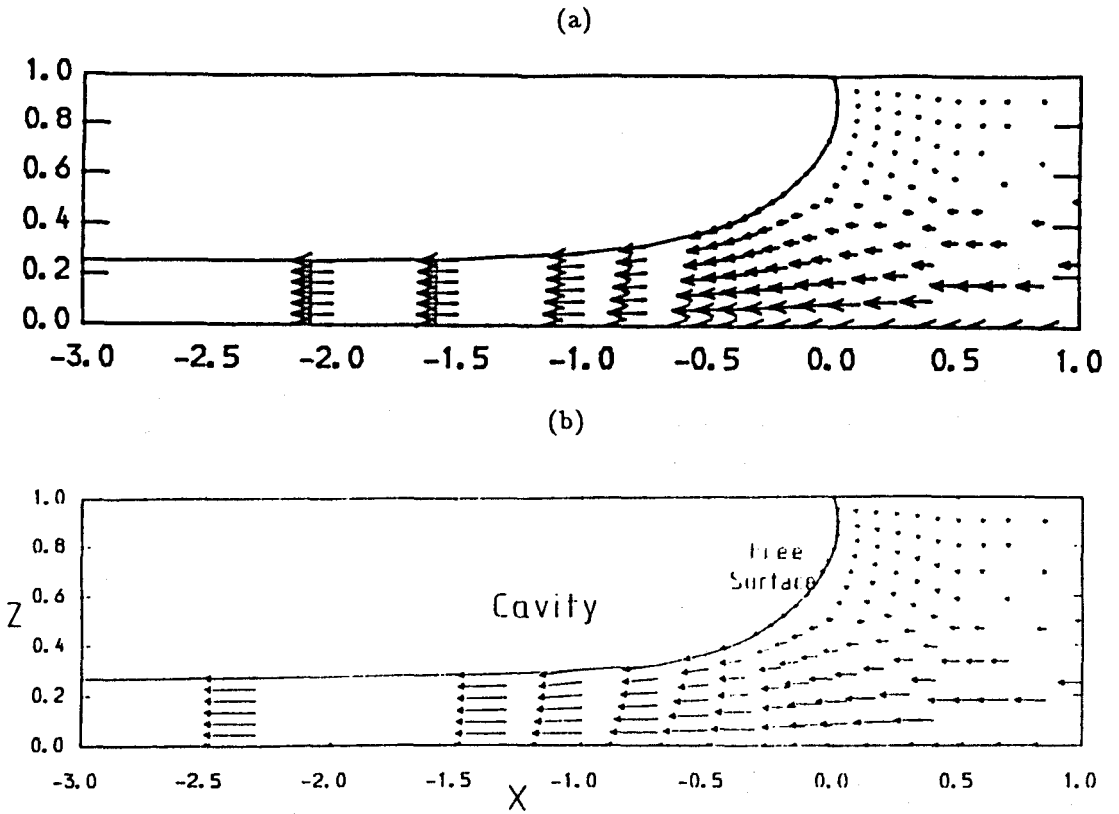
Figure 4.9: Free Surface Profiles and Velocity Vectors for a Slot Coater with $Re = 0.0$, $Ca = 0.4$, $q = 0.25$: (a) this work, (b) Carter [1985]

(a)

(b)
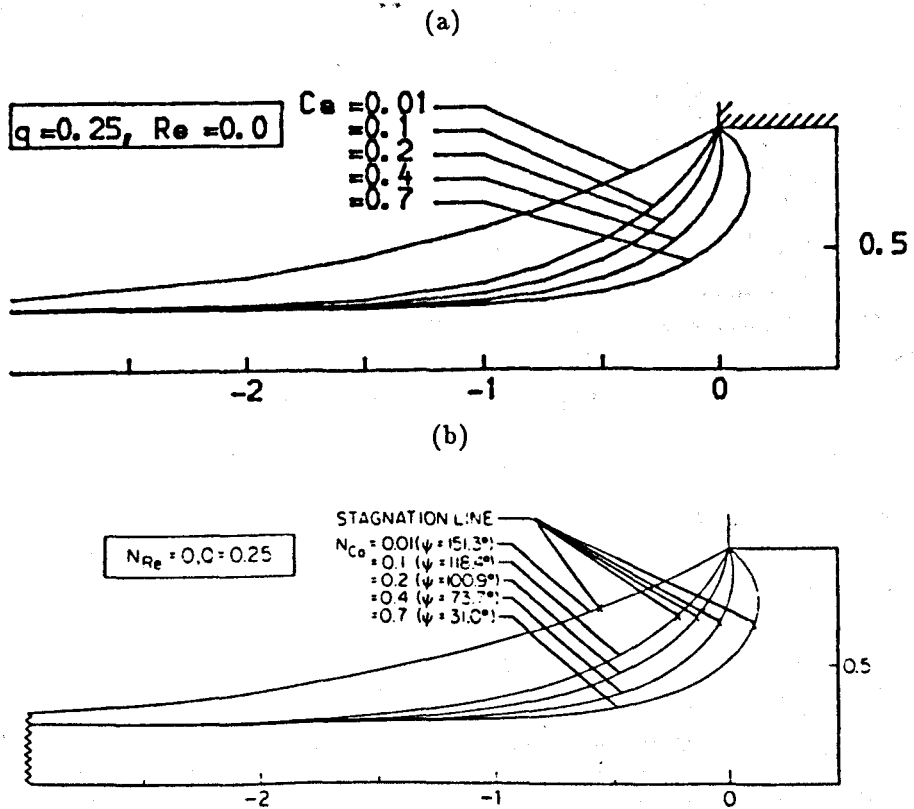
Figure 4.10: Free Surface Profiles For a Slot Coater – Dependence on Capillary Number for $Re = 0.0$, $q = 0.25$: (a) this work, (b) Saito and Scriven [1981]

CASE (a) – Ca =0.125, q =0.13, Re =50.0
THIS WORK
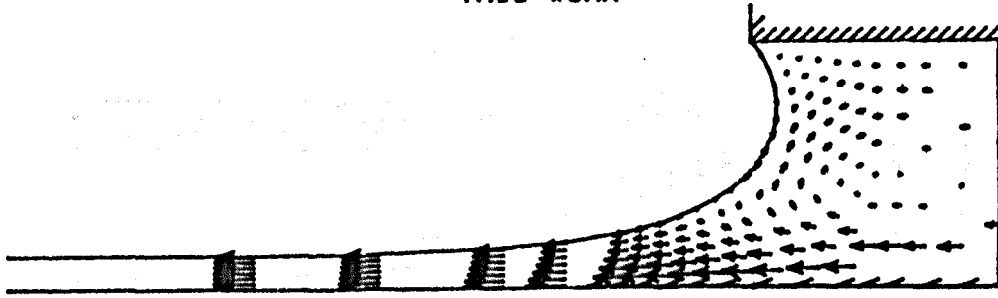
SAITO AND SCRIVEN [1981]
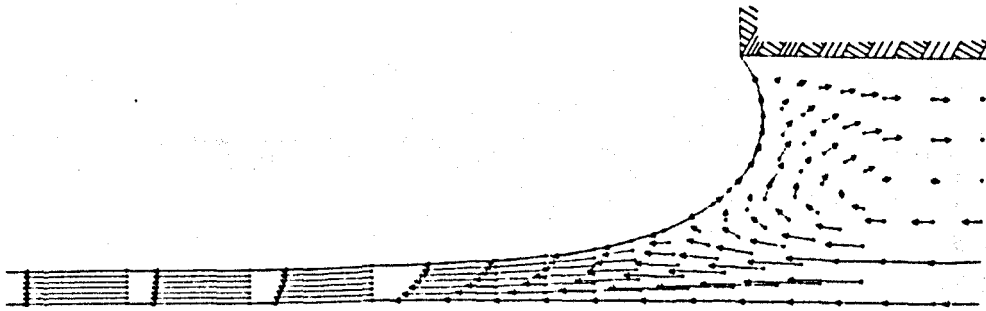
CASE (b) – Ca =0.125, q =0.25, Re =50.0
THIS WORK
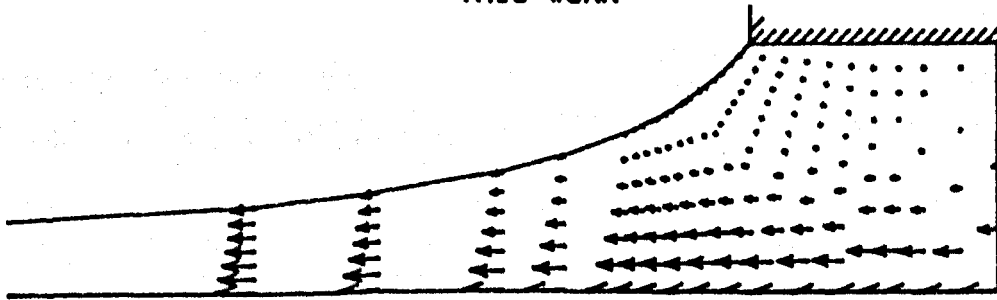
SAITO AND SCRIVEN [1981]
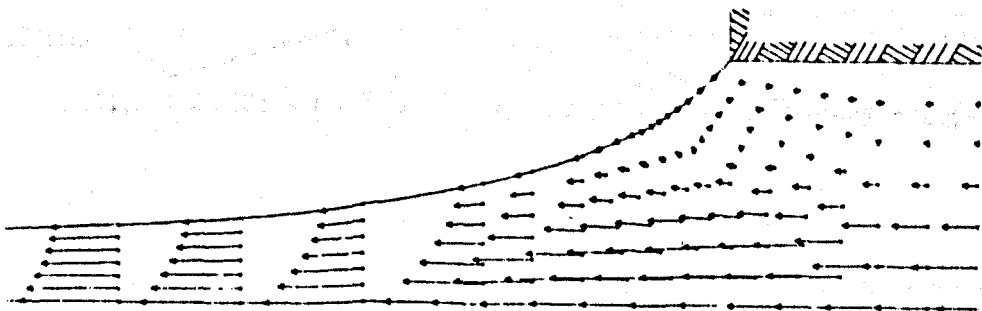
Figure 4.11: Slot Coating Results with $Re = 50$, $Ca = 0.125$ and (a) $q = 0.13$, (b) $q = 0.25$

(a)

$q = 0.3$
$= 0.2$
$= 0.15$
$= 0.12$

$Re = 50.0, \ Ca = 0.125$

0.5

-2 -1 0

(b)

STAGNATION LINE

$N_{Re} = 50, N_{Ca} = 0.125$

$Q = 0.3 (\psi = 143.3°)$
$= 0.2 (\psi = 110.3°)$
$= 0.15 (\psi = 76.4°)$
$= 0.12 (\psi = 29.2°)$

0.5

-2 -1 0
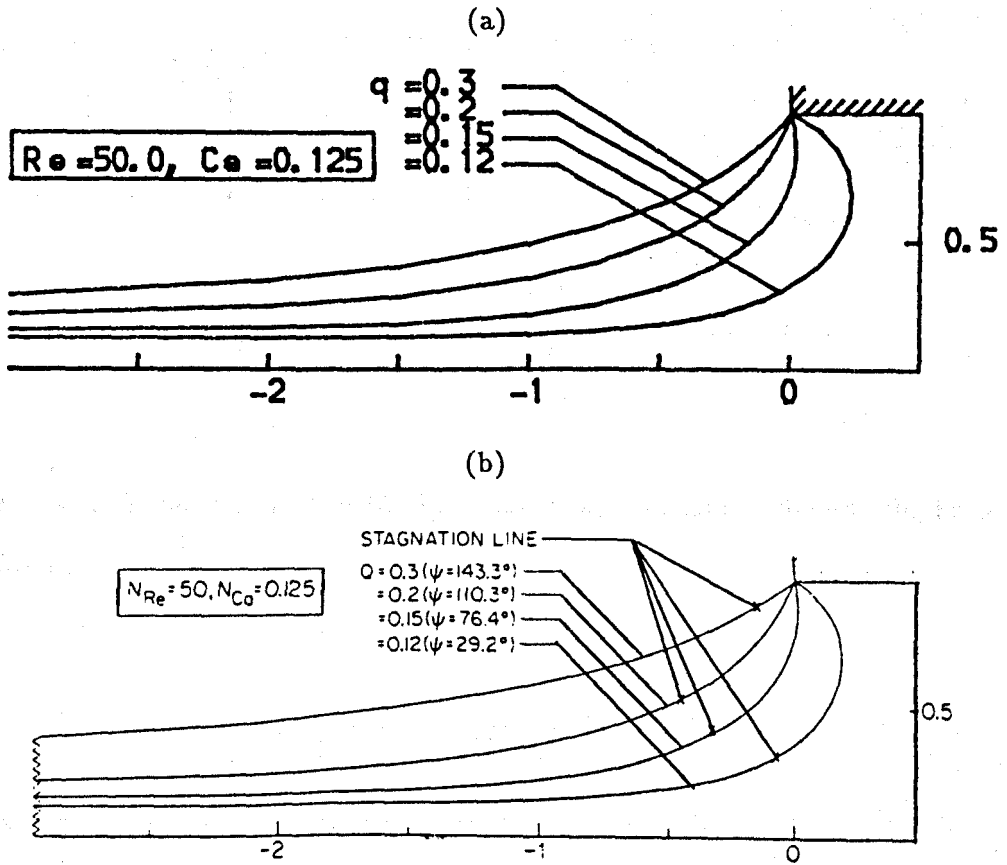
Figure 4.12: Free Surface Profiles for a Slot Coater with $Re = 50$, $Ca = 0.125$ – Dependence on Flux: (a) this work, (b) Saito and Scriven [1981]

SYMMETRY PLANE $- \left(\underline{n} \cdot \underline{\sigma} \right)_x = 0; \ v = 0$

NIP
LUBRICATION
CONDITIONS

P

SYMMETRY LINE
CONDITIONS $- \ u = v = 0; \ \underline{i} \cdot \underline{t} = 0$

FREE SURFACE $- \ \underline{n} \cdot \underline{\sigma} = \dfrac{1}{Ca} \dfrac{dt}{ds}; \ \underline{n} \cdot \underline{u} = 0$

ROLLER SURFACE $-$ NO SLIP $\ \underline{u} = \underline{t}$

OUTFLOW $- \ \underline{n} \cdot \underline{\sigma} = \underline{0}$
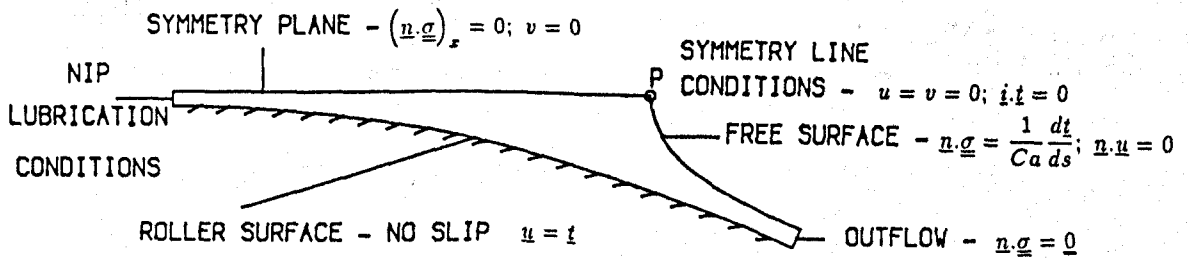
Figure 4.13: Boundary Conditions For Symmetric, Fully-Flooded, Forward Roll Coating
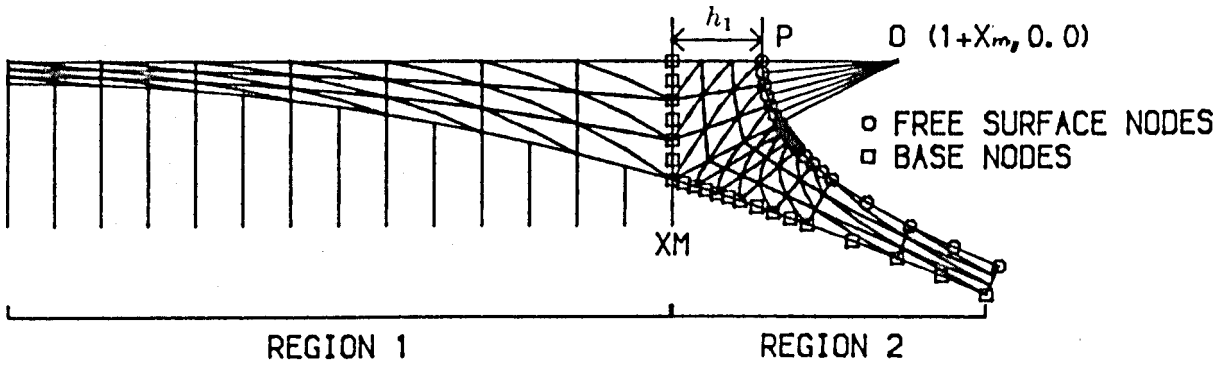
Figure 4.14: A Typical F.E. Grid Used in Numerical Solutions of Symmetric, Forward Roll Coating
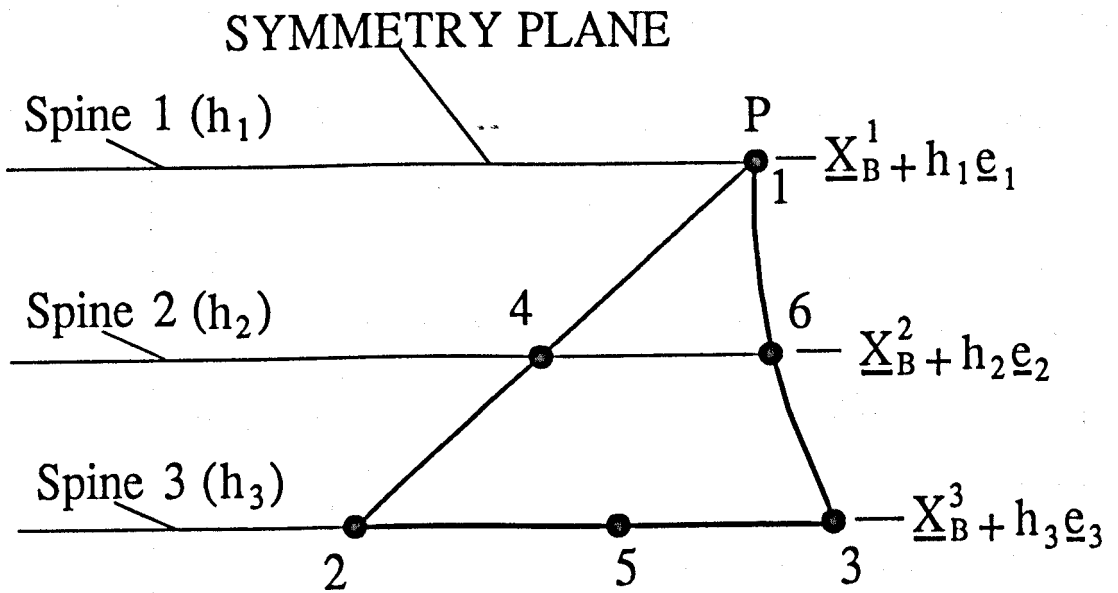
Figure 4.15: The Free Surface Representation Near the Symmetry Line P

こ
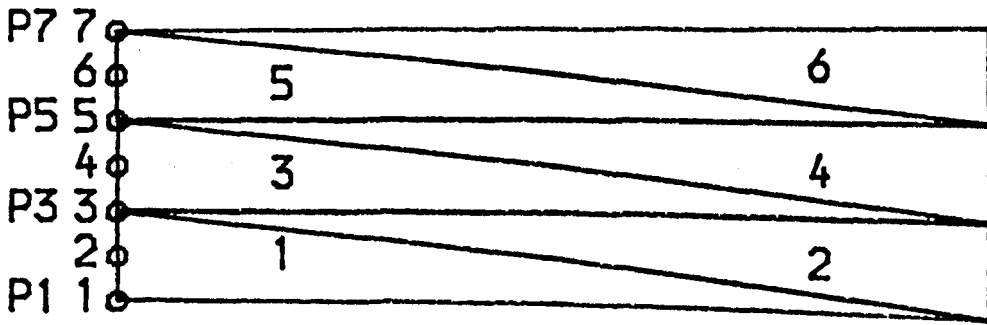
Figure 4.16: Elements Touching the Lower Half of the Nip in Symmetric, Forward Roll Coating

$$
\underline{\underline{J}}^e =
\begin{bmatrix}
\dfrac{\partial \underline{R}^e_x}{\partial \underline{u}^e} & \dfrac{\partial \underline{R}^e_x}{\partial \underline{v}^e} & \dfrac{\partial \underline{R}^e_x}{\partial \underline{p}^e} & \dfrac{\partial \underline{R}^e_x}{\partial \underline{h}^e} & \dfrac{\partial \underline{R}^e_x}{\partial X_m} & \dfrac{\partial \underline{R}^e_x}{\partial \lambda} \\[2.5ex]
\dfrac{\partial \underline{R}^e_y}{\partial \underline{u}^e} & \dfrac{\partial \underline{R}^e_y}{\partial \underline{v}^e} & \dfrac{\partial \underline{R}^e_y}{\partial \underline{p}^e} & \dfrac{\partial \underline{R}^e_y}{\partial \underline{h}^e} & \dfrac{\partial \underline{R}^e_y}{\partial X_m} & \dfrac{\partial \underline{R}^e_y}{\partial \lambda} \\[2.5ex]
\dfrac{\partial \underline{R}^e_C}{\partial \underline{u}^e} & \dfrac{\partial \underline{R}^e_C}{\partial \underline{v}^e} & \underline{0} & \dfrac{\partial \underline{R}^e_C}{\partial \underline{h}^e} & \dfrac{\partial \underline{R}^e_C}{\partial X_m} & \dfrac{\partial \underline{R}^e_C}{\partial \lambda} \\[2.5ex]
\dfrac{\partial \underline{R}^e_K}{\partial \underline{u}^e} & \dfrac{\partial \underline{R}^e_K}{\partial \underline{v}^e} & \underline{0} & \dfrac{\partial \underline{R}^e_K}{\partial \underline{h}^e} & \dfrac{\partial \underline{R}^e_K}{\partial X_m} & \underline{0} \\[2.5ex]
\underline{0} & \underline{0} & \dfrac{\partial R_\lambda}{\partial \underline{p}^e} & \underline{0} & \underline{0} & \dfrac{\partial R_\lambda}{\partial \lambda} \\[2.5ex]
\underline{0} & \underline{0} & \underline{0} & \dfrac{\partial R_{symmetry}}{\partial \underline{h}^e} & \dfrac{\partial R_{symmetry}}{\partial X_m} & \underline{0}
\end{bmatrix}
$$

Figure 4.17: The Structure of an Element-Level Jacobian in Symmetric, Forward Roll Coating

START

NELE=total number of elements
NITER=maximum number of
iterations allowed

READ —— flow parameters, mesh parameters,
essential B.C.'s, previously converged solution $\underline{\alpha}_n$

BEGIN ITERATION: ITER=0

ITER=ITER+1

CALCULATE MESH COORDINATES

LOOP OVER ELEMENTS, NELL=0

NELL=NELL+1

EVALUATE (i) element-level Jacobian matrix
(ii) element contributions to residuals

FRONTAL ASSEMBLY AND ELIMINATION OF
LINEAR SYSTEM EQUATIONS

IS NELL=NELE?   NO
YES

BACK SUBSTITUTION

UPDATE SOLUTION $\underline{\alpha}_{n+1} = \underline{\alpha}_n + \Delta\underline{\alpha}_n$

CONVERGED   NO
YES

IS ITER ≥ NITER?   NO

STOP

YES

NEWTON ITERATION

FRONTAL SOLVER

Figure 4.18: A Condensed Flow Chart of the Algorithm to Solve Viscous Free Surface

Flow by the F.E. Method
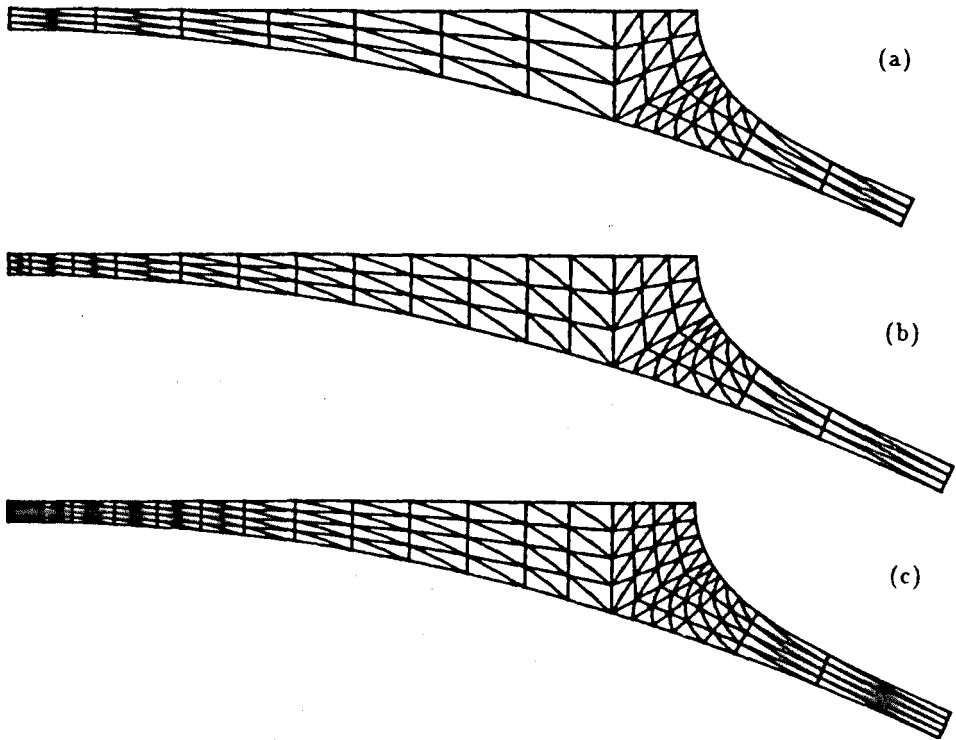
Figure 4.19: F.E. Grids used in the Numerical Solution of Symmetric, Fully-Flooded, Forward Roll Coating: (a) 102 elements, 245 nodes, (b) 132 elements, 315 nodes, (c) 208 elements, 477 nodes
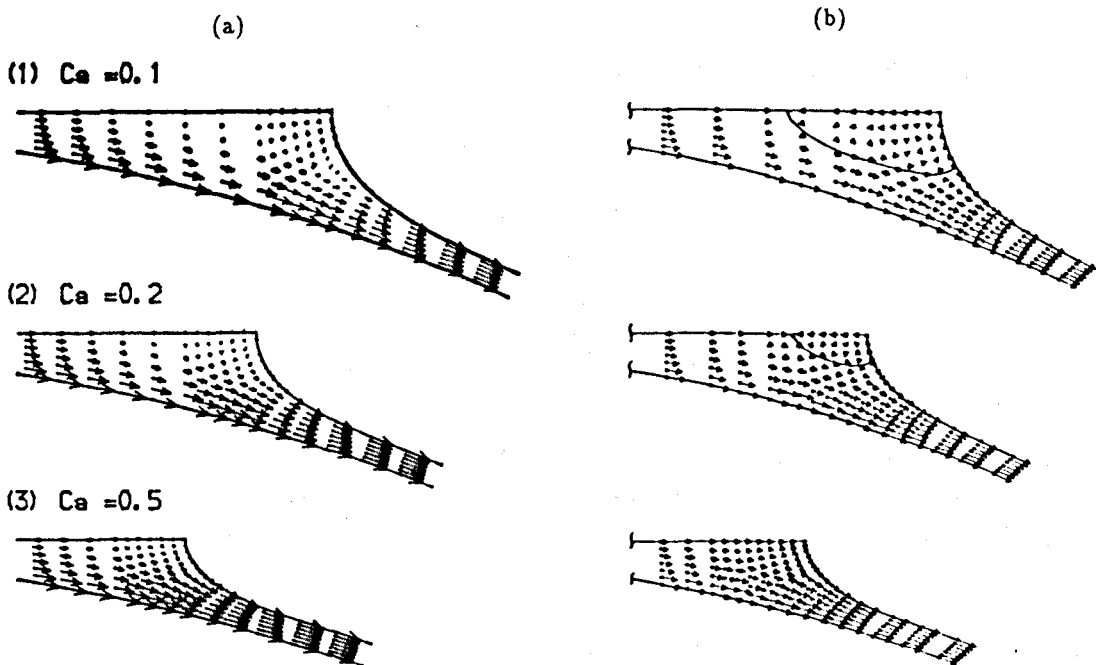
Figure 4.20: The Effect of Capillary Number on the Flow Field in Symmetric, Fully-Flooded Forward Roll Coating with $Re = 0.0$, $R/H_0 = 100$: (a) this work, (b) Coyle et al [1982]

(a)

(b)
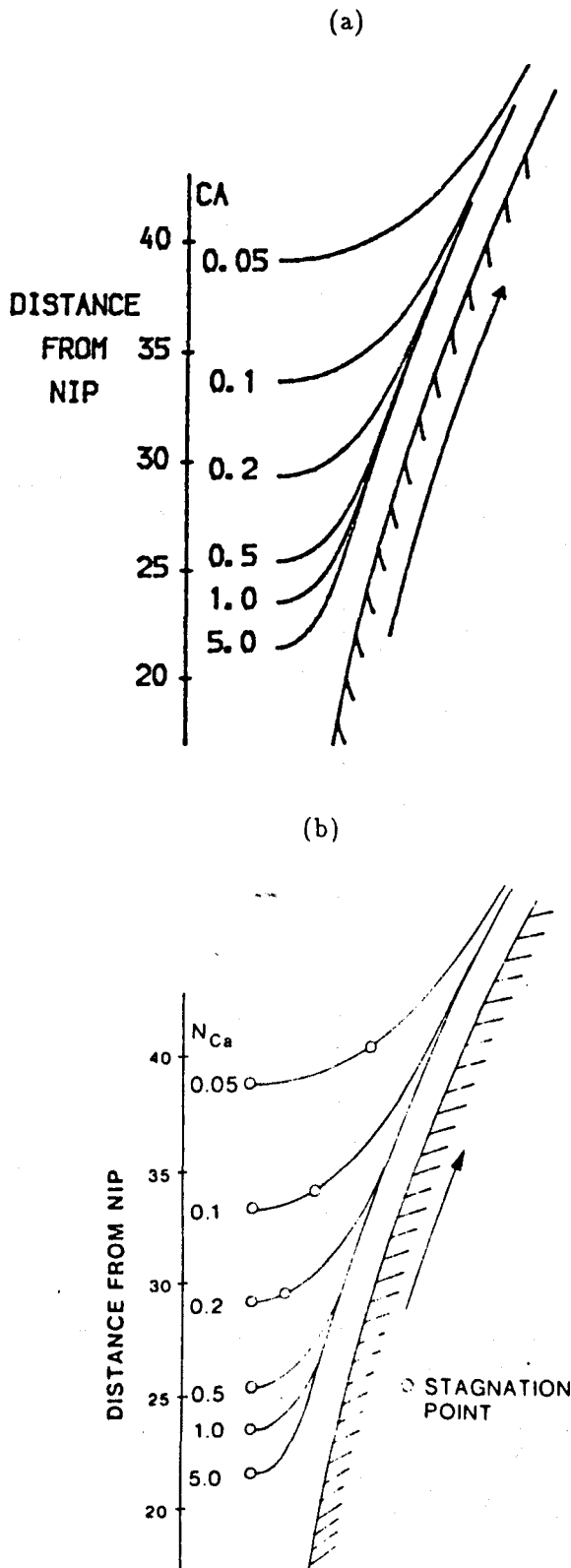
Figure 4.21: The Effect of Capillary Number on Free Surface Profiles in Symmetric, Fully-Flooded, Forward Roll Coating for $Re = 0.0$, $R/H_0 = 100$: (a) this work, (b) Coyle et al [1982]

(a)

(b)
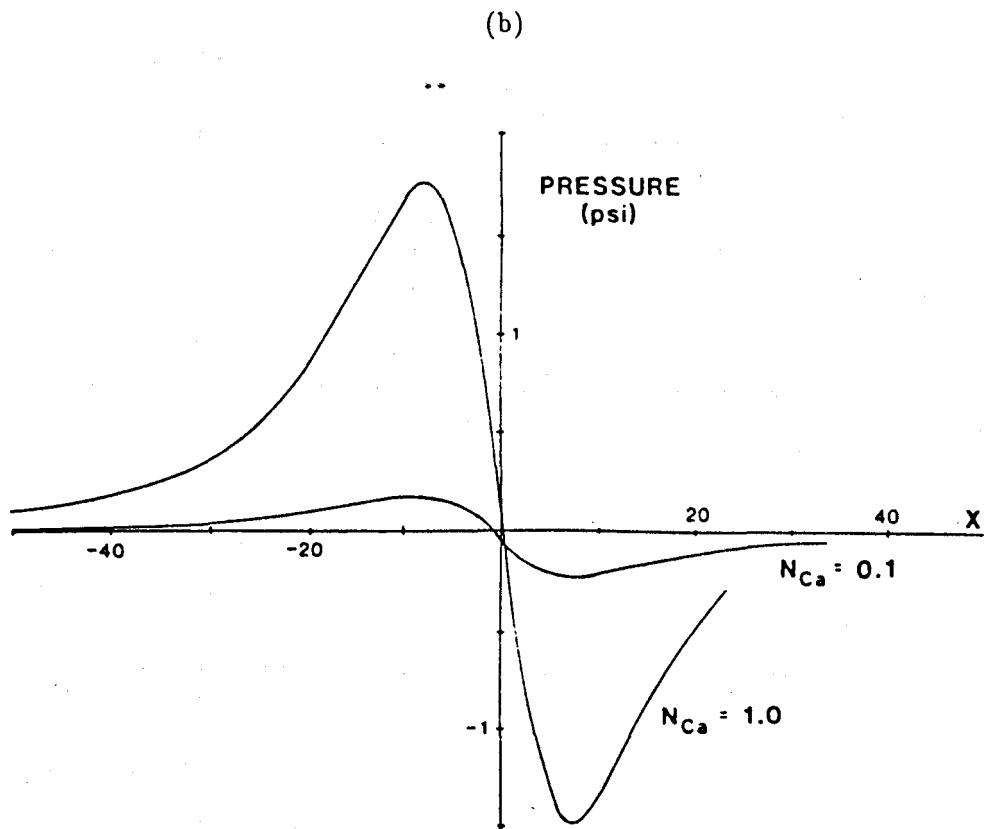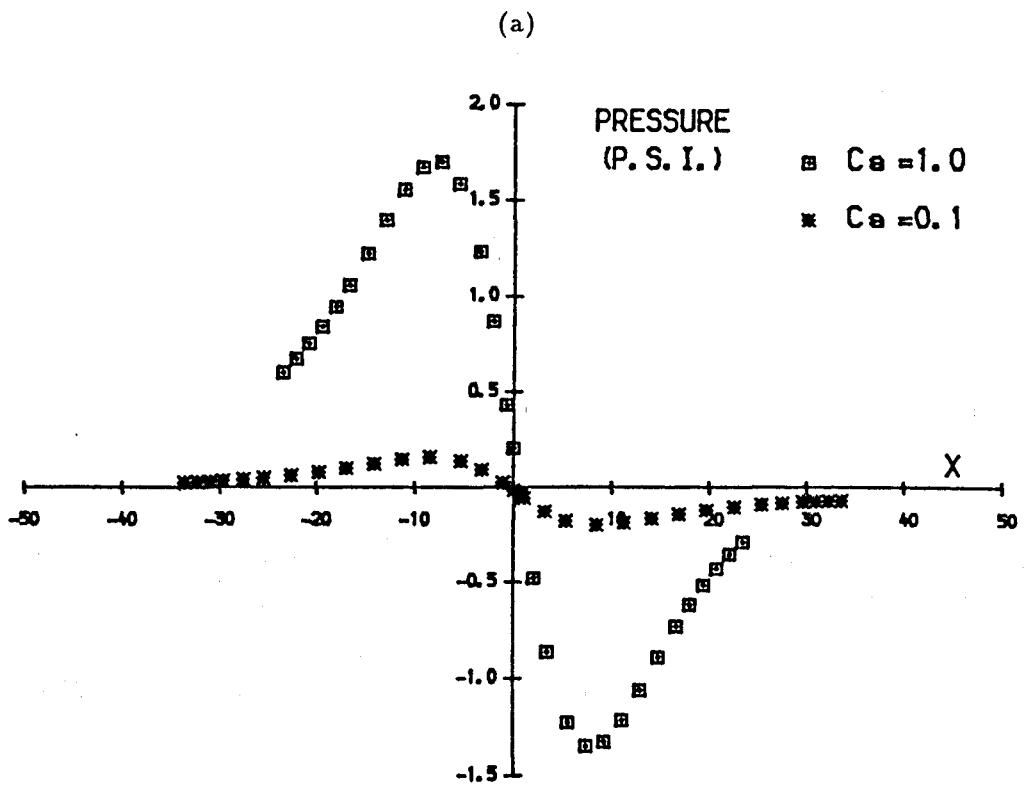
Figure 4.22: F.E. Pressures Generated in Numerical Solutions of Symmetric, Fully-Flooded, Forward Roll Coating for $Re = 0.0$, $R/H_0 = 100$: (a) this work, (b) Coyle et al [1982]
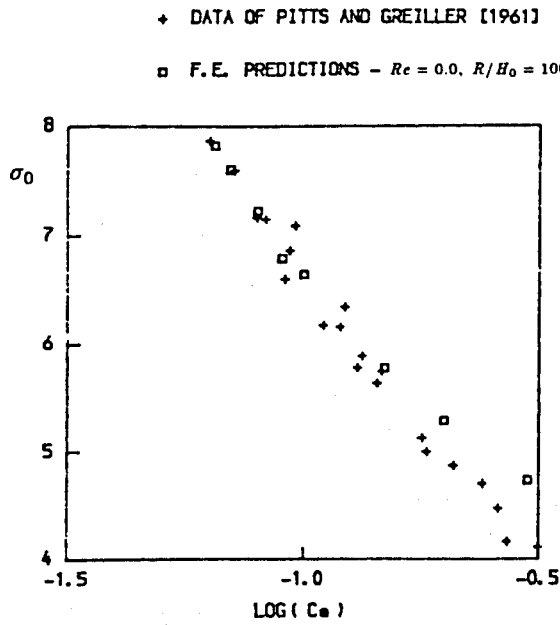
Figure 4.23: A Comparison between Theoretical Predictions (F.E.) and Experimental Measurements of σ_0
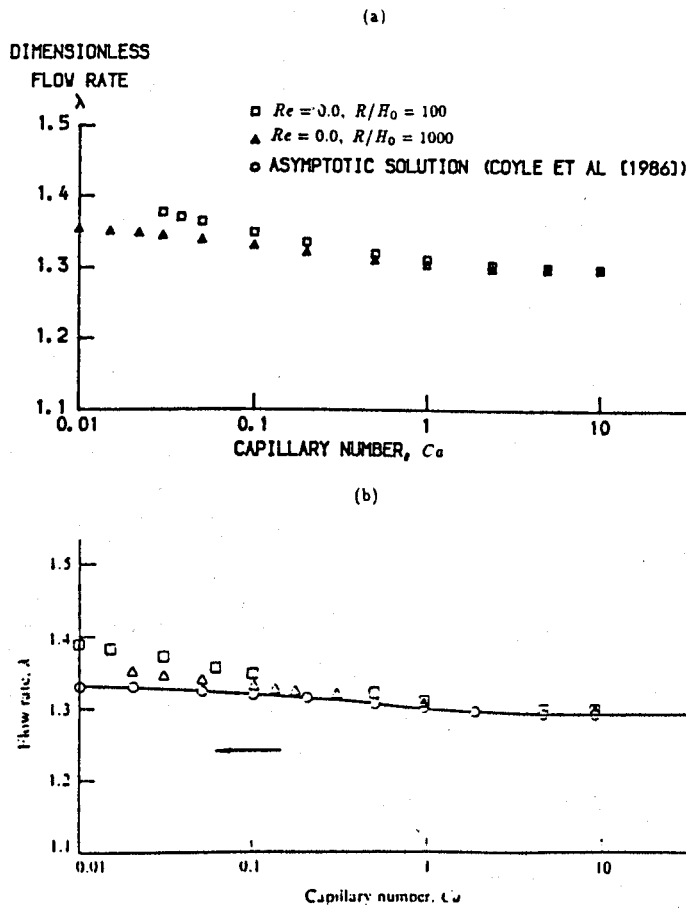
Figure 4.24: F.E. Predictions of the Dimensionless Flux in Symmetric, Fully-Flooded, Forward Roll Coating: (a) this work, (b) Coyle et al [1986]
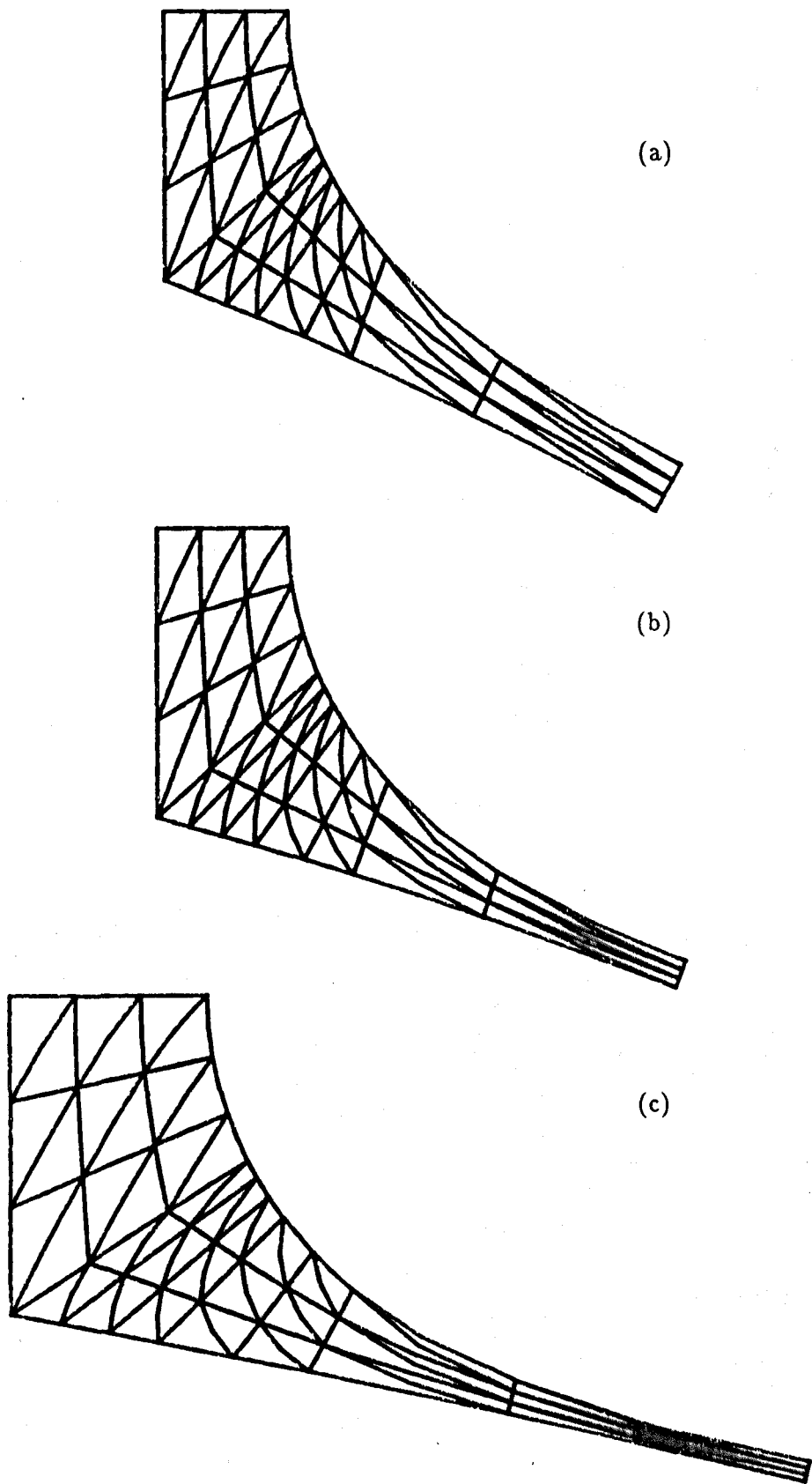
Figure 4.25:   Element   Distortions   in   Region   2   with Re =   0.0   and   (a) $Ca = 0.03$, $R/H_0 = 100$, (b) $Ca = 0.01$, $R/H_0 = 400$, (c) $Ca = 0.01$, $R/H_0 = 1000$
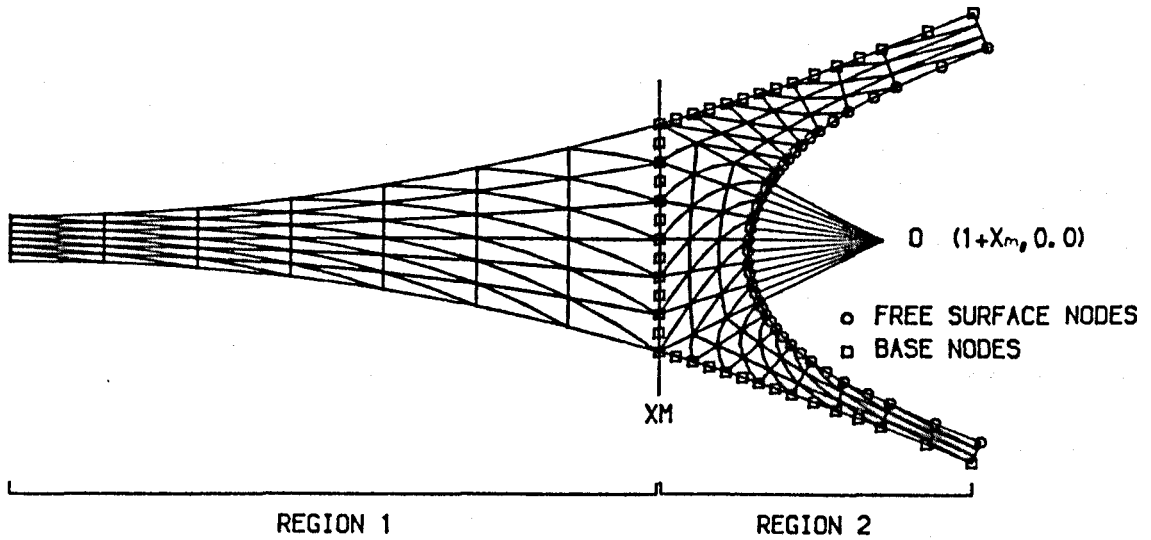
Figure 4.26: A Typical F.E. Grid Used in the Numerical Solution of Asymmetric Forward Roll Coating
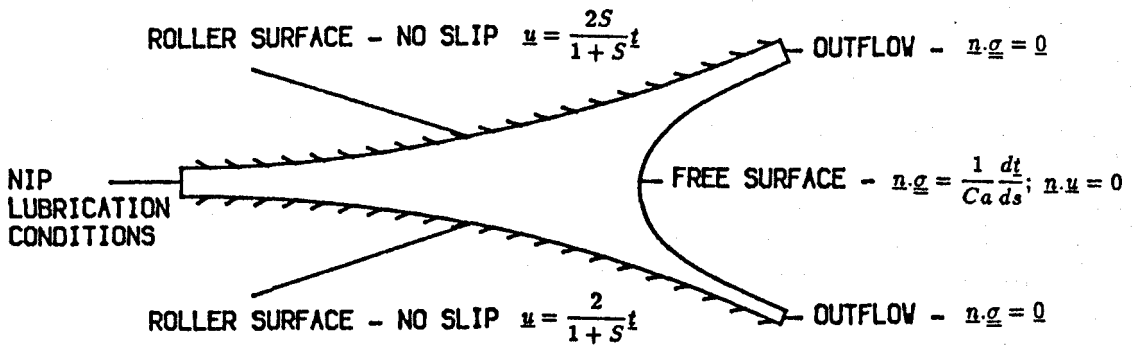
Figure 4.27: Boundary Conditions for Asymmetric, Fully-Flooded, Forward Roll Coating

FILM THICKNESS (a)

RATIO

T1/T2
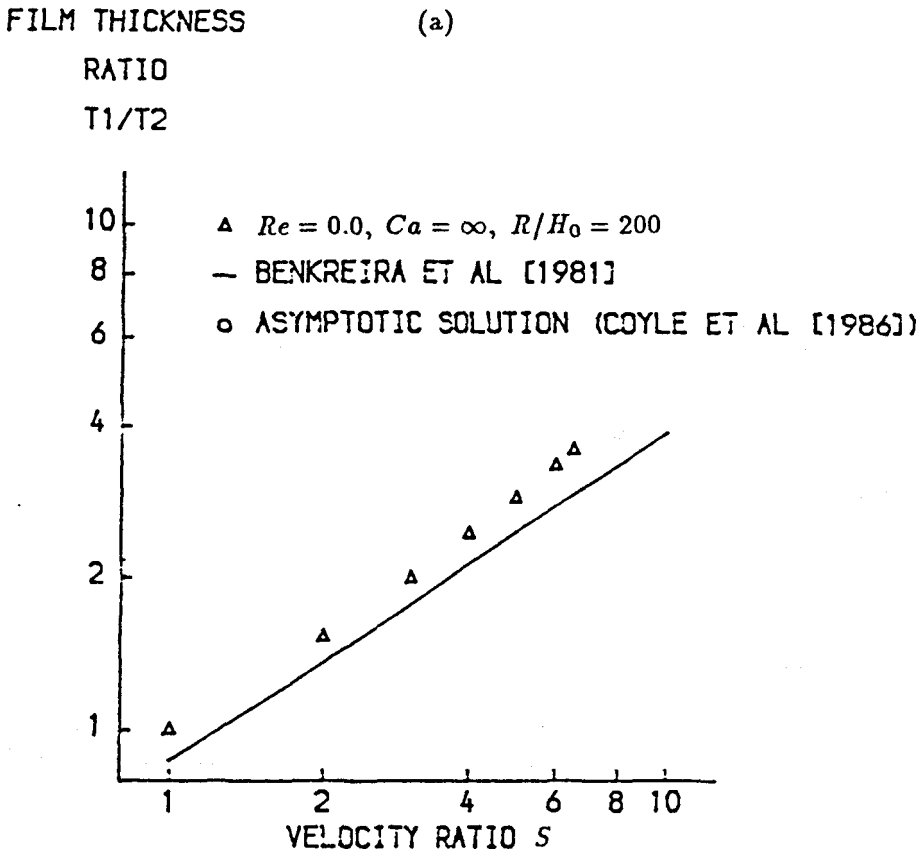
(b)
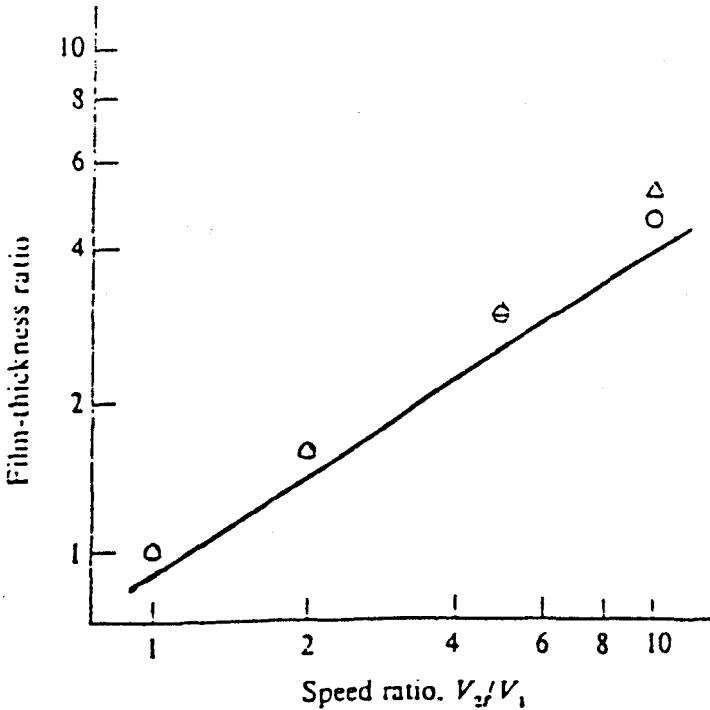
Figure 4.28: F.E. Film Thickness Ratio Predictions for Asymmetric, Fully-Flooded, Forward Roll Coating with $Re = 0.0$, $Ca = \infty$, $R/H_0 = 200$: (a) this work, (b) Coyle et al [1986]

(a)

(b)
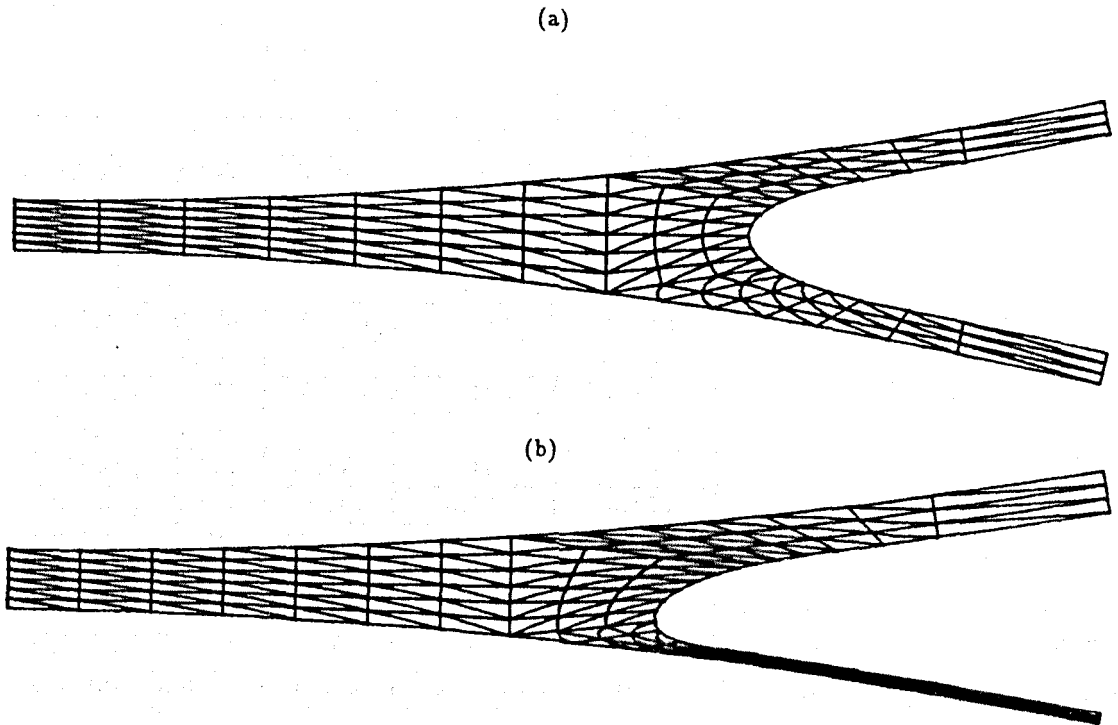
Figure 4.29: F.E. Grid Distortion In Asymmetric, Forward Roll Coating: (a) $Re = 0.0$, $Ca = \infty$, $R/H_0 = 200$, $S = 1.0$, (b) $Re = 0.0$, $Ca = \infty$, $R/H_0 = 200$, $S = 6.75$

(a) Horizontal Components of Liquid Velocity on the Vertical Centreline ($x = 0.0$)

$y =$	Semi-Analytical		Scheme A	Scheme D
	$N = 20$	$N = 40$		
2.000	1.082	0.947	1.000	1.000
1.875	0.651	0.651	0.653	0.666
1.750	0.355	0.355	0.363	0.353
1.625	0.127	0.127	0.136	0.146
1.500	-0.032	-0.032	-0.021	-0.028
1.375	-0.132	-0.132	-0.121	-0.113
1.250	-0.186	-0.186	-0.176	-0.174
1.125	-0.206	-0.206	-0.197	-0.190
1.000	-0.205	-0.205	-0.198	-0.192
0.875	-0.192	-0.192	-0.187	-0.181
0.750	-0.171	-0.171	-0.167	-0.164
0.625	-0.147	-0.147	-0.145	-0.143
0.500	-0.123	-0.123	-0.120	-0.119
0.375	-0.097	-0.097	-0.095	-0.095
0.250	-0.070	-0.070	-0.069	-0.068
0.125	-0.039	-0.039	-0.039	-0.036
0.000	0.0000	0.0000	0.0000	0.0000

(b) Vertical Components of Liquid Velocity on the Horizontal Centreline ($y = 1.0$)

$x =$	Semi-Analytical		Scheme A	Scheme D
	$N = 20$	$N = 40$		
-1.000	0.000	0.000	0.000	0.000
-0.875	0.095	0.095	0.094	0.083
-0.750	0.156	0.156	0.152	0.152
-0.625	0.183	0.183	0.178	0.170
-0.500	0.179	0.179	0.174	0.172
-0.375	0.152	0.152	0.147	0.142
-0.250	0.109	0.109	0.106	0.104
-0.125	0.057	0.057	0.054	0.053
0.000	0.000	0.000	0.000	0.000
0.125	-0.057	-0.057	-0.054	-0.053
0.250	-0.109	-0.109	-0.106	-0.104
0.375	-0.152	-0.152	-0.147	-0.142
0.500	-0.179	-0.179	-0.174	-0.172
0.625	-0.183	-0.183	-0.178	-0.170
0.750	-0.156	-0.156	-0.152	-0.152
0.875	-0.095	-0.095	-0.094	-0.083
1.000	0.0000	0.0000	0.0000	0.0000

Table 4.1: Liquid Velocity Components in Lid-Driven Cavity Flow ($A^* = 1.0$) – Comparison between Semi-Analytical and Numerical ($u - v - p$) Results

(a) Horizontal Components of Liquid Velocity on the Vertical Centreline ($x = 0.0$)

$y =$	Semi-Analytical ($N = 40$)	Numerical
2.0	0.94721	1.00000
1.9	0.71745	0.71918
1.8	0.46597	0.47092
1.7	0.25549	0.26178
1.6	0.08984	0.09829
1.5	-0.03245	-0.02387
1.4	-0.11642	-0.10765
1.3	-0.16890	-0.16067
1.2	-0.19703	-0.18971
1.1	-0.20730	-0.20059
1.0	-0.20519	-0.19990
0.9	-0.19496	-0.19089
0.8	-0.17979	-0.17626
0.7	-0.16186	-0.15913
0.6	-0.14255	-0.14027
0.5	-0.12259	-0.12095
0.4	-0.10213	-0.10078
0.3	-0.08081	-0.07987
0.2	-0.05778	-0.05788
0.1	-0.03157	-0.03116
0.0	0.00000	0.00000

(b) Vertical Components of Liquid Velocity on the Horizontal Centreline ($y = 1.0$)

$x =$	Semi-Analytical ($N = 40$)	Numerical
−1.0	0.00000	0.00000
−0.9	0.07813	0.07740
−0.8	0.13566	0.13345
−0.7	0.17068	0.16779
−0.6	0.18411	0.18066
−0.5	0.17885	0.17521
−0.4	0.15869	0.15563
−0.3	0.12751	0.12464
−0.2	0.08880	0.08707
−0.1	0.04549	0.04404
0.0	0.00000	0.00000
0.1	-0.04549	-0.04404
0.2	-0.08880	-0.08707
0.3	-0.12751	-0.12464
0.4	-0.15869	-0.15563
0.5	-0.17885	-0.17521
0.6	-0.18411	-0.18066
0.7	-0.17068	-0.16779
0.8	-0.13566	-0.13345
0.9	-0.07813	-0.07740
1.0	0.00000	0.00000

Table 4.2: Liquid Velocity Components in Lid-Driven Cavity Flow (A^*=1.0) obtained using Grid (b) of Figure 2.3

(a) Horizontal Components of Liquid Velocity on the Vertical Centreline ($x = 0.5$)

$y =$	Semi-Analytical ($N = 20$)	Numerical
0.0000	0.30575	0.29553
-0.0625	0.29550	0.28636
-0.1250	0.26638	0.25853
-0.1875	0.22260	0.21616
-0.2500	0.16931	0.16536
-0.3125	0.11120	0.10834
-0.3750	0.05168	0.05125
-0.4375	-0.00704	-0.00681
-0.5000	-0.06341	-0.06100
-0.5625	-0.11581	-0.11125
-0.6250	-0.16180	-0.15712
-0.6875	-0.19741	-0.19124
-0.7500	-0.21685	-0.21093
-0.8125	-0.21276	-0.20706
-0.8750	-0.17766	-0.17308
-0.9375	-0.10659	-0.10496
-1.0000	0.00000	0.00000

(b) Vertical Components of Liquid Velocity on the Horizontal Centreline ($y = -0.5$)

$x =$	Semi-Analytical ($N = 20$)	Numerical
0.0000	-0.00001	0.00000
0.0625	0.06090	0.05946
0.1250	0.10761	0.10518
0.1875	0.14431	0.14110
0.2500	0.17361	0.16949
0.3125	0.19668	0.19184
0.3750	0.21340	0.20769
0.4375	0.22225	0.21589
0.5000	0.22007	0.21253
0.5625	0.20188	0.19294
0.6250	0.16067	0.15150
0.6875	0.08757	0.07845
0.7500	-0.02732	-0.03634
0.8125	-0.19295	-0.19927
0.8750	-0.41442	-0.41914
0.9375	-0.69350	-0.68828
1.0000	-0.90219	-1.00000

Table 4.3: Liquid Velocity Components for the Flow in an Open, Driven Cavity (A^*=1.0) – Comparison between Semi-Analytical and Numerical ($u - v - p$) Results

Case (a): $S = 1$, $H^* = 0.5$

(i) Horizontal Components of Liquid Velocity on Vertical Centreline ($x = 0.0$)

$y =$	Analytical $(N = 40)$	Numerical
0.5000	0.99204	1.00000
0.4375	0.34377	0.35043
0.3750	-0.12500	-0.11354
0.3125	-0.40625	-0.39182
0.2500	-0.50000	-0.48455
0.1875	-0.40625	-0.39182
0.1250	-0.12500	-0.11354
0.0625	0.34377	0.35043
0.0000	0.99204	1.00000

(ii) Vertical Components of Liquid Velocity on Horizontal Centreline ($y = 0.25$)

$x =$	Analytical $(N = 40)$	Numerical
0.000	0.00000	0.00000
0.125	0.00000	0.00000
0.250	0.00000	0.00000
0.375	0.00000	0.00000
0.500	0.00000	0.00000
0.625	0.00000	0.00000
0.750	0.00000	0.00000
0.875	0.00000	0.00000
1.000	0.00000	0.00000

Case (b): $S = 2$, $H^* = 0.5$

(i) Horizontal Components of Liquid Velocity on Vertical Centreline ($x = 0.0$)

$y =$	Analytical $(N = 40)$	Numerical
0.5000	1.98409	2.00000
0.4375	0.89074	0.90072
0.3750	0.06262	0.07979
0.3125	-0.48429	-0.46266
0.2500	-0.75000	-0.72683
0.1875	-0.73446	-0.71280
0.1250	-0.43762	-0.42040
0.0625	0.14058	0.15057
0.0000	0.99204	1.00000

(ii) Vertical Components of Liquid Velocity on Horizontal Centreline ($y = 0.25$)

$x =$	Analytical $(N = 40)$	Numerical
0.000	0.33541	0.34719
0.125	0.08578	0.08593
0.250	0.00153	0.00049
0.375	-0.00113	-0.00113
0.500	0.00000	0.00000
0.625	0.00113	0.00113
0.750	-0.00153	-0.00049
0.875	-0.08578	-0.08593
1.000	-0.33541	-0.34719

Table 4.4: Liquid Velocity Components from the Zero Flux Model of Meniscus Roll Coating – Comparison between Analytical and Numerical ($u - v - p$) Results

Chapter 5: Further Results in Forward Roll Coating

5.1 - Introduction

5.2 - The Fully-Flooded Forward Roll Coater

    5.2.1 - Difficulties in Meshing Flows with Highly Curved Free Surfaces

5.3 - The Flow in a Flat Plate/ Roller Geometry

    5.3.1 - Introduction

    5.3.2 - A Numerical Model of Fully-Flooded Flow in a Flat Plate/ Roller Geometry

    5.3.3 - A Numerical Model of Starved Flow in a Flat Plate/ Roller Geometry

    5.3.4 - Results and Discussion

5.4 - The Effects of Starvation in Forward Roll Coating

    5.4.1 - Introduction

    5.4.2 - A Numerical Model of Starved Flow in a Forward Roll Coater

    5.4.3 - Results and Discussion

5.5 - Summary of F.E. Predictions for Starved Flow

Figures 5.1 - 5.23

Chapter 5

Further Results in Forward Roll Coating

5.1 Introduction

In Chapter 4 a F.E. free surface code was developed and applied to flow problems of gradually increasing complexity. At each stage, the numerical predictions were validated against, and in most cases agreed very well with, previously published data. In this chapter we modify this F.E. code in order to obtain theoretical predictions for fully-flooded and starved forward roll coating in regions of operating parameter space for which no previous results have been reported.

For example, previously published F.E. predictions of the film thickness ratio T_1/T_2 in the fully-flooded case (due to Coyle et al [1986]) were limited to the velocity ratio range most widely used in industry, namely $1 \leq S \leq 10$. In the next section, F.E. predictions of T_1/T_2 are obtained over the range $0.1 \leq S \leq 40$ in order to evaluate the suitability of (i) Savage's [1992] theoretical prediction and (ii) Benkreira et al's [1981] correlation for $S > 15$. In subsequent sections, the code is also used to investigate the effects of starvation on the associated velocity and pressure fields, and film thickness ratio T_1/T_2 in forward roll coating sytems. This is achieved by monitoring how the F.E. predictions of these quantities change as the dimensionless flux λ is reduced from its fully-flooded value. These numerical predictions are compared with Malone's

[1992] experimental flow visualisation, pressure and average film thickness ratio data for starved roll coating.

5.2   The Fully-Flooded Forward Roll Coater

In this section we return to the problem of fully-flooded forward roll coating with variable speed rollers. Once again, for convenience, attention is restricted to the case in which the roller radii are equal so that asymmetry is due only to unequal roller speeds. The boundary conditions for Coyle et al's [1986] model of this situation are shown in Figure 4.27.

In their F.E. study of this problem, Coyle et al [1986] published predictions for the dependence of the film thickness ratio T_1/T_2 on the velocity ratio in the range $1 \le S \le 10$ (see Figure 4.28). They concluded that, in the absence of gravity, $T_1/T_2 = S^{0.65}$ which is in qualitative agreement with the empirical formulation of Benkreira et al [1981]. However these predictions are limited to the *hypothetical* case in which $Ca = \infty$ (i.e. negligible surface tension), while in practice Ca is non-zero. Moreover, the value of Ca changes when the roll coater is operated at different velocity ratios S – in practice the lower roller speed is fixed whilst the upper one is changed (Malone [1992]) – so it is also necessary to test whether the F.E. predictions of T_1/T_2 have a Ca dependence. In the present section this is achieved by obtaining F.E. predictions of T_1/T_2 against S for a fixed value of Ca, and then repeating this process for a range of values of Ca.

Figure 5.1 shows F.E. predictions of T_1/T_2 for the case of fully-flooded forward roll coating. Results for three different values of Ca, namely $Ca = 0.1$, 0.5 and 2.0, are compared with Malone's [1992] experimental data, Benkreira et al's [1981] experimental correlation and Savage's [1992] 'stagnation-point' model (equation (1.9)). Note that, as in Figure 4.28, it is preferable to present results on a *logarithmic* rather than a normal scale because this (i) facilitates a convenient comparison with Benkreira et al's correlation, (ii) permits results to be shown over a wide range of velocity ratio. The F.E. results presented here employed the computational grid shown in Figure 4.26 and were

obtained by zeroth order continuation from results given in §§4.6.2. Once again, the F.E. equations are solved by the Frontal method, each iteration taking approximately 20 c.p.u. seconds. In most cases converged solutions were obtained after 5 iterations.

The results divide naturally into two regions: $0.1 \leq S \leq 15$ and $S > 15$. In the former, the F.E. predictions of T_1/T_2 are independent of Ca and agree reasonably well with Savage's prediction that $T_1/T_2 = S(S+3)/(1+3S)$. Moreover, since they are almost parallel to the solid line representing Benkreira et al's correlation, they also agree extremely well with Coyle et al's proposal that $T_1/T_2 = S^{0.65}$. Of course a proper assessment of the merits of any model can only be made by comparing its predictions with experimental data. However, in contrast to Benkreira et al who obtained data for the fully-flooded situation up to $S = 14.9$, Malone [1992] found that he was unable to obtain accurate data using Shell Tellus R5 oil outside the range $0.2 \leq S \leq 4.0$. He has attributed this to the differences in the physical properties between the liquid he used ($\eta = 0.008 \ Nm^2s$, $\mathcal{T} = 0.03 \ Nm^{-1}$) and those used by Benkreira et al [1981] ($0.06 \leq \eta \leq 1.68$, $0.032 \leq \mathcal{T} \leq 0.066$). Nevertheless his data agrees reasonably well with (i) Benkreira et al, (ii) the F.E. predictions, and (iii) Savage [1992] over this limited range.

When S is taken above 15, the F.E. predictions begin to exhibit a significant Ca dependence, most notably for $Ca = 2.0$. In the range $15 \leq S \leq 20$, this Ca dependence is only weak and the F.E. predictions are still in reasonable agreement with Savage's result, but they begin to show a palpable departure from the solid line correlation. When $S > 20$ this Ca dependence becomes stronger, with the result that the F.E. predictions are in poor agreement with the correlation, although they remain in broad agreement with Savage's prediction. Unfortunately there is an upper limit on the velocity ratio range over which F.E. predictions are achievable, for a given value of Ca, using the grid shown in Figure 4.26. For $Ca = 2.0$, F.E. results were obtainable for $S \leq 26$, whereas for $Ca = 0.5$ and 0.1 this upper limit increased to 30 and 40 respectively. The reasons for these convergence difficulties become apparent when we inspect elements in region 2 for flows with high velocity ratios.

Figure 5.2, for example, shows how elements in region 2 of the grid shown in Figure 4.26 are distorted for flows with $Re = 0.0$, $R/H_0 = 200$ and (a) $Ca = 0.1$, $S = 40.0$,

(b) $Ca = 0.5$, $S = 30.0$, and (c) $Ca = 2.0$, $S = 26.0$. Even though, in Figure 5.2, it is impossible to resolve the shape of those elements in the lower, thin film, it is evident that increasing S has the effect of increasing the curvature of the free surface portion near to the lower roller. Close inspection of these grids reveals that elements near this high curvature region have lost their triangularity. The author believes that the gradual loss of element triangularity, in this high curvature region, as the velocity ratio is increased explains why there is an upper limit on the velocity ratio range over which F.E. predictions are achievable: it leads to a critical situation at which the Jacobian of the transformation (B.40) vanishes with the result that the isoparametric mapping is no longer invertible. This idea is illustrated in Figure 5.3, which describes Strang and Fix's [1973] analysis of the relatively simple case in which two element sides are fixed and the mid-side node (P) of the third side can move. They showed that the isoparametric mapping (B.40) becomes singular when P moves into the shaded region in which either $0 \leq x \leq 1/4$ or $0 \leq y \leq 1/4$.

5.2.1 Difficulties in Meshing Flows with Highly Curved Free Surfaces

In previous sections we have emphasized that the accuracy of any F.E. solution whose computational grid contains distorted elements should always be questioned unless there is corroborating evidence to validate its predictions. For example, in Figure 5.1 the numerical predictions of T_1/T_2 up to $S = 14.9$ are supported by data from Benkreira et al's [1981] extensive experimental study. However above $S = 14.9$, there is no experimental evidence to confirm the F.E. predictions, although they are in qualitative agreement with Savage's [1992] theoretical prediction. In the present section we discuss the accuracy of the F.E. solutions for $S > 14.9$.

A first option would be to follow Coyle et al [1986], who seem to have assumed that if a solution is grid-independent for one set of parameters when a particular mesh generation algorithm is used, then solutions for a different set of parameters obtained using the same algorithm will also be grid-independent. The issues raised by this assertion will be discussed shortly. A second option might be to obtain a theoretical

error estimate for solutions with high S. Unfortunately most error analyses (e.g. the 'Patch Test') can only furnish global error estimates for solutions obtained on reasonably uniform F.E. grids. Consequently they are inapplicable for solutions obtained on the highly non-uniform grids used here. The other alternative, which has been used in earlier sections, is to obtain solutions on grids whose mesh generation algorithms differ from the one shown in Figure 4.26.

Of course, in practice it is simply not feasible to reproduce each of the F.E. solutions shown in Figure 5.1 on a number of different grids because the computational costs are prohibitively high. Instead we compromise by examining the effect of changing the number of elements and algorithmic parameters such as $XINC$ and the spine orientations (see §§4.5.3) on *one* particular high velocity ratio solution. We actually chose to obtain F.E. solutions for the parameter set $Re = 0.0$, $Ca = 0.1$, $R/H_0 = 200$ and $S = 30.0$ as this is representative of the high velocity ratio solutions shown in Figure 5.1. This should therefore indicate whether solutions in this parameter range are sensitive to the exact form of the grid chosen.

Testing the suitability of region 1 is easy: we found that adding more elements into region 1 of the grid shown in Figure 4.26 had no effect on the solution, which suggests that it is already sufficiently refined. However, evaluating the suitability of region 2 is far more difficult. Altering the grid in region 2 is very time-consuming because converged solutions for the chosen parameter set can only be obtained by zeroth order continuation from the initial solution (whose T_1/T_2 value is shown in Figure 5.1) when the grid is changed by small increments. Moreover the author's experience shows that the question of whether a grid is suitable for flows with high S is influenced far more by the relative orientation of the spines and the parameters $XINC$ than it is by the number of elements packed into region 2. Indeed, grids with inappropriate choices for the former are useless for flows with high S, regardless of how many elements are packed into region 2.

The last point illustrates the crux of the convergence difficulties experienced for the types of flow problems encountered in this thesis: the tesselation of region 2 by these primitive mesh generation algorithms is more of a 'black art' than a science. Ideally

one might circumvent these problems by packing many more elements into a uniform tessellation of region 2, but regrettably we are prevented from doing so here due to practical constraints on available storage (even with the Frontal method). Therefore the only useful test of the suitability of the tessellation in region 2 is to add more spines into the basic tessellation shown in Figure 4.26. When this was done, the predicted value of T_1/T_2 was found to be surprisingly insensitive to the number of extra spines added, which suggests that the tessellation of Figure 4.26 may be sufficiently refined for the chosen flow parameters.

We conclude this section by noting that although the heuristic test described above can be useful in some circumstances, its lack of mathematical rigour means that the high velocity ratio predictions shown in Figure 5.1 cannot be considered to be other than speculative in the absence of corroborating experimental data. Hence the simplicity of Savage's [1992] analytical result may render it to be of greater practical value than the F.E. results shown here; furthermore, at present it is impossible to determine whether the Ca dependence at high S is caused by mesh generation problems or actually occurs in reality. Finally, we have concentrated in this section on the inadequacies of the mesh generation schemes used in this thesis. It is also important to emphasize its not inconsiderable achievements. If the algorithmic mesh generation parameters for region 2 are chosen wisely, the F.E. method is able to predict the velocity and pressure fields and film thicknesses T_1, T_2 for flows with highly curved meniscii. At the present state of knowledge, these techniques provide the only means by which free surfaces, including the effects of surface tension, can be adequately incorporated into models for flow in this parameter range.

5.3 The Flow in a Flat Plate/ Roller Geometry

5.3.1 Introduction

In Chapters 2 and 3 we saw that the flow in a forward roll coater is transformed when the supply of liquid at inlet is substantially reduced below the level required to flood the inlet. In the remainder of this chapter, we show how the numerical methods

developed in Chapter 4 can be used to obtain theoretical predictions for the flow field

in a starved roll coater over the *entire* range of starvation from fully-flooded to ultra-

starved flow. These numerical predictions, which are compared with the analytical

predictions obtained earlier and Malone's [1992] experimental data, reveal interesting

transitions in both the velocity and pressure fields as the flux is decreased from its

fully-flooded value.

An important goal of the analysis presented here is to establish the validity or

otherwise of the prediction of the Zero flux model that the pressure profile is linear in

the central core of a meniscus roll coater (see §§2.5.2). Of course, this validation requires

experimental data with which to compare the theoretical predictions. However, from

an experimental viewpoint it is far more convenient to measure pressures in a simple

variant of the two roll system, consisting of a stationary upper plate and a moving lower

roller (see Figure 5.4), because this can be achieved by inserting 'pressure tappings'

into the plate – see also Chapter 6 of Malone's thesis. Note that the pressures in this

simplified 'flat plate/ roller geometry' are still relevant to the two roll system since this

configuration can be regarded as a special case – namely the upper roller stationary and

of infinite radius. Furthermore it forms a link between the forward and reverse modes

of roll coating, so the pressure distribution in this geometry should be characteristic of

both modes as the upper roller speed tends to zero (Adachi, Tamura and Nakamura

[1988]). For the above reasons, it is convenient to begin our investigation into the effects

of starvation by considering the flow in a flat plate/ roller geometry.

Despite its relative simplicity, the flow in this geometry has received much less at-

tention than the two roll system and moreover all authors seem to have restricted their

analyses to the fully-flooded situation. An important early contribution was made by

Hopkins [1957] whose lubrication model of the flow in the nip region was terminated

at separation boundary conditions. Meanwhile Sullivan and Middleman's [1979] study

had a different emphasis: they considered the case in which the plate is aligned verti-

cally and investigated how gravity affects the coating thickness produced on the roller.

Their analysis is similar to that of Hopkins, but they terminated the lubrication regime

by Reynolds conditions (1.5) instead. The only numerical solutions of this problem

which have appeared in the literature to date are those given by Coyle et al [1986]. Their numerical predictions agree reasonably well with those of the aforementioned lubrication theories and the experimental data of Sullivan and Middleman [1979] and Adachi et al [1988].

In the following two sections we describe models for flow in a flat plate/ roller geometry which can be solved numerically, using the techniques developed in Chapter 4, to yield theoretical predictions of the velocity and pressure fields over the entire range of starvation. The first of these models, which pertains to the fully-flooded situation, is actually a modified version of that given by Coyle et al [1986] for the two roll system. In each of these models, the flow problem shown in Figure 5.4 is non-dimensionalised by scaling liquid velocities by V, the velocity of the roller, while the length and pressure scalings are given by equation (4.69). Note that there is, however, one modification to the non-dimensionalisation used in §§4.5.2 because, for the present application, it is more convenient to define H_0 to be the *total* nip width between the plate and roller rather than the semi-nip width.

5.3.2   A Numerical Model of Fully-Flooded Flow in a Flat Plate/ Roller Geometry

The (dimensionless) model for fully-flooded flow in a flat plate/ roller geometry developed here is illustrated in Figure 5.5. There are many similarities between this model and the one described in §§4.5.2 for the two roll situation because once again we invoke lubrication theory in order to restrict the analysis to the flow region between the nip and the downstream free surface. In fact, the boundary conditions at the roller surface, free surface and outflow boundaries are identical to those shown in Figure 4.13 while those at the plate, nip and static contact line (where the downstream free surface meets the plate) differ from conditions (i), (v) and (vi) of §§4.5.2 respectively. In the present application they are replaced by

(i) On the Plate

The no-slip condition yields a stagnation point condition: $\underline{u} = 0$ which is imposed in the usual way.

(ii) At the Nip

As in §§4.5.2, it is possible to derive boundary conditions on the liquid velocity and pressure at the nip by a lubrication analysis of the flow in the nip region. This analysis is slightly different to the one presented in §§4.5.2 due to the different definition of H_0; in the flat plate/ roller geometry it is more natural to define the dimensionless flux λ by

$$\lambda = \frac{Q}{VH_0} \tag{5.1}$$

rather than by equation (4.74). The transformed nip region co-ordinates (θ, η) and the modified pressure, p^*, have the same definitions as those used in equations (4.73), (4.74) but note that $\eta = 1$ on the plate and $\eta = 0$ on the roller surface. In terms of these dimensionless quantities it may be shown that the pressure gradient (4.78) is replaced by

$$\frac{\partial p^*}{\partial x} = \frac{6}{(1 + x^2/2)^3} \left(1 + x^2/2 - 2\lambda\right) \tag{5.2}$$

which may be integrated subject to the usual fully-flooded assumption that pressure decays to atmospheric far upstream of the nip (i.e. $p^*(-\infty) = 0$), to yield an expression for the pressure at any point of the nip region in terms of λ. It is easily shown that the boundary conditions on velocity and pressure at the nip ($\theta = 0$) reduce to

$$u = 3(1 - 2\lambda)(\eta^2 - \eta) + 1 - \eta \tag{5.3}$$

$$v = 0 \tag{5.4}$$

$$p = \frac{3\sqrt{2}\pi}{2} \frac{R}{H_0} \left(1 - \frac{3\lambda}{2}\right) \tag{5.5}$$

These conditions are imposed in the numerical solution by the method described in §§4.5.3.

(iii) At the Static Contact Line P

The downstream free surface intersects the stationary plate at a static contact line P where the contact angle θ_c shown in Figure 5.5 is *unknown* in general. Consequently there are two parameters associated with the contact line, namely its position (which is parametrised by X_m, see §§4.5.3) and the contact angle θ_c, which must be determined

in any full solution of the problem. However in any numerical simulation a compromise must be reached because there is only *one* equation – the kinematic residual (4.50) associated with P – to determine the *two* unknowns θ_c and X_m. There are two possible courses of action that can be taken: (i) impose the position of the contact line, i.e. impose X_m, as a parameter and allow the contact angle θ_c to be determined as part of the solution, or (ii) impose the contact angle θ_c to a value measured experimentally.

In the solutions presented here we follow Coyle et al [1986] and choose alternative (ii). As explained in §§4.5.2, since there are stagnation point conditions on liquid velocity, $u = v = 0$, at P the extra equation needed to determine θ_c is not actually a kinematic residual, but instead takes the form $\underline{i}.\underline{t} = \cos\theta_c$, where $\underline{i}$ is the unit horizontal vector and $\underline{t}$ is the unit tangent vector to the free surface at the contact line, calculated in terms of those F.E. variables which specify the position of the downstream free surface. This completes the equation set for the fully-flooded case.

In the following section we show how this fully-flooded model can be refined to accomodate the effects of starvation.

5.3.3 A Numerical Model of Starved Flow in a Flat Plate/ Roller Geometry

The success of the analytical film thickness model for forward meniscus roll coating supports the hypothesis that lubrication theory provides an accurate description for the flow in the nip region of a forward roll coater in both the fully-flooded and ultra-starved cases. This observation motivates the key assumption of the starved model adopted here: we postulate that the flow in the nip region is well approximated by lubrication theory over the *entire* range of starvation , i.e. including the moderately-starved case.

In the above model for the fully-flooded situation, the equation needed to determine λ (equation (5.5)) is provided by a lubrication analysis of the flow in the nip region subject to the fundamental fully-flooded assumption that pressure decays to atmospheric far upstream of the nip, i.e. $P(-\infty) = 0$. However, Malone's [1992] experimental observations show that this assumption is no longer valid when the inlet is starved

because the upstream free surface moves much closer to the nip – see Figure 5.6 for a typical ultra-starved situation. Therefore in the starved case, it is no longer possible to provide a pressure condition at the nip as is required if λ is to be predicted.

Consequently, any analysis of starved flow in a flat plate/ roller geometry which seeks to determine the flux λ must necessarily include the effects of the upstream free surface, its associated static contact line and the inlet film. Such an analysis is beyond the scope of the present work. Fortunately, there is a simpler alternative which once more allows the analysis to be confined to the flow between the nip and the downstream free surface: simply impose λ as a parameter, thereby removing the need for a nip pressure condition.

It can easily be shown that, under the non-dimensionalisation used in this section, the small flux model (equations (3.4), (3.5)) furnishes the same velocity profile across the nip as that given by the lubrication equations (5.3), (5.4). Hence, under the key assumption described above, the model of starvation adopted here is to simply impose λ in the latter conditions to a value which is less than that predicted by the fully-flooded analysis of §§5.3.2. This provides a simple mechanism for altering the degree of starvation in the flow.

Apart from the condition at the nip, all other boundary conditions for the starved case, namely those at the roller surface, outflow boundary, flat plate and static contact line, are identical to those for the fully-flooded situation. In the following section we present theoretical predictions obtained by solving the above models numerically using the Galerkin F.E. method and compare the major features of the predicted flow transition with those observed experimentally.

5.3.4   Results and Discussion

The first F.E. predictions for the flow in this geometry were obtained for the fully-flooded case with $Re = 0.0$, $Ca = 0.1$, $R/H_0 = 100$ and a contact angle $\theta_c = 90°$ in order to make the geometry identical to that of the 'half-domain' solution for the symmetric, fully-flooded, forward roll coater. The grid used in this first solution consists of 245 nodes, 102 elements and 21 spines; region 2 of this grid is shown in Figure 5.7

(a), while region 1 is identical to that of grid (a) shown in Figure 4.19. The start-up approximation for this grid was estimated from the solution obtained in §§4.5.5 for the symmetric, fully-flooded, forward roll coater with the same set of parameters. However, in practice it was necessary to experiment with many different 'guesses' of the contact line location parameter X_m before the first converged solution was actually obtained.

To test the sensitivity of the calculated flows to the discretisation used, this initial solution was compared against solutions obtained using 2 finer grids whose downstream regions are shown in Figure 5.7: grid (b) with 357 nodes, 150 elements and 27 spines, and grid (c) with 567 nodes, 248 elements and 33 spines. Note that the upstream regions of grids (b), (c) have tessellations which are identical to those shown in Figures 4.19 (b), (c) respectively. Meanwhile a series of numerical results, in which the outflow boundary was placed at a number of different locations, were obtained on all 3 grids in order to ensure that the solutions were insensitive to changes in its position. It was observed that in all solutions obtained using grids (a), (b) and (c), each iteration took approximately 10, 12 and 14 c.p.u. seconds respectively. Moreover those numerical results which were insensitive to changes in the position of the outflow boundary revealed that in changing from (i) grid (a) $\rightarrow$ (b), (ii) grid (b) $\rightarrow$ (c) the most sensitive variables (X_m and the pressures at the nip) changed by less than 3% and 0.01% respectively of their previous values. This suggested that grid (b) was suitable for flows with parameters in this range; consequently the next two sets of results are obtained by zeroth order continuation from a suitable initial solution obtained using grid (b).

Figure 5.8 examines the effect of the imposed contact angle θ_c on the predicted downstream free surface profile for this flow. It shows that the position of the static contact line is very sensitive to the value of the contact angle; in particular, when θ_c increases the downstream free surface recedes towards the nip. This prediction concurs with those shown in Figure 18 of Coyle et al [1986]. Another interesting prediction relates to the flow rate through the nip. Note that as the effects of gravity are neglected in the theoretical predictions (i.e. $St=0$ in equation (4.1)), the film on the lower roller achieves an asymptotic thickness whose value is proportional to the flux through the nip. Therefore since this thickness is insensitive to θ_c in the range $70^o \leq \theta_c \leq 140^o$, so

too is λ. Actually the predicted values of λ in the solutions shown in Figure 5.8 satisfy $0.64 \leq \lambda \leq 0.66$, which are in reasonable agreement with Coyle et al's [1986] F.E. predictions (note that the λ values given in their Figure 17 are double those defined by equation (5.1)) and the experimental data of Sullivan and Middleman [1979], who measured $0.55 \leq \lambda \leq 0.65$, and Adachi et al [1988] who found the average value of λ to equal 0.6.

In his experimental study of the flow in a flat plate/ roller geometry, Malone [1992] measured the position and shape of the downstream free surface under different degrees of starvation. His free surface profile in the fully-flooded case (for which he estimated $Ca = 0.05$ and $R/H_0 = 110$) displayed an apparent contact angle $\theta_c = 33^o$ – quite different from those considered so far. Numerical predictions for fully-flooded flow with this set of parameters (and $Re = 0.0$), obtained using grids (b) and (c) of Figure 5.7, demonstrated that this low value of θ_c results in element distortion near the contact line P; this feature is illustrated in Figure 5.9, where elements in region 2 of these two grids are shown. Previous experience suggests that these distortions may render grid (b) unsuitable for flows with θ_c in this range, but the computed results suggest otherwise because they reveal that in changing from grid (b) $\rightarrow$ (c), the most sensitive variable (X_m in this case) changes by less than 0.3% of its previous value. Moreover, since Malone's experimental profiles had $\theta_c \approx 33^o$ over the entire range from fully-flooded to ultra-starved flow (see later), all subsequent F.E. solutions presented in this section have been calculated using grid (b).

Figure 5.10 examines the effect of changing the capillary number, Ca, on the predicted downstream free surface profile for a flow with $Re = 0.0$, $R/H_0 = 110$ and a *fixed* $\theta_c = 33^o$. As in the symmetric, fully-flooded, forward roll coater the free surface position is very sensitive to the value of Ca: increasing the value of Ca results in the free surface receding towards the nip (compare with Figure 4.21). Once again, the asymptotic film thicknesses, and consequently the dimensionless fluxes λ, are reasonably insensitive to changes in Ca; more precisely, the solutions shown in Figure 5.10 have $0.6 \leq \lambda \leq 0.66$. In the remainder of this section, Malone's [1992] experimental measurements of the free surface profiles, pressures and flow field in a flat plate/ roller

geometry, over the entire range of starvation, are compared with F.E. predictions for similar flow situations. However, any comparison between theory (F.E.) and experiment is only meaningful if the flow parameters Ca, R/H_0, θ_c and λ, which are required as input into any F.E. solution, can be estimated accurately. Hence, before presenting any theoretical results, it is worthwhile highlighting some of the practical difficulties Malone faced in estimating these parameters, because this promotes a more realistic appraisal of the agreement between theory and experiment which can be expected.

We consider the downstream free surface profile measurements, which were obtained on an experimental rig with the roller radius $R=25mm$, first. Estimation of the capillary number, $Ca = \eta V/T$, is relatively straightforward because the physical properties are known and the roller speed V can be measured accurately. On the other hand, the inaccuracy in the measurement of θ_c is expected to be greater than that in Ca, but is probably no greater than those caused by the empirical treatment of the contact line. However, inaccuracies in the measurement of the nip-width H_0, which impact upon the two remaining parameters R/H_0 and λ, are of far greater practical significance. Malone measured H_0 using a 'feeler guage' with 50 micrometre increments and found that while he could push the guage through the nip when it was set to 200 micrometres, he was unable to do so when the guage setting was increased to 250 micrometres. He subsequently estimated H_0 to be the average of these two values, i.e. 225 micrometres. This method, which was the best available to him, produces an uncertainty in H_0 of 11% which, even after ignoring the error in estimating the flux Q, leads to a potential error in both λ and R/H_0 of the same order of magnitude.

Malone estimated that his free surface profile measurements for the fully-flooded case related to a flow with parameters $Ca = 0.05$, $R/H_0 = 110$, $\theta_c = 33^o$ and $\lambda = 0.5$. Note that this value of the dimensionless flux is significantly lower than the value, $\lambda = 0.66$, given by the corresponding numerical solution of the fully-flooded model (with $Re = 0.0$ also) and the previously cited data of Sullivan and Middleman [1979] and Adachi et al [1988]. This discrepancy is surprising since it cannot be explained by even the most optimistic scenario of a 10% under measurement of λ – see discussion above. This may be the result of inertial effects becoming significant (for the low

viscosity Shell Tellus R5 oil) at the higher roller speeds needed to entrain larger fluxes λ, since both Tharmalingham and Wilkinson [1978] (p 1158) and Wu, Weng and Chen [1985] (p 250) have reported that inertial effects can limit the amount of liquid entrained by the roller surface.

It was deemed more appropriate to compare the fully-flooded experimental data with theoretical predictions from both the fully-flooded model (where λ is determined) and the starved model with λ set equal to 0.5. These results are shown in Figure 5.11 (a). The data agrees well with the fully-flooded prediction, whereas the agreement with the starved solution is at best only reasonable. The second, and final, free surface profile comparison is for an ultra-starved flow in which Malone estimated that $Ca = 0.0065$, $R/H_0 = 110$, $\lambda = 0.13$ with θ_c once more equal to 33°. Figure 5.11 (b) shows that the corresponding F.E. prediction from the starved model agrees reasonably well with his experimental data.

We now seek to determine the nature of the flow transition that occurs in a flat plate/ roller geometry when the flux passing through the nip is gradually reduced from a fully-flooded to an ultra-straved value. The strategy adopted here is to compare theoretical predictions for the flow, obtained from numerical solutions of the starved flow model for a range of values of the dimensionless flux λ, with Malone's experimental measurements for similar flow situations. Now, in his experiments Malone found it expedient to reduce the flux through the nip by simply reducing the roller speed V with the result that λ, Ca and θ_c all varied simultaneously. Fortunately, the F.E. predictions of the flow field over a range of Ca and θ_c values exhibit essentially the same transitional characteristics when λ is reduced. Therefore it is possible to illustrate the flow transition predicted by the F.E. method by the more convenient device of obtaining solutions in which only λ is changed, leaving Ca and θ_c fixed. Indeed this is the strategy adopted here.

Figure 5.12 demonstrates the theoretical transition between fully-flooded and moderately-starved flow predicted by the F.E. method by presenting velocity vectors and *dimensionless* F.E. pressures generated on the surface of the plate obtained from numerical solutions for the parameter set $Re = 0.0$, $Ca = 0.05$, $R/H_0 = 110$, $\theta_c = 33°$

with $\lambda = 0.66$ (fully-flooded), $0.55, 0.5, 0.45, 0.35$ and 0.25. Note that in order to ensure that the velocity vectors are clearly visible, it was necessary to present each solution on different scales since unilaterally reducing the flux actually results in the downstream free surface receding towards the nip. This point is illustrated in Figure 5.12 (g) where the free surfaces are drawn on a common scale. These results predict that starving the flow results in the recirculation next to the downstream free surface extending closer to the nip. Note that for $\lambda = 0.25$, the recirculation actually extends upstream of the nip because the lubrication velocity profile condition (5.3) imposes reverse flow at the nip for $\lambda < 1/3$.

The pressure transition is, perhaps, more interesting. Each point in a given pressure profile indicates the (dimensionless) F.E. pressure generated at the position on the plate immediately above that point – no pressure scales are shown here since we are only interested in the *shape* of the pressure profile (see later). Note also that the solid line denotes the atmospheric pressure level $(p = 0)$, which means that pressures below it are sub-ambient. In the fully-flooded case, the pressure profile shows the characteristic sub-ambient pressure loop demonstrated in Figure 1.10. As the flux is reduced, the pressure at the nip (i.e. the one shown in the figure immediately below the nip) falls and by $\lambda = 0.5$ there no longer exists a turning point in the entirely sub-ambient pressure profile. When the flux is reduced still further from $\lambda = 0.5$ to $\lambda = 0.25$, it is possible to identify two qualitatively different, but adjoining, regions of the pressure profile. In the first region, which begins at the nip, the profile is reasonably linear whereas in the second, which extends up to the meniscus, the pressure is almost constant.

Figure 5.13 illustrates the theoretical transition between moderately-starved and ultra-starved flow in a flat plate/ roller geometry predicted by the F.E. method. As the flow parameters in Malone's free surface profile measurements of ultra-starved flow, shown in Figure 5.11, were estimated to be $Ca = 0.0065$, $R/H_0 = 110$, $\theta_c = 33°$ and $\lambda = 0.13$, it was deemed appropriate to exemplify this theoretical transition by presenting numerical solutions for the parameter set $Re = 0.0$, $Ca = 0.0065$, $\theta_c = 33°, R/H_0 = 110$ with $\lambda = 0.2, 0.13$ and 0.07. These results predict that gradually reducing the flux λ from a moderately-starved to an ultra-starved value strengthens

the recirculation until the flow becomes essentially eddy flow coupled with a thin film of liquid attached to the roller. Once again note that reducing the flux unilaterally results in the downstream free surface receding towards the nip – a point illustrated in Figure 5.13 (d). Finally, the ultra-starved pressure profiles are qualitatively similar to those shown in Figure 5.12 for $\lambda \leq 0.45$, although the constant pressure region extends further upstream towards the nip when λ is reduced to an ultra-starved value.

These theoretical flow transition predictions are now compared with Malone's experimental findings for similar flow situations. We consider the flow visualisations, which he performed on the same experimental rig as was used in his free surface profile measurements, first. Figures 5.14 (a)-(d) show typical flow visualisations which he obtained for starved flow in a flat plate /roller geometry where the starvation increases from fully-flooded (Figure 5.14 (a)) to ultra-starved (5.14(d)). In each of these situations, he injected blue dye into the inlet film (the roller is moving from left to right) with the result that dark blue dye regions indicate the path taken by the majority of the liquid entering the nip; whereas those which are relatively clear indicate the presence of a recirculation. Note that the downstream meniscus positions are not shown in these photographs – unfortunately Malone was unable to capture a sufficiently wide enough field of view to include all features of the flow field. These visualisations are in qualitative agreement with the theoretical transition predicted in Figures 5.12 - 5.13 because they clearly demonstrate that the recirculation extends further upstream towards the nip as starvation is increased. Moreover, ultra-starved flow is seen to consist of a large recirculation which extends upstream of the nip coupled with a thin liquid film (i.e. the dark region of Figure 5.14 (d)) attached to the lower roller.

We now compare the above theoretical pressure transition predictions against experimental pressure measurements. In order to measure the pressure profile in a flat plate/ roller geometry over the entire range of starvation, Malone inserted a series of 'pressure tappings' (at $2mm$ intervals) into the plate of a second, larger experimental rig with $R = 0.13m$ and H_0 (estimated by the 'feeler guage' technique outlined above)=325 micrometres. In Figure 5.15 (a), his pressure data for the fully-flooded and moderately-starved situations have been converted to units of *Pascal* (N/m^2) while the

horizontal distance from the nip in the downstream direction, X, is measured in mm. Once again, the experimental measurement of $\lambda = 0.503$ for the fully-flooded case, which agrees extremely well with the value, $\lambda = 0.5$, obtained earlier on the smaller rig, is significantly lower than the predicted value ($\lambda = 0.66$) and the data of Sullivan and Middleman [1979] and Adachi et al [1988]. Since, on this larger rig, the maximum error in λ which can be attributed to uncertainty in measuring H_0 by the feeler guage method (where $H_0 = 325 \pm 25$ micrometres) is only 8%, this divergence cannot be explained by experimental error.

These pressure profiles show that reducing the flux from a fully-flooded value results in a fall in both the upstream pressure maximum and the pressure at the nip so that pressures downstream of the nip are entirely sub-ambient. They have the same general characteristics as those shown in Figures 5.12 - 5.13 except for the fact that there is still a pressure minimum when $\lambda = 0.388$ which disagrees with both the F.E. method and the lubrication theory pressure gradient (5.2), which predict that there should be no turning points, i.e. points at which $\partial p/\partial x = 0$, for a flow with $\lambda < 0.5$. Finally, note that when the flux is reduced the downstream contact line position is almost invariant whereas the upstream one moves closer to the nip. The former is contrary to what one might expect given the effect of reducing λ shown in Figures 5.12 (g) and 5.13 (d), but the reason for this is that Malone reduced λ by simply reducing the roller speed so the consequent decrease in Ca $(=\eta V/T)$ counteracts the usual effect of reducing λ (see Figure 5.10).

Malone's data for the pressure transition between moderately- and ultra-starved flow in a flat plate/ roller geometry is shown in Figure 5.15 (b). These profiles are in qualitative agreement with the theoretical profiles for moderately-starved flow shown in Figure 5.13 because they are entirely sub-ambient and consist of an (almost) linear region near the nip adjoining a constant pressure region near the downstream free surface. Furthermore, the size of the latter increases as λ is decreased to an ultra-starved value. Note that these findings are consistent with the analytical prediction of the zero flux model that the pressure gradient is constant in the central core of a meniscus roll coating bead.

In contrast, however, the experimental results show that the downstream pressure minimum disappears when $\lambda \approx 0.3$ rather than at the predicted value of $\lambda = 0.5$. As in the moderately-starved cases, the downstream contact line position is almost invariant, but the extremely low speeds needed to attain an ultra-starved condition result in the upstream contact line actually moving *away* from the nip. This surprising feature of ultra-starved flow is discussed at greater length in Chapter 6 of Malone [1992].

So far the comparison between theory and experiment has been qualitative in nature. It is possible, however, to give a *quantitative* comparison by converting the dimensionless pressures, p, which are generated in any F.E. solution to actual pressures, P, by the transformation $P = \eta V/(RH_0)^{\frac{1}{2}} p$. For example, in Figure 5.16 (a) experimental data for a fully-flooded flow, in which Malone estimated the flow parameters to be given by $\lambda = 0.503$, $Ca = 0.067$, $R/H_0 = 400$ and $\theta_c = 33^o$, is compared with theoretical predictions for the same set of parameters (and $Re = 0.0$) from (i) the fully-flooded model, (ii) the starved model with λ set equal to 0.5. Theoretical predictions from the former (where λ is predicted to equal 0.66) agree well with the experimental data, although there is a discrepancy between their contact line positions. Meanwhile, those from the latter show a marked divergence from the data near the nip – this is to be expected since their shapes are quite different when $\lambda = 0.5$ – but they agree reasonably well near the downstream contact line. The pressures shown in Figure 5.16 (b) relate to an ultra-starved flow with parameters $Ca = 0.0087$, $R/H_0 = 400$, $\theta_c = 33^o$ and $\lambda = 0.139$. In this case the agreement between the F.E. predictions and experimental data is excellent, except in the region close to the nip. Note that the magnitudes of the pressures shown in Figures 5.15 - 5.16 are $O(100 \ Nm^{-2})$ which is extremely small compared to atmospheric pressure ($2 \times 10^5 \ Nm^{-2}$). We conclude this section by proposing a physical mechanism which explains why the pressures in the ultra-starved case are entirely sub-ambient.

In Chapter 4 we saw that at a curved surface equilibrium is maintained by a balance of normal stresses due to viscosity, surface tension and atmospheric pressure. Since, in most situations, the contribution to the viscous term due to liquid velocities near the free surface is small compared to the liquid pressure (see Batchelor [1985] p 100), this

normal stress balance is usually written as

$$P - P_a = -\frac{T}{R_{curv}} \tag{5.6}$$

P, P_a, T and R_{curv} having been defined earlier. Consequently, there is a 'pressure drop' across the free surface of magnitude T/R_{curv} due to the surface tension of the liquid.

In a typical fully-flooded situation, the magnitudes of these pressure reductions due to surface tension are negligible compared to the magnitudes of the hydrodynamic pressures generated by the 'squeezing action' of the converging geometry on the inlet side and the converse effect due to the diverging geometry on the downstream side. However, in a typical ultra-starved case the lower roller speeds and viscosities (see §§1.3.3) mean that the 'squeezing action' is drastically curtailed with the result that the hydrodynamic pressures are only the same order of magnitude as the negative pressures caused by surface tension effects (see Malone [1992], Chapter 6). Now because Figure 5.6 demonstrates that the radius of curvature of the upstream free surface is much smaller than that of the downstream one in an ultra-starved flow, it also implies that the liquid pressure near the former is significantly lower (i.e. more sub-ambient) than it is near the latter. This observation, allied to the fact that the magnitudes of the hydrodynamic pressures due to liquid motion are fixed for any given ultra-starved flow, led to the hypothesis that the free surface positions (and hence their curvatures) adjust until the difference in the sub-ambient pressures $(-T/R_{curv})$ between the free surfaces can be bridged by these monotonically increasing, hydrodynamically-generated pressures. Moreover, in Chapter 7 of his thesis, Malone [1992] develops this argument to explain his experimental observation that the upstream free surface is more prone to instability than the downstream one; however this point is not pursued here.

5.4 The Effects of Starvation in Forward Roll Coating

5.4.1 Introduction

In previous sections, we have obtained theoretical predictions for the flow in a forward roll coater, under the two extremes of starvation, which agree reasonably well with experiment. We are now able to undertake the first sytematic investigation into the flow field transition that occurs in a forward roll coater as the flux is reduced from a fully-flooded to an ultra-starved value. This is achieved by monitoring how the velocity and pressure fields, obtained from numerical solutions of a starved flow model similar to the one described in §§5.3.3, change as the dimensionless flux λ is decreased over the *entire* range of starvation, i.e. also including moderately-starved flow.

These F.E. predictions exhibit interesting transitions in both the velocity and pressure fields as the flux is reduced from its fully-flooded value which are compared with the analytical predictions given in Chapters 2-3 and Malone's flow visualisations of fully-flooded, moderately-starved and ultra-starved forward roll coating. Unfortunately, the fact that both rollers are moving meant that he was unable to measure pressures in the two-roll system, so the F.E. pressure predictions are compared with the experimental data for the flat plate/ roller geometry instead. Finally, F.E. predictions of the film thickness ratio T_1/T_2 for $S \neq 1$ are obtained over the whole starvation range in order to test the hypothesis of §§3.3.3 that T_1/T_2 is all but independent of the degree of starvation.

5.4.2 A Numerical Model of Starved Flow in a Forward Roll Coater

The model of starved forward roll coating adopted here is strongly influenced by the model described in §§5.3.3. Once again we assume that lubrication theory gives an accurate description of the flow in the nip region, regardless of the degree of starvation, and impose λ (defined now by equation (4.89)) as a parameter into the nip lubrication velocity profile (4.90), thereby removing the need for a nip pressure condition (see §§5.3.3). As in §4.6, we restrict attention to the case in which the roller radii are equal, i.e. any asymmetry is due only to unequal roller speeds.

Apart from the conditions at the nip, all other boundary conditions for the starved case, namely those at the roller surfaces, the downstream free surface and outflow boundaries are identical to those for the fully-flooded situation shown in Figure 4.27. In the next section we present theoretical predictions obtained by solving this starved forward roll coating model numerically by the Galerkin F.E. method and compare the main features of the predicted flow transition with those observed experimentally.

5.4.3 Results and Discussion

In this section we investigate the nature of the flow transition that occurs in a forward roll coater when the flux passing through the nip is gradually reduced from a fully-flooded to an ultra-starved value. As in §§5.3.4, this is achieved by comparing theoretical flow predictions, obtained from F.E. solutions of the starved flow model over a range of values of the dimensionless flux λ, with Malone's experimental findings for similar situations. Once again, we are able to illustrate the flow transition predicted by the F.E. method more conveniently by simply presenting solutions in which only λ varies since the transition is qualitatively unchanged by variations in either Ca, S or R/H_0 (c.f. Figures 5.12, 5.13).

The computational grids/ mesh generation algorithms chosen to tessellate the flow domain, which as before extends between the nip and the downstream free surface, are similar to those used in §4.6 for the asymmetric, fully-flooded, forward roll coater. However, when the flux λ is reduced, continuity considerations imply that the film thicknesses on the upper and lower rollers will also be reduced accordingly. This effect can cause meshing problems because it is possible that those elements which are downstream of the film-splitting location may become so long and thin that their high aspect ratios pose a threat to the accuracy of the solution (see Chung [1978] pp 133-138). Hence it is possible that the asymmetric forward roll coating grid shown in Figure 4.26 (with 204 elements, 469 nodes and 41 spines), which was shown to be suitable for the fully-flooded flow with $Re = 0.0$, $Ca = 0.1$, $S = 1$ and $R/H_0 = 100$ in §§4.5.5, may not be suitable for moderately- and ultra-starved applications.

In order to test this hypothesis, numerical solutions were obtained in which λ was

gradually reduced from its fully-flooded value, $\lambda = 1.35$, to an ultra-starved value of 0.3 by performing zeroth order continuation on λ – the effect that this ultra-starvation has on the elements in region 2 is shown in Figure 5.17 (a). This solution was then compared with the corresponding solution obtained on a second, finer grid – shown in Figure 5.17 (b) – consisting of 300 elements, 683 nodes and 53 spines. Note that in the solutions obtained using grids 5.17 (a), (b), each iteration took approximately 20, 26 c.p.u. seconds respectively. This study revealed that in changing from grid (a) to (b), the most sensitive variable was the film-split parameter X_m which changed by less than 0.1% of its previous value. We conclude from this that the grid shown in Figure 4.26 is suitable for flows with $Ca = 0.1$, $S = 1$, $R/H_0 = 100$ in the range $0.3 \leq \lambda \leq 1.35$, and can be used to demonstrate the theoretical transition between fully-flooded and moderately-starved forward roll coating.

Figure 5.18 illustates this transition by presenting velocity vectors and dimensionless F.E. pressures generated on the *symmetry plane* (which is equidistant from the upper and lower rollers, see Figure 4.13) obtained from numerical solutions with $\lambda = 1.35$ (fully-flooded), 1.15, 1.0, 0.9, 0.75 and 0.6. Once again, for clarity of presentation each solution is shown on different scales since unilaterally reducing λ results in the downstream free surface receding towards the nip – see Figure 5.18 (g) where the free surfaces are drawn on a common scale. Meanwhile each point on a given pressure profile indicates the (dimensionless) F.E. pressures generated at that position on the symmetry plane immediately above the point. As in §§5.3.4, no pressure scales are shown here because we are only interested in the shape of the pressure profile and the solid line denotes the atmospheric pressure level ($p = 0$), i.e. pressures below it are sub-ambient.

The flow field transition predicts that starving the flow between $\lambda = 1.35$ and $\lambda = 0.6$ results in the recirculations next to the downstream free surface (which are indicated by the presence of small velocity vectors) extending further upstream towards the nip. The pressure profile transition is also similar to that observed in the flat plate/ roller geometry: in the fully-flooded case the pressure profile has the familiar sub-ambient pressure loop, but as the flux is reduced the pressure at the nip falls and for

flows with $\lambda < 1.0$, the profile is entirely sub-ambient and without a pressure minimum. Furthermore, the pressure profiles for $\lambda \leq 0.9$ possess the linear pressure and constant pressure regions identified earlier in §§5.3.4.

In the forward roll coating results presented so far, the starvation is only moderate. We now investigate the effects of increasing the starvation further until the flow becomes ultra-starved. Although the transition between moderately-starved and ultra-starved flow in a forward roll coater could be exemplified by presenting solutions for the same parameter set, in which λ is decreased to an ultra-starved value, this could lead to meshing problems as the downstream free surface recedes ever closer to the nip – see Figure 5.18 (g). For this reason it is preferable to counteract this consequence of unilaterally reducing λ to an ultra-starved value by decreasing Ca to a more realistic value for meniscus roll coating because this strengthens the effect of surface tension and tends to 'push' the free surface away from the nip (see Figure 4.21). Since Malone estimated that $Ca \approx 0.017$ in his meniscus roll coating experiments, it was deemed appropriate to illustrate this transition by presenting solutions with $Ca = 0.017$. In order to test whether the grids shown in Figure 5.17 are suitable for ultra-starved flow with $Ca = 0.017$, numerical solutions for $\lambda = 0.2$ were obtained using each tessellation shown in Figure 5.17. A comparison between these solutions showed that in changing from grid (a) → (b), the most sensitive variable (X_m) changed by less than 0.3% of its previous value, which implies that both these grids are suitable for ultra-starved flow in this parameter range. However, owing to the fact that F.E. solutions for ultra-starved flow were required over a wide velocity ratio range (see later), it was decided to use grid (b) to obtain all ultra-starved solutions.

Figure 5.19 illustrates the theoretical transition between moderately-starved and ultra-starved flow in a forward roll coater predicted by the F.E. method by presenting velocity vectors and dimensionless F.E. pressures generated on the symmetry plane for $\lambda = 0.4$, 0.3 and 0.2. These results predict that an effect of decreasing λ in this range is to strengthen the recirculations until they eventually pass through the nip, while the effect on the downstream free surface position is shown in Figure 5.19 (d). Note that for $\lambda = 0.3$ and $\lambda = 0.2$, these recirculations actually extend upstream of the nip

because the lubrication velocity profile condition (4.90) imposes reverse flow at the nip for $\lambda < 1/3$ when $S = 1$. Finally, the ultra-starved pressure profiles are similar to those shown in Figure 5.18 for $\lambda \leq 0.9$, although their constant pressure regions extend further upstream from the free surface towards the nip.

These flow transition predictions are now compared with Malone's experiments for similar flow situations which he performed on an experimental rig where the radius of each roller=$25mm$ and H_0 (also estimated by the feeler guage technique)=225 micrometres. We consider the velocity field transition first. A typical flow visualisation for the fully-flooded situation, already shown in Figure 1.7, agrees with G.I. Taylor's [1963] observation that the flow field divides into two parts: a two-dimensional portion in the immediate vicinity of the (downstream) coating mensicus and a nearly rectilinear portion elsewhere.

The flow visualisations of starved forward roll coating shown in Figures 5.20 (a), (b) (with the rollers moving from left to right and starvation in the latter greater than in the former) form the link between the fully-flooded (Figure 1.7) and ultra-starved (Figure 2.15 (a)) situations. They clearly demonstrate that the recirculations extend further upstream towards the nip when the starvation is increased, which is in qualitative agreement with the predictions of Figure 5.18, 5.19. Finally, when starvation is increased further from the level in Figure 5.20 (b) the recirculations eventually pass through the nip, leading to the ultra-starved (meniscus roll coating) situation depicted in figure 2.15 (a) where the existence of two large eddies is apparent.

Turning now to the pressures for starved forward roll coating, it is evident that the theoretical pressure transition in this case shares all the features of that predicted in the flat plate/ roller geometry, except that in the former the 'critical' value of λ marking the disappearance of a downstream pressure minimum is $\lambda = 1.0$ (note that this is also predicted by the pressure gradient (4.78)) compared to $\lambda = 0.5$ in the latter. Consequently, the F.E. predictions for the two roll system are also in qualitative agreement with the experimental pressure profiles given in Figure 5.15, although the theory predicts a more rapid disappearance of the pressure minimum than is manifested by the data. The free surface curvature argument given in §§5.3.4 can also be invoked

to explain the existence of entirely sub-ambient pressures in the meniscus roll coating situation – see Figure 1.5. Finally, we note that both the F.E. pressure predictions and experimental data support the analytical prediction of the zero flux model that the pressure gradient is constant in the central core of a meniscus roll coating bead.

The next set of F.E. predictions investigates how the velocity field of a forward roll coater is affected by changing the velocity ratio S. For presentational purposes, it is convenient to illustrate this feature by reducing λ and Ca below those values which have already been used in Figure 5.19 because this reinforces the 'double-eddy' structure of meniscus roll coating. After a process of trial and error, it was decided that this characteristic is amply demonstrated by the velocity vectors from numerical solutions of ultra-starved flow with parameters $Re = 0.0$, $Ca = 0.002$, $R/H_0 = 100$, $\lambda = 0.08$ with $S=1$, 2 and 3. These results, shown in Figure 5.21, clearly demonstrate the 'double-eddy' structure of forward meniscus roll coating and predict that the ratio of the sizes of the upper and lower eddies increases when S increases – in agreement with the experimental and analytical predictions shown in Figures 2.15, 2.13 respectively.

The last two sets of numerical results exhibit F.E. predictions for the film thickness ratio T_1/T_2 in forward roll coating over the entire range of starvation from fully-flooded to ultra-starved flow. Figure 5.22, for example, shows F.E. predictions of T_1/T_2 for flow with $Re = 0.0$, $Ca = 0.1$, $R/H_0 = 100$ in the velocity ratio range $0.1 \leq S \leq 4.0$ where the inlet is (i) fully-flooded ($\lambda \approx 1.35$), (ii) moderately-starved ($\lambda=1.0$, 0.6). These results, which have been obtained using grid (a) of Figure 5.17, are compared with Malone's average film thickness data, Benkreira et al's [1981] correlation and Savage's [1992] 'stagnation-point' model, all of which relate to the fully-flooded situation. Note that once again the results are presented on a logarithmic scale in order to expedite a convenient comparison with Benkreira et al's correlation. These results are extremely interesting since the F.E. predictions are almost independent of the degree of (moderate) starvation. Moreover, they are in good agreement with the fully-flooded predictions, shown in Figure 5.1, for the same velocity ratio range (i.e. they closely satisfy $T_1/T_2 \approx S^{0.65}$) and are also in reasonable agreement with Malone's fully-flooded data and Savage's theoretical prediction.

Finally, Figure 5.23 shows F.E. predictions of T_1/T_2 for flows with $Re = 0.0$, $Ca = 0.017$, $R/H_0 = 100$ in the range $0.1 \leq S \leq 2.0$ where $\lambda = 0.4$, 0.3 and 0.2. These F.E. predictions, which in this case are obtained using grid (b) of Figure 5.17, are similar to the moderately-starved results shown in Figure 5.22 (i.e. once again $T_1/T_2 \approx S^{0.65}$) and agree reasonably well with Malone's average film thickness data for meniscus roll coating, except near $S = 0.2$. Note that they also support the analytical film thickness model for meniscus roll coating, developed in Chapter 3, since these F.E. predictions satisfy $T_1/T_2 \approx S(S + 3)/(1 + 3S)$ over the entire velocity ratio range.

5.5 Summary of F.E. Predictions for Starved Flow

A summary is now given of the main features of above F.E. predictions for starved flow in roll coating systems and a more precise definition of ultra-starvation than has been possible up until now is proposed.

Consider the velocity field predictions first. In the fully-flooded case, the flow field divides into two regions: a two-dimensional portion in the immediate vicinity of the downstream meniscus and a nearly rectilinear portion elsewhere. Meanwhile when the flux is reduced from its fully-flooded value, the relative sizes of the two-dimensional and rectilinear portions increases until the recirculation region eventually extends upstream of the nip. This theoretical transition is supported by Malone's flow visualisations in both the flat plate/ roller and two roll systems.

The transition in the pressure field, predicted by the F.E method, is also very interesting. In the fully-flooded case, the profile exhibits the familiar sub-ambient pressure loop, but as the flux is reduced the pressure at the nip falls until the profile has no minimum point and is entirely sub-ambient. When the flux is reduced below the critical point at which the downstream pressure minimum disappears – $\lambda = 1.0$, 0.5 for the two roll and flat plate/ roller systems respectively – the profile quickly assumes a shape in which a linear pressure region near the nip is connected to a constant pressure region which extends up to the downstream meniscus. These predictions are in broad agreement with Malone's experimental profiles for flow in the flat plate/ roller geometry,

although the downstream pressure minimum disappears more rapidly when the inlet is starved in the former than it does in the latter. Furthermore, the linear experimental profile measurements in the central core of ultra-starved flow in a flat plate/ roller geometry provide strong evidence in support of the linear pressure profile predictions from the zero flux model and consequently lends credence to the assumptions of the small flux model developed in Chapter 3.

The F.E. film thickness ratio predictions for starved roll coating shown in Figures 5.22, 5.23 agree reasonably well with available experimental data (except for low S values) and are almost independent of the degree of starvation, appearing to be proportional to $S^{0.65}$ in their respective velocity ratio ranges. Hence, notwithstanding the inevitable meshing problems caused by, and consequent unreliability associated with, numerical predictions for ultra-starved flows with low velocity ratios, these predictions seem to support the hypothesis of §§3.3.3 that T_1/T_2 is unaffected by starvation. Actually, the F.E. predictions can be summarized more succinctly by noting that, owing to the neglect of gravity in the numerical solutions, if the predicted ratio for a flow with $S > 1$ is α say, then the corresponding ratio for a flow with velocity ratio $1/S$ should be equal to $1/\alpha$. Indeed this is the case in all the F.E. solutions reported here. Hence, by the above argument, even though the F.E. predictions shown in Figures 5.22, 5.23 only extend over the ranges $0.1 \leq S \leq 4.0$ and $0.1 \leq S \leq 2.0$ respectively, they encapsulate information over the range $0.1 \leq S \leq 10.0$. Therefore these predictions encourage one to speculate that the F.E. method yields $T_1/T_2 \approx S^{0.65}$ for $0.1 \leq S \leq 10$ over the entire range of starvation, although greater confidence in this assertion can only be provided by a more extensive F.E. study with more robust numerical methods.

Finally, we are now in a position to give a more precise definition of ultra-starvation which allows it to be distinguished from cases of moderate-starvation. This is simply that a flow becomes ultra-starved when the recirculations first touch the upstream free surface – the situation depicted in Figure 5.20 (b). Unfortunately, since our starved flow models are restricted to the region between the nip and the downstream free surface, they are unable to predict when this critical point arises in practice. Nevertheless, owing to the fact that the upstream free surface is close to the nip in the meniscus roll

coating situation (see Figure 1.5), a useful indicator for the onset of ultra-starvation is when the recirculations first pass upstream of the nip. This feature *can* be predicted by the starved flow models since they show that the recirculations extend past the nip in (i) a flat plate/ roller geometry, (ii) the two roll system with $S = 1$ when λ (defined in their respective sections) $< 1/3$ because their associated velocity profiles, (5.3), (4.90) respectively, impose reverse flow at the nip.

FILM THICKNESS   × FULLY-FLOODED EXPERIMENTAL DATA (MALONE [1992])
      RATIO   ▫ $Ca = 0.1$
     T_1/T_2 ▲ $Ca = 0.5$
                 ▼ $Ca = 2.0$
                 — BENKREIRA ET AL [1981] ($T_1/T_2 = 0.87S^{0.65}$)
                 ○ SAVAGE [1992] ($T_1/T_2 = S(S+3)/(1+3S)$)
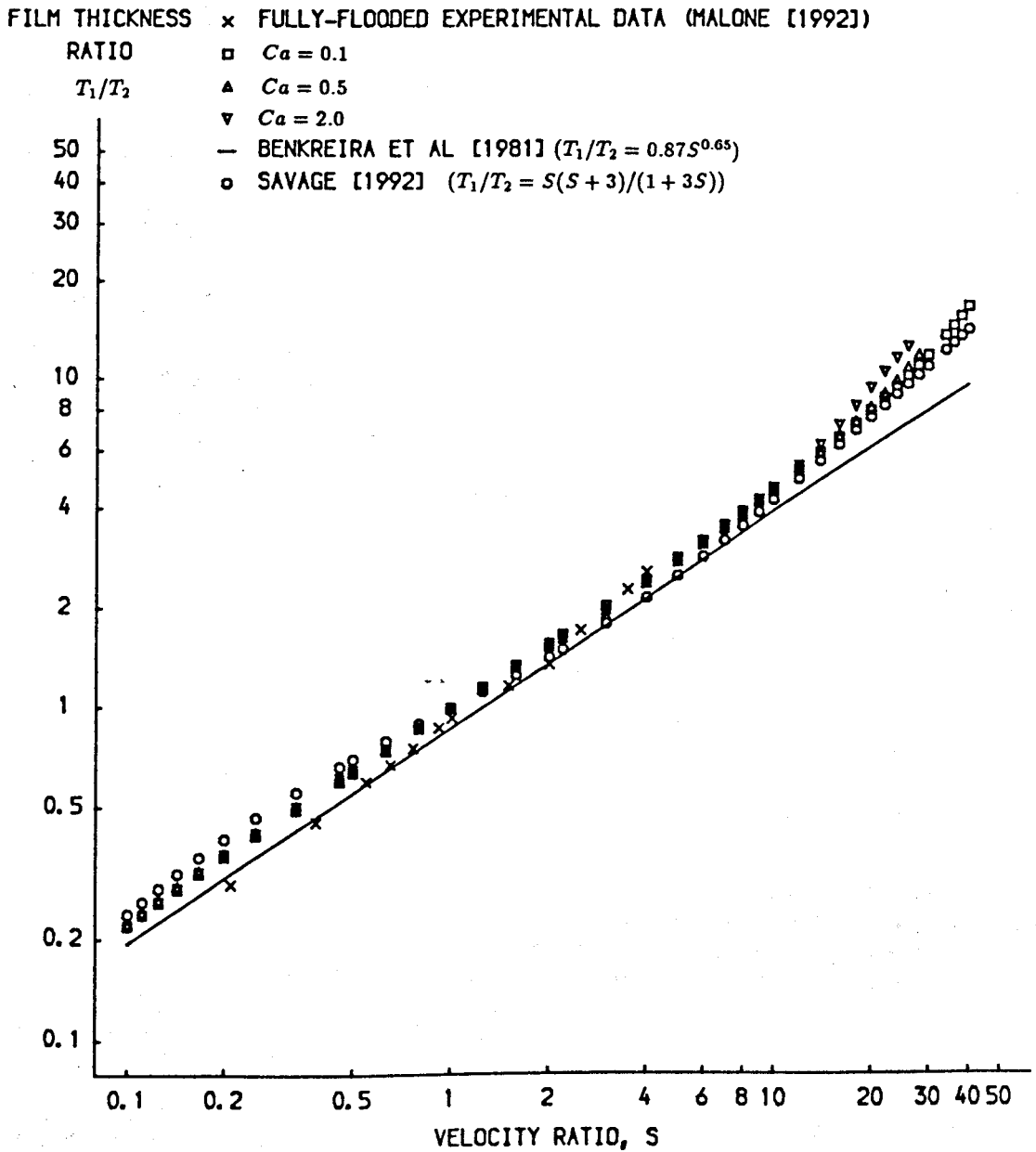
Figure 5.1: F.E. Predictions of T_1/T_2 in Asymmetric, Fully-Flooded, Forward Roll Coating with $Re = 0.0$, $R/H_0 = 200$
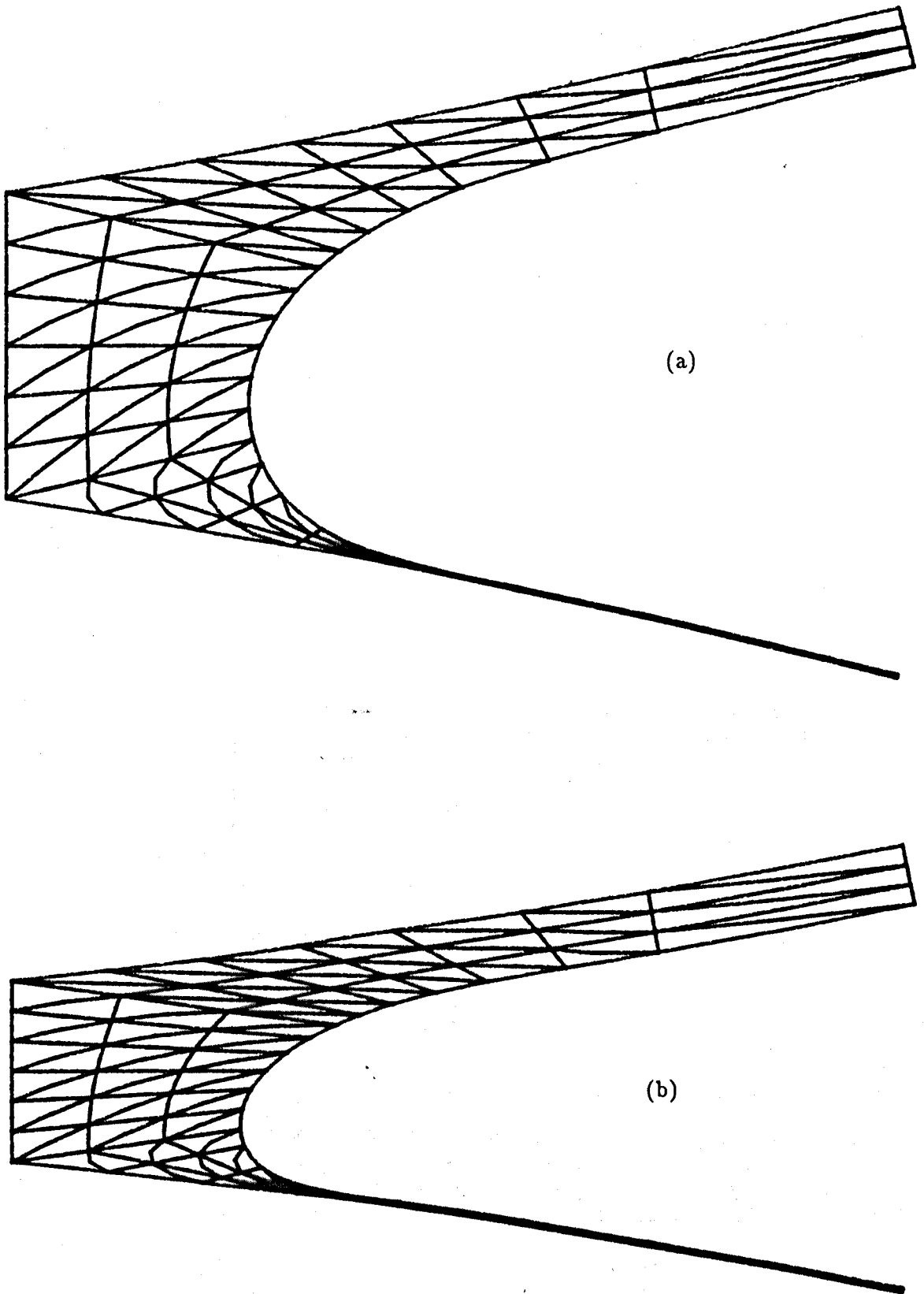
Figure 5.2: Element Distortion in Region 2 of Asymmetric Roll Coating Grids with $Re = 0.0$, $R/H_0 = 200$: (a) $Ca = 0.1$, $S = 40.0$, (b) $Ca = 0.5$, $S = 30.0$, (c) $Ca = 2.0$, $S = 26.0$

(c)

Figure 5.2 (continued)

The Jacobian of the Isoparametric Mapping (B.40) becomes singular when P moves into the shaded region.

(0,1)

(0,1/2)

P

y=1/4

(0,0) (1/2,0) (1,0)

x=1/4
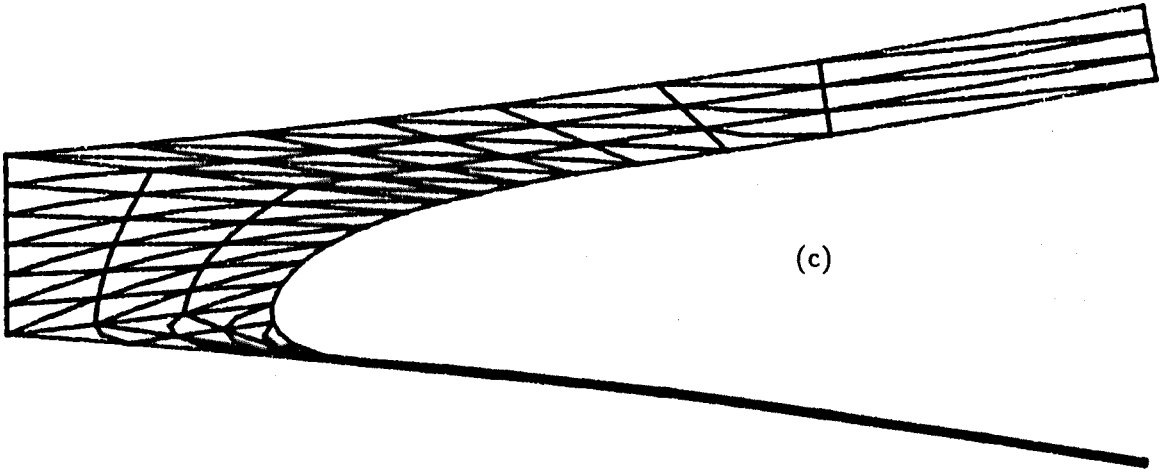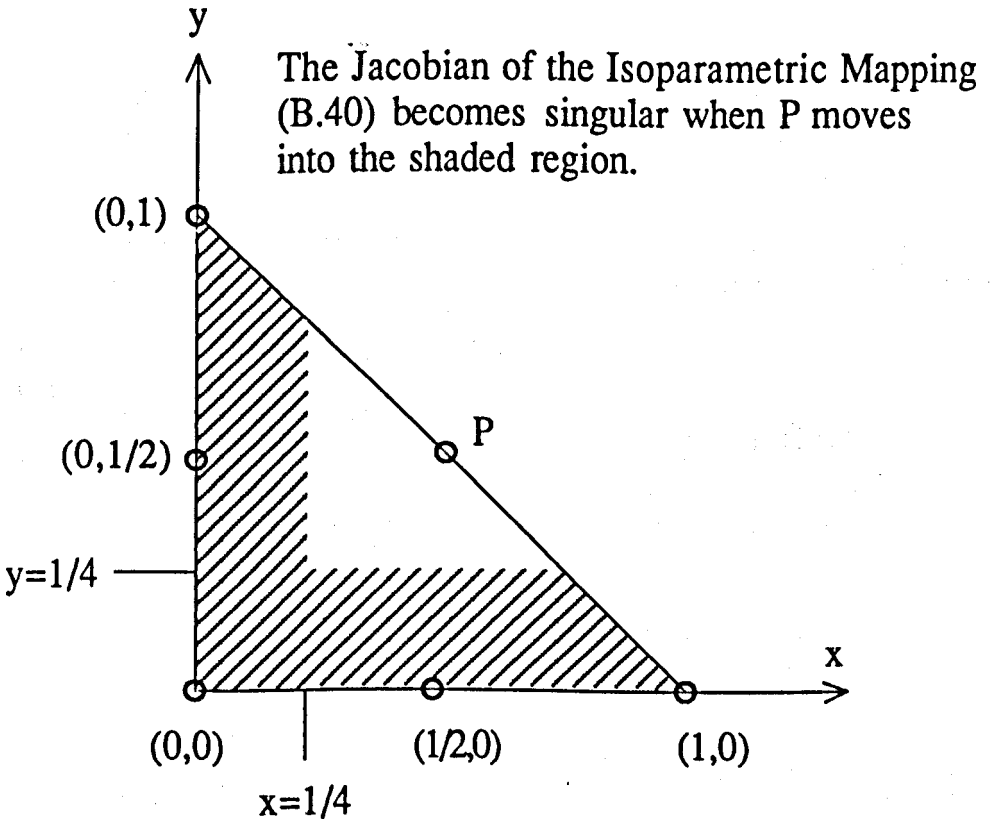
Figure 5.3: The Effect of Element Distortion on the Invertibility of an Isoparametric Mapping (Strang and Fix [1973])
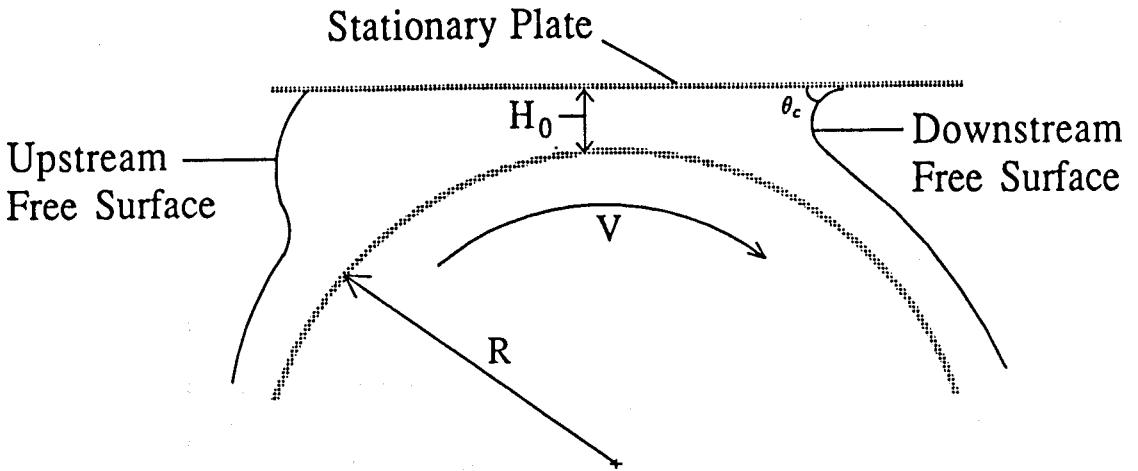
Figure 5.4: The Flat Plate/ Roller Geometry
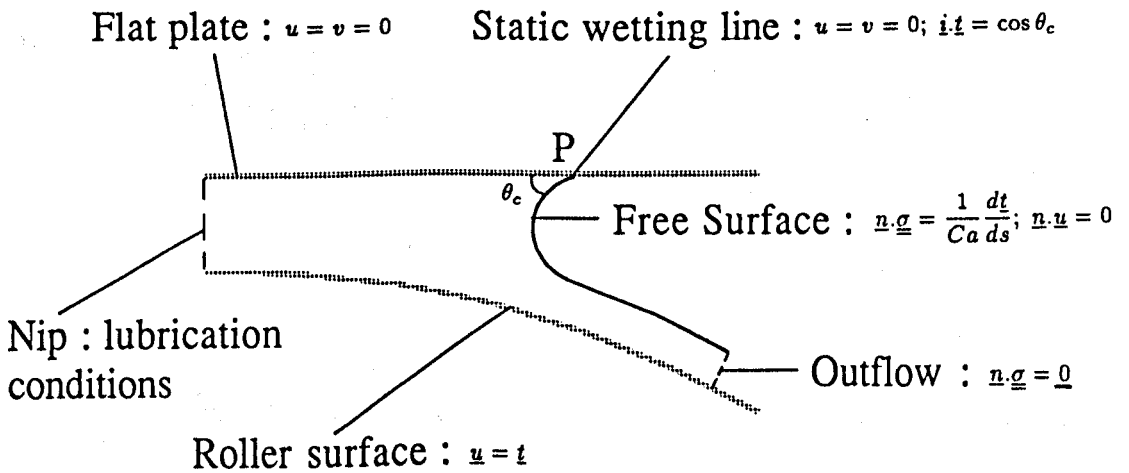
Figure 5.5: A Simplified Model For Flow in a Flat Plate/ Roller Geometry (Coyle et al [1986])
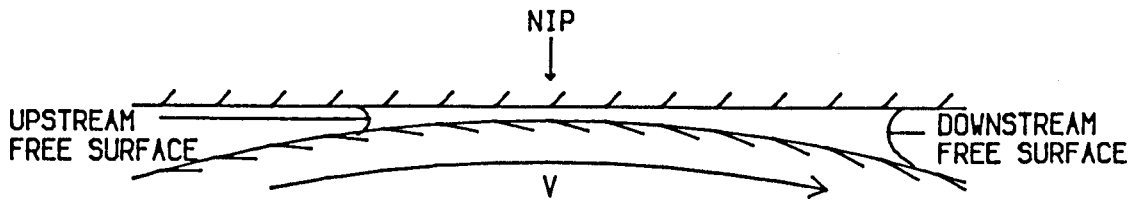
Figure 5.6: Typical Free Surface Positions in an Ultra-Starved Flow in the Flat Plate / Roller Geometry
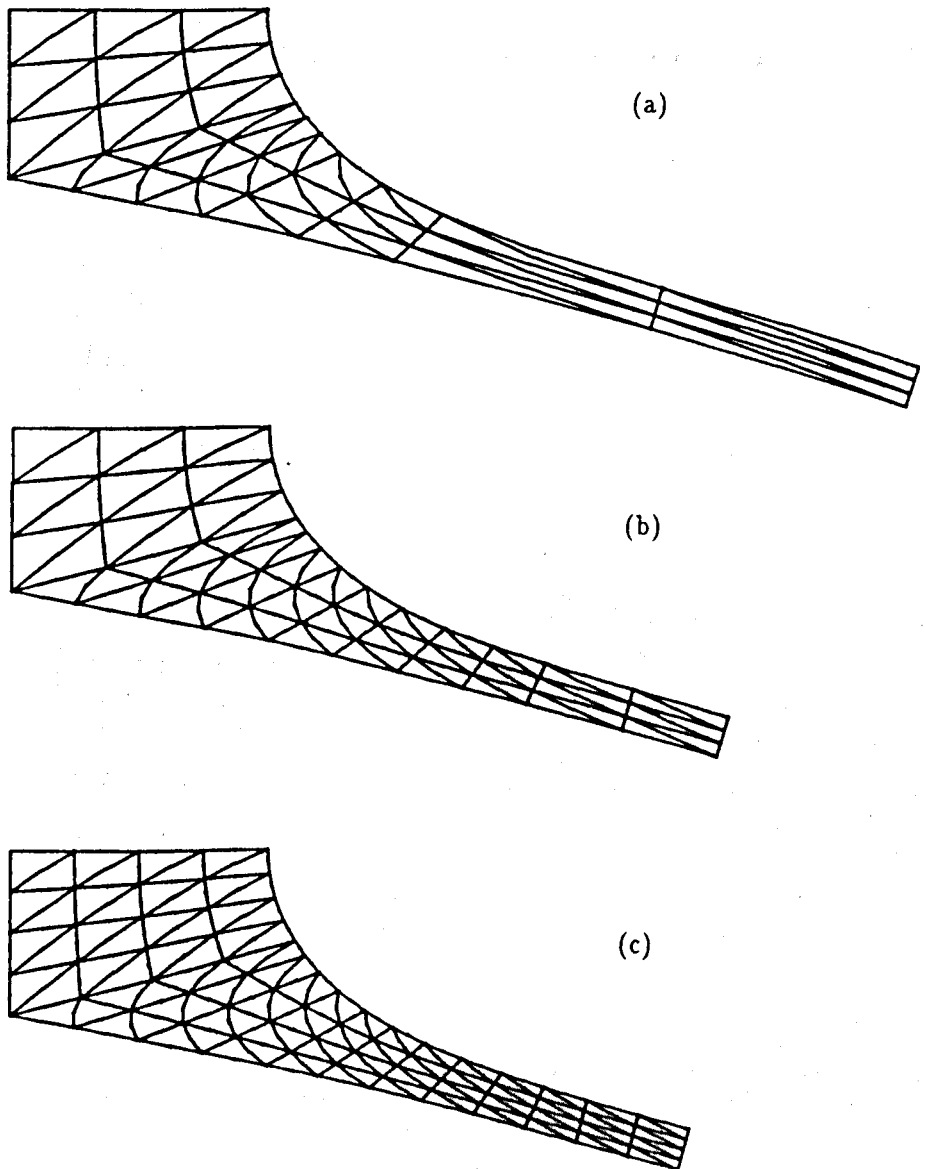
Figure 5.7: Elements in Region 2 of Grids used to Obtain F.E. Solutions of Flow with $Re = 0.0$, $Ca = 0.1$, $R/H_0 = 100$, $\theta_c = 90°$: (a) 102 elements, 245 nodes; (b) 150 elements, 357 nodes; (c) 248 elements, 567 nodes
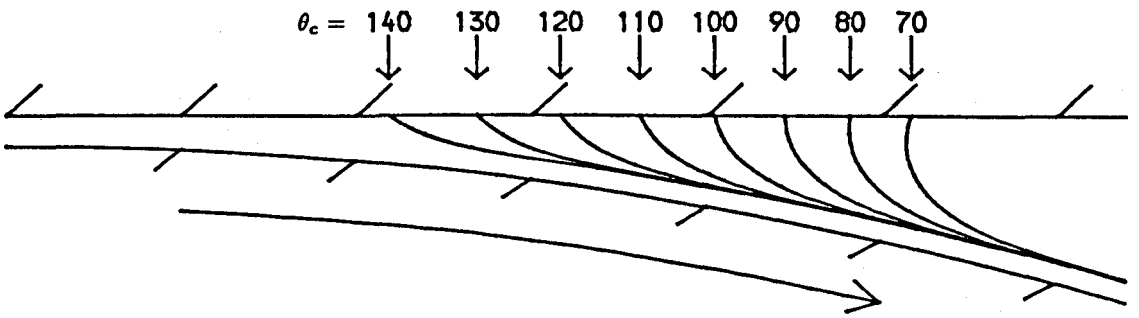
Figure 5.8: The Effect of Imposed Contact Angle θ_c on Downstream Free Surface Profiles for Flow in a Flat Plate/ Roller Geometry ($Re = 0.0$, $Ca = 0.1$, $R/H_0 = 100$)
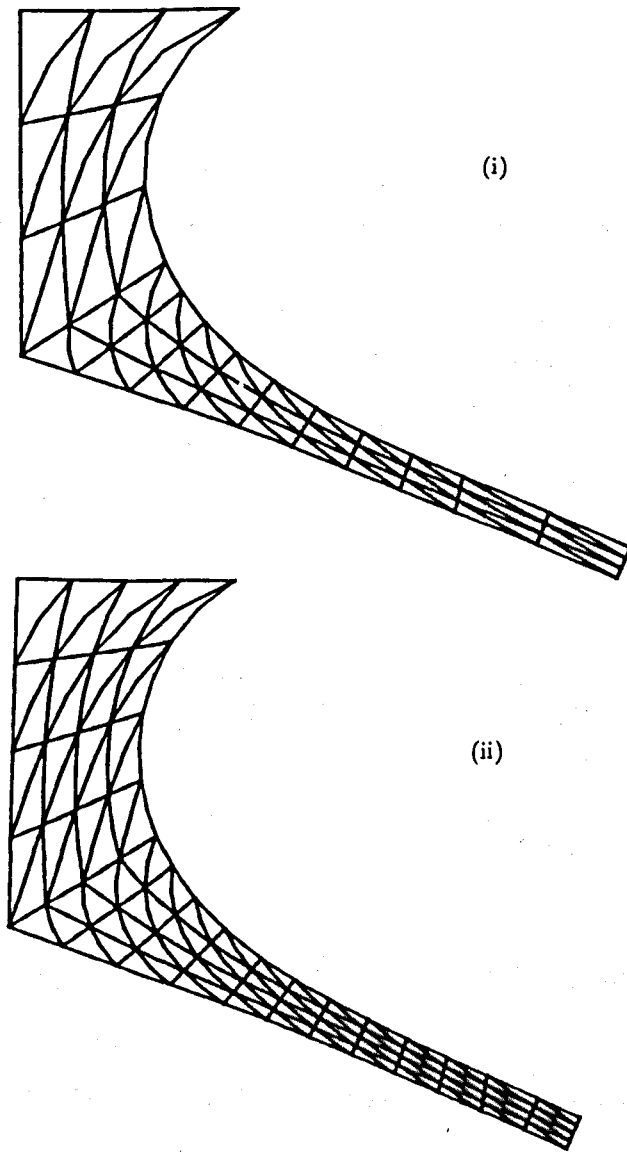
Figure 5.9: The Effect of Imposing $\theta_c = 33^\circ$ (and $Re = 0.0$, $Ca = 0.05$, $R/H_0 = 110$) on Elements in Region 2 of (i) grid (b), (ii) grid (c) of Figure 5.7
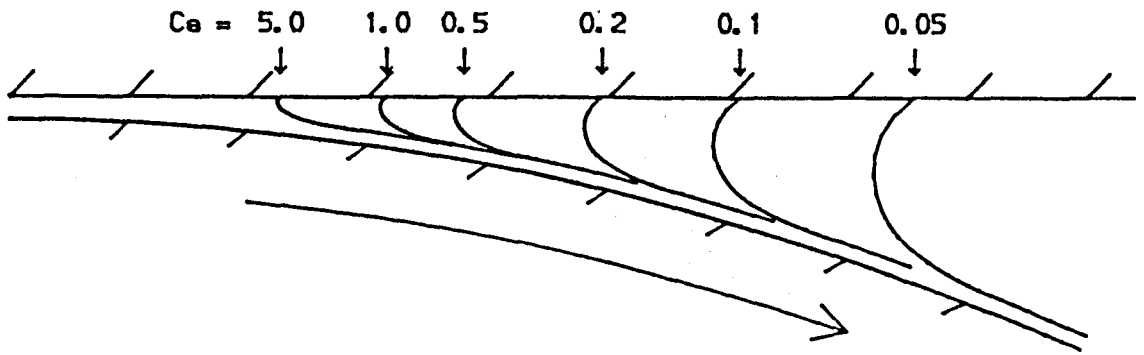
Figure 5.10: The Dependence of the Downstream Free Surface Profile on Capillary Number, Ca, for Fully-Flooded Flow in a Flat Plate/ Roller Geometry with $Re = 0.0$, $R/H_0 = 110$, $\theta_c = 33^\circ$

(a)
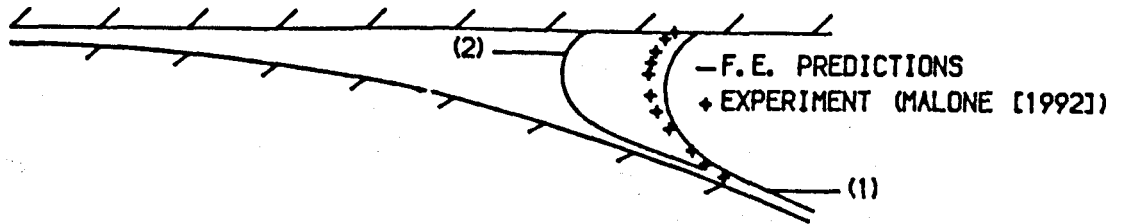
(b)
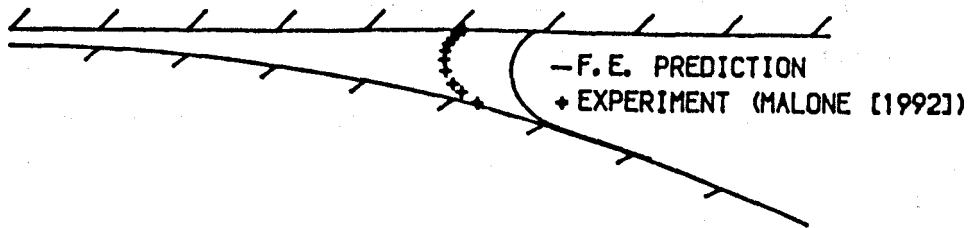
Figure 5.11: Comparison Between Theoretical Prediction and Experimental Measurements of Downstream Free Surface Profiles in a Flat Plate/ Roller Geometry: (a) Fully-Flooded ($Ca = 0.05$, $R/H_0 = 110$, $\theta_c = 33^\circ$), (b) Ultra-Starved ($\lambda = 0.13$, $Ca = 0.0065$, $R/H_0 = 110$, $\theta_c = 33^\circ$)

(a)

(1) FLOW FIELD

(2) DIMENSIONLESS F.E. PRESSURES ON UPPER PLATE

NIP

CONTACT LINE

ATMOSPHERIC PRESSURE LEVEL

(b)

(1) FLOW FIELD

(2) DIMENSIONLESS F.E. PRESSURES ON UPPER PLATE

NIP

CONTACT LINE

ATMOSPHERIC PRESSURE LEVEL

Figure 5.12: The Effects of Starvation on Flow in a Flat Plate/ Roller Geometry I: Moderate-Starvation with $Re = 0.0$, $Ca = 0.05$, $R/H_0 = 110$, $\theta_c = 33^\circ$; (a) Fully-Flooded ($\lambda = 0.66$); (b) $\lambda = 0.55$; (c) $\lambda = 0.5$; (d) $\lambda = 0.45$; (e) $\lambda = 0.35$; (f) $\lambda = 0.25$; (g) Effect on Downstream Free Surface Profile

(c)

(1) FLOW FIELD

(2) DIMENSIONLESS F. E. PRESSURES ON UPPER PLATE

(d)

(1) FLOW FIELD

(2) DIMENSIONLESS F. E. PRESSURES ON UPPERPLATE

Figure 5.12 (continued)

(e)

(1) FLOW FIELD

(2) DIMENSIONLESS F. E. PRESSURES ON UPPER PLATE

NIP   CONTACT LINE

ATMOSPHERIC PRESSURE LEVEL

(f)

(1) FLOW FIELD

(2) DIMENSIONLESS F.E. PRESSURES ON UPPER PLATE

NIP   CONTACT LINE

ATMOSPHERIC PRESSURE LEVEL

(g)

$$\lambda = 0.25 \quad 0.35 \quad 0.45 \quad 0.50 \quad 0.55 \quad 0.66$$

Figure 5.12 (continued)

(a)

(1) FLOW FIELD

(2) DIMENSIONLESS F. E. PRESSURES ON UPPER PLATE

NIP

CONTACT LINE

ATMOSPHERIC PRESSURE LEVEL

(b)

(1) FLOW FIELD

(2) DIMENSIONLESS F. E. PRESSURES ON UPPER PLATE

NIP

CONTACT LINE

ATMOSPHERIC PRESSURE LEVEL

Figure 5.13: The Effects of Starvation on Flow in a Flat Plate / Roller Geometry II: Ultra-Starvation with $Re = 0.0$, $Ca = 0.0065$, $R/H_0 = 110$, $\theta_c = 33^\circ$; (a) $\lambda = 0.2$; (b) $\lambda = 0.13$; (c) $\lambda = 0.07$; (d) Effect on Downstream Free Surface Profile

(c)

(1) FLOW FIELD

(2) DIMENSIONLESS F.E. PRESSURES ON UPPER PLATE

NIP   CONTACT LINE

ATMOSPHERIC PRESSURE LEVEL

(d)

$\lambda = 0.07$ 0.13   0.20

Figure 5.13 (continued)

(a)

(b)

(c)

(d)
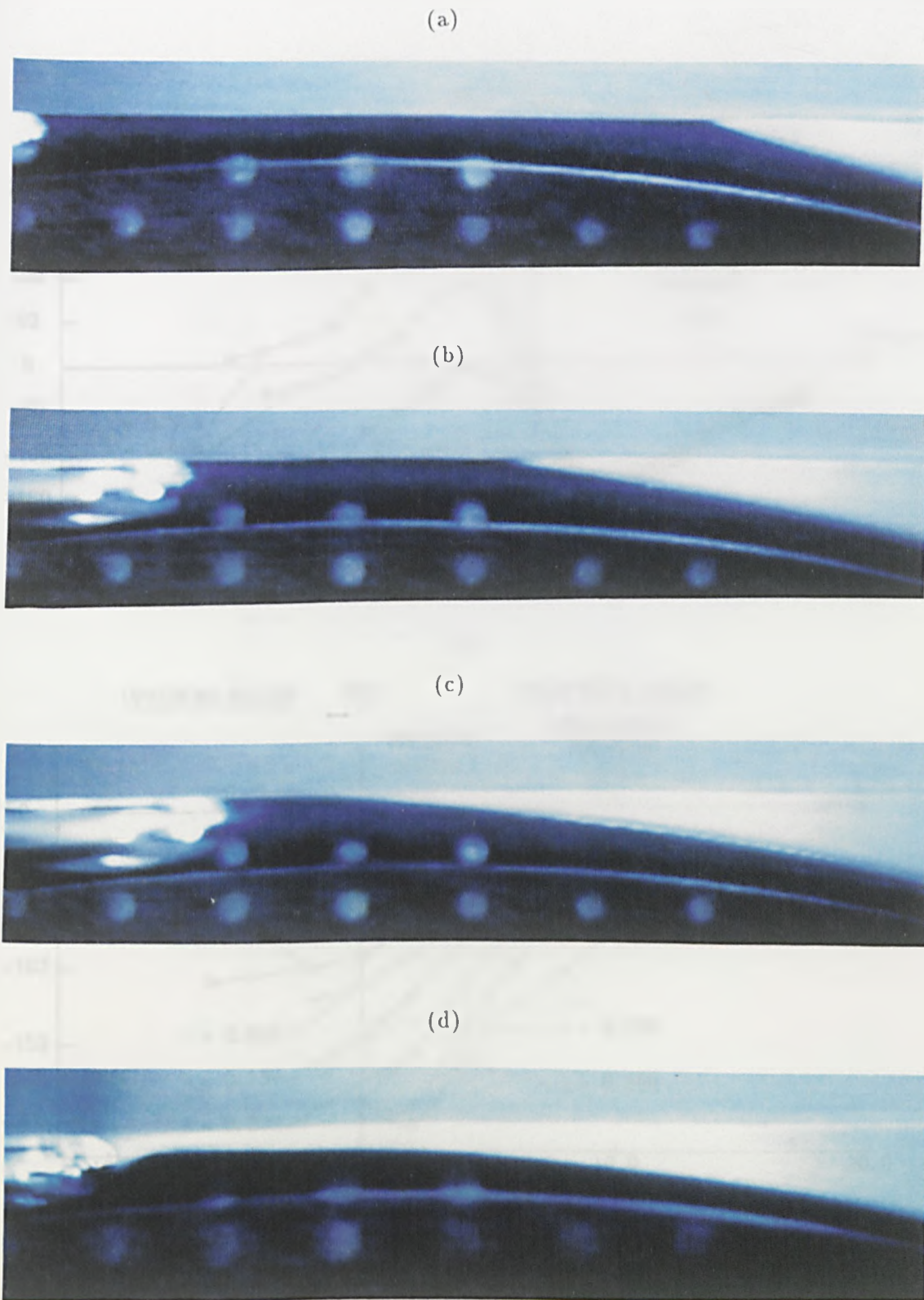
Figure 5.14: Malone's Experimental Flow Visualisations of Flow in a Flat Plate/ Roller Geometry: (a) Fully-Flooded; (b) Moderately-Starved; (c) Moderately-Starved; (d) Ultra-Starved
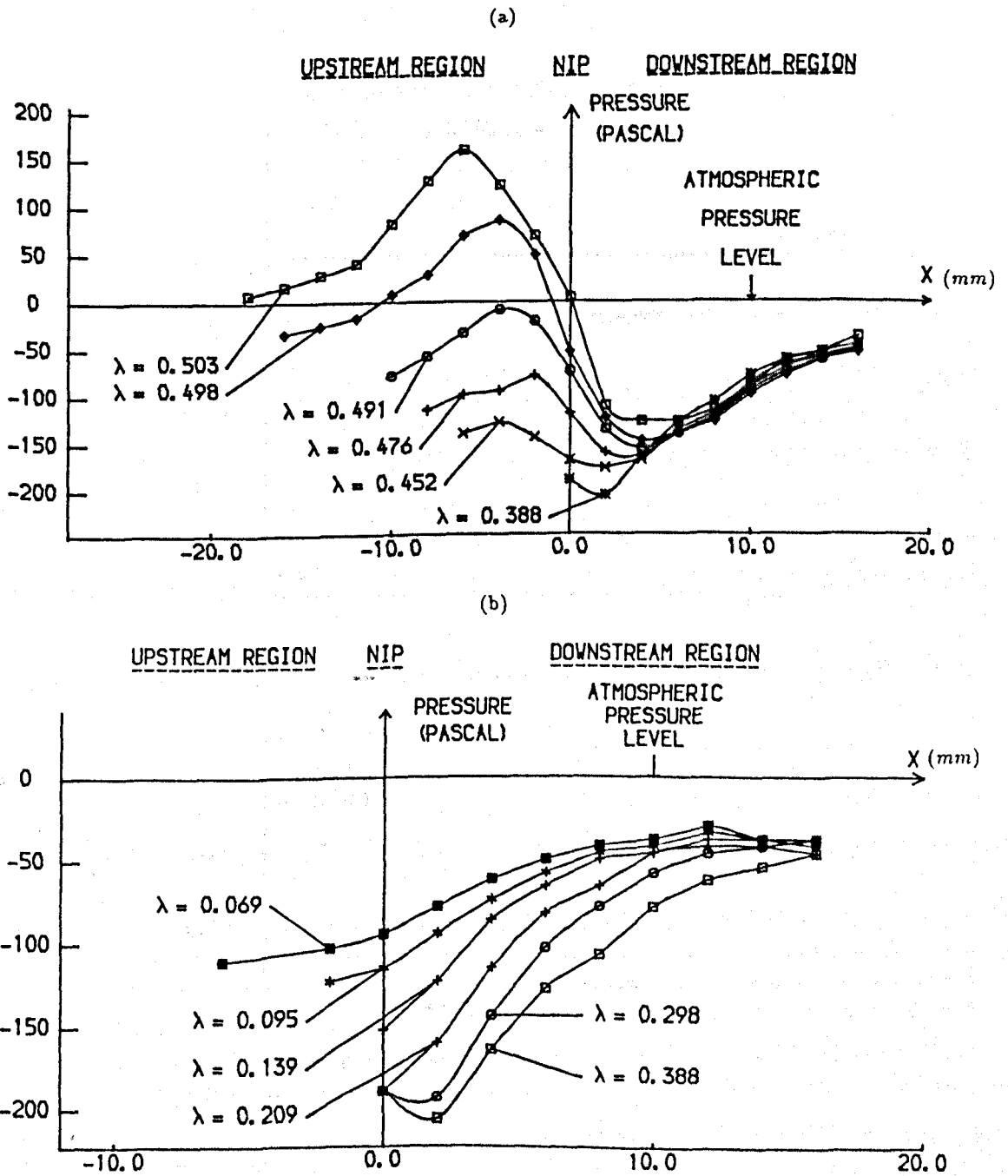
Figure 5.15: Malone's Experimental Pressure Profiles in a Flat Plate/ Roller Geometry: (a) Fully-Flooded to Moderately-Starved Flow; (b) Moderately-Starved to Ultra-Starved Flow

(a)

(b)
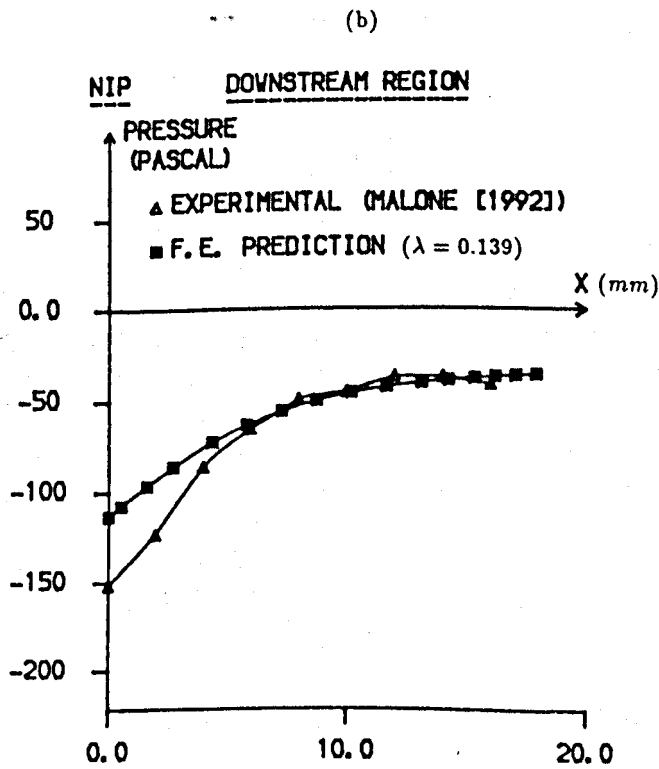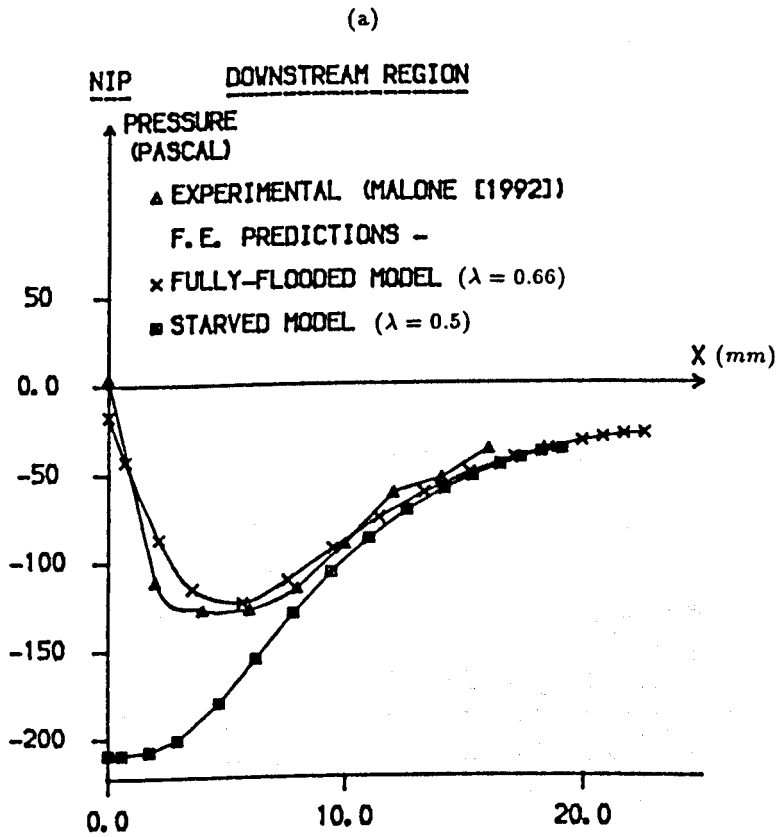
Figure 5.16: A Quantitative Comparison Between Theoretical (F.E.) and Experimental (Malone [1992]) Pressure Profiles in a Flat Plate/ Roller Geometry: (a) Fully-Flooded – $Ca = 0.067$, $\theta_c = 33°$, $R/H_0 = 400$, (b) Ultra-Starved – $Ca = 0.0087$, $\theta_c = 33°$, $R/H_0 = 400$

(a)

(b)

(1) ELEMENTS UPSTREAM OF XM

(2) ELEMENTS DOWNSTREAM OF XM
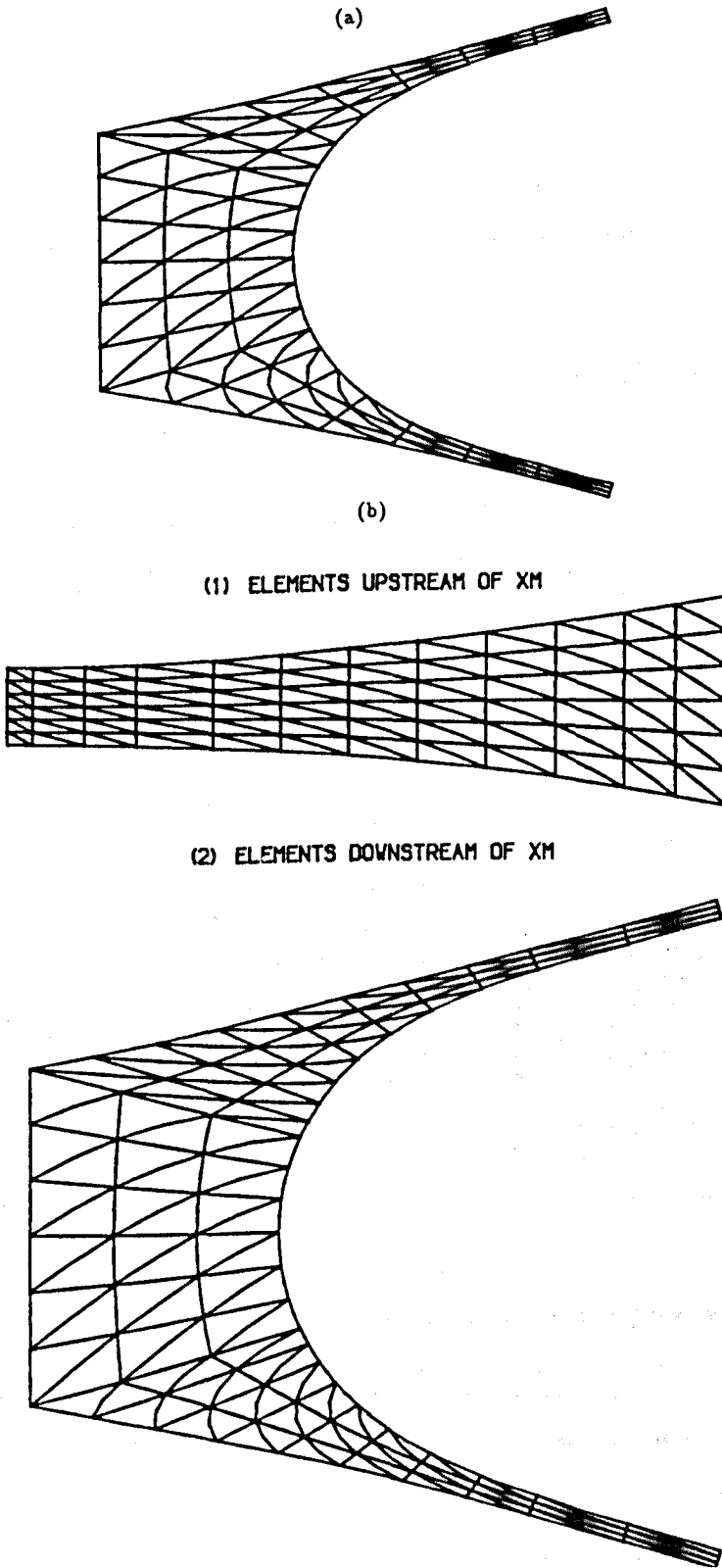
Figure 5.17: F.E. Grids Used in Ultra-Starved Forward Roll Coating with $Re = 0.0$, $Ca = 0.1$, $R/H_0 = 100$, $\lambda = 0.3$, $S = 1.0$: (a) 204 elements, 469 nodes, (b) 300 elements, 683 nodes

(a)

(1) FLOW FIELD

(2) DIMENSIONLESS F.E. PRESSURES ON SYMMETRY PLANE

ATMOSPHERIC PRESSURE LEVEL

NIP

(b)

(1) FLOW FIELD

(2) DIMENSIONLESS F.E. PRESSURES ON SYMMETRY PLANE

NIP

ATMOSPHERIC PRESSURE LEVEL
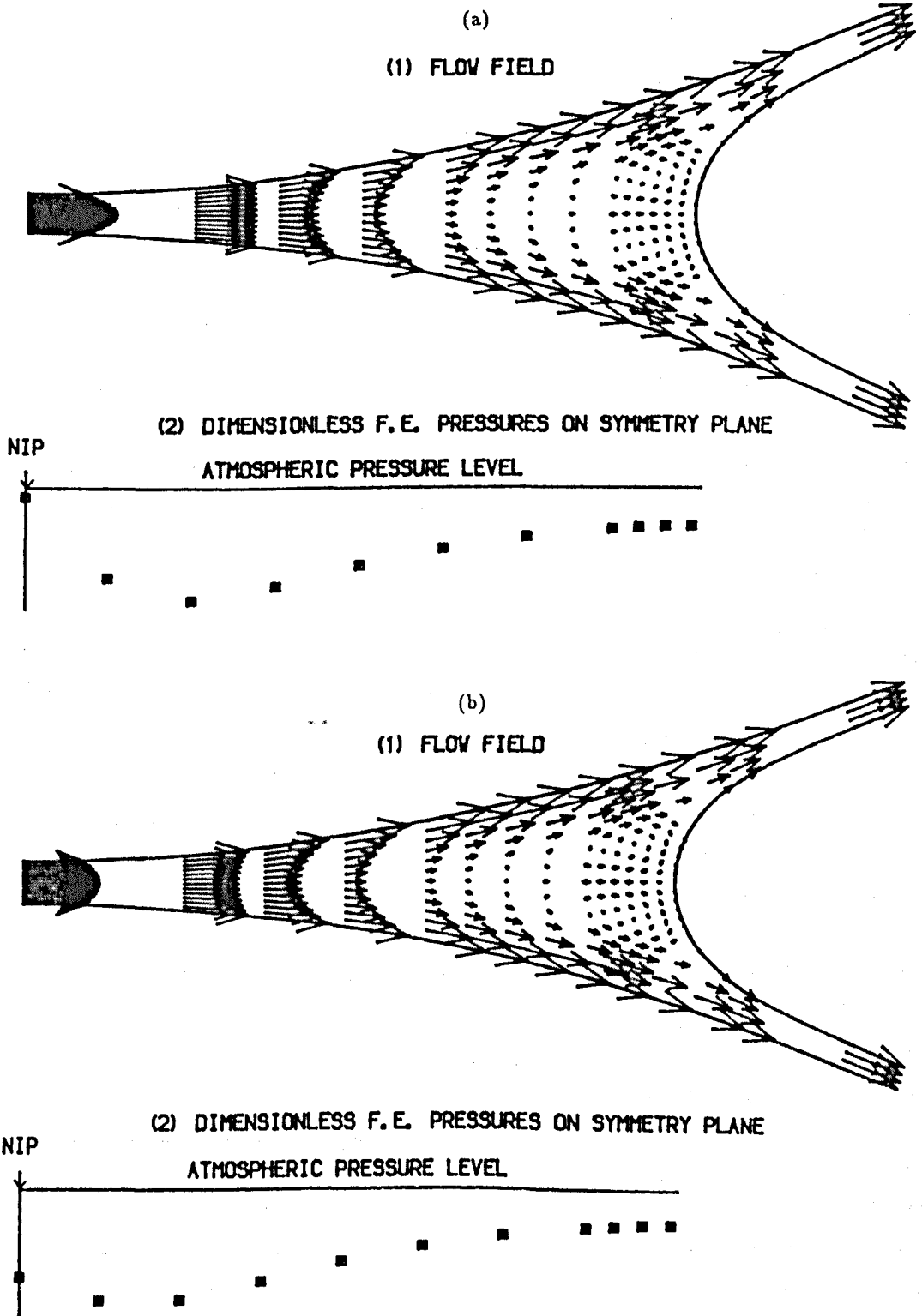
Figure 5.18: The Effects of Starvation in a Forward Roll Coater I: Fully-Flooded to Moderate-Starvation with $Re = 0.0$, $Ca = 0.1$, $S = 1.0$, $R/H_0 = 100$; (a) Fully-Flooded ($\lambda = 1.35$); (b) $\lambda = 1.15$; (c) $\lambda = 1.0$; (d) $\lambda = 0.9$; (e) $\lambda = 0.75$; (f) $\lambda = 0.6$; (g) Effect on the Downstream Free Surface Profile

(c)

(1) FLOW FIELD

(2) DIMENSIONLESS F.E. PRESSURES ON SYMMETRY PLANE

NIP

ATMOSPHERIC PRESSURE LEVEL

(d)

(1) FLOW FIELD

(2) DIMENSIONLESS F.E. PRESSURES ON SYMMETRY PLANE

NIP

ATMOSPHERIC PRESSURE LEVEL

Figure 5.18 (continued)

(e)

(1) FLOW FIELD

(2) DIMENSIONLESS F.E. PRESSURES ON SYMMETRY PLANE

NIP

ATMOSPHERIC PRESSURE LEVEL

(f)

(1) FLOW FIELD

(2) DIMENSIONLESS F.E. PRESSURES ON SYMMETRY PLANE

NIP

ATMOSPHERIC PRESSURE LEVEL

Figure 5.18 (continued)

(g)

$\lambda = 0.60 \quad 0.75 \quad 0.90 \quad 1.00 \quad 1.15 \quad 1.35$

Figure 5.18 (continued)

(a)

(1) FLOW FIELD

(2) DIMENSIONLESS F.E. PRESSURES ON SYMMETRY PLANE

NIP

ATMOSPHERIC PRESSURE LEVEL

Figure 5.19: The Effects of Starvation in a Forward Roll Coater II: Moderate- to Ultra-Starvation with $Re = 0.0$, $Ca = 0.017$, $S = 1.0$, $R/H_0 = 100$; (a) $\lambda = 0.4$; (b) $\lambda = 0.3$; (c) $\lambda = 0.2$; (d) Effect on the Downstream Free Surface Profile

(b)

(1) FLOW FIELD

(2) DIMENSIONLESS F. E. PRESSURES ON SYMMETRY PLANE

NIP

ATMOSPHERIC PRESSURE LEVEL

(c)

(1) FLOW FIELD

(2) DIMENSIONLESS F. E. PRESSURES ON SYMMETRY PLANE

NIP

ATMOSPHERIC PRESSURE LEVEL

Figure 5.19 (continued)

(d)

$$\lambda = 0.2 \qquad 0.3 \qquad 0.4$$
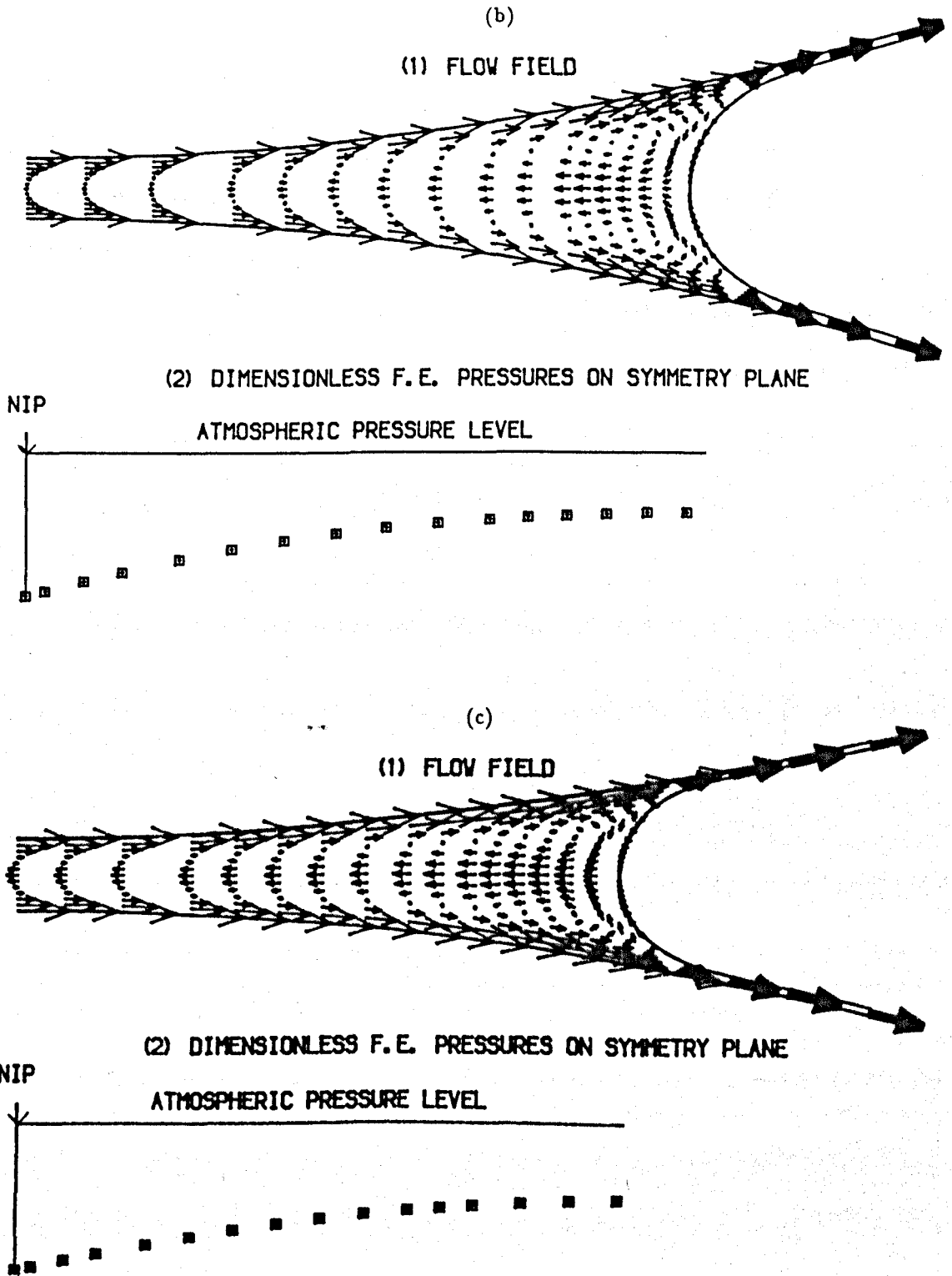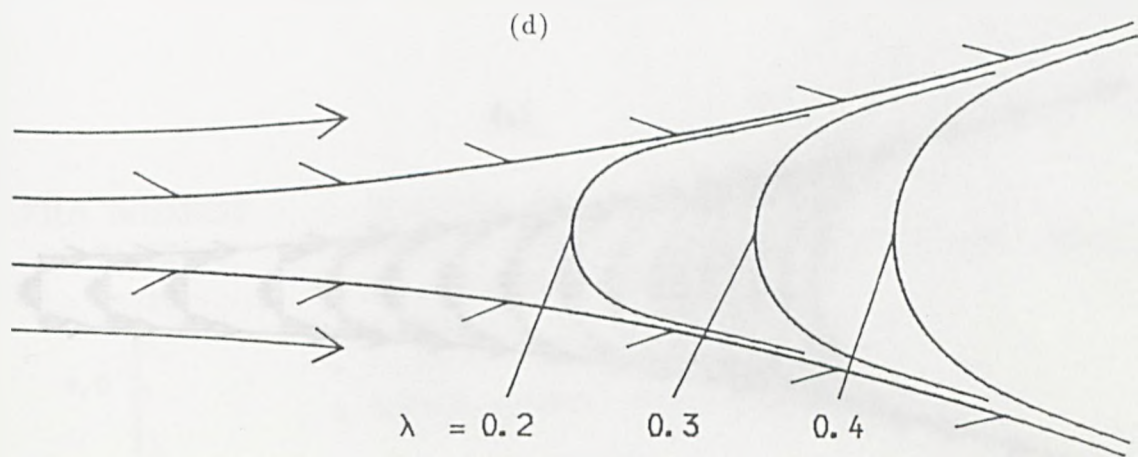
Figure 5.19 (continued)

(a)
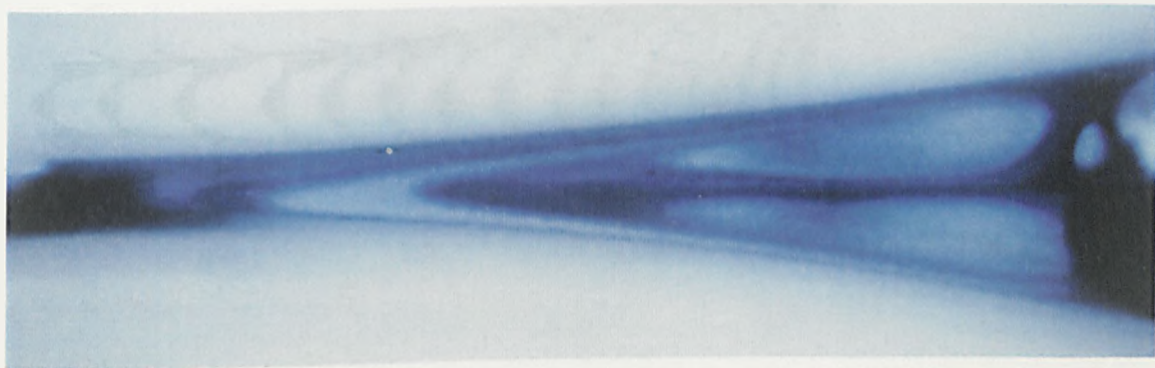
(b)
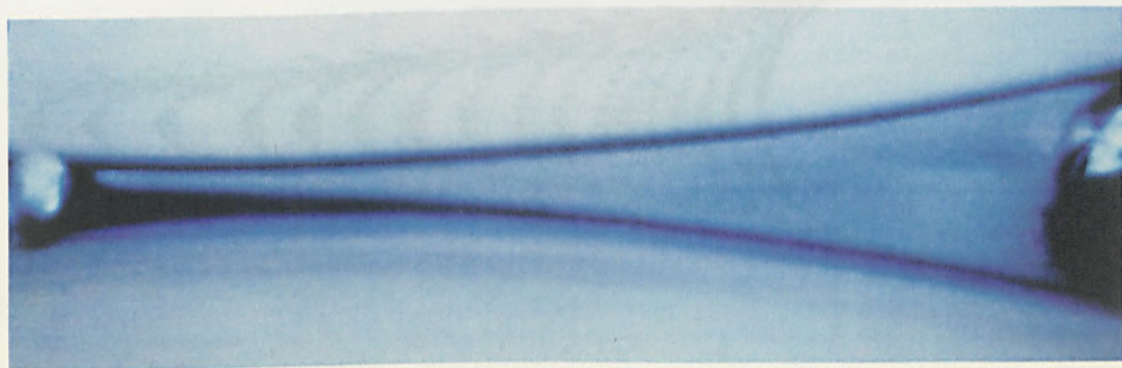
Figure 5.20: Malone's Flow Visualisations of Starved Forward Roll Coating
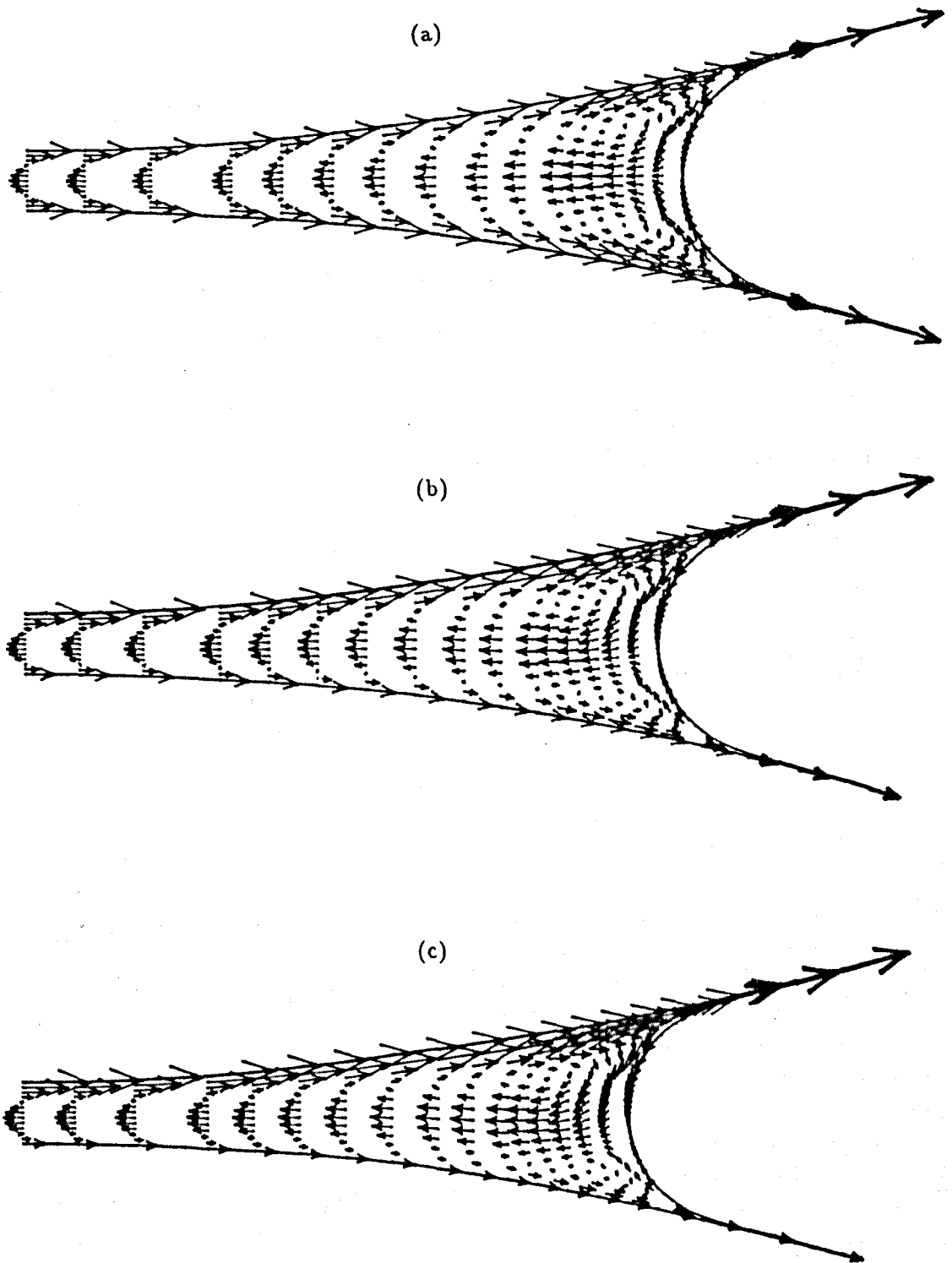
Figure 5.21: Forward Meniscus Roll Coating – Dependence on Velocity Ratio For $Re = 0.0$, $Ca = 0.002$, $\lambda = 0.08$, $R/H_0 = 100$: (a) $S = 1.0$, (b) $S = 2.0$, (c) $S = 3.0$

FILM THICKNESS
RATIO

T_1/T_2

— BENKREIRA ET AL [1981] ($T_1/T_2 = 0.87S^{0.65}$)
× FULLY-FLOODED EXPERIMENTAL DATA (MALONE [1992])
◻ FULLY-FLOODED ($\lambda \approx 1.35$)
▲ $\lambda = 1.0$
▼ $\lambda = 0.6$
○ SAVAGE [1992] ($T_1/T_2 = S(S + 3)/(1 + 3S)$)
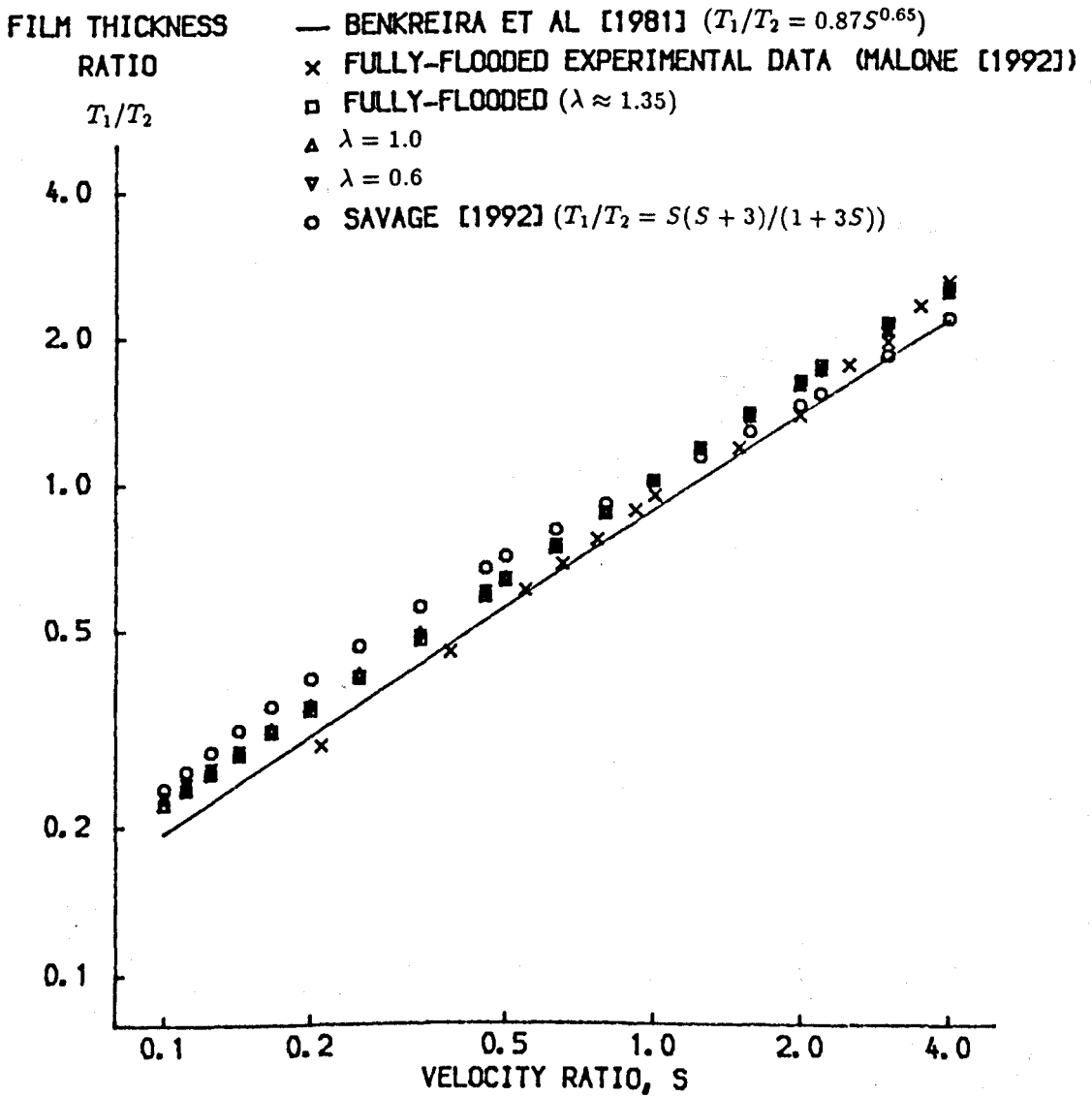
Figure 5.22: F.E. Predictions of T_1/T_2 in Moderately-Starved Forward Roll Coating with $Re = 0.0$, $Ca = 0.1$, $R/H_0 = 100$

FILM THICKNESS
RATIO

T_1/T_2

— BENKREIRA ET AL [1981] $(T_1/T_2 = 0.87S^{0.65})$

× ULTRA-STARVED EXPERIMENTAL DATA (MALONE [1992])

□ $\lambda = 0.4$

▲ $\lambda = 0.3$

▼ $\lambda = 0.2$

○ ULTRA-STARVED MODEL $(T_1/T_2 = S(S+3)/(1+3S))$
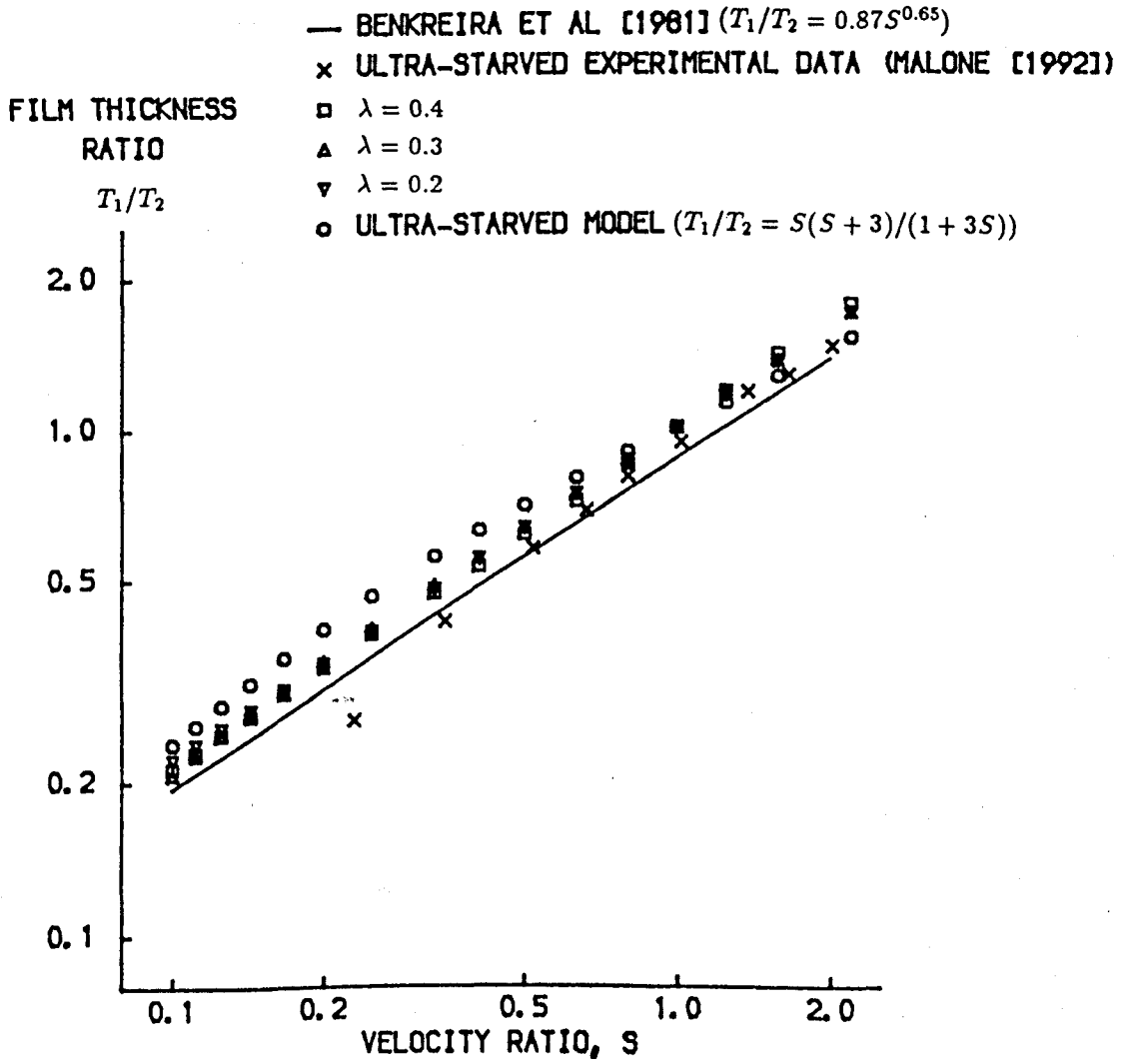
Figure 5.23: F.E. Predictions of T_1/T_2 in Ultra-Starved Forward Roll Coating with $Re = 0.0$, $Ca = 0.017$, $R/H_0 = 100$

Chapter 6: Conclusions

6.1 - General Discussion

6.2 - Suggestions for Future Work

Chapter 6

Conclusions

6.1 General Discussion

The aim of the present chapter is to provide a brief review of the work contained in this thesis and to discuss (i) how it complements previously published work on roll coating, (ii) how it might be extended to provide further insights into the fluid mechanics of roll coating processes.

In Chapter 2, the flows in lid-driven and open, driven cavities were modelled as 'creeping' flows in rectangular domains. Both problems were formulated as boundary value problems for the streamfunction and solved in a semi-analytical form. Streamlines obtained from the semi-analytical solutions were found to be in excellent agreement with (i) previously published results, (ii) solutions obtained numerically using a streamfunction-vorticity F.E. method. These flows pointed the way to a model for meniscus roll coating under the assumption that the flux through the bead can be neglected – the Zero Flux Model. Streamline patterns obtained both analytically and numerically for this problem predicted that, in the forward case, the flow consists of two eddies of which the largest eddy is associated with, and adjacent to, the faster lid. This prediction agrees well with Malone's experimental flow visualisations of forward meniscus roll coating in which he observed two eddies whose relative sizes depended on the velocity ratio.

This 'double-eddy' streamline pattern is significantly different from that observed

in the fully-flooded case in which the flow in the nip region is uni-directional. Moreover the Zero Flux model predicts that in the central 'core' of the bead, i.e. sufficiently far from the meniscii, the flow is horizontal and has a constant pressure gradient whose value is proportional to $(1 + S)/H^{*2}$ – this is in marked contrast to that observed in fully-flooded roll coating which has pressure maxima and minima.

In Chapter 3 the prediction that there is a constant pressure gradient in the central 'core' of the bead led to the development of a simple model for the 'core' flow when a small, non-zero flux passes through the bead – the small flux model. This 'Poiseuille+Couette' model, combined with the experimental observation that in forward meniscus roll coating the eddies are separated by a jet of liquid moving in an 'S'-shape between them, enabled a predictive model for the *average* film thicknesses in forward mensicus roll coating to be developed. This model predicts that the ratio of average film thicknesses on the upper and lower rollers $T_1/T_2 = S(S + 3)/(3S + 1)$ – a function of the roll-speed ratio only – and agrees well with Malone's experimental data. Surprisingly, this is the same result as was obtained by Savage [1992] for the fully-flooded case; there is no obvious reason why they are the same. These film thickness ratio predictions were used to refine the boundary value problem arising from the Zero Flux model to incorporate a small flux through the bead. Streamlines obtained from a numerical (F.E.) solution of this refined boundary value problem agreed well with Malone's flow visualisations of forward meniscus roll coating.

Unfortunately, the analytical models of meniscus roll coating developed in Chapters 2 and 3 are unable to properly account for surface tension effects at a curved free surface. As a result, a F.E. free surface FORTRAN code, based on Kistler's [1983] 'Spine Method', was developed in Chapter 4. It was applied, at first, to relatively simple problems, namely the flows in lid-driven and open, driven cavities, and to the Zero Flux model. As explained in Appendix B, the practical problem of evaluating the F.E. equations was alleviated by Isoparametrically mapping each element into a standard shape; F.E. results were obtained using different quadrature schemes in order to evaluate their suitability.

The code was then extended to accomodate the 'Spine Method' for solving free

surface flow problems and the practical complications introduced by the presence of free surfaces (e.g. balancing stresses at the free surface and the need to evaluate free surface integrals) discussed. This method was described by solving the relatively simple slot coating problem and the F.E. results obtained using the code developed here are in excellent agreement with previously published results. The slot coating code was then modified to solve Coyle et al's [1986] model of fully-flooded forward roll coating in which the flow upstream of the nip was simulated by the imposition of lubrication conditions at the nip; the relatively simple symmetric case was solved first.

Owing to the extreme sensitivity of both the position and shape of the downstream free surface in forward roll coating to the operating parameters, it was necessary to employ a mesh generation algorithm due to Coyle et al [1986] in order to produce an even tessellation of the flow domain into elements. This algorithm, coupled with the 'Spine Method', enabled predictions for (i) the velocity and pressure fields as a function of Ca, (ii) the dimensionless flux through the nip, and (iii) the film-splitting position to be obtained, all of which were in excellent agreement with previously published experimental data and F.E. predictions. However, it was apparent that a particular mesh generation algorithm cannot be suitable for every conceivable set of flow parameters since severe convergence difficulties were experienced for high velocity ratio flows. A possible mechanism for the cause of these difficulties was proposed in terms of element distortion in the downstream region of the F.E. grids. The code was then modified to accomodate asymmetry: F.E. predictions of the film thickness ratio, T_1/T_2, were found to be in reasonable agreement with the F.E. predictions of Coyle et al [1986]. As in the symmetric case, the range of velocity ratio values over which solutions could be obtained, using F.E. grids based on Coyle et al's [1986] mesh generation algorithm, was limited by element distortion.

Chapter 5 began with a more extensive investigation into the relationship between the film thickness ratio T_1/T_2 and the velocity ratio S (in the range $0.1 \le S \le 40$) during fully-flooded forward roll coating. In the range $0.1 \le S \le 15$, the F.E. predictions for T_1/T_2 are proportional to $S^{0.65}$ – in good agreement with Benkreira et al [1981], Coyle et al [1986] and reasonable agreement with Savage's [1992] model – but for $S > 15$ the

predictions begin to exhibit a Ca dependence and diverge from the $S^{0.65}$ power law. Even though the F.E. predictions for $S > 15$ are in broad agreement with Savage's [1992] analytical result, we concluded that there is a need for more robust numerical techniques and fuller experimental data before these high velocity ratio predictions can be accepted with any degree of confidence. Attention was then turned to the effects of starvation in roll coating, beginning with the simplified flat plate/ roller geometry. Models for both fully-flooded and starved flow in this geometry were described, in which the flow domain extended between the nip and downstream free surface, and the resulting free surface boundary value problems solved by the F.E. method. Theoretical predictions for the downstream free surface position and pressure profile in the bead for examples of both flows are in reasonable agreement with experiment.

A numerical (F.E.) study into the effects of starvation in the flat plate/ roller geometry produced many interesting predictions. For example, the velocity field was found to experience a transition in passing from a fully-flooded to an ultra-starved inlet condition. In the former, the flow field divides into two adjoining portions with rectilinear flow in the nip region and a recirculation region in the immediate vicinity of the downstream mensicus. As the flux is reduced, the ratio of the sizes of the two-dimensional and rectilinear portions increases until the recirculation eventually extends upstream of the nip and the ultra-starved situation is achieved where the flow field consists of a single eddy above a thin film of liquid attached to the roller surface. These predictions are borne out by Malone's experimental flow visualisations for similar situations.

Meanwhile, the predicted transition in the pressure field showed a transformation from the characteristic fully-flooded profile, with pressure maxima and minima, to the ultra-starved case where the pressure field is entirely sub-ambient and consists of a linear pressure region near the nip adjoining a constant pressure region near the downstream meniscus. This prediction is also in accord with Malone's findings, although the predicted disappearance of the downstream pressure minimum (at $\lambda \approx 0.5$) occurs more rapidly than is manifested by the data ($\lambda \approx 0.298$). A mechanism for the existence of an entirely sub-ambient pressure field, in the ultra-starved case, was proposed in terms

of the observation that the curvatures of the upstream and downstream free surfaces are quite different.

Chapter 5 concluded with a simple model of starved flow in forward roll coating in which, as in the model of starved flow in a flat plate/ roller geometry, the flow domain is restricted to the region between the nip and downstream free surface. The numerical (F.E.) solutions of the resulting free surface problem predicted transitions in the velocity and pressure fields similar to those obtained in the flat plate/ roller geometry. For example, in the former reducing λ also had the effect of increasing the relative sizes of the rectilinear and two-dimensional portions, but for the two roll system the ultra-starved flow field consists of upper and lower eddies with liquid flowing in a reverse jet between them. This transition is also in qualitative agreement with Malone's flow visualisations of the two roll system. The theoretical transition in the latter is basically the same as that predicted for the flat plate/ roller geometry, although in the two roll system the 'critical' value of λ (defined now by equation (4.89)) marking the disappearance of the pressure minimum is predicted to be at around $\lambda = 1.0$.

Finally a F.E. investigation into how the film thickness ratio T_1/T_2 depends on the degree of starvation for S in the range $0.1 \leq S \leq 10$ was performed. The F.E. predictions are almost independent of the degree of starvation, with $T_1/T_2 \approx S^{0.65}$, and agree well with Malone's data for fully-flooded *and* ultra-starved forward roll coating. They are also in good agreement with the analytical film thickness model developed in Chapter 3 since the F.E. predictions satisfy $T_1/T_2 \approx S(S+3)/(3S+1)$ in this velocity ratio range. Nevertheless, we concluded that these F.E. predictions still need to be corroborated by alternative ones obtained using more robust numerical techniques.

6.2   Suggestions for Future Work

An important feature of the work presented in this thesis has been the interdependence between analytical, computational and experimental analyses of roll coating. The following suggestions for future work, although directed to the theoretician, would be meaningless without reliable experimental data against which theoretical predictions

can be compared.

(i) Although the Zero Flux and small flux models described in Chapters 2 and 3 respectively are applicable to both the forward and reverse modes of roll coating, the film thickness model given is only valid in the forward meniscus roll coating case. An analytical film thickness model is still to be found in the reverse case.

(ii) The instabilities to which meniscus roll coating are susceptible have not been described here, but those described by Malone [1992] may prove to be tractable to a simple analytical model, perhaps similar to those given by Savage [1984] and Carter and Savage [1987] for the fully-flooded case.

(iii) The greatest difficulty experienced in the F.E. analysis of roll coating presented here is due to element distortion under certain circumstances. What is needed is a systematic means of mesh generation in which the positions of the nodes are chosen to satisfy rigorous mathematical criteria; ideally this should include a facility to refine the grid locally, for example near a dynamic wetting line, and the flexibility to handle elements with different shapes, for example triangular and quadrilateral, in the same tessellation – see Shephard [1988] for an extensive review of mesh generation techniques. If this can be done, then the ultimate objective of a 'universal' grid, in the sense that it is suitable for most conditions which occur in practice, may be achievable.

(iv) The F.E. analysis should be extended to include both upstream and downstream free surfaces, and the dynamic wetting line where the upstream free surface meets the upper roller. This ought to be feasible since Coyle et al [1990 a] have surmounted similar difficulties in their F.E. analysis of fully-flooded reverse roll coating. Once this has been achieved the analysis should then be extended to the full reverse meniscus roll coating problem.

(v) Bixler [1982] and Coyle [1984] have developed a technique for analysing the stability of coating flows based on the F.E. method. Their technique, which has been recently applied to the fully-flooded case (Coyle et al [1990 b]), should also

be applicable to mensicus roll coating.

(vi) In this thesis the liquid in the roll coater is assumed to be Newtonian; however most industrial coating liquids are non-Newtonian. Hence the F.E. analysis should be extended to embody a non-Newtonian rheology (see e.g. Schunk and Scriven [1990]). This has already been done for a shear-thinning rheology (Coyle et al [1987]) and may be possible for liquids with, for example, elastic or thixotropic properties.

(vii) In the work reported in this thesis the rollers have been assumed to be rigid and of equal size. A final suggestion for an extension to the theory developed here is to have *deformable* rollers of unequal size. The latter is easy to implement whereas the former presents greater difficulties, although at first the analysis of flows with deformable rollers could proceed along the lines of the work presented by Coyle [1988].

Appendix A: Biorthogonal Series Solutions of Cavity-Driven Flows

A.1 - Smith's Biorthogonality Relation

A.2 - The Flow in a Lid-Driven Cavity

    A.2.1 - Determination of the Expansion Coefficients

A.3 - The Flow in an Open, Driven Cavity

Table A.1

Appendix A

Biorthogonal Series Solutions of Cavity-Driven Flows

A.1 Smith's Biorthogonality Relation

In his [1952] paper, Smith examined the bending of a thin, semi-infinite strip using the method of *Biorthogonal Series Expansions*. The equation governing this bending is the biharmonic equation

$$\nabla^4 w = 0 \qquad (A.1)$$

where w is the normal deflection. This equation is solved in the region $y > 0$, $-1 < x < 1$ subject to the 'Clamped-Edge' boundary conditions:

$$w = \frac{\partial w}{\partial x} = 0 \quad \text{at } x = \pm 1 \qquad (A.2)$$

He proposed to separate variables and write the variables $\partial^2 w / \partial x^2$, $\partial^2 w / \partial y^2$ as

$$\frac{\partial^2 w}{\partial y^2} = \sum_{s_n} c_n \phi_1^n(x, s_n) e^{-s_n y} \quad , \quad \frac{\partial^2 w}{\partial x^2} = \sum_{s_n} c_n \phi_2^n(x, s_n) e^{-s_n y} \qquad (A.3)$$

where the eigenfunctions $\phi_1^n(x, s_n)$, $\phi_2^n(x, s_n)$ and the eigenvalues s_n are determined subsequently. Equation (A.1) allied to the compatibility relation

$$\frac{\partial^4 w}{\partial y^2 \partial x^2} = \frac{\partial^4 w}{\partial x^2 \partial y^2} \qquad (A.4)$$

233

may be rewritten as a single vector equation

$$\frac{d^2}{dx^2} \begin{bmatrix} \phi_1^n \\ \phi_2^n \end{bmatrix} + s_n^2 \begin{bmatrix} 0 & -1 \\ 1 & 2 \end{bmatrix} \begin{bmatrix} \phi_1^n \\ \phi_2^n \end{bmatrix} = 0 \tag{A.5}$$

The 'clamped-edge' conditions become

$$\phi_1^n = \frac{d\phi_1^n}{dx} = 0 \quad \text{at } x = \pm 1 \tag{A.6}$$

The form of the expression for $\partial^2 w/\partial y^2$ may be readily integrated to yield

$$w = \sum c_n \phi_1^n(x, s_n) \frac{e^{-s_n y}}{s_n^2} \tag{A.7}$$

He now faced the problem of determining the coefficients c_n. In order to achieve this he introduced a generalized Wronskian W given by

$$W = [\psi_1^m, \psi_2^m] \begin{bmatrix} d\phi_1^n/dx \\ d\phi_2^n/dx \end{bmatrix} - [d\psi_1^m/dx, d\psi_2^m/dx] \begin{bmatrix} \phi_1^n \\ \phi_2^n \end{bmatrix} \tag{A.8}$$

where ψ_1^m, ψ_2^m are defined below. It may easily be shown that

$$\frac{dW}{dx} = [\psi_1^m, \psi_2^m] \begin{bmatrix} d^2\phi_1^n/dx^2 \\ d^2\phi_2^n/dx^2 \end{bmatrix} - [d^2\psi_1^m/dx^2, d^2\psi_2^m/dx^2] \begin{bmatrix} \phi_1^n \\ \phi_2^n \end{bmatrix} \tag{A.9}$$

By definition $[\phi_1^n, \phi_2^n]^T$ is a solution of (A.5) hence

$$\frac{dW}{dx} = - \left\{ s_n^2 [\psi_1^m, \psi_2^m] \begin{bmatrix} 0 & -1 \\ 1 & 2 \end{bmatrix} + [d^2\psi_1^m/dx^2, d^2\psi_2^m/dx^2] \right\} \begin{bmatrix} \phi_1^n \\ \phi_2^n \end{bmatrix} \tag{A.10}$$

At this stage define the equation *adjoint* to (A.5) as

$$\frac{d^2}{dx^2} [\psi_1^m, \psi_2^m] + s_m^2 [\psi_1^m, \psi_2^m] \begin{bmatrix} 0 & -1 \\ 1 & 2 \end{bmatrix} = 0 \tag{A.11}$$

If W is to vanish whenever $\phi_1^n = d\phi_1^n/dx = 0$, then $\psi_2^m = d\psi_2^m/dx = 0$ also. The boundary conditions adjoint to (A.6) are

$$\psi_2^m = \frac{d\psi_2^m}{dx} = 0 \quad \text{at } x = \pm 1 \tag{A.12}$$

Now if $[\psi_1^m(x), \psi_2^m(x)]$ is an eigenvector of (A.11) corresponding to s_m^2 and $[\phi_1^n(x), \phi_2^n(x)]^T$ is an eigenvector of (A.5) with boundary conditions (A.6) corresponding to s_n^2, then

$$(s_m^2 - s_n^2) [\psi_1^m, \psi_2^m] \begin{bmatrix} 0 & -1 \\ 1 & 2 \end{bmatrix} \begin{bmatrix} \phi_1^n \\ \phi_2^n \end{bmatrix} = \frac{dW}{dx} \tag{A.13}$$

Integrating and using the boundary conditions (A.6), (A.12) yields

$$(s_m^2 - s_n^2) \int_{-1}^{+1} [\psi_1^m, \psi_2^m] \begin{bmatrix} 0 & -1 \\ 1 & 2 \end{bmatrix} \begin{bmatrix} \phi_1^n \\ \phi_2^n \end{bmatrix} dx = 0 \qquad (A.14)$$

Therefore

$$\int_{-1}^{+1} [\psi_1^m, \psi_2^m] \begin{bmatrix} 0 & -1 \\ 1 & 2 \end{bmatrix} \begin{bmatrix} \phi_1^n \\ \phi_2^n \end{bmatrix} dx = 0 \text{ if } s_m^2 \neq s_n^2 \qquad (A.15)$$

This is the 'biorthogonality' relation and will now be used to solve creeping flows in lid-driven and open, driven cavities (see §2.3, 2.4 respectively).

A.2   The Flow in a Lid-Driven Cavity

The boundary value problem shown in Figure 2.2 (b) is even. Hence the eigenfunctions $\phi_1^n(x, s_n)$ in the solution of this problem must also be even; they are even 'Papkovich-Fadle' eigenfunctions defined by

$$\phi_1^n(x, s_n) = s_n \sin s_n \cos s_n x - s_n x \cos s_n \sin s_n x \qquad (A.16)$$

$$\phi_2^n(x, s_n) = -(s_n \sin s_n + 2\cos s_n)\cos s_n x + s_n x \cos s_n \sin s_n x \quad (A.17)$$

$$\psi_1^n(x, s_n) = (s_n \sin s_n - 2\cos s_n)\cos s_n x - s_n x \cos s_n \sin s_n x \quad (A.18)$$

$$\psi_2^n(x, s_n) = s_n \sin s_n \cos s_n x - s_n x \cos s_n \sin s_n x = \phi_1^n \qquad (A.19)$$

The parameter s_n is determined from the conditions (A.6) which yield the eigenvalue equation for s_n:

$$\sin 2s_n = -2s_n \qquad (A.20)$$

The solutions, s_n, of this eigenvalue relation are complex and must be determined. Robbins and Smith [1948] have published a table of the first 10 roots of (A.20) in the upper right hand quadrant in increasing order of $|s_n|$. In practice, these roots may be conveniently determined by using the simple Newton iteration procedure described by Robbins and Smith [1948]. For large $|s_n|$, the nth root of (A.20) with positive real and imaginary parts is approximated by

$$2s_n \approx (2n + 1.5)\pi + i \log(4n + 3)\pi \qquad (A.21)$$

This is a convenient start-up approximation for the Newton iteration. The first 40 upper right hand quadrant solutions of $\sin 2s_n = -2s_n$ (where $s_n = u_n + iv_n$) are given in Table A.1.

A.2.1 Determination of the Expansion Coefficients

The technique described in this section is due to Joseph and Sturges [1978]. The proposed solution to the lid-driven cavity flow at zero Reynolds number is of the form

$$\psi(x,y) = \sum_{-\infty}^{\infty} \left(A_n e^{s_n(y-2A^*)} + B_n e^{-s_n y} \right) \frac{\phi_1^n(x,s_n)}{s_n^2} \tag{A.22}$$

where $\phi_1^n(x,s_n)$ is an even Papkovich-Fadle eigenfunction and s_n are roots of (A.20). If the streamfunction is to be physically meaningful then it must be real. Therefore as $\phi_1^{-n}(x) = \overline{\phi}_1^n(x)$ where – denotes complex conjugate, reality of the streamfunction implies $A_{-n} = \overline{A}_n, B_{-n} = \overline{B}_n$.

The boundary conditions on the upper and lower lids (see §2.3) mean that the coefficients A_n, B_n must be selected to match

$$1 = \sum_{-\infty}^{\infty} (A_n - B_n e^{-2s_n A^*}) \, \phi_1^n/s_n \tag{A.23}$$

$$0 = \sum_{-\infty}^{\infty} (A_n + B_n e^{-2s_n A^*}) \, \phi_1^n/s_n^2 \tag{A.24}$$

$$0 = \sum_{-\infty}^{\infty} (A_n e^{-2s_n A^*} - B_n) \, \phi_1^n/s_n \tag{A.25}$$

$$0 = \sum_{-\infty}^{\infty} (A_n e^{-2s_n A^*} + B_n) \, \phi_1^n/s_n^2 \tag{A.26}$$

The critical step in determining A_n, B_n is to apply the biorthogonality relation (A.15) to these 4 equations. To prepare for this application, first differentiate (A.24) twice with respect to x, using the relation that $d^2\phi_1^n/dx^2 = s_n^2 \phi_2^n(x)$ to eliminate ϕ_1^n. It is then possible to write (A.23) and the twice differentiated (A.24) as

$$\begin{pmatrix} 1 \\ 0 \end{pmatrix} = \sum_{-\infty}^{\infty} \left\{ (A_n + B_n e^{-2s_n A^*}) \begin{pmatrix} \phi_1^n \\ \phi_2^n \end{pmatrix} + \left[\frac{A_n(1-s_n)}{s_n} - B_n e^{-2s_n A^*} \frac{(1+s_n)}{s_n} \right] \begin{pmatrix} \phi_1^n \\ 0 \end{pmatrix} \right\} \tag{A.27}$$

Similarly, (A.25) and twice differentiated (A.26) are combined to give

$$
\begin{pmatrix} 0 \\ 0 \end{pmatrix} = \sum_{-\infty}^{\infty} \left\{ (A_n e^{-2s_n A^*} + B_n) \begin{pmatrix} \phi_1^n \\ \phi_2^n \end{pmatrix} + \left[A_n e^{-2s_n A^*} \frac{(1 - s_n)}{s_n} - \frac{B_n(1 + s_n)}{s_n} \right] \begin{pmatrix} \phi_1^n \\ 0 \end{pmatrix} \right\}
$$

(A.28)

The operator $\int_{-1}^{+1} (\psi_1^l, \psi_2^l) \begin{pmatrix} 0 & -1 \\ 1 & 2 \end{pmatrix} \begin{pmatrix} \cdot \\ \cdot \end{pmatrix} dx$ is then applied to (A.27) and (A.28)

yielding

$$
(A_l + B_l e^{-2s_l A^*}) K_l + \sum_{-\infty}^{\infty} \left\{ \left[A_n \frac{(1 - s_n)}{s_n} - B_n e^{-2s_n A^*} \frac{(1 + s_n)}{s_n} \right] M_{l,n} \right\} = 4 \text{ (A.29)}
$$

$$
(A_l e^{-2s_l A^*} + B_l) K_l + \sum_{-\infty}^{\infty} \left\{ \left[A_n e^{-2s_n A^*} \frac{(1 - s_n)}{s_n} - B_n \frac{(1 + s_n)}{s_n} \right] M_{l,n} \right\} = 0 \text{ (A.30)}
$$

where

$$
K_l = \int_{-1}^{1} [\psi_1^l, \psi_2^l] \begin{bmatrix} 0 & -1 \\ 1 & 2 \end{bmatrix} \begin{bmatrix} \phi_1^l \\ \psi_2^l \end{bmatrix} dx = -4 \cos^4 s_l
$$

(A.31)

and

$$
M_{l,n} = \int_{-1}^{+1} \psi_2^l \phi_1^n dx =
$$

$$
s_l s_n \{ 2 \cos s_l \cos s_n \left[\frac{\sin(s_l + s_n)}{(s_l + s_n)^3} - \frac{\sin(s_l - s_n)}{(s_l - s_n)^3} \right] +
$$

$$
(1 + \cos(s_l - s_n) \cos(s_l + s_n)) \left[\frac{1}{(s_l - s_n)^2} - \frac{1}{(s_l + s_n)^2} \right] \}
$$

(A.32)

for $l \neq n$ and for $l = n$,

$$
A_{l,l} = -\cos^2 s_l \left(\frac{2}{3} s_l^2 + \cos^2 s_l \right)
$$

(A.33)

(A.29) and (A.30) form an infinite set to be solved for the coefficients A_n, B_n for

$n = \pm 1, \pm 2, \ldots$ which of course cannot be solved in practice. However, they may be

solved if the streamfunction is truncated after N terms. In this case (A.29), (A.30)

yield 4N equations for the 4N unknowns, i.e. the real and imaginary parts of A_n, B_n

for $n = 1, \ldots, N$. This enables the truncated solution to be found.

A.3   The Flow in an Open, Driven Cavity

The eigenfunctions $\tilde{\phi}_1^n$ used in §2.4 for the solution of the flow in an open, driven cavity

are odd; they are defined by

$$
\tilde{\phi}_1^n(y, p_n) = p_n \cos p_n \sin p_n y - p_n y \sin p_n \cos p_n y
$$

(A.34)

$$\tilde{\phi}_2^n(y, p_n) = -(p_n \cos p_n - 2 \sin p_n) \sin p_n y + p_n y \sin p_n \cos p_n y \quad (A.35)$$

$$\tilde{\psi}_1^n(y, p_n) = (p_n \cos p_n + 2 \sin p_n) \sin p_n y - p_n y \sin p_n \cos p_n y \quad (A.36)$$

$$\tilde{\psi}_2^n(y, p_n) = p_n \cos p_n \sin p_n y - p_n y \sin p_n \cos p_n y = \tilde{\phi}_1^n \quad (A.37)$$

The parameters p_n are determined from the condition $\tilde{\phi}_1^n = d\tilde{\phi}_1^n/dy = 0$ at $y = -1$ giving the following eigenvalue relation for p_n

$$\sin 2p_n = 2p_n \quad (A.38)$$

The solutions p_n of this equation are complex. Hillman and Salzer [1943] have published a table of the first ten roots of (A.38) in the upper right hand quadrant. These roots may be determined by Newton iteration using the approximation

$$2p_n \approx (2n + 0.5)\pi + i \log(4n + 1)\pi \quad (A.39)$$

for the nth root with positive real and imaginary parts. The first 40 roots of (A.38) (where $p_n = x_n + iy_n$) are given in Table A.1. As noted earlier, the streamfunction ψ (see equation (2.19)) is real hence $C_{-n} = \overline{C}_n$, $D_{-n} = \overline{D}_n$. The boundary conditions on the side walls (see Figure 2.8) mean that the coefficients C_n and D_n must be selected to match

$$1 = \sum_{-\infty}^{\infty} (C_n - D_n e^{-p_n A^*}) \frac{\tilde{\phi}_1^n}{p_n} \quad (A.40)$$

$$0 = \sum_{-\infty}^{\infty} (C_n + D_n e^{-p_n A^*}) \frac{\tilde{\phi}_1^n}{p_n^2} \quad (A.41)$$

$$0 = \sum_{-\infty}^{\infty} (C_n e^{-p_n A^*} - D_n) \frac{\tilde{\phi}_1^n}{p_n} \quad (A.42)$$

$$0 = \sum_{-\infty}^{\infty} (C_n e^{-p_n A^*} + D_n) \frac{\tilde{\phi}_1^n}{p_n^2} \quad (A.43)$$

Using the same technique as in §A.2, these equations are prepared for the application of a biorthogonality condition giving

$$\begin{pmatrix} 1 \\ 0 \end{pmatrix} = \sum_{-\infty}^{\infty} \left\{ (C_n + D_n e^{-p_n A^*}) \begin{pmatrix} \tilde{\phi}_1^n \\ \tilde{\phi}_2^n \end{pmatrix} + \left(\frac{C_n(1 - p_n)}{p_n} - D_n e^{-p_n A^*} \frac{(1 + p_n)}{p_n} \right) \begin{pmatrix} \tilde{\phi}_1^n \\ 0 \end{pmatrix} \right\}$$

$$(A.44)$$

$$\begin{pmatrix} 0 \\ 0 \end{pmatrix} = \sum_{-\infty}^{\infty} \left\{ (C_n e^{-p_n A^*} + D_n) \begin{pmatrix} \tilde{\phi}_1^n \\ \tilde{\phi}_2^n \end{pmatrix} + \left(C_n e^{-p_n A^*} \frac{(1 - p_n)}{p_n} - D_n \frac{(1 + p_n)}{p_n} \right) \begin{pmatrix} \tilde{\phi}_1^n \\ 0 \end{pmatrix} \right\}$$

$$(A.45)$$

In this case, apply the modified biorthogonality operator

$$\int_{-1}^{0} (\tilde{\psi}_1^l, \tilde{\psi}_2^l) \begin{pmatrix} 0 & -1 \\ 1 & 2 \end{pmatrix} \begin{pmatrix} \cdot \\ \cdot \end{pmatrix} dy \tag{A.46}$$

to the equations (A.44), (A.45). This can be shown to give

$$2 - \cos p_l - 1/\cos p_l = (C_l + D_l e^{-p_l A^*}) \tilde{K}_l$$
$$+ \sum_{-\infty}^{\infty} \left\{ \left[\frac{C_n(1 - p_n)}{p_n} - D_n e^{-p_n A^*} \frac{(1 + p_n)}{p_n} \right] \tilde{M}_{l,n} \right\} \tag{A.47}$$

$$0 = (C_l e^{-p_l A^*} + D_l) \tilde{K}_l + \sum_{-\infty}^{\infty} \left\{ \left[C_n e^{-p_n A^*} \frac{(1 - p_n)}{p_n} - D_n \frac{(1 + p_n)}{p_n} \right] \tilde{M}_{l,n} \right\} \tag{A.48}$$

where

$$\tilde{K}_l = \int_{-1}^{0} (\tilde{\psi}_1^l, \tilde{\psi}_2^l) \begin{bmatrix} 0 & -1 \\ 1 & 2 \end{bmatrix} \begin{bmatrix} \tilde{\phi}_1^l \\ \tilde{\phi}_2^l \end{bmatrix} dy = -2 \sin^4 p_l \tag{A.49}$$

$$\tilde{M}_{l,n} = \int_{-1}^{0} \tilde{\psi}_2^l \tilde{\phi}_1^n dy = p_l p_n \left\{ \frac{\sin(p_l + p_n)}{(p_l + p_n)^2} \left(\frac{-\sin p_l \sin p_n}{(p_l + p_n)} - \frac{\sin(p_l + p_n)}{2} \right) \right.$$
$$+ \frac{\sin(p_n - p_l)}{(p_n - p_l)^2} \left(-\frac{\sin p_n \sin p_l}{(p_l - p_n)} + \frac{\sin(p_l - p_n)}{2} \right)$$
$$\left. + \sin p_n \sin p_l \left(\frac{\cos(p_l + p_n)}{(p_l + p_n)^2} + \frac{\cos(p_l - p_n)}{(p_l - p_n)^2} \right) \right\} \tag{A.50}$$

for $l \neq n$ and for $l = n$,

$$A_{l,l} = -\sin^2 p_l \left(\frac{p_l^2}{3} + \frac{\sin^2 p_l}{2} \right) \tag{A.51}$$

This infinite system of equations is truncated after N terms so that (A.47), (A.48) yield 4N equations for the 4N unknowns, i.e. the real and imaginary parts of C_n, D_n for $n = 1, ... N$.

(a) $\sin 2s_n = -2s_n$: $s_n = u_n + iv_n$

(b) $\sin 2p_n = 2p_n$: $p_n = x_n + iy_n$

n	u_n	v_n	x_n	y_n
1	2.10620	1.12536	3.74884	1.38434
2	5.35627	1.55157	6.94998	1.67611
3	8.53668	1.77554	10.11926	1.85838
4	11.69918	1.92940	13.27727	1.99157
5	14.85406	2.04685	16.42987	2.09663
6	18.00493	2.14189	19.57941	2.18340
7	21.15341	2.22172	22.72704	2.25732
8	24.30034	2.29055	25.87338	2.32171
9	27.44620	2.35105	29.01883	2.37876
10	30.59130	2.40501	32.16362	2.42996
11	33.73581	2.45372	35.30790	2.47640
12	36.87989	2.49810	38.45180	2.51890
13	40.02363	2.53887	41.59539	2.55807
14	43.16709	2.57656	44.73873	2.59439
15	46.31032	2.61161	47.88187	2.62825
16	49.45337	2.64436	51.02484	2.65997
17	52.59627	2.67510	54.16766	2.68979
18	55.73903	2.70407	57.31037	2.71794
19	58.88168	2.73144	60.45297	2.74459
20	62.02424	2.75740	63.59549	2.76988
21	65.16671	2.78207	66.73792	2.79396
22	68.30912	2.80558	69.88029	2.81694
23	71.45145	2.82804	73.02260	2.83890
24	74.59373	2.84953	76.16486	2.85994
25	77.73597	2.87014	79.30706	2.88014
26	80.87815	2.88993	82.44923	2.89954
27	84.02030	2.90897	85.59136	2.91823
28	87.16241	2.92731	88.73345	2.93624
29	90.30449	2.94500	91.87552	2.95362
30	93.44654	2.96209	95.01755	2.97042
31	96.58856	2.97861	98.15956	2.98667
32	99.73056	2.99461	101.30155	3.00241
33	102.87253	3.01010	104.44351	3.01768
34	106.01449	3.02514	107.58546	3.03249
35	109.15642	3.03973	110.72739	3.04687
36	112.29834	3.05391	113.86930	3.06085
37	115.44025	3.06770	117.01119	3.07445
38	118.58213	3.08112	120.15307	3.08769
39	121.72401	3.09418	123.29494	3.10059
40	124.86587	3.10692	126.43680	3.11317

Table A.1: The first 40 Upper Right Hand Quadrant Roots of (a) $\sin 2s_n = -2s_n$ and (b) $\sin 2p_n = 2p_n$

Appendix B: The Streamfunction-Vorticity F.E. Method

B.1 - Introduction

    B.1.1 Variational Principles

B.2 - The Philosophy of the F.E. Method

B.3 - The F.E. Equations

B.4 - Corner Singularities

B.5 - Local Co-ordinates: The Isoparametric Mapping

B.6 - Numerical Integration

B.7 - Solution of the F.E. Equations

Figures B.1 - B.7

Appendix B

The Streamfunction-Vorticity

F.E. Method

B.1 Introduction

The purpose of this appendix is to introduce a linear F.E. technique for flows with negligible fluid inertia (known as the Streamfunction-Vorticity method) and to describe how it can be used to obtain numerical solutions of the 3 boundary value problems derived in Chapter 2. The philosophy behind and practical implementation of this method is discussed with particular reference to the treatment of the corner singularities that exist in each boundary value problem.

However, before describing the streamfunction-vorticity method, it is necessary to introduce the concept of a 'variational principle'.

B.1.1 Variational Principles

Often continuum problems have different but equivalent formulations - a differential formulation and a variational formulation. In the differential formulation the problem is to integrate a differential equation subject to given boundary conditions. In the variational formulation, however, the problem is to *extremize*, i.e. make stationary, a functional, Π say, subject to the same boundary conditions (Heubner [1975] p 67). The

functional Π is defined as an integral form over the domain Ω and boundary ∂Ω,

$$\Pi = \int_{\Omega} F(\underline{a}) \, d\Omega + \int_{\partial\Omega} G(\underline{a}) \, ds \qquad (B.1)$$

in which $\underline{a}$ is the unknown function and F and G are specified operators. The solution $\underline{a}$ is that which makes Π stationary with respect to small changes $\delta\underline{a}$. Hence we require

$$\delta\Pi = 0 \qquad (B.2)$$

In fact the problem of finding stationarity with respect to the parameters $\underline{a}$ is an old one and is associated with the names of Rayleigh [1870] and Ritz [1909]. In §B.3 we will obtain functionals Π for each of the 3 boundary value problems described in Chapter 2 and show how they enable the F.E. equations to be obtained.

B.2   The Philosophy of the F.E. Method

Let Ω be a fluid domain with boundary ∂Ω in which the solution of the governing equations, subject to known boundary conditions, is sought. The basic idea of the F.E. method is to reduce the original continuous flow problem to a discrete analogue by subdividing the domain into a number of elements. Within each element the solution of the governing differential equations (in this problem ψ and ω) are approximated by low-order polynomials which are functions of the values of ψ and ω at a finite number of points (the nodes) touching that element. By combining many small elements we obtain a global approximation to the solution of the governing equations in terms of the nodal values of ψ and ω. If there are a total of N nodes and the values of ψ and ω at node k are $\overline{\psi}_k, \overline{\omega}_k$ respectively then this polynomial approximation takes the following form

$$\psi(x,y) = \sum_{k=1}^{N} N_k(x,y)\overline{\psi}_k \quad , \quad \omega(x,y) = \sum_{k=1}^{N} N_k(x,y)\overline{\omega}_k \qquad (B.3)$$

The interpolating functions $N_k(x,y)$ (known as 'shape functions') are chosen to satisfy

$$N_k = \begin{cases} 1 & \text{at node k} \\ 0 & \text{at all other nodes} \end{cases} \qquad (B.4)$$

Equation (B.4) is important because it means that $N_k = 0$ inside any element which node k does not touch. In practice this leads to a considerable simplification to (B.3)

enables equation (B.6) to be rewritten as

$$I(\psi, \omega) = \int_\Omega \left[\nabla . (\delta\psi \nabla\omega + \delta\omega \nabla\psi) - \nabla(\delta\psi) . \nabla\omega - \nabla(\delta\omega) . \nabla\psi + \delta \left(\frac{\omega^2}{2} \right) \right] d\Omega \quad \text{(B.8)}$$

Applying the divergence theorem to the purely divergent terms yields

$$I = \int_\Omega \left[-\nabla(\delta\psi) . \nabla\omega - \nabla(\delta\omega) . \nabla\psi + \delta \left(\frac{\omega^2}{2} \right) \right] d\Omega + \int_{\partial\Omega} \left(\delta\psi \frac{\partial\omega}{\partial n} + \delta\omega \frac{\partial\psi}{\partial n} \right) ds \quad \text{(B.9)}$$

Since ∇ is a linear operator,

$$\nabla(\delta\psi) = \delta\nabla\psi , \ \nabla(\delta\omega) = \delta\nabla\omega \quad \text{(B.10)}$$

which means

$$I(\psi, \omega) = \delta \left\{ \int_\Omega \left[-\nabla\psi . \nabla\omega + \frac{\omega^2}{2} \right] d\Omega \right\} + \int_{\partial\Omega} \left(\delta\psi \frac{\partial\omega}{\partial n} + \delta\omega \frac{\partial\psi}{\partial n} \right) ds \quad \text{(B.11)}$$

This is almost a variational principle – unfortunately we also need to be able to write the boundary integral term as $\delta\Pi$ for some Π. However this can be achieved when the boundary conditions for the 3 boundary value problems of interest are included. In each problem the boundaries consist of either solid walls, at which no-slip conditions apply, or planar fluid interfaces, at which a condition of zero shear stress is applied. Note that since $\psi = 0$ on each boundary, $\delta\psi = 0$ on $\partial\Omega$, so the boundary integral term in equation (B.11), $I_{\partial\Omega}$, reduces to

$$I_{\partial\Omega} = \int_{\partial\Omega} \delta\omega \frac{\partial\psi}{\partial n} ds \quad \text{(B.12)}$$

(i) At the Solid Boundaries

The tangential boundary velocity, $V_t = \partial\psi/\partial n$, is prescribed. Hence if $\partial\Omega^1$ denotes the portion of the boundary formed by solid walls, then the contribution to the boundary term in (B.11) due to $\partial\Omega^1$ is simply

$$\int_{\partial\Omega^1} \delta\omega \, V_t ds \quad \text{(B.13)}$$

(ii) At Planar Zero Shear Stress Boundaries

In §2.4 we saw that $\partial u/\partial y + \partial v/\partial x$ represents the (dimensionless) shear stress at a planar fluid boundary . Hence in terms of the velocity components $u = \partial\psi/\partial y, v = -\partial\psi/\partial x$,

$$\frac{\partial u}{\partial y} + \frac{\partial v}{\partial x} = \frac{\partial^2\psi}{\partial y^2} - \frac{\partial^2\psi}{\partial x^2} \quad \text{(B.14)}$$

Since the boundary is flat this enables us to show that either $\partial^2 \psi / \partial x^2$ or $\partial^2 \psi / \partial y^2$ is zero, depending on the orientation of the boundary. However it has been seen that

$$\omega = -\nabla^2 \psi = -\left(\frac{\partial^2 \psi}{\partial x^2} + \frac{\partial^2 \psi}{\partial y^2} \right) \tag{B.15}$$

Hence, at a planar fluid boundary, the zero shear stress condition is equivalent to $\omega = 0$. Therefore in the boundary value problems shown in Figures 2.8 and 2.12 we impose the condition $\omega = 0$ at the planar 'free' surface. Consequently $\delta\omega = 0$ also on the fluid boundary so if $\partial\Omega^2$ denotes the portion of the boundary at which the zero shear stress condition is imposed, the contribution to the boundary term in (B.12) due to $\partial\Omega^2$ is zero.

This means that, in each boundary value problem, the boundary integral term (B.12) is simply given by (B.13), which may be rewritten as

$$\delta \left\{ \int_{\partial\Omega^1} V_t \, \omega \, ds \right\} \tag{B.16}$$

This implies that

$$I(\psi, \omega) = \delta \left\{ \int_{\Omega} \left[-\nabla\psi.\nabla\omega + \frac{\omega^2}{2} \right] d\Omega + \int_{\partial\Omega^1} V_t \, \omega ds \right\} \tag{B.17}$$

so we have demonstrated the existence of a variational principle for each problem where the functional Π is defined by

$$\Pi(\psi, \omega) = \int_{\Omega} \left[-\nabla\psi.\nabla\omega + \frac{\omega^2}{2} \right] d\Omega + \int_{\partial\Omega^1} V_t \, \omega ds \tag{B.18}$$

Substituting the F.E. approximations (B.3) into (B.18) yields

$$\Pi(\overline{\psi}_j, \overline{\omega}_k) = \sum_{j,k=1}^{N} \left\{ \int_{\Omega} \left(\frac{N_j N_k}{2} \overline{\omega}_j \overline{\omega}_k - \nabla N_j.\nabla N_k \, \overline{\omega}_k \overline{\psi}_j \right) d\Omega \right\}$$

$$+ \sum_{j=1}^{N} \left\{ \int_{\partial\Omega} N_j V_t \, \overline{\omega}_j ds \right\} \tag{B.19}$$

The F.E. equations are obtained by requiring stationarity of (B.19) with respect to each of the nodal parameters $\overline{\psi}_j$, $\overline{\omega}_k$ (see e.g. Heubner [1975] p 77, Zienkiewicz [1977] p 66). Stationarity with respect to $\overline{\omega}_l$ yields

$$\frac{\partial\Pi}{\partial\overline{\omega}_l} = \sum_{k=1}^{N} \int_{\Omega} [N_l N_k \overline{\omega}_k - \nabla N_l.\nabla N_k \overline{\psi}_k] d\Omega + \int_{\partial\Omega^1} N_l V_t ds = 0 \tag{B.20}$$

Stationarity with respect to $\overline{\psi}_l$ yields

$$\frac{\partial \Pi}{\partial \overline{\psi}_l} = -\sum_{k=1}^{N} \int_{\Omega} \nabla N_l . \nabla N_k \, \overline{\omega}_k \, d\Omega = 0 \qquad \text{(B.21)}$$

Equations (B.20), (B.21) provide 2N F.E. equations for the 2N unknowns $(\overline{\psi}_k, \overline{\omega}_k, k = 1, ... N)$.

B.4   Corner Singularities

In the cavity-driven flows of Chapter 2, there are difficulties in analysing the flow near the corners of the cavity. These corners may be conveniently categorized into 3 types: those formed at junctions of (i) a moving wall and a planar 'free surface'; (ii) a moving and a stationary wall; and (iii) two stationary walls.

Junctions of type (iii) offer no special difficulties however those of types (i) and (ii) are troublesome because under the assumption of no-slip between solid and fluid, the fluid velocity is undefined. This leads to the prediction of unphysical singularities in the stress and vorticity at the corner (Moffatt [1964], Huh and Scriven [1971]). In fact a junction of type (i) is an example of a dynamic wetting line, the subject of which has been discussed in §§1.3.2.

In the past, in the numerical solution of problems with corner singularities of types (i) and (ii), the inevitable inaccuracies introduced into the solution have been alleviated by fine resolution of the computational mesh near these corners. This has proved to be reasonably effective in limiting any numerical error to a small neighbourhood of the corners, but it can be tedious as more effort has to be expended in producing the mesh.

In this thesis the corner singularities are handled by using a method developed by Moffatt [1964] in his classic paper in which he presented simple similarity solutions to the creeping flow of a viscous fluid near a sharp corner between two planes. In this method, the problem of prescribing boundary conditions on the vorticity very near the corners is solved by expanding the streamfunction in a series of separated solutions which are functions of r, the distance from the corner and an azimuthal angle θ. This

expression takes the form

$$\psi = \sum_p r^p f_p(\theta) \tag{B.22}$$

where $p > 0$ and is increasing. Sufficiently close to the corner the leading order term, given by $\psi_1 = r f_1(\theta)$, is dominant and in the following analysis it will be obtained for examples of both types of corner singularity.

Type (i) Singularity

A type (i) singularity (dynamic wetting line) is formed at the junction of a moving wall with a 'planar' free surface. An example is illustrated in Figure B.2. In this example the moving lid is at $\theta = 0$ and the 'planar' free surface, at which a condition of zero shear stress is imposed, is at $\theta = \pi/2$.

The streamfunction ψ in the vicinity of the corner is given by the solution of the boundary value problem shown in Figure B.2. Following Dean and Montagnon [1949], Moffatt [1964] showed that the first order term ψ_1, may be written as $\psi_1 = r f_1(\theta)$ where

$$f_1(\theta) = A\cos\theta + B\sin\theta + C\theta\cos\theta + D\theta\sin\theta \tag{B.23}$$

Note that the boundary conditions may be rewritten in terms of derivatives with respect to r and θ (see Batchelor [1985]); in particular, the condition of zero shear stress is expressed by the condition

$$\frac{\partial^2 \psi}{\partial \theta^2} = 0 \qquad \text{at } \theta = \pi/2 \tag{B.24}$$

The first order solution to the boundary value problem shown in Figure B.2 is

$$\psi_1 = Ur\sin\theta\,(1 - 2\theta/\pi) \tag{B.25}$$

In polar co-ordinates

$$\nabla^2 \psi = \frac{1}{r}\frac{\partial}{\partial r}\left(r\frac{\partial \psi}{\partial r}\right) + \frac{1}{r^2}\frac{\partial^2 \psi}{\partial \theta^2} \tag{B.26}$$

so, the first order vorticity defined by $\omega_1 = -\nabla^2 \psi_1$ is

$$\omega_1 = \frac{4U\cos\theta}{\pi r} \tag{B.27}$$

Note that the vorticity on the free surface is already known to be zero, therefore the only condition on vorticity needed is that for the moving lid ($\theta = 0$)

$$\omega_1 = \frac{4U}{\pi r} \tag{B.28}$$

In the F.E. solution of a flow with a type (i) singularity, the magnitude of the vorticity at the node on the lid closest to, but not at, the corner is given by (B.28). The actual sign of the vorticity depends on the relative orientation of the moving lid and the free surface. At a corner node we impose $\omega = 0$ since it lies on the zero shear stress planar 'free surface'.

Type (ii) Singularity

A type (ii) singularity is formed at the junction of a moving and a stationary wall. An example is illustrated in Figure B.3. The moving (velocity U) and stationary lids are positioned at $\theta = 0$, $\pi/2$ respectively. The first order solution to the boundary value problem shown in Figure B.3 is

$$\psi_1 = \frac{Ur}{(\pi^2 - 4)}(\pi^2 \sin\theta - 4\theta \cos\theta - 2\pi\theta \sin\theta) \tag{B.29}$$

with

$$\omega_1 = \frac{U}{(\pi^2 - 4)r}(4\pi \cos\theta - 8\sin\theta) \tag{B.30}$$

Hence the appropriate boundary conditions on vorticity for the lids are

(a) Moving Lid ($\theta = 0$)

$$\omega_1 = \frac{4\pi U}{(\pi^2 - 4)r} \tag{B.31}$$

(b) Stationary Lid ($\theta = \pi/2$)

$$\omega = -\frac{8U}{(\pi^2 - 4)r} \tag{B.32}$$

In the F.E. solutions of flows with a type (ii) singularity, the magnitude of the vorticity at the node closest to, but not at the corner of (a) the moving lid, (b) the stationary lid is given by the magnitudes of (B.31) and (B.32) respectively. The actual sign of the vorticity depends on the relative orientation of the moving and stationary lids. At the corner, $r = 0$ so it is not possible to use the above conditions on vorticity. In §§1.3.2 we saw that in most theoretical analyses of

Note that the vorticity on the free surface is already known to be zero, therefore the only condition on vorticity needed is that for the moving lid ($\theta = 0$)

$$\omega_1 = \frac{4U}{\pi r} \tag{B.28}$$

In the F.E. solution of a flow with a type (i) singularity, the magnitude of the vorticity at the node on the lid closest to, but not at, the corner is given by (B.28). The actual sign of the vorticity depends on the relative orientation of the moving lid and the free surface. At a corner node we impose $\omega = 0$ since it lies on the zero shear stress planar 'free surface'.

Type (ii) Singularity

A type (ii) singularity is formed at the junction of a moving and a stationary wall. An example is illustrated in Figure B.3. The moving (velocity U) and stationary lids are positioned at $\theta = 0$, $\pi/2$ respectively. The first order solution to the boundary value problem shown in Figure B.3 is

$$\psi_1 = \frac{Ur}{(\pi^2 - 4)}(\pi^2 \sin\theta - 4\theta\cos\theta - 2\pi\theta\sin\theta) \tag{B.29}$$

with

$$\omega_1 = \frac{U}{(\pi^2 - 4)r}(4\pi\cos\theta - 8\sin\theta) \tag{B.30}$$

Hence the appropriate boundary conditions on vorticity for the lids are

(a) Moving Lid ($\theta = 0$)

$$\omega_1 = \frac{4\pi U}{(\pi^2 - 4)r} \tag{B.31}$$

(b) Stationary Lid ($\theta = \pi/2$)

$$\omega = -\frac{8U}{(\pi^2 - 4)r} \tag{B.32}$$

In the F.E. solutions of flows with a type (ii) singularity, the magnitude of the vorticity at the node closest to, but not at the corner of (a) the moving lid, (b) the stationary lid is given by the magnitudes of (B.31) and (B.32) respectively. The actual sign of the vorticity depends on the relative orientation of the moving and stationary lids. At the corner, $r = 0$ so it is not possible to use the above conditions on vorticity. In §§1.3.2 we saw that in most theoretical analyses of dynamic wetting lines the singularity is

removed by allowing perfect slip at the wetting line; this condition may be reinterpreted as requiring zero shear stress at the wetting line. This device is also used here to remove a type (ii) singularity, i.e. we impose $\omega = 0$ at the corner.

B.5 Local Co-ordinates: The Isoparametric Mapping

The computation of the F.E. equations (B.20), (B.21) would seem to present an onerous task because for elements of general size and orientation the shape functions N_k become very complicated functions of the cartesian co-ordinates. The purpose of this section is to describe how this problem can be alleviated by *isoparametrically* mapping a standard element, defined in local co-ordinate space, into each of the deformed elements in the flow domain. The precise definition of the shape functions depends on the shape of the element being used and the local node numbering scheme adopted (see Carter [1985] pp 199-200). Since 6-node triangular elements are used in this thesis, we will limit this section to the details for this type of element.

Figure B.1 shows the standard triangular element in local co-ordinate (ξ, η) space, henceforth known as A_0, and the local node numbering scheme used in this application. Carter [1985] has shown that the shape functions N_k may be conveniently expressed in terms of local 'area' co-ordinates L_1, L_2, L_3. Referring to Figure B.4, let the whole element have area A whilst each of the smaller, separate triangles have areas A_1, A_2, A_3. The 'area' co-ordinates L_1, L_2, L_3 are defined as

$$L_1 = \frac{A_1}{A} \quad , \quad L_2 = \frac{A_2}{A} \quad , \quad L_3 = \frac{A_3}{A} \tag{B.33}$$

and are not independent variables since

$$L_1 + L_2 + L_3 = 1 \tag{B.34}$$

Carter [1985] showed that in the local triangle A_0

$$L_1 = \frac{1}{3}(1 + 2\xi) \quad , \quad L_2 = \frac{1}{3}(1 - \xi + \sqrt{3}\eta) \quad , \quad L_3 = \frac{1}{3}(1 - \xi - \sqrt{3}\eta) \tag{B.35}$$

and if N_k denotes the shape function associated with *local* node k, under the local node numbering scheme of Figure B.1, then

$$N_1 = L_1(2L_1 - 1) \quad , \quad N_2 = 4L_1L_2 \tag{B.36}$$

$$N_3 = L_2(2L_2 - 1) \ , \ N_4 = 4L_2L_3 \qquad \text{(B.37)}$$

$$N_5 = L_3(2L_3 - 1) \ , \ N_6 = 4L_1L_3 \qquad \text{(B.38)}$$

It can be seen that these shape functions not only satisfy requirement (B.4), but also yield

$$\sum_{k=1}^{6} N_k(\xi, \eta) = 1 \qquad \text{(B.39)}$$

at any point of the element.

In §B.2 we saw that if $(\overline{\psi}_k, \overline{\omega}_k)$ denote the values of the streamfunction and vorticity at the kth local node, the value of ψ and ω at any point inside the element is given by (B.3). If $\underline{x}^k = (x_k, y_k)$ are the global co-ordinates of the kth local node, then an element is said to be *isoparametric* if any point in the interior of the element is given by (Kistler and Scriven [1983], Carter [1985])

$$\underline{x} = \sum_{k=1}^{6} \underline{x}^k N_k(\xi, \eta) \qquad \text{(B.40)}$$

i.e. the expressions for x and y involve the same shape functions as the dependent variables. This isoparametric relation is of crucial importance because it enables the equations in global (x, y) space to be evaluated in local (ξ, η) space via the relation

$$\int_{element} f(x, y) dx dy = \int_{A_0} f(x(\xi, \eta), y(\xi, \eta)) |\mathcal{J}| \ d\xi d\eta \qquad \text{(B.41)}$$

where $|\mathcal{J}|$ is the determinant of the Jacobian of the transformation, $\mathcal{J}$, defined by

$$\mathcal{J} = \frac{\partial(x, y)}{\partial(\xi, \eta)} = \begin{bmatrix} \partial x/\partial \xi & \partial x/\partial \eta \\ \partial y/\partial \xi & \partial y/\partial \eta \end{bmatrix} \qquad \text{(B.42)}$$

Note that $\partial x/\partial \xi$, $\partial x/\partial \eta$, $\partial y/\partial \xi$, $\partial y/\partial \eta$ follow directly from the isoparametric mapping (B.40), namely

$$\frac{\partial \underline{x}}{\partial \xi} = \sum_{k=1}^{6} \underline{x}^k \frac{\partial N_k}{\partial \xi} \ , \ \frac{\partial \underline{x}}{\partial \eta} = \sum_{k=1}^{6} \underline{x}^k \frac{\partial N_k}{\partial \eta} \qquad \text{(B.43)}$$

Now in the F.E. equations we need to evaluate $\partial N_k/\partial x$ and $\partial N_k/\partial y$. These may be obtained in terms of derivatives with respect to the local (ξ, η) co-ordinates via the relation (see Kistler and Scriven [1983] p 274)

$$\frac{\partial N_k}{\partial x} = \frac{1}{|\mathcal{J}|} \left(\frac{\partial y}{\partial \eta} \frac{\partial N_k}{\partial \xi} - \frac{\partial y}{\partial \xi} \frac{\partial N_k}{\partial \eta} \right) \qquad \text{(B.44)}$$

$$\frac{\partial N_k}{\partial y} = \frac{1}{|\mathcal{J}|} \left(-\frac{\partial x}{\partial \eta} \frac{\partial N_k}{\partial \xi} + \frac{\partial x}{\partial \xi} \frac{\partial N_k}{\partial \eta} \right) \qquad \text{(B.45)}$$

To complete the F.E. equations it is necessary to evaluate the line integral

$$\int_{\partial\Omega^1} N_j V_t \, ds \tag{B.46}$$

where $\partial\Omega^1$ is the portion of the boundary formed by solid walls and V_t is the velocity of the wall. This is trivial for all nodes which do not lie on $\partial\Omega^1$ because (B.46) will equal zero.

However, when node j lies on $\partial\Omega^1$ this integral is more conveniently evaluated in *local* rather than global (x, y) space by using the isoparametric mapping. In practice, (B.46) is calculated by adding all the contributions along element sides which lie along $\partial\Omega^1$. Without loss of generality suppose that node j lies on $\partial\Omega^1$ and on the side of an element containing local nodes 1, 5 and 6, see Figure B.5. Along the solid boundary,

$$L_2 = N_2 = N_3 = N_4 = 0 \tag{B.47}$$

hence from equation (B.34) L_1 and L_3, which are non-zero along this side, satisfy

$$L_1 + L_3 = 1 \tag{B.48}$$

This means that the biquadratic shape functions N_i collapse to quadratic functions of a single area co-ordinate. Since the direction of integration in (B.46) is anticlockwise, it is convenient to choose to parametrise the shape functions along this side solely in terms of L_1 because it increases along the element boundary in the direction of integration, i.e. $ds/dL_1 > 0$.

Along this element side it is easily shown that

$$N_1 = L_1(2L_1 - 1) \ , \quad N_6 = 4L_1(1 - L_1) \ , \quad N_5 = 1 - 3L_1 + 2L_1^2 \tag{B.49}$$

Moreover, if (x_1, y_1), (x_6, y_6), (x_5, y_5) are the co-ordinates of local nodes 1, 6 and 5 respectively then the isoparametric mapping (B.40) yields

$$x = x_1 N_1(L_1) + x_6 N_6(L_1) + x_5 N_5(L_1) \tag{B.50}$$

$$y = y_1 N_1(L_1) + y_6 N_6(L_1) + y_5 N_5(L_1) \tag{B.51}$$

and in particular

$$\frac{dx}{dL_1} = (4L_1 - 1)x_1 + (4 - 8L_1)x_6 + (4L_1 - 3)x_5 \tag{B.52}$$

$$\frac{dy}{dL_1} = (4L_1 - 1)y_1 + (4 - 8L_1)y_6 + (4L_1 - 3)y_5 \tag{B.53}$$

This enables the integration along the element side to be completed since

$$\int_{side} V_t N_j ds = \int_{L_1=0}^{L_1=1} V_t N_j \frac{ds}{dL_1} dL_1 \qquad (B.54)$$

where $ds/dL_1 = \sqrt{((dx/dL_1)^2 + (dy/dL_1)^2)}$ can be calculated from (B.52), (B.53). Therefore the actual value of (B.46), which is calculated by adding up all the contributions along element sides which lie along $\partial\Omega^1$, is

$$\int_{\partial\Omega^1} N_j V_t ds = \sum_{sides} \left\{ \int_{L_1=0}^{L_1=1} V_t N_j \frac{ds}{dL_1} dL_1 \right\} \qquad (B.55)$$

B.6 Numerical Integration

In order to evaluate the F.E. equations we need to evaluate element-level contributions of the form

$$\int_{element} f(x,y) \, dx dy \quad , \quad \int_{side} g(s) \, ds \qquad (B.56)$$

In the previous section we saw how these integrals can be evaluated in local co-ordinate space since

$$\int_{element} f(x,y) \, dx dy = \int_{A_0} f(\xi,\eta) \, |\mathcal{J}| \, d\xi d\eta \qquad (B.57)$$

where $|\mathcal{J}|$ is the determinant of the Jacobian of the isoparametric mapping and

$$\int_{side} g(s) \, ds = \int_0^1 g(L_i) \frac{ds}{dL_i} dL_i \qquad (B.58)$$

where L_i is an area co-ordinate. In F.E. methods it is usual to perform this integration numerically using Gaussian quadrature. For area integrals, this method involves approximating (B.57) by

$$\int_{A_0} F(\xi,\eta) \, d\xi d\eta = \sum_{i=1}^n F(\xi_i,\eta_i) w_i \qquad (B.59)$$

where $F(\xi,\eta) = f(\xi,\eta) |\mathcal{J}|$, (ξ_i, η_i) are n specified points (called Gauss points), and w_i are n specified constants (called the weights). For boundary integrals, replace (B.58) by

$$\int_0^1 G(\xi) \, d\xi \doteq \sum_{i=1}^n G(\xi_i) w_i \qquad (B.60)$$

where $G(\xi) = g(\xi) \, ds/dL_i$ and ξ_i, w_i $(i = 1,...n)$ are the Gauss points and weights respectively for this one-dimensional integral. Most text books on F.E. methods contain

tables of these values. The Gaussian quadrature formulae are derived by approximating the integrand by a polynomial; the order of the integrand for which the scheme is exact increases with the number of Gauss points. However they are not unique, even for a particular order of accuracy.

In practice before one can have any confidence in the F.E. results obtained using a particular quadrature scheme, they must be compared with results obtained using different schemes and, if possible, results from an analytical solution of the problem. The quadrature schemes for area and boundary intergals used in this thesis are shown in Figures B.6 and B.7 respectively. Note that the area integral schemes refer to the integration over the standard triangular element A_0, defined in *local* (ξ, η) co-ordinate space (see Figure B.1). Scheme A is obtained from the NAg F.E. library whereas schemes B, C and D are modified versions of those given by Zienkiewicz [1977 p 201]. All the boundary integral schemes, however, are for integrals over the interval [0,1]; they are modified forms of schemes given by Zienkiewicz [1977 p 198] for integration over the interval [-1,1].

B.7   Solution of the F.E. Equations

The F.E. equations (B.20), (B.21) are solved using a 'banded-matrix' solver from the NAg F.E. library of subroutines; the banded-matrix solution method is described in Appendix C. The bandwidth of these equations is minimised by a judicious node numbering scheme developed by Gaskell and Mobbs [1985]. This successfully reduced the bandwidth of the equations to a manageable size.

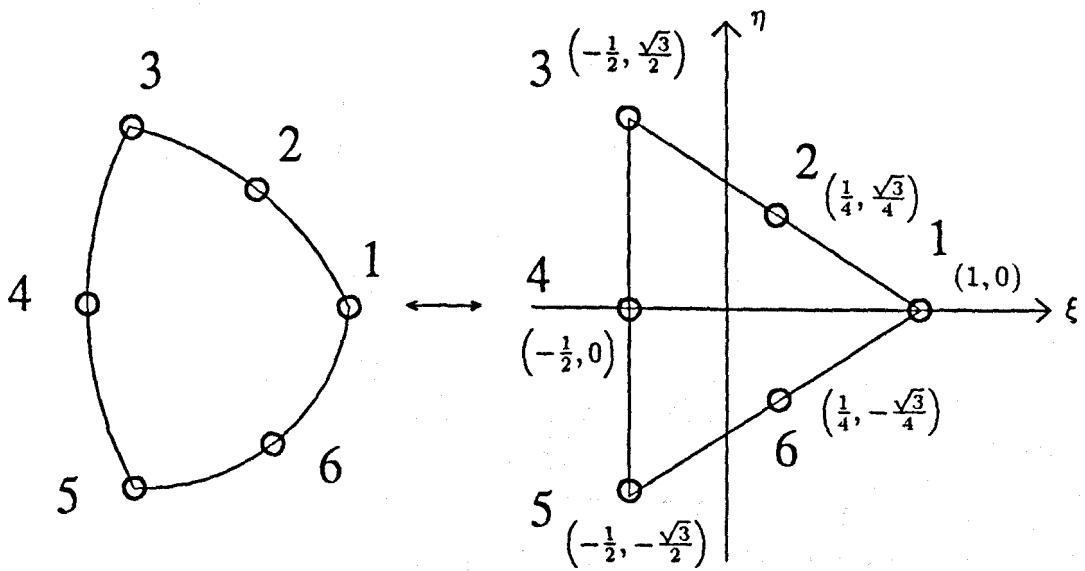Global Space   Local Space A_0

Figure B.1: Six Node Triangular Elements with Local Node Numbering Scheme and Local Co-ordinate Space A_0
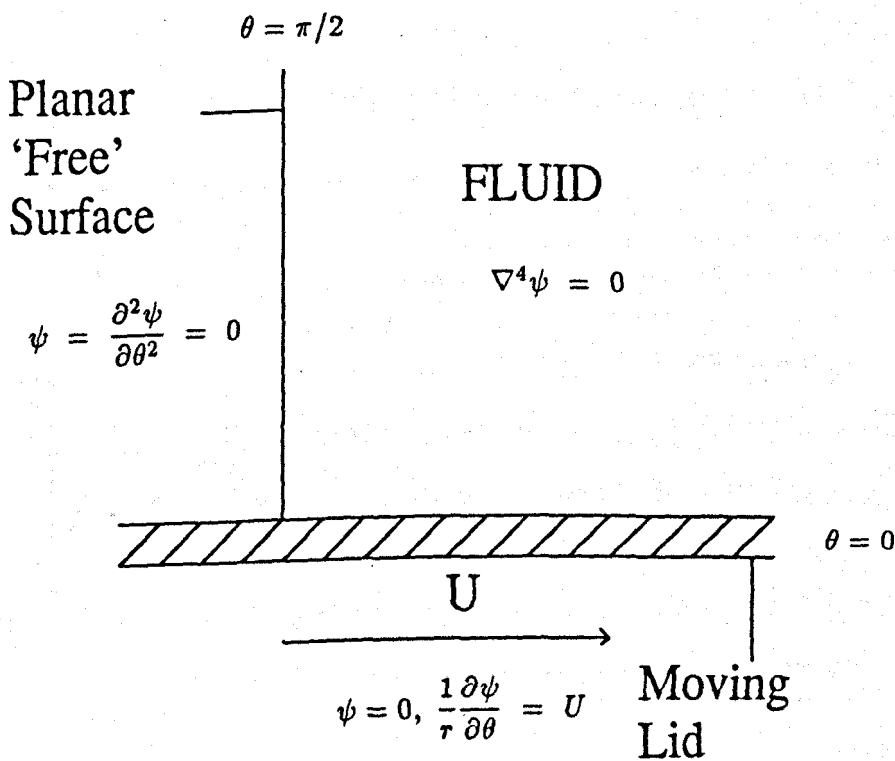
Figure B.2: A Type (i) Singularity – Dynamic Wetting Line

$$\theta = \pi/2$$

Stationary Lid

FLUID

$$\nabla^4 \psi = 0$$

$$\psi = \frac{1}{r}\frac{\partial \psi}{\partial \theta} = 0$$

$$\theta = 0$$

U

$$\psi = 0, \; \frac{1}{r}\frac{\partial \psi}{\partial \theta} = U$$

Moving Lid
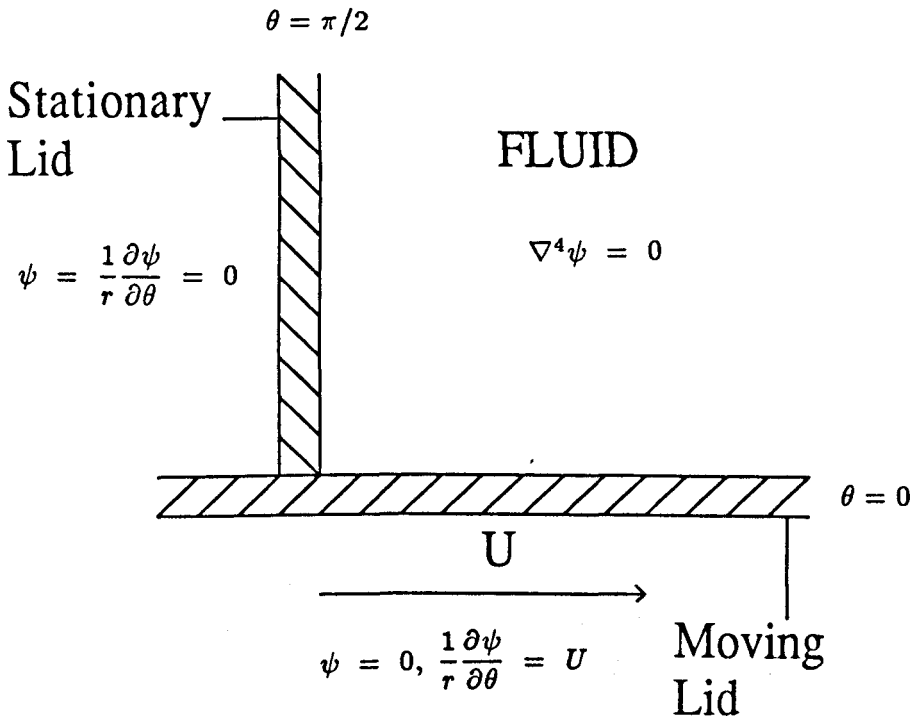
Figure B.3: A Type (ii) Singularity

$$L_1 = \frac{A_1}{A} \quad L_2 = \frac{A_2}{A} \quad L_3 = \frac{A_3}{A}$$

where

$$A = A_1 + A_2 + A_3$$

Figure B.4: Subtriangles of a Triangular Element – 'Area Co-ordinates'

Figure B.5: Local Node Numbering Scheme Along a Solid Boundary

Scheme (A) - 4 quadrature points (all positive weights)

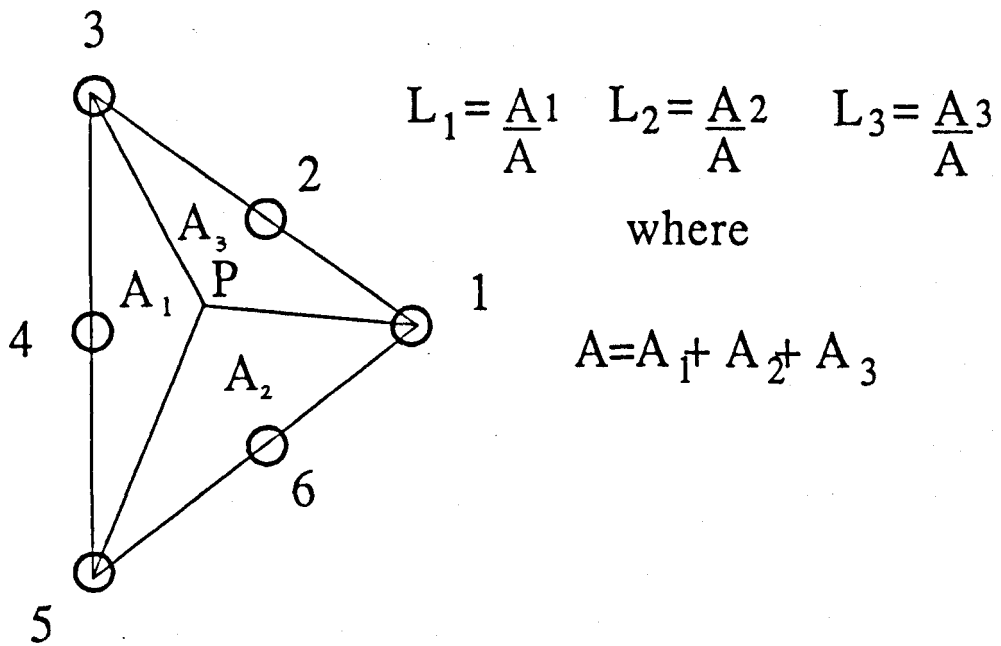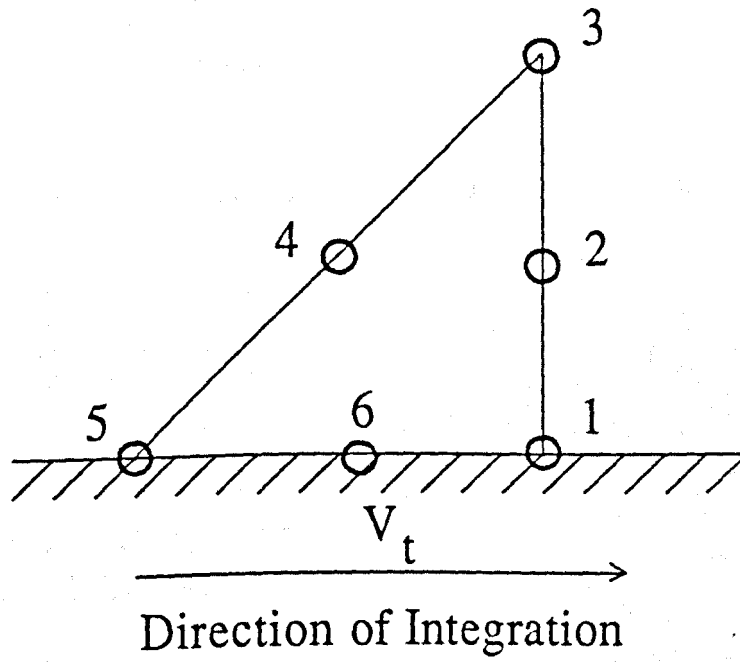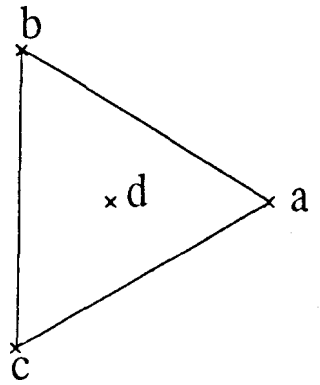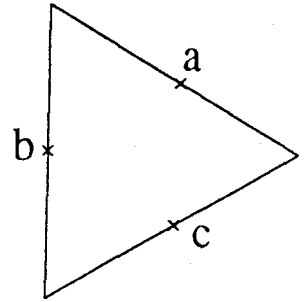|	L_1	L_2	L_3	w
a	1	0	0	$\sqrt{3}/16$
b	0	1	0	$\sqrt{3}/16$
c	0	0	1	$\sqrt{3}/16$
d	1/3	1/3	1/3	$9\sqrt{3}/16$

Scheme (B) - 3 quadrature points (all positive weights)

	L_1	L_2	L_3	w
a	1/2	1/2	0	$\sqrt{3}/4$
b	0	1/2	1/2	$\sqrt{3}/4$
c	1/2	0	1/2	$\sqrt{3}/4$

Scheme (C) - 7 quadrature points (all positive weights)

	L_1	L_2	L_3	w
a	1/3	1/3	1/3	w_1
b	α_1	β_1	β_1	w_2
c	β_1	α_1	β_1	w_2
d	β_1	β_1	α_1	w_2
e	α_2	β_2	β_2	w_3
f	β_2	α_2	β_2	w_3
g	β_2	β_2	α_2	w_3
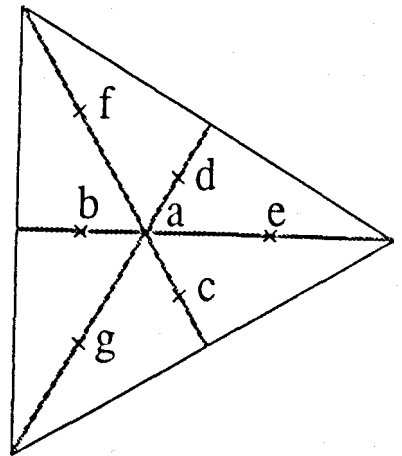
where
$\alpha_1 = 0.05971587$
$\alpha_2 = 0.79742699$
$\beta_1 = 0.47014206$
$\beta_2 = 0.10128651$
and
$w_1 = 0.29228357$
$w_2 = 0.17198505$
$w_3 = 0.1635998$

Scheme (D) - 4 quadrature points (one negative weight)

	L_1	L_2	L_3	w
a	1/3	1/3	1/3	$-w_1$
b	11/15	2/15	2/15	w_2
c	2/15	11/15	2/15	w_2
d	2/15	2/15	11/15	w_2
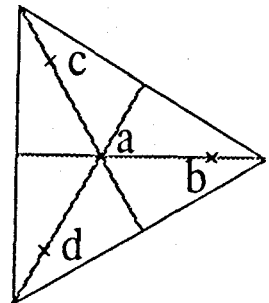
where $w_1 = 0.73070893$ and $w_2 = 0.67658235$

Figure B.6: Gaussian Quadrature Schemes For Area Integrals

Scheme (a) - 2 quadrature points

	ξ	w
a	0.21132487	1/2
b	0.78867513	1/2

Scheme (b) - 3 quadrature points

	ξ	w
a	0.11270167	5/18
b	0.5	4/9
c	0.88729833	5/18
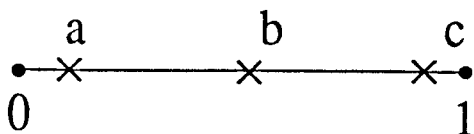
Scheme (c) - 4 quadrature points

	ξ	w
a	0.06943184	w_1
b	0.33000948	w_2
c	0.66999052	w_2
d	0.93056816	w_1
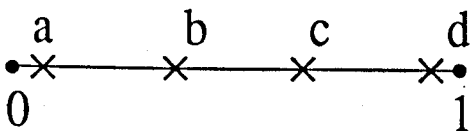
where $w_1 = 0.17392742$ and $w_2 = 0.32607258$

Figure B.7: Gaussian Quadrature Schemes For Boundary Integrals

Appendix C: F.E. Storage Algorithms

Appendix C

F.E. Storage Algorithms

C.1 Introduction

It is desirable to have an efficient storage method for large global matrices, coupled of course with an efficient algebraic solver. Two techniques have been used in this thesis, the pertinent features of which are outlined below.

C.2 The Banded-Matrix Solution Method

Since any global matrix produced by the F.E. method always has a non-zero *banded* structure, it has become a common practice to store only those terms falling within this band. For a symmetric matrix the stored array will have a size equal to the total number of variables multiplied by the *half-bandwidth* of the matrix, while for a non-symmetric matrix the stored array size will be the product of the total number of variables and the *bandwidth*. Both are illustrated schematically - see Figure C.1 (a) and (b) for a system with 8 unknowns.

Clearly, the smaller the bandwidth, the more efficient the storage. The bandwidth relies heavily on the global node numbering procedure adopted. In order to achieve the minimum bandwidth, the difference between the biggest and smallest node number, for any element, must be kept as small as possible.

As regards the solver, Gaussian Elimination is used, modified in accordance with the band storage (see e.g. Bohte [1975], Hager [1988]). The present work employs a

subroutine from the NAg F.E. library which incorporates pivoting via row interchange.

C.3   The Frontal Solution Method

The banded-matrix technique used in the solution of 'cavity-driven' flows is ineffective for problems such as roll coating because every element moves with the free surface, thereby destroying the banded structure of the global matrix. Another method exists which is ideally suited to the solution of F.E. problems: the 'Frontal Solution Method'. This technique is also based on Gaussian Elimination but is more efficient in terms of storage space than the banded-matrix method.

In 1970, Irons published a 'Frontal Solution Program' for use in finite element analysis. However, it was restricted to use with symmetric matrices and it was not until 1976 with a paper by Hood that it was adapted to solve problems producing matrices which are not symmetric. It is the formulation due to Hood which is followed here.

C.3.1   The Philosophy of the Frontal Method

This can briefly be summarized as follows. We commence by assembling each of the element stiffness matrices in turn (i.e. element 1, element 2, etc) until the storage area allocated to the solution routine is full. Then with the assembled part of the complete matrix, a pivotal search is made to determine the largest entry from those rows and columns to which there will be no further contribution from subsequent element assembly. Gauss elimination is then used (with the pivotal row) to eliminate all the coefficients in the pivotal column. The pivotal row is then stored in an external file. The elimination process is repeated until sufficient storage is available to assemble further stiffness matrices. Finally, when all the elements have been assembled, the solution is obtained via a back substitution process. This is best illustrated by considering the simple 3-element problem shown in Figure C.2.

After assembling the equations for element 1 say, we have the following local stiffness

matrix.

$$
\begin{pmatrix} a_{11}^1 & a_{12}^1 & a_{13}^1 \\ a_{21}^1 & a_{22}^1 & a_{23}^1 \\ a_{31}^1 & a_{32}^1 & a_{33}^1 \end{pmatrix} \begin{pmatrix} x_1 \\ x_2 \\ x_3 \end{pmatrix} = \begin{pmatrix} b_1^1 \\ b_2^1 \\ b_3^1 \end{pmatrix} \tag{C.1}
$$

where the superscript refers to the element number. At this stage it can be seen that there will be no more contributions to the equation for x_1 and hence a_{11} may be used to eliminate x_1 from all the equations so far assembled. Equation 1 is then stored in an external file. Note at this stage, equations 2 and 3 are not complete and may not be eliminated until further elements have been assembled. We are now left with the following matrix equation.

$$
\begin{pmatrix} \left(a_{22}^1 - \frac{a_{21}^1 a_{12}^1}{a_{11}^1}\right) & \left(a_{23}^1 - \frac{a_{21}^1 a_{13}^1}{a_{11}^1}\right) \\ \left(a_{32}^1 - \frac{a_{31}^1 a_{12}^1}{a_{11}^1}\right) & \left(a_{33}^1 - \frac{a_{31}^1 a_{13}^1}{a_{11}^1}\right) \end{pmatrix} \begin{pmatrix} x_2 \\ x_3 \end{pmatrix} = \begin{pmatrix} b_2^1 - \frac{a_{21}^1 b_1^1}{a_{11}^1} \\ b_3^1 - \frac{a_{31}^1 b_1^1}{a_{11}^1} \end{pmatrix} \tag{C.2}
$$

Within the program we actually retain the (3x3) matrix and move the remaining entries back one column and up one row as illustrated below.

$$
\begin{pmatrix} X & X & X \\ O & X & X \\ O & X & X \end{pmatrix} \rightarrow \begin{pmatrix} X & X & O \\ X & X & O \\ O & O & O \end{pmatrix}
$$

Row 3 and column 3 are now free for the assembly of element 2.

<u>Note</u> It was seen earlier that node numbering was important to keep the bandwidth of the matrix as small as possible. This does not matter here since the equations are stored in the order in which they are formed. However, element numbering is important (see later).

We can now add the element stiffness matrix from element 2 to the global matrix. The only extra variable introduced is x_4. Equation 4 is assembled in the now vacant line 3 and the coefficients of x_4 in column 3. Hence using the same notation as above we obtain the element stiffness matrix for element 2.

$$
\begin{pmatrix} a_{22}^2 & a_{23}^2 & a_{24}^2 \\ a_{32}^2 & a_{33}^2 & a_{34}^2 \\ a_{42}^2 & a_{43}^2 & a_{44}^2 \end{pmatrix} \begin{pmatrix} x_2 \\ x_3 \\ x_4 \end{pmatrix} = \begin{pmatrix} b_2^2 \\ b_3^2 \\ b_4^2 \end{pmatrix}
$$

The global matrix now becomes

$$
\begin{pmatrix}
\left(a_{22}^1 - \frac{a_{21}^1 a_{12}^1}{a_{11}^1} + a_{22}^2\right) & \left(a_{23}^1 - \frac{a_{21}^1 a_{13}^1}{a_{11}^1} + a_{23}^2\right) & a_{24}^2 \\[2mm]
\left(a_{32}^1 - \frac{a_{31}^1 a_{12}^1}{a_{11}^1} + a_{32}^2\right) & \left(a_{33}^1 - \frac{a_{31}^1 a_{13}^1}{a_{11}^1} + a_{33}^2\right) & a_{34}^2 \\[2mm]
a_{42}^2 & a_{43}^2 & a_{44}^2
\end{pmatrix}
$$

Since assembly of element 3 contributes nothing to the equation for x_2 we can eliminate x_2 in the same way as we eliminated x_1. The solution process continues in this way until all the elements are assembled.

In practice it is possible to assemble many elements before being required to eliminate. Hence, when we come to eliminate we may have several fully assembled equations and may choose to use total pivoting. This is preferable to partial pivoting since there are a limited number of equations to pivot on. By choosing the largest pivot we will increase the stability of the solution process. Descriptions of the method of total pivoting can be found in most text books on numerical methods.

C.3.2   The Front

Consider the finite element mesh shown in Figure C.3. Let us suppose that elements 1 to 7 have been assembled. The 'active' variables, i.e. the ones not yet fully summed are known collectively as the front. The minimum number of equations required to be assembled before elimination can proceed is known as the front width. In order to save storage we need to minimise the front width. In practice this is achieved by keeping the range of element numbers surrounding any node as small as possible. The Frontal Solution Process is summarized in Figure C.4.

(a)

$$
\begin{bmatrix}
K_{11} & K_{12} & K_{13} & & & & & \\
 & K_{22} & K_{23} & K_{24} & & & & \\
 & & K_{33} & K_{34} & K_{35} & & & \\
 & & & K_{44} & K_{45} & K_{46} & & \\
 & & & & K_{55} & K_{56} & K_{57} & \\
 & & & & & K_{66} & K_{67} & K_{68} \\
 & & & & & & K_{77} & K_{78} \\
 & & & & & & & K_{88}
\end{bmatrix}
\quad \underset{\text{---}}{STORE} \quad
\begin{bmatrix}
K_{11} & K_{12} & K_{13} \\
K_{22} & K_{23} & K_{24} \\
K_{33} & K_{34} & K_{35} \\
K_{44} & K_{45} & K_{46} \\
K_{55} & K_{56} & K_{57} \\
K_{66} & K_{67} & K_{68} \\
K_{77} & K_{78} & \\
K_{88} & &
\end{bmatrix}
$$

(b)

$$
\begin{bmatrix}
K_{11} & K_{12} & K_{13} & & & & & \\
K_{21} & K_{22} & K_{23} & K_{24} & & & & \\
K_{31} & K_{32} & K_{33} & K_{34} & K_{35} & & & \\
 & K_{42} & K_{43} & K_{44} & K_{45} & K_{46} & & \\
 & & K_{53} & K_{54} & K_{55} & K_{56} & K_{57} & \\
 & & & K_{64} & K_{65} & K_{66} & K_{67} & K_{68} \\
 & & & & K_{75} & K_{76} & K_{77} & K_{78} \\
 & & & & & K_{86} & K_{87} & K_{88}
\end{bmatrix}
\quad \underset{\text{---}}{STORE} \quad
\begin{bmatrix}
 & & K_{11} & K_{12} & K_{13} \\
 & K_{21} & K_{22} & K_{23} & K_{24} \\
K_{31} & K_{32} & K_{33} & K_{34} & K_{35} \\
K_{42} & K_{43} & K_{44} & K_{45} & K_{46} \\
K_{53} & K_{54} & K_{55} & K_{55} & K_{57} \\
K_{64} & K_{65} & K_{66} & K_{67} & K_{68} \\
K_{75} & K_{76} & K_{77} & K_{78} & \\
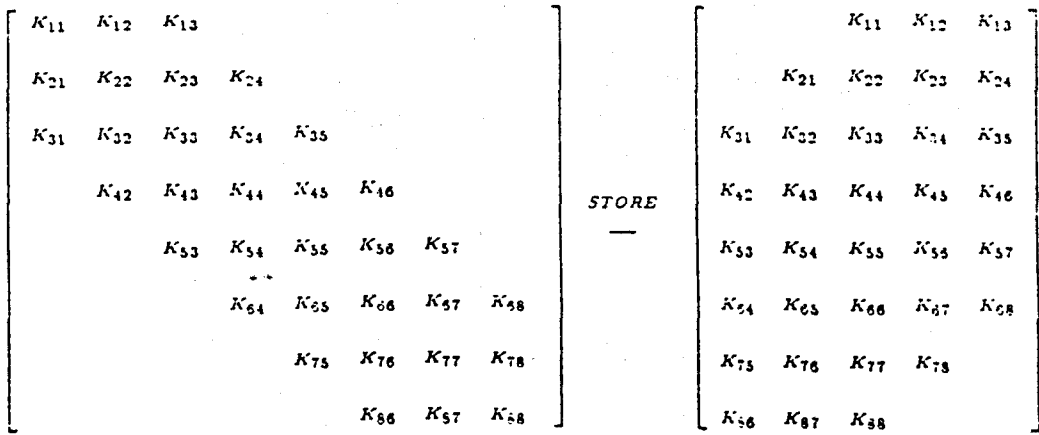K_{86} & K_{87} & K_{88} & &
\end{bmatrix}
$$

Figure C.1: Banded-Matrix Storage Method For (a) Symmetric, (b) Non-Symmetric Matrices

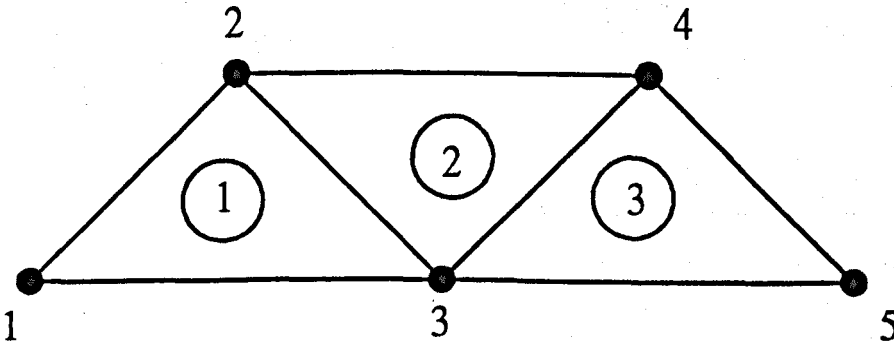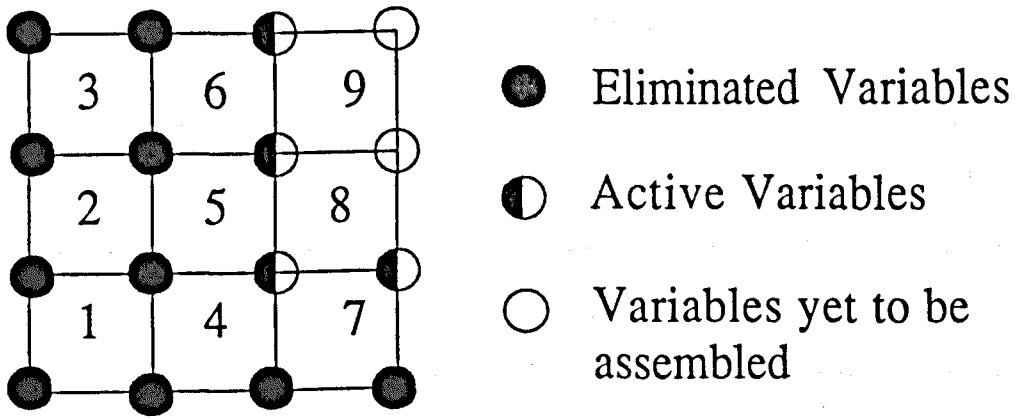Figure C.2: A Simple 3-element problem

Figure C.3: A Simple F.E. Mesh

Let,
(i) NE= total number of elements
(ii) NELL= number of elements assembled
(iii) KROW= number of rows already assembled
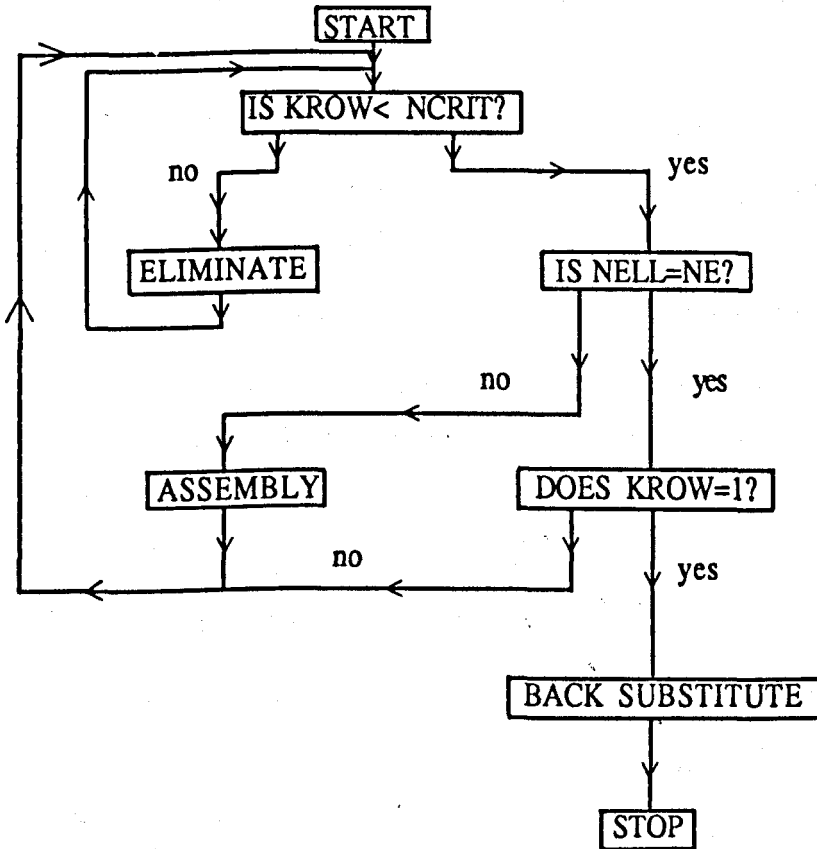(iv) NCRIT= the maximum number of rows to be assembled before storage space is full

Figure C.4: A Flow Chart of the Frontal Solution Process

Bibliography

ADACHI, K., TAMURA, T., NAKAMURA, R., "Coating Flows in a Nip Region and Various Critical Phenomena", *A. I. Ch. E. J*, <u>34</u>, No 3, pp 456-464, March [1988]

BABUSKA, I., AZIZ, A.K., "Lectures on the Mathematical Foundations of the Finite Element Method", *Mathematical Foundations of the Finite Element Method with Applications to Partial Differential Equations (Ed. Aziz, A.K.), Academic Press, New York*, pp 1-135, [1972]

BATCHELOR. G.K., " An Introduction to Fluid Dynamics", *Camb. Univ. Press*, [1985]

BEER, G., HAAS, W.,"A Partitioned Frontal Solver For Finite Element Analysis", *Int. J. Numer. Meth. Eng.*, <u>18</u>, pp 1623-1654, [1982]

BENKREIRA, H., EDWARDS, M.F., WILKINSON, W.L.,"Roll Coating of Purely Viscous Liquids",*Chem. Eng. Sci.*,<u>36</u>, pp 429-434, [1981]

BIRKHOFF, G., HAYS, D.F., "Free Boundaries in Partial Lubrication", *J. Math. Phys. (M.I.T.)* , <u>42</u>, No 2, [1963]

BIXLER, N.E., *Phd Thesis*, University of Minnesota, Minneapolis, [1982]

BOHTE, Z., "Bounds For Rounding Errors in the Gaussian Elimination For Band Systems", *J. Inst. Maths. Applics.*, <u>16</u>, pp 133-142, [1975]

BURGGRAF, O.R., "Analytical and Numerical Studies of the Structure of Steady Separated Flows", *J. F. M.*, <u>24</u>, part 1, pp 113-151, [1966]

BURLEY, R., KENNEDY, B.S., "An Experimental Study of Air Entrainment at a Solid/ Liquid/ Gas Interface", *Chem. Eng. Sci.*, <u>31</u>, pp 901-911, [1976]

CANEDO, E.L., DENSON, C.D., "Flow in Driven Cavities with a Free Surface", *A. I. Ch. E. J.*, <u>35</u>, No 1, Jan [1989]

CARTER, G.C., *PhD Thesis*, University of Leeds, [1985]

CARTER, G.C., SAVAGE, M.D., "Ribbing in a Variable Speed Two-Roll Coater", *Math. Engng. Ind.*, <u>1</u>, pp 83-95, [1987]

CHEN J-X, *PhD Thesis*, University of Leeds, [1991]

CHEN, S.A., HIGGINS, B.G., "Study of the Flow in the Upstream Bank of Liquid

in a Forward Roll Coater by the Finite Element Method", *Chem. Eng. Sci.*, 43, pp 2867-2875, [1988]

CHENG, D.C-H., "Onset of Ribbing in Direct Rolling of Newtonian Fluids", T.L.P. Report No 40, Warren Spring Laboratories, [1981]

CHUNG, T.J., "Finite Element Analysis of Fluid Dynamics", *McGraw-Hill, New York*, [1978]

COOK, R.D., "Concepts and Applications of Finite Element Analysis (2nd Edition)", *Wiley*, [1981]

COX, R.G., "The Dynamics of the spreading of liquids on a solid surface. Part 1. Viscous Flow", *J. F. M.*, 168, pp 169-194, [1986]

COYLE, D.J., MACOSKO, C.W., SCRIVEN, L.E., "Computer Simulation of Nip Flow in Roll Coating", *in (T. Povder (ed.) Computer Applications in Applied Polymer Science, ACS Symposium Series 197, American Chemical Society, Washington*, [1982]

COYLE, D.J., *PhD Thesis*, University of Minnesota, Minneapolis, [1984]

COYLE, D.J., MACOSKO, C.W., SCRIVEN, L.E., "Film-Splitting Flows in Forward Roll Coating", *J. F. M.*, 171, pp 183-207, [1986]

COYLE, D.J., MACOSKO, C.W., SCRIVEN, L.E., "Film-Splitting Flows of Shear-Thinning Liquids in Forward Roll Coating", *A. I. Ch. E. J.*, 33, No 5, p 741, May [1987]

COYLE, D.J., "Forward Roll Coating with Deformable Rolls: A simple one-dimensional elastohydrodynamic model", *Chem. Eng. Sci.*, 43, No 10, pp 2673-2684, [1988]

COYLE, D.J., "Nonlinear Theory of squeeze roll coating", *Paper No 35h, A. I. Ch. E. Spring National Meeting, Orlando,*, March [1990]

COYLE, D.J., MACOSKO, C.W., SCRIVEN, L.E., "The Fluid Dynamics of Reverse Roll Coating", *A. I. Ch. E. J.*, 36, No 2, p 161, Feb [1990 a]

COYLE, D.J., MACOSKO, C.W., SCRIVEN, L.E., "Stability of Symmetric Film-Splitting Between Counter Rotating Cylinders", *J. F. M.*, 216, pp 437-458, [1990 b]

COYNE, J.C., ELROD, H.G., "Conditions For the Rupture of a Lubricating Film. Part 1: Theoretical Model", *Trans. A. S. M. E., J. Lubr. Technol.*, 92, p 451, [1970]

COYNE, J.C., ELROD, H.G., "Conditions For the Rupture of a Lubricating Film.

Part 2: New Boundary Conditions For Reynolds Equation", *Trans. A. S. M. E., J. Lubr. Technol.*, 93, p 156, [1971]

DEAN, W.R., MONTAGNON, P.E., "On The Steady Motion of Viscous Liquid in a Corner", *Proc. Camb. Phil. Soc.*, 45, p 389, [1949]

DOWSON, D., TAYLOR, C.M., "Cavitation in Bearings", *Ann. Rev. Fluid. Mech.*, 11, pp 35-66, [1979]

DUSSAN V, E.B., "The Moving Contact Line: The Slip Boundary Condition", *J. F. M.*, 77, part 4, pp 665-684, [1976]

DUSSAN V, E.B., " On the Spreading of Liquids on Solid Surfaces: Static and Dynamic Contact Lines", *Ann. Rev. Fluid. Mech.*, 11, pp 371-400, [1979]

ESMAIL, M.N., HUMMEL, R.L., "Nonlinear Theory of Free Coating onto a Vertical Surface", *A. I. Ch. E. J.*, 21, No 5, p 958, Sept [1975]

FLOBERG, L., "On hydrodynamic lubrication with special reference to sub-cavity pressures and numbers of streamers in cavitation regions", *Acta. Polytech. Scand. Mech. Eng. Ser. M. E.*, 19, [1965]

FORTIN, M., THOMASSET, F., "Mixed Finite Element Methods For Incompressible Flow Problems", *J. Comput. Phys.*, 31, pp 113-145, [1979]

GASKELL, P.H., LAU, A.K.C., WRIGHT, N.G., "Comparison of Two Solution Strategies for Use with Higher Order Discretisation Schemes for Fluid Flow Simulation", *Int. J. Numer. Meth. Fluids*, 8, p 1203, [1988]

GASKELL, P.H., MOBBS, S.D., "An Efficient Vorticity-Streamfunction Finite Element Method For Viscous Flow", *23rd Brit. Theo. Mech. Coll. Leeds*, [1985]

GASKELL, P.H., SAVAGE, M.D., THOMPSON, H.M., "Creeping Flow: Novel Analytic and Finite Element Solutions", *7th International Conference on Numerical Methods in Laminar and Turbulent Flow (eds. Taylor, Chin, Homsy)*, pp 1743-1753, [1991]

GHIA, U., GHIA, K.N., SHIN, C.T., "High Re Solutions For Incompressible Flows using the Navier-Stokes Equations and a Multigrid Method", *J. Comp. Phys.*, 48, pp 387-411, [1982]

GREENER, J., MIDDLEMAN, S., "A Theory of Roll Coating of Viscous and Viscoelastic Fluids", *Polymer Engng and Science*, 15, p 1, [1975]

GREENER, J., SULLIVAN, T., TURNER, B., MIDDLEMAN, S., "Ribbing Instability of a Two Roll Coater: Newtonian Fluids", *Chem. Eng. Commun.*, 5, pp 73-83, [1980]

GREENER, J., MIDDLEMAN, S., "Reverse Roll Coating of Viscous and Viscoelastic Liquids", *Ind. Eng. Chem. Fundam.*, 20, pp 63-66, [1981]

GREENOUGH, C., ROBINSON, K. (eds), *NAg-Finite Element Library, Level 0 and Level 1 Documentation, Rutherford Appleton Laboratory, S.E.R.C.*, [1981]

HAGER, W.W., "Applied Numerical Linear Algebra", *Prentice-Hall*, [1988]

HARPER, J.F., WAKE, G.C., "Stokes Flow Between Parallel Plates Due to a Transversely Moving End Wall", *I. M. A. Journal of Applied Maths*, 30, pp 141-149, [1983]

HEUBNER, K.H., "The Finite Element Method For Engineers", *Wiley*, [1975]

HILLMAN, A.P., SALZER, H.E., "Roots of $\sin z = z$", *Philosophical Magazine*, 34, p 575, [1943]

HIRSCH, C., "Numerical Computation of Internal and External Flows. Vol 1: Fundamentals of Numerical Discretisation", *Wiley*, [1988]

HO, W.S., HOLLAND, F.A., "Between-Rolls Metering Coating Technique: A Theoretical and Experimental Study", *T. A. P. P. I.*, 61, No 2, p 53, Feb [1978]

HOARE, W.E., "Variation in Thickness of the Tin Coating of Tinplate and its Effect on Porosity", *J. Iron. Steel. Inst.*, 136, p 99, [1937]

HOCKING, L.M., "A Moving Fluid Interface on a Rough Surface", *J. F. M.*, 76, part 4, pp 801-817, [1976]

HOCKING, L.M., "A Moving Fluid Interface. Part 2. The Removal of the Force Singularity by a Slip Flow", *J. F. M.*, 79, part 2, pp 209-229, [1977]

HOOD, P., TAYLOR, C., "Navier-Stokes Equations using Mixed Interpolation", *Finite Element Methods in Flow Problems (eds. Oden, J.T., et al), University of Alabama, Huntsville Press*, pp 121-132, [1974]

HOOD, P., "Frontal Solution Program For Unsymmetric Matrices", *Int. J. Numer. Meth. Eng.*, 10, pp 379-399, [1976]

HOPKINS, M.R., "Viscous Flow Between Rotating Cylinders and a Sheet Moving Between Them", *Brit. J. Appl. Phys.*, 8, p 442, [1957]

HUGHES, T.J.R., "The Finite Element Method: Linear Static and Dynamic Finite

Element Analysis", [1987]

HUH, C., SCRIVEN, L.E., "Hydrodynamic Model of Steady Movement of a Solid/ Liquid/ Fluid Contact Line", *J. Colloid and Interface Science*, 35, No 1, p 85, Jan [1971]

HUYAKORN, P.S., TAYLOR, C.T., LEE, R.L., GRESHO, P.M., "A Comparison of Various Mixed-Interpolation Finite Elements in the Velocity-Pressure Formulation of the Navier-Stokes Equations", Computers and Fluids, 6, pp 25-35, [1978]

IRONS, B.M., "A Frontal Solution Program For Finite Element Analysis", *Int. J. Numer. Meth. Eng.*, 2, pp 5-32, [1970]

ISAACSON, E., KELLER, H.B., "Analysis of Numerical Methods", *Wiley, New York*, [1966]

JOSEPH, D.D., STURGES, L., "The Convergence of Biorthogonal Series For Biharmonic and Stokes Flow Edge Problems: Part II", *S. I. A. M. J. Appl. Math.*, 34, pp 7-26, [1978]

KELMANSON, M.E., "Boundary Integral Equation Solution of Viscous Flows with Free Surfaces", *J. Eng. Math.*, 17, pp 329-343, [1983]

KISTLER, S.F., *PhD Thesis*, University of Minnesota, Minneapolis, [1983]

KISTLER, S.F., SCRIVEN, L.E., "Coating Flows", *in Computational Analysis of Polymer Processing (eds. J.R.A. Pearson and S.M. Richardson), London and New York: Applied Science*, p 243, [1983]

KISTLER, S.F., SCRIVEN, L.E., "Coating Flow Theory By Finite Element and Asymptotic Analysis of the Navier-Stokes System", *Int. J. Numer. Meth. Fluids*, 4, pp 209-229, [1984]

LANDAU, L., LEVICH, B., "Dragging of a Liquid By a Moving Plate", *Acta Physicochimica U.R.S.S.*, Vol XVII, No 1-2, p 42, [1942]

LAUDER, W., "Hydrodynamic lubrication of Proximate Cylindrical Surfaces of Large Relative Curvature", *Proc. Inst. Mech. Engrs. Elastohydrodynam. Lubr.*, 180, part 3B, pp 101-106, [1966]

LEE, R.L., GRESHO, P.M., SANI, R.L., "Smoothing Techniques For Certain Primitive Variable Solutions of the Navier-Stokes Equations", *Int. J. Numer. Meth. Engng.*, 14,

pp 1785-1804, [1979]

MALONE, B., *PhD Thesis*, University of Leeds, [1992]

MICHAEL, D.H., "The Separation of a Viscous Fluid at a Straight Edge", *Mathematika*, 5, pp 82-84, [1958]

MILL, C.C., SOUTH, G.R., "Formation of Ribs on Rotating Rollers", *J. F. M.*, 28, p 523, [1967]

MOFFATT, H.K., "Viscous and Resistive Eddies Near a Sharp Corner", *J. F. M.*, 18, p 1, [1964]

MOFFATT, H.K., "Behaviour of a Viscous Film on the Outer Surface of a Rotating Roll", *Journal de Mecanique*, 18, part 15, pp 77-93, [1977]

NICKELL, R.E., TANNER, R.I., CASWELL, B., "The Solution of Viscous Incompressible Jet and Free Surface Flows Using Finite Element Methods", *J. F. M.*, 65, part 1, pp 189-206, [1974]

ODEN, J.T., CAREY, J.F., "Finite Elements: Mathematical Aspects", *Vol 4, Prentice-Hall*, [1984]

OLSON, M.D., TUANN, S.Y., "Primitive Variable Versus Streamfunction Finite Element Solutions of the Navier-Stokes Equations", *Finite Elements in Fluids, (eds Gallagher R.H. et al)*, 3, pp 73-87, [1978]

PAN, F., ACRIVOS, A., "Steady Flows in rectangular cavities", *J. F. M.*, 28, part 4, pp 643-655, [1967]

PEARSON, J.R.A., "The Instability of Uniform Viscous Flow Under Rollers and Spreaders", *J. F. M.*, 7, p 481, [1960]

PITTS, E., GREILLER, J., "The Flow of Thin Liquid Films Between Rollers", *J. F. M.*, 11, p 33, [1961]

PRASAD, A.K., PERNG, C-Y., KOSEFF, J.R., "Some Observations on the Influence of Longditudinal Vortices in a Lid-Driven Cavity Flow", *1st National Fluid Dynamics Congress, A. I. A. A./ A. S. M. E./ S. I. A. M./ A. P. S.*, p 288, [1988]

LORD RAYLEIGH (J.W. STRUTT), "On the Theory of Resonance", *Trans. Roy. Soc. (London)*, A161, pp 77-118, [1870]

REYNOLDS, O., "On the Theory of Lubrication and its Applications to Mr Beauchap

Towers' Experiments, Including an Experimental Determination of the Viscosity of Olive Oil", *Phil. Trans. Roy. Soc. A*, <u>177</u>, [1886]

RICHARDSON, S., "A "stick-slip" problem related to the motion of a free jet at Low Reynolds numbers", *Proc. Camb. Phil. Soc.*, <u>67</u>, pp 477-489, [1970]

RICHARDSON, S., *Private Communication*, [1988]

RITZ, W., "Uber eine neue Methode zur Losung gewissen Variations – Probleme der Mathematischen Physik", *J. Neue Angew. Math.*, <u>135</u>, pp 1-61, [1909]

ROBBINS, C.I., SMITH, R.C.T., "A Table of Roots of $\sin z = -z$", *Philosophical Magazine*, <u>39</u>, pp 1004-1005, [1948]

RUCKENSTEIN, E., DUNN, C.S., "Slip Velocity During Wetting of Solids", *J. Colloid and Interface Science*, <u>59</u>, No 1, p 135, March [1977]

RUCKENSTEIN, E., RAJORA, P., "On the No-Slip Boundary Condition of Hydrodynamics", *J. Colloid and Interface Science*, <u>96</u>, No 2, p 488, Dec [1983]

RUSCHAK, K.J., "A Method For Incorporating Free Boundaries with Surface Tension in Finite Element Fluid-Flow Simulators", *Int. J. Numer. Meth. Engng.*, <u>15</u>, pp 639-648, [1980]

RUSCHAK, K.J., "Boundary Conditions at a Liquid/Air Interface in Lubrication Flows", *J. F. M.*, <u>119</u>, pp 107-120, [1982]

RYSKIN, G., LEAL, L.G., "Numerical Solution of Free-Boundary Problems in Fluid Mechanics. Part 1. The finite-difference technique", *J. F. M.*, <u>148</u>, pp 1-17, [1984]

SAITO, H., SCRIVEN, L.E., "Study of Coating Flow by the Finite Element Method", *J. Comput. Phys.*, <u>42</u>, pp 53-76, [1981]

SAMAN, W.Y., *PhD Thesis*, University of Leeds, [1974]

SANI, R.L., GRESHO, P.M., LEE, R.L., GRIFFITHS, D.F., "The Cause and Cure (?) of the Spurious Pressures Generated by Certain F.E.M. Solutions of the Incompressible Navier-Stokes Equations: Part 1 and Part 2", *Int. J. Numer. Meth. Fluids*, <u>1</u>, [1981]

SAVAGE, M.D., "Cavitation in Lubrication. Part 1. On boundary conditions and cavity-fluid interfaces", *J. F. M.*, <u>80</u>, part 4, pp 743-755, [1977 a]

SAVAGE, M.D., "Cavitation in Lubrication. Part 2. Analysis of wavy interfaces", *J. F. M.*, <u>80</u>, part 4, pp 757-767, [1977 b]

SAVAGE, M.D., "Mathematical Models For Coating Processes", *J. F. M.*, 117, pp 443-455, [1982]

SAVAGE, M.D., "Mathematical Models For the Onset of Ribbing", *A. I. Ch. E. J.*, 30, No 6, pp 999-1002, [1984]

SAVAGE, M.D., *Private Communication*, [1992]

SCHUNK, P.R., SCRIVEN, L.E., "On Modelling the Effects of Polymer Additives in Coating Flows", *Paper No. 35 B, A. I. Ch. E. Spring National Meeting, Orlando*, [1990]

SHEPHARD, M.S., "Approaches to Automatic Generation and Control of Finite Element Meshes", *App. Mech. Rev.*, 41, No 4, April [1988]

SILLIMAN, W.J., SCRIVEN, L.E., "Slip of Liquid Inside a Channel Exit", *Phys. Fluids*, 21, pp 2115-2116, [1978]

SILLIMAN, W.J., *PhD Thesis*, University of Minnesota, Minneapolis, [1979]

SILLIMAN, W.J., SCRIVEN, L.E., "Separation Flow Near a Static Contact Line: Slip at a Wall and Shape of a Free Surface", *J. Comput. Phys.*, 34, pp 287-313, [1980]

SMITH, E.H., *PhD Thesis*, University of Leeds, [1975]

SMITH, I.M., "Programming the Finite Element Method With Applications to Geomechanics", *Wiley*, [1982]

SMITH, R.C.T., "The Bending of a Semi-Infinite Strip", *Austral. J. Sci. Res.*, 5, pp 227-237, [1952]

SOROKA, A.J., TALLMADGE, J.A., "Velocity Profiles For Plate Withdrawal at High Speeds", *Appl. Sci. Res.*, 25, p 413, March [1972]

STEIBER, W., "Das Schwimmlager, Hydrodynamische Theorie des Gleitlagers", *Berlin V.D.I.*, [1933]

STRANG, G., FIX, G.J., "An Analysis of the Finite Element Method", *Prentice-Hall*, [1973]

SULLIVAN, T.M., MIDDLEMAN, S., "Roll Coating in the Presence of a Fixed Constraining Boundary", *Chem. Engng. Commun.*, 3(6), p 469, [1979]

SWIFT, H.W., "The Stability Analysis of Lubricating Films in Journal Bearings", *Proc. Inst. Civ. Engrs*, 223, p 267, [1931]

TANNER, R.I., NICKELL, R.E., BILGER, R.W., "Finite Element Methods For the Solution of some Incompressible Non-Newtonian Fluid Mechanics Problems with Free Surfaces", *Comput. Meth. Appl. Mech. Eng.*, 6, pp 155-174, [1975]

TAYLOR, G.I., "Cavitation of a Viscous Fluid in Narrow Passages", *J. F. M.*, 16, pp 595-619, [1963]

TEKIC, M.N., JOVANOVIC, S., "Liquid Coating Onto a Rotating Roll", *Chem. Eng. Sci.*, 37, No 12, pp 1815-1817, [1982]

THARMALINGHAM, S., WILKINSON, W.L., "The Coating of Newtonian Liquids onto a Roll Rotating at Low Speeds", *Polymer Engineering and Science*, 18, No 15, Nov [1978]

THOMPSON, E.G., LAWRENCE, R.E., FONG-SHENG, L., "The Finite Element Method For Slow Incompressible Viscous Flow with a Free Surface", *Developments in Mechanics*, 5, pp 93-111, [1969]

WHITE, D.A., TALLMADGE, J.A., "Theory of Drag Out of Liquids on Flat Plates", *Chem. Eng. Sci.*, 20, pp 33-37, [1965]

WILLIAMSON, A.S., "The Tearing of an Adhesive Layer Between Flexible Tapes Pulled Apart", *J. F. M.*, 52, pp 639-656, [1972]

WILSON, S.D.R., "The Drag-Out Problem in Film Coating Theory", *J. Engng. Math.*, 16, pp 209-221, [1982]

WOLVERIDGE, P.E., BAGLIN, K.P., ARCHARD, J.F., "The Starved Lubrication of Cylinders in Line Contact", *Proc. Inst. Mech. Eng.*, 185, pp 1159-1169, [1971]

WU, C-Y., WENG, C-I., CHEN, C-K., "Analysis of Free Coating Onto a Rotating Roll", *Chem. Eng. Commun.*, 33, pp 245-254, [1985]

YIH, C-S, "Instability of a Rotating Liquid Film with a Free Surface", *Proc. Roy. Soc. (A)*, 258, pp 63-86, [1960]

ZIENKIEWICZ, O.C., "The Finite Element Method", *(3rd edition), McGraw-Hill,* [1977]